# Control System for the Next Generation In-flight Separator Super-FRS applied to New Isotope Search with the FRS

**Kontrollsystem für die nächste Generation Flugseparator Super FRS angewendet für die neue Isotopensuche mit dem FRS**

Zur Erlangung des Grades eines Doktors der Naturwissenschaften (Dr. rer. nat.)
Vom Fachbereich Physik der Technischen Universität Darmstadt
Genehmigte Dissertation von Jan-Paul Alexander Hucka M. Sc. aus Frankfurt am Main
Tag der Einreichung: 01.12.2022, Tag der Prüfung: 30.01.2023

1. Gutachten: Prof. Dr. Joachim Enders
2. Gutachten: Prof. Dr. Thorsten Kröll
Darmstadt, Technische Universität Darmstadt – D17
Jahr der Veröffentlichung der Dissertation auf TUprints: 2023

TECHNISCHE UNIVERSITÄT DARMSTADT

Physics Department
Institut für Kernphysik
AG Enders

Control System for the Next Generation In-flight Separator Super-FRS applied to New Isotope Search with the FRS
Kontrollsystem für die nächste Generation Flugseparator Super FRS angewendet für die neue Isotopensuche mit dem FRS

Accepted doctoral thesis by Jan-Paul Alexander Hucka M. Sc.

1. Review: Prof. Dr. Joachim Enders
2. Review: Prof. Dr. Thorsten Kröll

Date of submission: 01.12.2022
Date of thesis defense: 30.01.2023

Darmstadt, Technische Universität Darmstadt – D17
Jahr der Veröffentlichung der Dissertation auf TUprints: 2023

Bitte zitieren Sie dieses Dokument als:
URN: urn:nbn:de:tuda-tuprints-232991
URL: http://tuprints.ulb.tu-darmstadt.de/23299

Dieses Dokument wird bereitgestellt von tuprints,
E-Publishing-Service der TU Darmstadt
http://tuprints.ulb.tu-darmstadt.de
tuprints@ulb.tu-darmstadt.de

This thesis is dedicated to my wife Sharlen Smith and my parents Zuzana and Jan Hucka. Without their unconditional love, support and encouragement this work would have never been finished.

# Erklärungen laut Promotionsordnung

## §8 Abs. 1 lit. c PromO

Ich versichere hiermit, dass die elektronische Version meiner Dissertation mit der schriftlichen Version übereinstimmt.

## §8 Abs. 1 lit. d PromO

Ich versichere hiermit, dass zu einem vorherigen Zeitpunkt noch keine Promotion versucht wurde. In diesem Fall sind nähere Angaben über Zeitpunkt, Hochschule, Dissertationsthema und Ergebnis dieses Versuchs mitzuteilen.

## §9 Abs. 1 PromO

Ich versichere hiermit, dass die vorliegende Dissertation selbstständig und nur unter Verwendung der angegebenen Quellen verfasst wurde.

## §9 Abs. 2 PromO

Die Arbeit hat bisher noch nicht zu Prüfungszwecken gedient.

Darmstadt, 01.12.2022

J.P. Hucka

# Acknowledgements

Financial Support by the German Ministry for Education and Research (BMBF), grants 05P15RDFN1, 05P19RDFN1, and 05P21RDFN1, the GSI-TU Darmstadt cooperation contract, and the State of Hesse through the Helmholtz Forschungsakademie Hessen für FAIR (HFHF) is gratefully acknowledged.

The personal as well as professional support and supervision given by Dr. Stephane Pietri, Prof. Dr. Joachim Enders, the members of the FRS and Super-FRS working groups, the colleagues from the GSI and FAIR facilities together with all the members of the S468 experiment, Super-FRS Experimental and NuSTAR Collaborations is greatly and deeply appreciated. Without you, the experiment would not have been possible and this thesis would have never seen the light of day. Thank you.

# Zusammenfassung

Der Bau der neuen FAIR-Anlage bringt eine Aufrüstung der bestehenden GSI-Beschleunigeranlage mit sich. Eine der Aufrüstungen ist die Integration des neuen LSA-Kontrollsystems, das vom CERN lizenziert und angepasst wurde, um eine einheitliche Kontrollumgebung für alle Beschleuniger, Ringe und Transferlinien sowohl an der GSI- als auch an der FAIR-Anlage zu schaffen. Im Rahmen dieser Arbeit war es möglich, den FRS als Maschinenmodell in LSA einzubinden, indem Parameterhierarchien und Makerules entwickelt und implementiert wurden, um einen organisierten und maximal parallelen Betrieb zu ermöglichen. Zu diesem Zweck wurde eine allgemeine FRS Target Hierarchie implementiert, um Targets, Targetleitern, Degrader, Degraderdisks, Degraderleitern, Detektoren und Detektorleitern so realistisch wie möglich abzubilden, mit zusätzlichen Makerules, um automatisierte Online-Energieverlustberechnungen, Sekundärstrahlerzeugung innerhalb von Targets, bedienergesteuertes Überschreiben der magnetischen Steifigkeit und Berechnungen zur ionenoptischen Targetausrichtung zu ermöglichen. Zusätzlich wurden auch Schlitze, pneumatische Antriebe und Schrittmotoren in das Maschinenmodell integriert.
Beim Benchmarking erwiesen sich das Maschinenmodell und LSA als äquivalent zu früheren Kontrollsystemen, indem sie alte experimentelle Einstellungen mit einer Genauigkeit von $10^{-4}$ bzw. $10^{-3}$ für die magnetische Steifigkeit und den Strom reproduzierten. Zeitgenössische Experimente können sogar im Rahmen der Mess- und Einstellgenauigkeit identisch reproduziert werden. Zusätzliche Tests mit einem $^{40}$Ar- und $^{238}$U-Primärstrahl zeigten, dass das Maschinenmodell in der Lage ist, Primär- und Sekundärstrahlfragmente ohne vorherige Einstellungsberechnung über LISE++ korrekt an die vorgesehene Experimentierstation zu transportieren, und bewiesen, dass alle Funktionen funktionsfähig sind.
Diese Grundlage wurde während der FAIR Phase-0 Experimente an der GSI genutzt, um mit einem relativistischen $^{208}$Pb-Primärstrahl bei 1050 $A\mathrm{MeV}$ auftreffend auf ein Beryllium-Target von 4 $\mathrm{g\,cm^{-2}}$ Dicke mit einem Niob-Stripper von 225 $\mathrm{mg\,cm^{-2}}$ Dicke potentiell bis zu 21 neue Isotope zu erzeugen und mit den hier beschriebenen Methoden vorläufig zu identifizieren. Hinweise auf die erstmalige Identifizierung der Nuklide $^{200,201,202}$Re, $^{198,199}$W, $^{195,196,197}$Ta, $^{191,192,193}$Hf, $^{189,190,191}$Lu, $^{186,187}$Yb, $^{182,183,184,185}$Tm und $^{181}$Er werden vorgestellt.

# Abstract

The construction of the upcoming FAIR facility entails an upgrade of the existing GSI accelerator facility. One of the upgrades is the integration of the new LSA control system framework, which is licensed and adapted from CERN, in order to provide a unified control environment for all accelerators, rings and transfer lines at both the GSI and FAIR facility. As part of this work, it was possible to incorporate the FRS as a machine-model within LSA by developing and implementing Parameter hierarchies and Makerules to enable streamlined and maximum parallel operations. For this purpose a FRS General Target Hierarchy was implemented to virtually map targets, target ladders, degraders, degrader disks, degrader ladders, detectors and detector ladders as realistically as possible with additional Makerules to facilitate automated online energy-loss calculations, secondary beam production within targets, operator driven magnetic rigidity overwriting and ion-optical target alignment calculations. Additionally slits, pneumatic drives and stepper motors were introduced into the machine-model, as well.

Benchmarking proved for the machine-model and LSA to be equivalent to previous control systems by reproducing old experimental settings within an accuracy of $10^{-4}$ and $10^{-3}$ for the magnetic rigidity and current, respectively. Contemporary experiments can be even identically reproduced within the measurement and setting precision. Additional testing with a $^{40}$Ar and $^{238}$U primary beam showed the machine-model's capabilities in correctly transporting primary and secondary beam fragments to the destined experimental station without previous setting calculation via LISE++, proving all functionalities operative.

This foundation was used during FAIR Phase-0 experiments at the GSI to produce and using the methods described here it was possible to preliminarily identify up to 21 new isotopes with a relativistic $^{208}$Pb primary beam at 1050 $A\mathrm{MeV}$ impinging on a beryllium target of 4 $\mathrm{g\,cm^{-2}}$ thickness with a niobium stripper backing of 225 $\mathrm{mg\,cm^{-2}}$ thickness to first produce $^{200,201,202}$Re, $^{198,199}$W, $^{195,196,197}$Ta, $^{191,192,193}$Hf, $^{189,190,191}$Lu, $^{186,187}$Yb, $^{182,183,184,185}$Tm and $^{181}$Er.

# Contents

# 1. Introduction

The study of nuclear structure information of stable nuclei alone is limited, both in a sense that that stable nuclei have been studied already in some detail and that extrapolation of nuclear-structure properties to radioactive isotopes is not always possible. Isotopes that are located far away from the valley of stability have to be produced and studied directly at large-scale facilities like the GSI, that produce radioactive heavy-ion beams [1, 2, 3]. This window allows to pierce the veil of the unknown into highly neutron-rich and -deficient isotopes that contribute via different nuclear astrophysical processes to the mass abundances that can be studied nowadays. One of these processes is the r-process [4, 5], the rapid neutron-capture process, which is hoped to be studied in greater detail at the GSI and FAIR facilities with the help of radioactive beams [6, 7]. These processes depend upon the measured masses, lifetimes, $\gamma$- and $\beta$-decay spectra and production cross sections, leading to an understanding of binding energies, the nuclear shell structure or deviation thereof, branching ratios and ultimately the path the r-process takes.
Projectile fragmentation [1, 8, 9] is a feasible alternative to produce both neutron-rich and -deficient nuclei, in which a heavy-ion beam impinges on a target at high, relativistic energies ($\sim 1\ A\mathrm{GeV}$ at GSI) and in a simple representation the ions are being abraded by the target nucleus. The resulting ejectile fragments carry most of their initial forward-facing momentum distributions and consist of a mixed number of various isotopes whose Z and A are lower than that of its initial beam. Since the addition of the Schwerionen-synchrotron (SIS18) and Fragment Separator (FRS) in 1990 [10] the potential of the GSI to push the boundaries of the nuclide chart towards more exotic nuclei by producing relativistic heavy-ion beams and applying projectile fragmentation and fission with the magnetic in-flight separation capabilities of the FRS [11] has been unlocked.
More than 150 new nuclides have been produced and their properties measured at the FRS [12] and additionally six new elements [13, 14, 15, 16, 17, 18] have been discovered at the GSI with the UNILAC [19]. The further one moves away from stable isotopes in the nuclide chart the lower the resulting production rate and yield become. This can be improved by finding optimized target setups, improving the transmission of the FRS or more simply by increasing the intensity of the main beam impinging on the target. The first two points are related to the FRS and is part of its ongoing research whereas the last point is the limiting factor for the whole GSI and its experimental collaborations. This led to the ongoing upgrade of the GSI to the FAIR (Facility for Antiproton and Ion Research in Europe) facility, as can be seen in Fig. 1.1, which has started its civil construction in 2017 [10] and encompasses the new ring accelerator Schwerionensynchrotron 100 (SIS100), the Superconducting Fragmentseparator (Super-FRS), several new experimental and storage rings and new experimental areas with either newly developed or upgraded detectors.
Together with the new hardware and machinery that will allow for higher energetic and more intense beams, a new joint control-system framework for GSI and FAIR is being implemented to allow the control of tens of thousands of components and streamlined automated operations in order to maximize experimental beam time for up to four experiments in parallel. Starting in 2015 [20] a setting generator for the FRS was designed within the newly adapted LHC Software Architecture (LSA) from CERN [21] and benchmarked with older experimental data as a conceptual proof of principle for the Super-FRS. The simple model

which consisted of matter and ion-optical elements was already capable to execute automatic energy-loss calculations via ATIMA [22] routines and set the correct $B\rho$ values to the individual virtual devices.

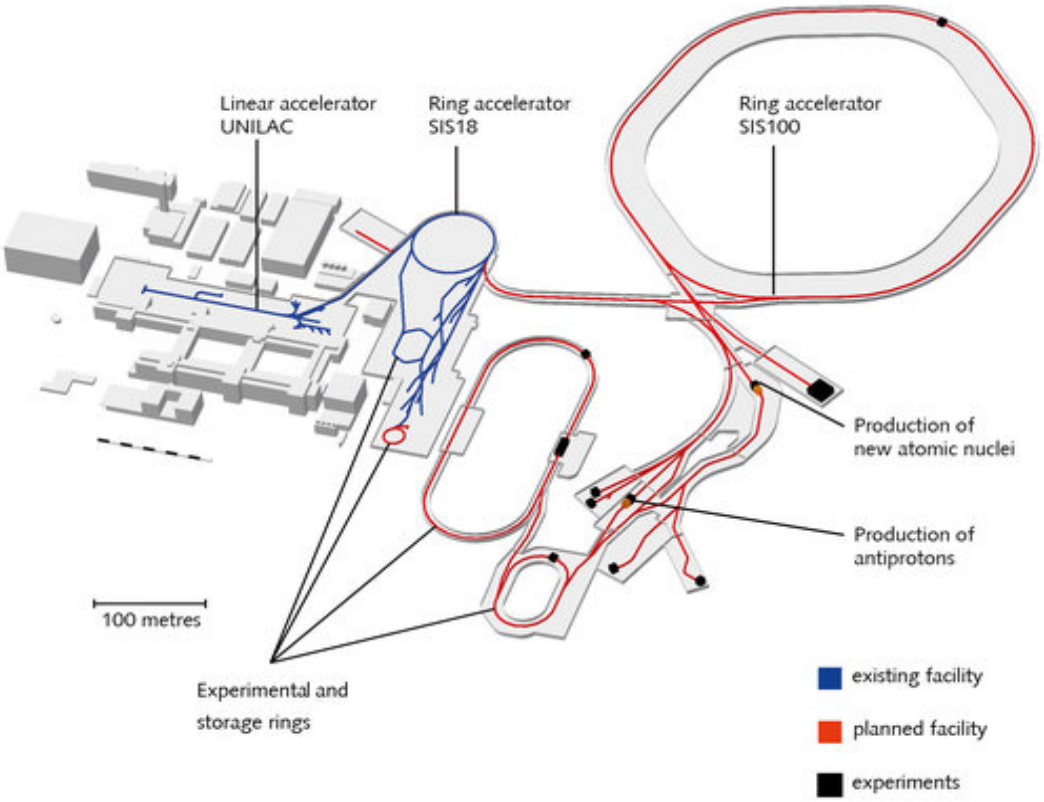


**Figure 1.1.:** Overview of the current GSI (blue) and planned FAIR (red) facility [23]. Firstly a heavy-ion beam is accelerated in the UNILAC up to 20% the speed of light and then sent into the SIS18 to be accelerated up to 90% the speed of light. From here on the beam can then be sent directly into the different experimental areas or into the FRS to produce either a secondary singular exotic beam or a cocktail of different isotopes. Additionally, it would also be possible to use SIS18 as a pre-accelerator stage for SIS100 and achieve higher energies. Afterwards it can be sent to the FAIR experimental areas and rings. Copyright at GSI/FAIR, used with permission.

Thus the problem definition of this dissertation is twofold: Firstly, continue development such that the designed model in [20] represents the FRS as realistically as possible, port the solution into the production server to enable hardware communication, ensure that former functionalities are preserved for the operators and test the concepts with a heavy-ion beam. Secondly, conduct an experiment where nuclide identification is crucial with the developed solutions at the FRS. For the first aspect the machine-model of the FRS was extended in two ways, the machine-model does not only contain the main branch, going from TA to S4 but also the side branches, i.e. TA-S6 and TA-Cave C, for nomenclature see Sec. 2.1. Additionally missing devices and device types have been added to complete the machine-model, which led to the implementation of slits, stepper motors, pneumatic drives and their respective methods inside LSA. Slits have the functionality to change the $B\rho$ by applying cuts in the position space and drives/motors can hold position information. In order to preserve functionalities, a method has been implemented which circumvents the automatic energy-loss calculation and lets operators input the magnetic rigidity for each section individually. Furthermore,

several external sequences were implemented which allowed a) all magnets to be cycled along their hysteresis curve, in order to guarantee reproducibility of settings, b) Hall-effect probes inside the dipoles to be calibrated and c) all drives to be read out and set automatically according to their LSA settings. All these developments were continuously tested during Dry-Runs (simulated machine operation without beam) to assure flawless operation and the final test of the machine-model was done during Engineering-Runs with a heavy-ion beam during the last quarter of 2019, which proved that it was possible to operate the FRS within the LSA framework and the developed solutions.

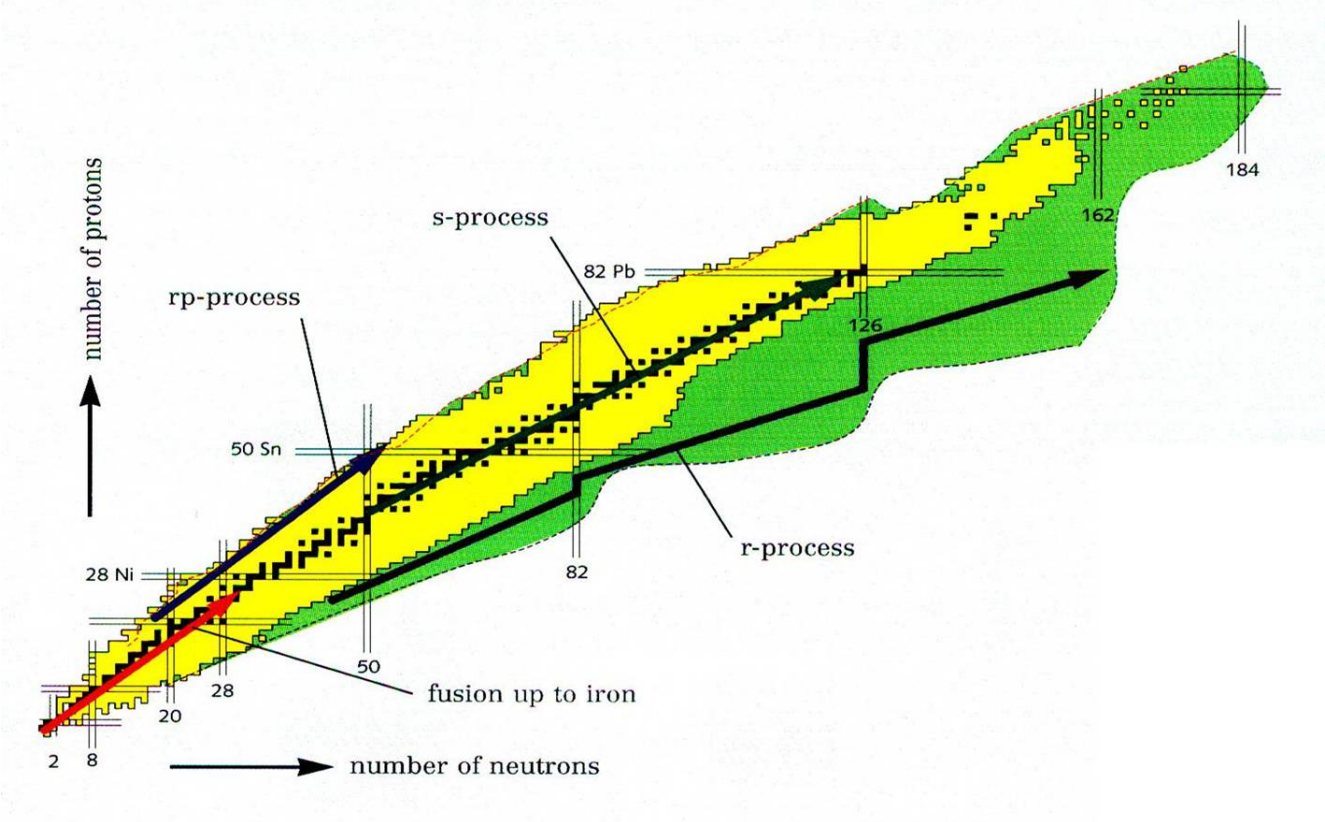


**Figure 1.2.:** Chart of nuclides taken from [24], copyright at University of Tennesse Knoxville, used with permission, with indicated main processes of nucleosynthesis (red and black arrows) within the universe. Stable isotopes are shown in black and all other radioactive isotopes are yellow. Especially more neutron-rich isotopes towards the r-process path are expected to be discovered with FAIR, as symbolized by the green marked areas.

This work laid the foundation for the immediate operation of the FRS throughout 2020 after the Engineering-Runs during the GSI FAIR Phase-0 experimental beam time and future beam times. The goal for this beam time was to utilize equipment, which has been in development or was being upgraded for the FAIR facility and reached a stage that allowed its use in an experiment relating to the physical topics of FAIR. For NuSTAR (Nuclear STructure, Astrophysics and Reactions) the goal is to understand the processes which happen inside stars, supernovas, neutron stars and mergers on a nuclear level and result in both their respective attributes and the synthesis of elements in the universe. It is not only the beauty of producing and discovering isotopes never seen before that drives this research, it is also the information one receives in turn to understand the aforementioned processes, especially the r-process, see Fig. 1.2, by producing neutron-rich isotopes towards the N=126 line. All this information combined leads to a better theoretical understanding and helps to reproduce the production rates and ratios for each stable isotope in the universe. The second part of this dissertation is linked to the experiment ”Search for new neutron-rich isotopes and

exploratory studies in the element range from terbium to rhenium" S468 [25] conducted by the Super-FRS Experimental Collaboration [26] as part of its Physics Topic 1 program to produce new isotopes and study their basic properties. This thesis emphasizes on the identification of new isotopes. The $\beta$-decay lifetimes are currently analyzed by H. Rösch-Kabadayi [27] and M. Luoma [28] and of new mass measurements by D. Amanbayev [29].

# Part I.

# Principles

# 2. FRS and Super-FRS

In the following Secs. 2.1 to 2.4 all necessary principles for the topic of this dissertation will be presented and explained. It will be elaborated how the fragment separators FRS and Super-FRS are set up and how they differ, how isotopes can be identified by their charge and charge-to-mass ratios within the Fragmentseparator and how ATIMA conducts its energy-loss calculation.
In the next Ch. 3 the control system framework LSA will be presented and its core principles as well as the architecture explained.
In order to conclude this Part the nuclear reaction mechanism that was utilized to produce new isotopes within this work will be illustrated in Ch. 4 and explained as well as its respective theoretical calculation model EPAX.

## 2.1. Setup

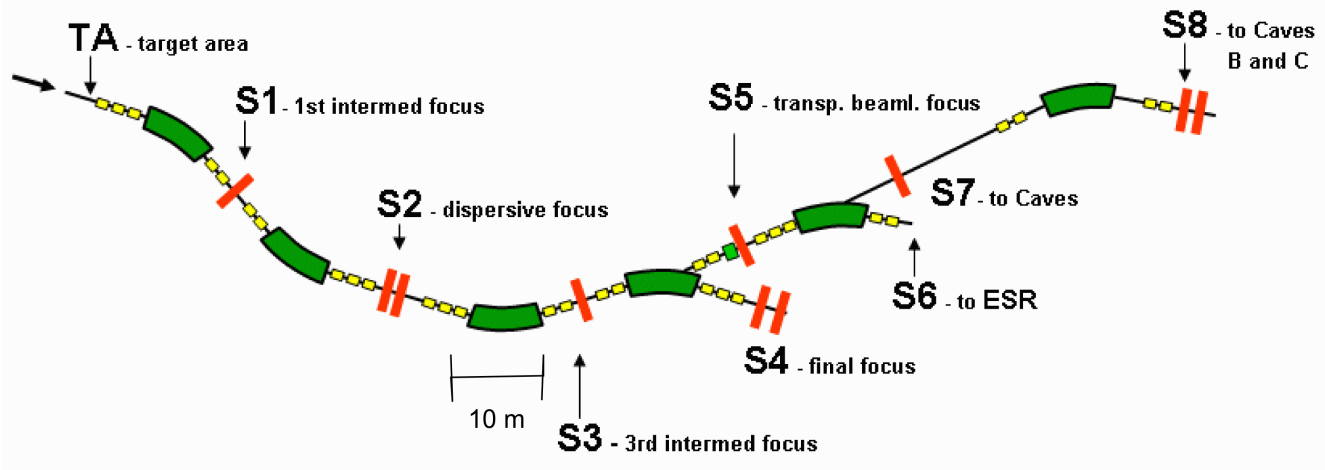


**Figure 2.1.:** Sections of the FRS, taken from [30], and its branching paths to S4, ESR or Cave C. The green elements are the 30 degree deflecting dipoles whereas the yellow elements are the focussing quadrupoles. The red markings represent the respective focal planes. Not visible in this graphic are the sextupoles, horizontal and vertical steerers as well as dipoles before TA and after S8. Copyright at GSI/FAIR, used with permission.

The Fragment Separator, abbreviated FRS, is a magnetic high-resolution forward mass spectrometer, which fulfills the purpose to separate the desired fragments from a multitude of nuclear reactions occurring in a pre-specified target. It was constructed and commissioned in the year 1990 [31] at the GSI Helmholtzzentrum für Schwerionenforschung. It is situated as one of several connecting beam limes

between the Heavy Ion Synchrotron SIS18 (Schwerionensynchrotron), the Experimental Storage Ring ESR (Experimentierspeicherring) and several other experimental areas. An overview can be found in Fig. 2.1. The FRS consists in total of six main dipole segments and nine focal planes, which are TA and S1 to S8, that have also been implemented inside the FRS machine-model to accomodate for R$^3$B experiments. For the experimental part of this work in Part IV, the beam line going from the target area TA to the final focus S4 will be discussed.
Each segment consists of one dipole magnet deflecting by 30 degrees and separating the reaction fragments, one quadrupole triplet consisting of horizontally, vertically and again horizontally focussing quadrupoles along with a doublet of horizontally and vertically or vertically and horizontally focussing quadrupoles. Additional correctional elements are two sextupole magnets, one each immediately in front and behind each dipole, to correct for chromatic aberration. After S1 one vertical steerer can be found in each quadrupole multiplet, which allows for vertical steering and angular correction.
For the separation inside the FRS the $B\rho$-$\Delta E$-$B\rho$-method is being utilized and allows for several modes of operation for the FRS. The one that was used in Part IV and that is being focused on is the ”achromatic mode”, see Fig. 2.2. In this mode all ion-optical elements are adjusted such that the constituents of the secondary particle beam from the target to S2 are being separated by their respective momenta and re-focussed again at the final focal plane S4. This basically creates an identical image of the beam from TA at S4.

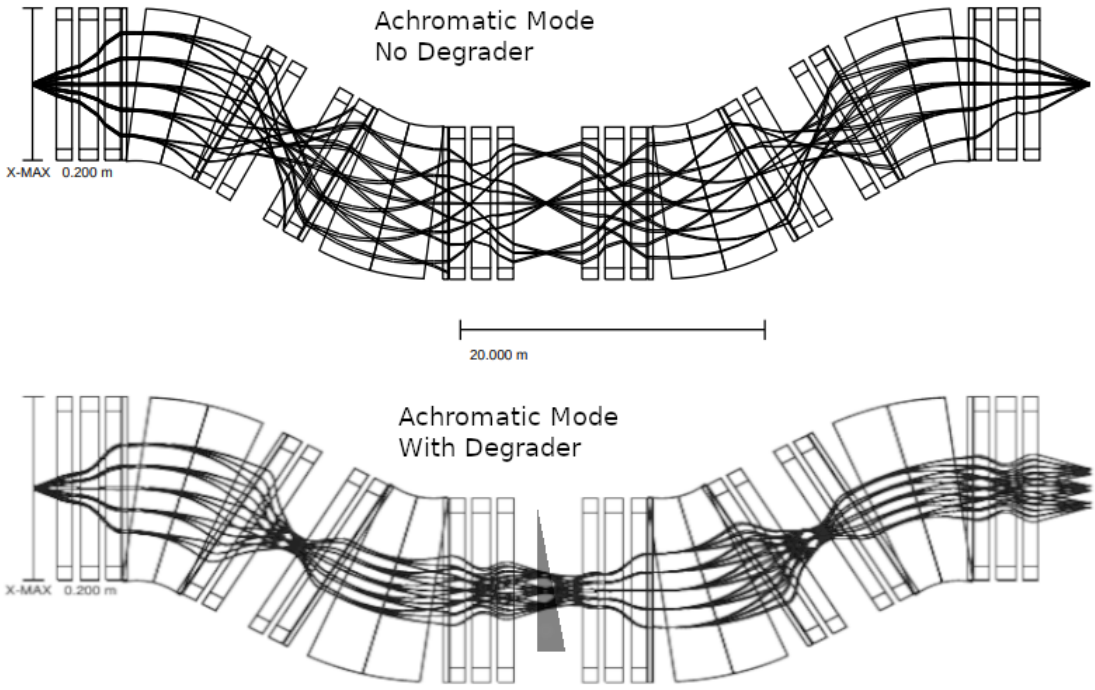


**Figure 2.2.:** Beam paths inside the FRS plotted with the help of GICOSY [32] for different fragments in the achromatic optic mode. The y-axis has a different scale ($\pm$ 100 $\mathrm{mm}$) than the x-axis ($\sim$ 100 $\mathrm{m}$), especially in the lower plot to visualize the spacial separation fragments. Top plot provided by [33] and bottom plot produced via GICOSY.

As a result fragments with a similar mass-to-charge ratio would not be able to be separated and instead they would pass the FRS and be bundled in the same spot. This can be prevented by utilizing a degrader

system at S2 which consists of an aluminium wedge and a disk system causing a position-dependent and therefore momentum-dependent energy-loss for the individual isotopes. Consequently fragments traveling from S2 to S4 possess a charge-state dependent $B\rho$ different from the previous stage TA to S2. The second stage magnifying properties now lead to the horizontal separation of each individual isotope's focus. By introducing slits at each focal plane one can fine-tune their respective position such that either only a small selection or one individual isotope reaches the final focal plane.
In addition to the ion-optical elements and the degrader system, the FRS is equipped with a multitude of detectors, which are used for several purposes and are considered standard equipment. In the target area TA there is the SEETRAM [34], a plastic scintillator and an ionization chamber. These three detectors are used in combination to measure the intensity of the primary beam and to calibrate each other, since they are applied at different intensity regimes. SEETRAM stands for SEcondary Electron TRAnsmission Monitor and utilizes secondary electrons excited and emitted from a thin metal surface layer, through which the primary heavy-ion beam passes, to produce a current in an electric field, which is proportional to the intensity and charge of the impinging particle beam. Due to the usually high intensity of the primary beam hitting the FRS target, two additional CGs (Current Grids [35]) are used for primary beam position monitoring on target and alignment optimization. The most important detectors can then be found at S2 and S4, where there are two TPCs (Time Projection Chambers [36, 37]) and one plastic scintillator at S2 as well as additional two TPCs, two MUSICs (Multiple Sampling Ionization Chamber [38]) and 2 plastic scintillators at S4. The respective pairs of TPCs are used for particle tracking, i.e. the determination of the particle's trajectories from the positions and angles close to the S2 and S4 focal planes, respectively. Both MUSICs are used for energy-loss and therefore charge-state measurement, and finally the plastic scintillators measure the time-of-flight between the focal planes S2 and S4. These detectors are needed to properly and unambiguously identify the fragments passing through the FRS. How the in-flight particle identification works in detail will be discussed in Sec. 2.2. High particle rates in the range of 100 $\mathrm{kHz}$ and higher pose a serious challenge to the detectors mentioned above, because the resolution in position, charge or time-of-flight measurement can be negatively impacted and the efficiency of the individual detectors suffers from too high a rate. In the worst case scenario this might even lead to a permanently damaged detector and unusable data. New and improved detectors [39, 40] are currently being developed and tested at the FRS for use at the Super-FRS, see Fig. 2.3.

| Facility | Max. Magnet. Rigidity $B\rho_{max}$/[Tm] | Momentum Acceptance $\Delta p/p$ | Angular Acceptance $\phi_x$/[mrad] \| $\phi_y$/[mrad] | Momentum Resolution $p/\Delta p$ |
|---|---|---|---|---|
| FRS | 18 | $\pm 1\%$ | $\pm 7.5$ \| $\pm 7.5$ | 1500 ($\epsilon = 20\pi$ mm mrad) |
| Super-FRS | 20 | $\pm 2.5\%$ | $\pm 40$ \| $\pm 20$ | 1500 ($\epsilon = 40\pi$ mm mrad) |

**Table 2.1.:** Comparison of the parameters of FRS and Super-FRS [41]. One can see the higher emittance $\epsilon$ and angular acceptance that can be achieved with the Super-FRS. With $\epsilon$ being a measure for the volume of the heavy-ion beam in the position-and-momentum phase space.

The main benefit of the Super-FRS, in comparison to the FRS, is the usage of superconducting magnet groups, which are composed of a dipole triplet, and each dipole deflects the beam by 11 degrees in the pre-separator and by 9.75 degrees in the main-separator part. Each main dipole group has a superconducting quadrupole triplet before and in front of it together with a number of sextupolar and octupolar ion-optical elements that corresponds to the number of short quadrupolar elements, in order to correct second- and

third-order image aberrations. This results in a higher phase-space acceptance and better transmission, see Tab. 2.1 and Fig. 2.4.

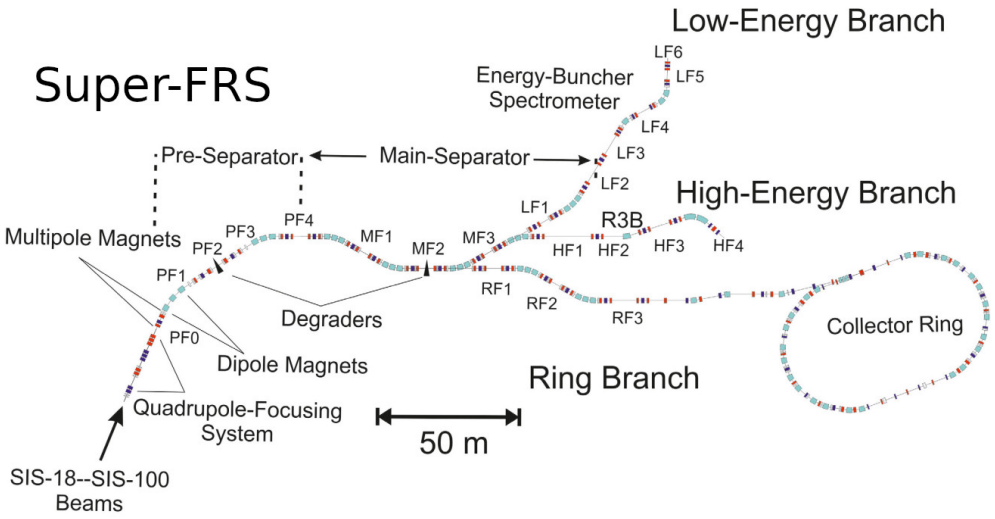


**Figure 2.3.:** Planned layout of the Super-FRS [42]. The heavy-ion beams come from the synchrotrons and are focussed on a production target, where after a pre separation the secondary beam is transfered into the main separator and into one of tree possible experimental branches. Copyright 2021, with permission from Elsevier.

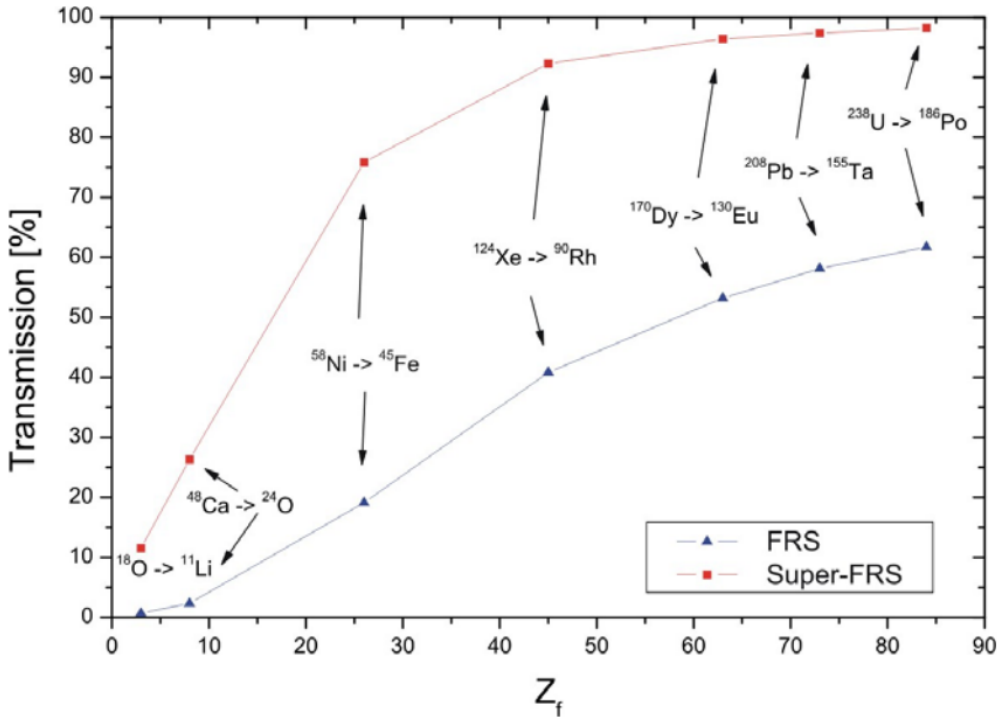


**Figure 2.4.:** Transmission of the FRS (blue) compared with the transmission of the Super-FRS (red) [41]. Copyright at GSI/FAIR, used with permission.

Paired with the two part design of a pre- and a main-separator, the Super-FRS will use the same $B\rho$-$\Delta E$-$B\rho$-method twice in a three-stage design to provide better separation and higher resolving power for secondary relativistic radioactive beams at higher main energies of up to $1.5\ A\mathrm{GeV}$ and main intensities of up to $5 \cdot 10^{11}$ particles per spill. The beam can then be transported to the three different branches, the Low-Energy Branch, the High-Energy-Branch and the Ring Branch, housing different experimental setups. For different primary-beam configurations the transmission for secondary products resulting from projectile fragmentation are calculated at the S4 focal plane (FRS) and FLF2 focal plane (Super-FRS). The energy of the fragments after the production target was 700 $A\mathrm{MeV}$ and the aluminium degrader thicknesses were chosen to be $d/R = 0.5$ and $0.6$, respectively. Here $d$ is the chosen thickness of the degrader in $\mathrm{mg\,cm^{-2}}$ and $R$ the range of the ion in an aluminium equivalent thickness in $\mathrm{mg\,cm^{-2}}$. For the lightest fragments an improvement of up to a factor of 16 can be achieved, whereas for heavier fragments and improvement of up to a factor 1.5 is possible.

## 2.2. In-flight Particle Identification

Unambigious identification of a particle beam and secondary fragments can be achieved by measuring the ratio of mass number $A$ and charge $Q$, i.e. $A/Q$, together with the elementary charge number $Z$. This is necessary to distinguish between isotopes with same charge-states and similar mass-to-charge ratio, which can lead to misidentification and miscounting of events. This will be discussed in the following Sec.

### Mass Identification

Let there be a particle with charge $Q$ which moves with the velocity $\vec{v}$ through a magnetic Field $\vec{B}$. The force that acts on the charged particle is then given by the Lorentz force defined as such $\vec{F_L} = Q(\vec{v} \times \vec{B})$. As a direct result, the particle moves unto an orbit and the force required to keep the particle on this orbit is given by the centripetal force $\vec{F_Z} = m\vec{\omega} \times (\vec{\omega} \times \vec{r})$, where $m$ denotes the mass of the particle, $\vec{\omega}$ the angular velocity vector and $\vec{r}$ the position vector. Therefore the following expression holds true:

$$\vec{F_L} = \vec{F_Z} \tag{2.1}$$

$$Q(\vec{v} \times \vec{B}) = m\vec{\omega} \times (\vec{\omega} \times \vec{r}) \tag{2.2}$$

Now assuming that the magnetic field $\vec{B}$ is homogeneous and the particle moves with $\vec{v}$ on an orbit which is perpendicular to $\vec{B}$, it follows that the resulting trajectory is a circular orbit with constant radius $\rho$. The aforementioned expression (2.2) can therefore be written in scalar form as such using $\omega = \frac{v}{\rho}$

$$QvB = m\,\frac{v^2}{\rho}, \tag{2.3}$$

depending on the experiment this equation already allows the identification of several observables, be it mass $m$, charge $Q$ or the specific charge $\frac{Q}{m}$. At the FRS the ratio of mass-to-charge is $\frac{A}{Q}$ determined. In this case the expression (2.3) can be solved for $B\rho$ and one has to consider the charged particle as relativistic with $m = \gamma m_0 = \gamma Au$ and $\beta = \frac{v}{c}$. It follows that:

$$B\rho = \frac{mv}{Q} = \frac{\gamma Au\beta c}{Q} = \frac{A}{Q}\gamma\beta C, \tag{2.4}$$

where $\gamma$ is the Lorentz factor, $A$ the mass number, $Q$ the charge, the atomic mass unit $u$, the speed of light $c$ and $C = c \cdot u$. The observable $B\rho$ is called the magnetic rigidity with the unit Tesla times meter $[\mathrm{T\,m}]$. This observable is predominantly used in accelerator physics as a gauge for the difficulty to magnetically deflect a particle with momentum $p = mv$ and charge $Q$ unto a circular orbit with radius $\rho$.
In order to achieve $\frac{A}{Q}$ identification, one needs to measure the speed $v$ of the particle and its rigidity $B\rho$, as follows from (2.4). The speed is determined via a time-of-flight measurement utilizing the plastic scintillators at S2 and S4 and their respective time difference. Therefore $\beta$ is

$$\beta = \frac{v}{c} = \frac{L}{t_{tof}c}, \tag{2.5}$$

with $L$ being the distance along the beam axis from the scintillator at S2 to the scintillator at S4 and $t_{tof}$ its respective time-of-flight. The Lorentz factor $\gamma$ can then be easily calculated from $\beta$. In order to determine $B\rho$ itself the four individual dipole magnets and their respective magnetic fields are adjusted and set to a

specific isotope of interest which passes through the FRS on a centered trajectory. Due to the geometrical construction of the dipoles the radius $\rho$ is given for a centered trajectory and constant. These two values determine the $B\rho_0$ of a centered isotope. The rigidity for a non-centered ion is then given by

$$B\rho = B\rho_0 + \Delta B\rho, \tag{2.6}$$

where $\Delta B\rho$ depends on the centered rigidity and the deviation $\delta_{S2-S4}$ from the momentum of the isotope of interest and can be rewritten to

$$B\rho = B\rho_0(1 - \delta_{S2-S4}). \tag{2.7}$$

From first order ion-optical matrix elements it is given that

$$x_{S4} = M_{S2-S4}x_{S2} + D_{S2-S4}\delta_{S2-S4}, \tag{2.8}$$

where $x_{S2}$ and $x_{S4}$ are the horizontal positions inside the S2 and S4 focal plane, $M_{S2-S4}$ the magnification and $D_{S2-S4}$ the dispersion coefficient this leads to the following expression:

$$B\rho = B\rho_0 \left(1 - \frac{(x_{S4} - M_{S2-S4}x_{S2})}{D_{S2-S4}}\right) \tag{2.9}$$

From Eqs. (2.5) and (2.9) we see that the mass-to-charge ratio $\frac{A}{Q}$ of one isotope can be determined by a time-of-flight and horizontal position measurement at S2 and S4.

### Charge Identification

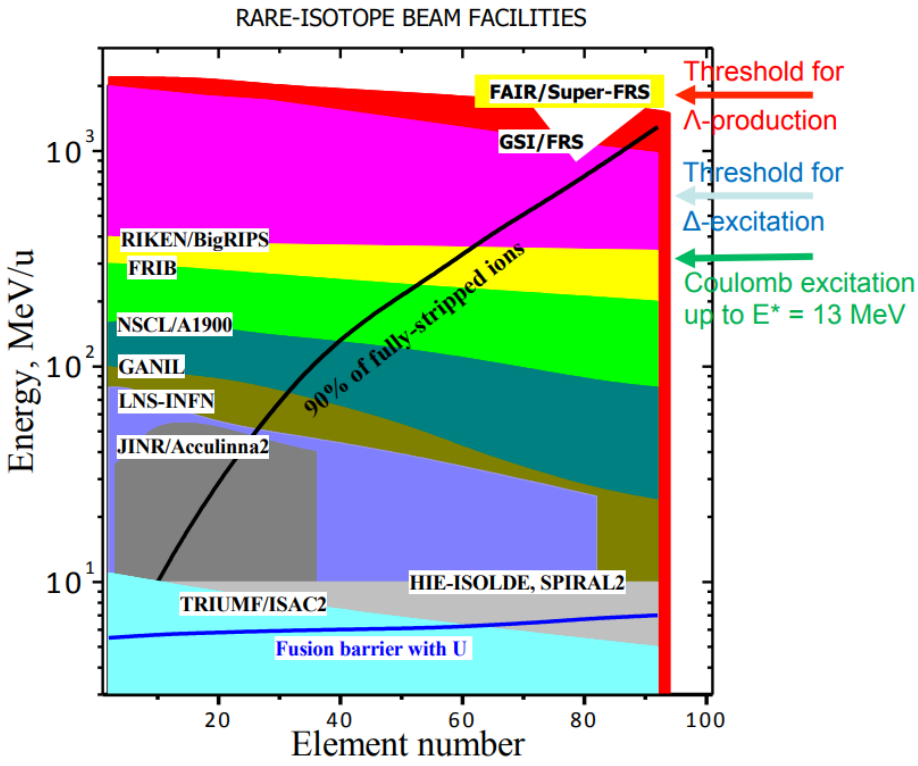


**Figure 2.5.:** Comparison of rare-isotope beam facilities and their capability to produce fully stripped ions at their respective energy and element ranges, taken and adapted from [43, 44]. It is important to note that the GSI in combination with the FRS can deliver a very high proportion of fully stripped ions in the region of Z $\geq$ 80, due to its high energy. Copyright 2000, used with permission from NuPECC.

The determination of $\frac{A}{Q}$ alone doesn't allow the disambiguous identification of an ion since several combinations of different masses and charge-states can lead to the same value. Figure 2.5 shows the capability of different facilities to produce fully stripped ions, with the GSI and FAIR facilities marked, respectively. Given the high possible energies at which heavy-ion beams can be accelerated to with the SIS18, it can be shown with GLOBAL or CHARGE [45] that most heavy-ion beams and their production fragments pass the FRS target and stripper setups as fully-stripped ions. Only the heaviest ion beams and fragments ($Z \geq 70$) show admixture of charge-states $Z-1$ or $Z-2$. Therefore another observable has to be measured in conjunction with the mass-to-charge ratio. Most commonly this is the measurement of the elemental charge number Z of an isotope via energy-loss measurements. This energy-loss occurs when charged projectiles pass through any form of matter due to the Coulomb interaction of the heavy-ion projectile with the surrounding atoms or molecules and results in the medium's ionization. Since the probability for any kind of nuclear reaction is greatly diminished in comparison to atomic reactions, as a direct result of the nuclei size ($\sim 10^{-15}\mathrm{m}$) in contrast to the atom size ($\sim 10^{-10}\mathrm{m}$), the ionization process dominates and can be considered as the only reaction. Given this consideration it follows that the resulting free charges become a quantitative measure for the energy-loss of the projectile, which again scales with the charge and the kinetic energy of the incoming particle. An expression for the relation of these observables is given by the Bethe-Bloch formula [46], which describes the energy-loss of heavy charged particles passing through matter and is as such:

$$-\frac{dE}{dx} = \frac{N_A e^4}{8\pi\epsilon_0^2 m_e c^2}\frac{Z^2 z}{\rho A}\frac{1}{\beta}\left[\ln\left(\frac{2m_e c^2\beta^2\gamma^2 T_{max}}{\overline{I}^2}\right) - 2\beta^2 - \frac{\delta}{2} - \frac{C}{Z}\right] \tag{2.10}$$

Here, $Z$ denotes the projectile elemental charge and $z$ the elemental charge of the medium together with $A$ for its mass number. For the heaviest ions, $Z$ becomes the charge-state $Q$, as discussed. The average ionization energy is denoted by $\overline{I}$ and approximated empirically via

$$\overline{I} \approx Z \cdot 11.5\ \mathrm{eV} \tag{2.11}$$

The maximum transferable kinetic energy unto one free electron is denoted with $T_{max}$ and defined via the expression

$$T_{max} = \frac{2m_e c^2\beta^2\gamma^2}{1 + \frac{2\gamma m_e}{m} + (\frac{m_e}{m})^2} \tag{2.12}$$

Here $m$ denotes the mass of the incoming particle. Additional corrections are added via the terms containing $\delta$ and $C$. The first is called the density term and introduced to correct for the relativistic flattening of the projectile's electric field for increasing energies whereas the term containing C is added for lower energies to take atomic binding energies into account. In the same manner as with the mass identification the incoming particle's speed and $\beta$ is determined via a time-of-flight measurement which allows for equation (2.10) to be solved for $Z$ and calculated. In order to guarantee that the measured energy-loss corresponds to the elemental charge and not another charge-state, both MUSIC detectors at the FRS are mounted in a row with an ionization foil between them. This allows for unwanted charge pick-ups to be assigned correctly ot their elemental charge by assigning each event their respective maximum energy-loss.

## 2.3. Matter Inside the Transfer Line

Before it could be shown in [20], it was not foreseen that matter within a beam line could be considered in the new LSA control system framework. In fact, before the implementation of the conceptual FRS setting

generator and a reliant energy-loss calculation routine in LSA, any kind of matter was simply ignored. Because energy-loss, nuclear reactions and ionization posed a great challenge for any machine, it tended to be resolved via homebrew solutions in the respective collaborations. Since the machine-model[1] from [20] has been ported unto the real FRS and upgraded it is now possible to consider not only energy-loss but also nuclear and atomic reactions inside every possible piece of matter. This means that up to now targets, target ladders, degraders, detectors, detector ladders, stripper foils, distances in air, slits and all their respective stepper motors or pneumatic drives have been implemented within the LSA framework and should be briefly described here.

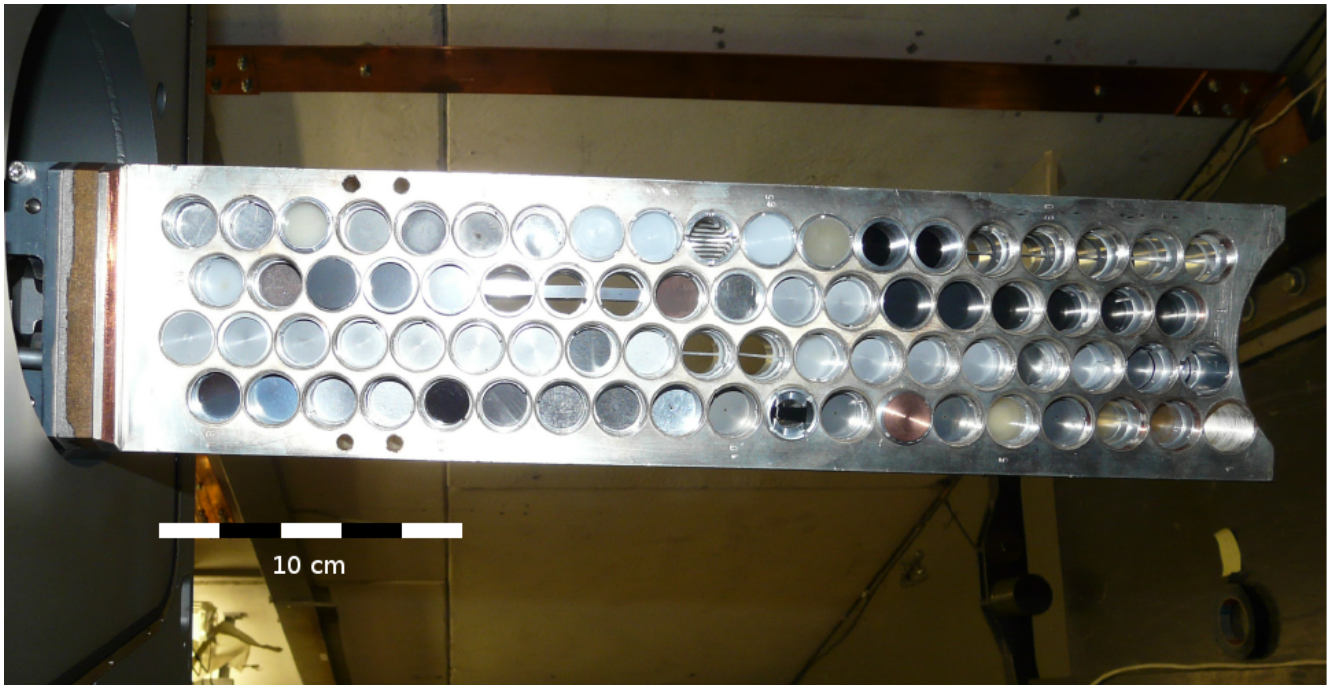


**Figure 2.6.:** Picture of the first target ladder of the FRS, taken from [47]. The 75 different targets and their respective positions are visible here. All of these can be selected via vertical and horizontal stepper motors and are made out of different materials and geometries. The photo was rotated by 90°. Copyright at GSI/FAIR, used with permission.

Detailed figures for the FRS matter and their individual order at the respective focal planes can be found in Appendix A together with a detailed list of targets and matter composition for detectors.
The first area of interest is the target area TA and begins with the SIS18 vacuum window made out of titanium with a thickness of $4.5\ \mu\mathrm{m}$. Since this window is always in the beam during an experiment and absolutely no one is supposed to open it, the first energy-loss has been hard coded to always occur here. Afterwards the SEETRAM intensity monitor, two CGs, two target ladders with up to 75 individual targets each, a detector pocket with an integrated IC and plastic scintillator, a scintillator finger detector and a slit system consisting of two horizontal and two vertical elements.
In the next area S1 one finds one CG, one MWPC, wo horizontal slit elements and a degrader system consisting of two aluminium wedges, whereas the latter wedge possesses a stepped design with each step having its own individual continuous wedge shape. With this degrader the first two dipole stages can be used for separation purposes to select a specific secondary beam and conduct an experiment at S2 with

[1] This is the name given to the totality of Parameters and methods required to represent a machine like the SIS18 or FRS within LSA, see Appendix B.1.

this beam.
Besides the target area is S2 the second most important area since it contains the main degrader system consisting of two more wedge shaped disks to optimize the energy-loss along the horizontal axis for the separation via $B\rho$-$\Delta E$-$B\rho$-method, one ladder with five differently thick $AlMg_4$ plates and two $AlMg_4$ wedges. Besides the degrader system, S2 houses the first part of the particle identification detectors with two MWPCs, two TPCs, a plastic scintillator ladder, a horizontal and vertical slit system, one CG and additional 5 target ladders.
The matter at S3 consists of one CG, one MWPC, one TPC, one horizontal slit pair, another scintillator ladder and one target ladder for stripper foils. A very similar setup can be found at S8 consisting of one stripper ladder, two MWPCs, two CGs and a horizontal slit pair.
The final focal plane S4 consists of two TPCs, two MUSICs, a horizontal and a vertical slit pair, three plastic scintillators and a degrader system consisting of two pairs of degrader wedges and one degrader disk. It is interesting to note that no other ion-optical elements follow S4 and therefore the implementation of this matter would not be necessary, especially since most detectors are manually mounted and do not possess any drive setups at S4, that can change quickly and frequently. Though for the sake of completeness, setting archiving, easier understanding of experimental execution and a second layer of logging this matter has been implemented as well, at least what is considered standard[1].

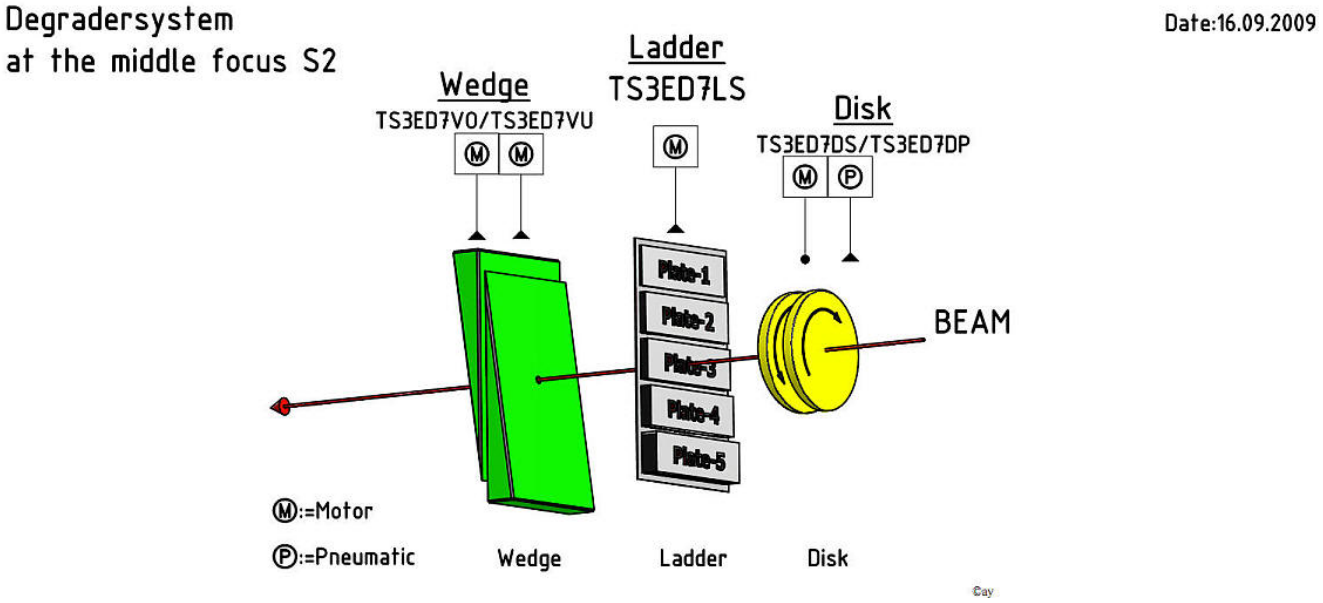


**Figure 2.7.:** Overview of the degrader system at the FRS at S2, taken from [48]. Copyright at GSI/FAIR, used with permission.

Going further next is S5. Here the matter consists of one CG, one MWPC, one horizontal slit pair and one plastic scintillator. After that at S7 the matter solely consists of one MWPC. The last important focal plane is S6. Even though the matter is comprised of only one horizontal pair of slits, two CGs, one collimator, one beam stop and one faraday cup, it is important to note that the CGs are used to monitor the beam position when initially injecting and aligning the beam in the ESR through the FRS and therefore the energy-loss inside the CGs plays a huge role in optimizing magnetic settings for centered injection.
After discussing all the matter inside the FRS it was possible to deduce a handful of archetypes of matter that were implemented as new device types inside the LSA framework. These types are firstly Targets, to

[1]This means all matter up to the second plastic scintillator as well as all distances in air, since the S4 setup is completely in air.

which experimental targets, be it single or multi-layered targets, all types of detectors and stripper foils can be assigned. Secondly Targetladders, which are all collections of targets, stripper foils, detectors and even degraders. Degraders and degraderdisks are put together in the type of degrader. Furthermore the types of slits, horizontal slits, vertical slits, upper slits, lower slits, left slits and righ slits were introduced. Although very similar to each other, they are distinguished in the official GSI nomenclature for devices, as of v15.9. [49], and it was required to be implemented as such. And lastly two types had to be implemented to distinguish between stepper motors (step drives), which can move to any position between their well defined IN and OUT position, and pneumatic drives (air drives), which can only move to their respective IN or OUT position. All the mentioned types and their respective Parameter hierarchies will discussed in more detail in Ch. 5.

## 2.4. ATIMA

ATIMA as a program has been in development at the GSI Helmholtzzentrum für Schwerionenforschung since its inception in the nineties and is being continuously updated to accommodate new experimental findings in the field of heavy-ion energy-loss inside matter [22, 50]. The main function of ATIMA is to calculate physical properties related to an ion slowing down as it passes through matter in the kinetic energy range of 1 $A\mathrm{keV}$ to 450 $A\mathrm{GeV}$. It finds application at the FRS to calculate the energy of the beam, as it passes through every layer of matter, and required $B\rho$ to set the magnets to the respective ion of interest. The following observables are being calculated:

- The stopping power $S(E) = -\frac{dE}{dx}$
- The energy-loss (like stopping power, related to charged particle)
- The energy-loss straggling
- The particle's angular straggling
- The range inside the material
- The range straggling inside the material
- The mean particle charge
- Beam parameters ($B\rho$, TOF, particle speed, etc.)

The original source code has ben written in Fortran 77 and can be accessed from within the GSI pool of linux machines. Alternatively, ATIMA can be accessed via a web interface or downloaded as either a C program, a Python wrapped Fortran library or a Java built graphical user interface utilizing C wrapped Fortran libraries via JNI (Java Native Interface). All these versions are equivalent in their functionalities and missing features can be easily added by a motivated user. Since all these version are very similar and all functionalities are derived from the wrapped original Fortran code, it was chosen to show the structure of JavaAtima in Fig. 2.8 since the LSA framework is Java based as well.
ATIMA calculates the energy-loss of a heavy ion passing through matter differently than just simply applying the Bethe-Bloch-equation from (2.10). Considering kinetic energies higher than 30 $A\mathrm{MeV}$ the LS-theory [51], named after Lindhard and Sörensen, is applied and corrected with the following terms, the shell correction [52], Barkas correction [53, 54] and the Fermi density effect [55]. For kinetic energies lower than 10 $A\mathrm{MeV}$ ATIMA uses J.F. Ziegler's SRIM (Stopping and Range in Matter) approach [56, 57]. In the intermediary region between $10$ and 30 $A\mathrm{MeV}$ the energy-loss is calculated by interpolation of the aforementioned descriptions.
The actual numerical calculation works in the following way. For every possible combination of beam isotope and target material the differential equations for range, range straggling, angular straggling and time-of-flight are solved by integrating in the local interval $a \leq x \leq b$, where x denotes the variable for kinetic energy, a and b the lower and upper limit of the interval. Each solution for each interval is saved as a fifth order de Boor B-spline [58] and has to fulfill the condition that the spline and its first order derivative is continous as well as that their values at the limits a and b are equal to the respective neighbouring spline's and its first order derivative's value. The knots for the intervals are automatically chosen to cover the whole energy range of ATIMA in a continuously increasing non-equidistant way. The resulting coefficients and their respective knots are saved together with the information about the beam's ion of interest and the target material.
The corresponding numerical functions can be found in the library colsys of the original source, see Fig. 2.8

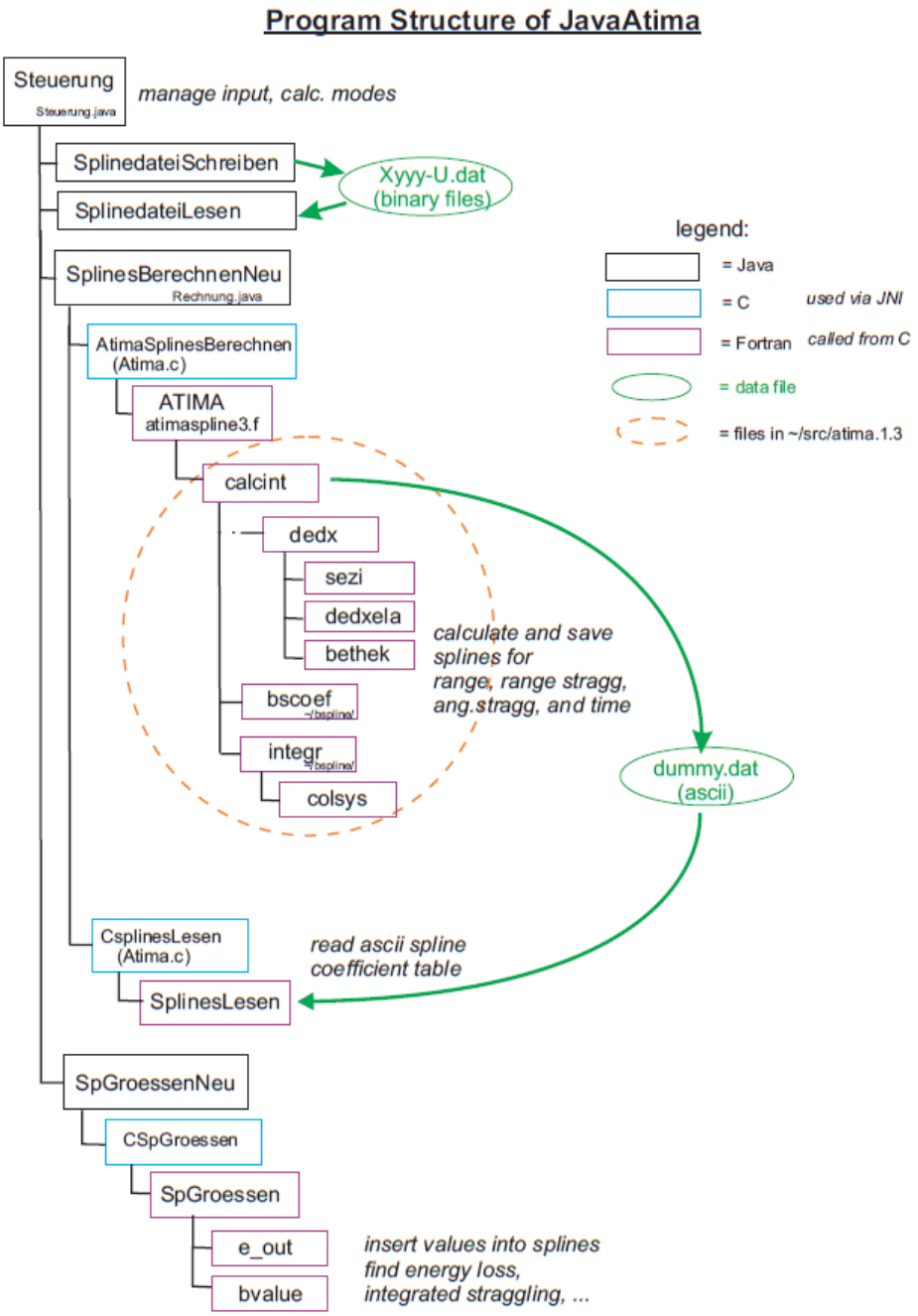


**Figure 2.8.:** Structure of JavaAtima, taken from [59]. It is important to note that for the development of the energy-loss calculation within the LSA framework only the routines e_out and bvalue were necessary and therefor translated from Fortran to Java to be incorporated within LSA. The other routines are not necessary since the splines are only calculated once, when an ATIMA update occurs, and remain static otherwise. Copyright at GSI/FAIR, used with permission.

and are called within integr. Consecutively bscoef reads out the B-spline coefficients and calcint then calculates the range, range straggling, angular straggling and time-of-flight and their B-splines are saved as a combination of knots and coefficients. The routines e_out and bvalue are essential in the evaluation of the

B-splines to calculate observables like the energy-loss and the outgoing energy of a heavy charged particle. For a given kinetic energy and combination of beam and target the routine e_out finds the corresponding interval within the B-spline via the Brent algorithm [60] and the routine bvalue evaluates the spline for the corresponding energy and propagates the value to the calculation of the corresponding observable.
It is possible within JavaAtima to calculate the outgoing energy of a particle for any number of targets with different thicknesses and any material. Both routines e_out and bvalue play a major part in the development of the machine-model for the FRS and will be discussed in further detail in Part II.

# 3. LHC Software Architecture (LSA)

This Ch. of the principles will give a brief overview of a select few concepts of the LSA control system framework in order to understand the development that has been done for the operation of the FRS. A full overview of all concepts and the architecture can be found in the Appendix Ch. B.

## 3.1. Concepts

LSA has been in development and maintenance since 2001 at CERN [21] with the goal to provide a unified control system for all particle accelerator rings and guarantee their timing as well as data supply. Other control system frameworks like EPICS (Experimental Physics and Industrial Control Systems) [61] or TANGO [62] at that time were not able to fulfill the requirements CERN had, which was to allow for both parallel and serial operation of each ring accelerator and transfer line. In this spirit LSA was developed as a new decentralized, Java based, generic framework for the modeling of accelerators fulfilling the following conditions.

- Separation of accelerator modeling and software engineering. Developers who design the models of the individual machines can work independently from developers who maintain the control system infrastructure and don't require deeper knowledge of the framework, e.g. the inheritance structure, and vice versa.
- Deployment of modern software. Current Standards and APIs have to be used in order to avoid obsolescence, which also have to be able to either be upgraded or exchanged in case projects reach the end of their life time.
- Based on databases. This condition is two-fold, firstly such that relevant information for devices, data supply or the control system infrastructure can be centrally accessed and is permanently available. Secondly that generated data, i.e. Settings or machine status, is preserved and archived.
- Provide generic structures. Avoiding redundancy and optimizing the modeling process.

LSA has been licensed from CERN in 2007 and adapted to be compatible with the current hard- and software at the GSI Helmholtzzentrum as well as the coming FAIR facility in order to supply all machines with necessary data, meaning device data, calibration data, timing, etc. such that the accelerators can be controlled and experiments conducted. Special focus for the development is being put on paradigms, which maximize the parallel operation of accelerators, collector rings, transfer and other experiments, enable for beam diagnostics to be embedded within the framework, supplying data for error scenarios by defining exit conditions or alternative cycles, facilitate data analysis of devices, utilize a control room space along with integrating experiments through assimilation of experimental hardware into the framework and experimental groups developing control solutions autonomously. This was the case for the FRS with LSA. The development of the control system has come a long way from its first inception to the first successful

test in March 2010 with the SIS18 [63] and culminating in the successful use of the control system in the FAIR Phase-0 experimental beam time from 2020 onward.
At this point it is now necessary to describe four concepts from the LSA framework for further understanding of this work and before continuing with a brief overview of the LSA architecture.

**Parameter** Every observable which can be measured is called a Parameter and belongs to a device. A good example is the electrical current provided by the power supply and the resulting magnetic rigidity of a dipole magnet. Every piece of hardware is called a device and can either be a real instrument that is controlled, like a power supply, not controlled, like a magnet or a virtual device. An important virtual device which has no directly controllable piece of equipment is the beam itself. All Parameters follow the nomenclature "Devicename/Propertyname" and are of a certain type, which is either a base type like Boolean or its own definition, which transcribes the properties of all Parameters of this type. All Parameters and their connections with other that belong to a device are grouped into the Parameter hierarchy of this device. Some Parameters can not be calculated but instead have to be given by the operator, are top-level Parameters and therefore called root. From these Parameters all other depending Parameters are being calculated, including low-level hardware Parameters like the electrical current, which are called leaves and are sent to the actual hardware.

**Setting** Once a Parameter gets assigned a value within a Beamprocess (see B.1) this value becomes the Setting and consists of two parts, a nominal value and a correction. The nominal value can either be the result of a calculation within the Parameter hierarchy or it could be given by the operator, in contrast to the correction which has to be given as a manual input but can also be generated with the help of auxiliary programs and routines. An example is the $B\rho$ Setting for dipole magnets, which is calculated from beam properties but due to mechanical misalignments the beam might not be centered and thus require a correction.

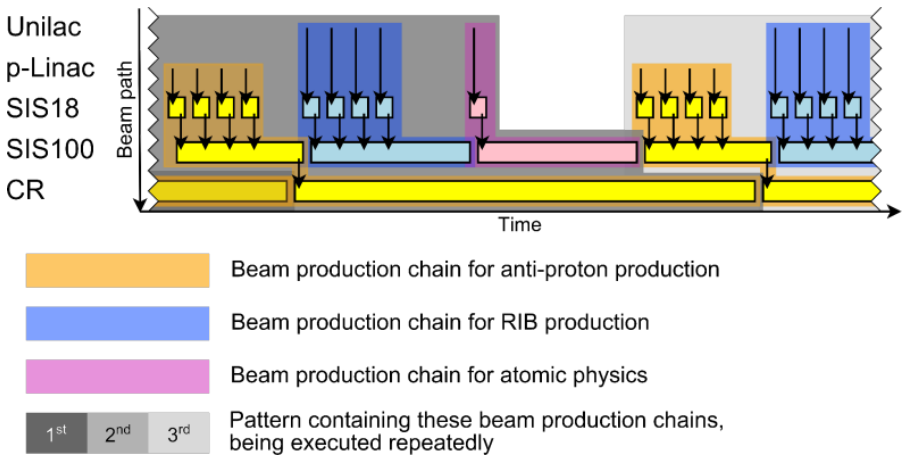


**Figure 3.1.:** Illustration of Patterns (gray scale) and Beam Production Chains (colored), taken from [64]. On the left axis the names of different accelerators are shown and on the horizontal axis time is represented. Utilizing Beam Production Chains and Patterns it is possible to maximize parallel operation of accelerators and machines while simultanouesly minimizing idle machine states. Copyright at GSI/FAIR, used with permission.

**Pattern** A Pattern is a collection of Beam Production Chains or simply put beam paths, which incorporate the respective devices. If a Pattern is active it provides the timing to all involved devices and can either run repeatedly an indefinite amount of times until the stop signal is sent or a predefined number of times. Figure 3.1 illustrates how a Pattern can incorporate several beam paths and run sequentially.

**Makerule** A Makerule is a relation between two or more Parameter types and defines how the Settings of one Parameter are calculated depending on the Settings of other Parameters. It is even possible to define a Makerule for more than just one depending Parameter, which opens the possibility that it can be used for multiple Devices and Device types. The Makerule which calculates the outgoing energy of the heavy-ion beam after passing through matter is one such central example and will be presented in Sec. 6.1.

## 3.2. Architecture

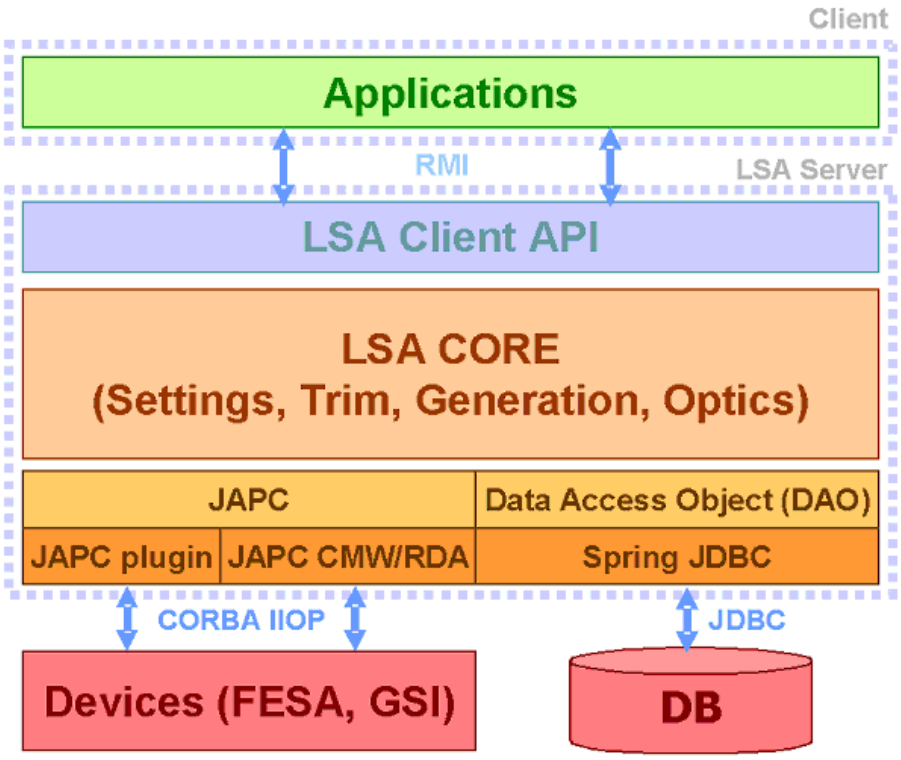


**Figure 3.2.:** The LSA 3-tier architecture, taken from [65], is divided into three closed layers that can be developed and deployed separately. The client side (green) is home to all applications, whereas the LSA server is a combination of the core and several APIs and communication protocols. Lastly the database and physical Devices (red) upon the whole framed is based. Copyright at GSI/FAIR, used with permission.

The three main principles that were defined for the LSA architecture are decentralization[1], modularity and layering. It is possible to fulfill the software requirements that were posed unto the architecture before development, under consideration of these principles. Data repositories had to be distributed and detached from the actual logic of the framework, therefore databases for archiving and data persistence were developed separated from the central LSA server running the LSA Core. Additionally Applications designed by users house their own visualizations and manipulation routines separate from the LSA server. It is guaranteed with these steps that a decentralized architecture can be achieved and each layer is its own closed subset, where communication between layers is facilitated by different standard APIs (Application

[1]Decentralization in the sense of a Blockchain technology is not meant.

Programming Interface), adhering to the paradigm of deployment of modern software from the previous Sec.
The LSA-Core was designed especially with the aspect of modularity in mind. Each module has a well defined scope of tasks and incorporates a coherent set of functionalities and methods, this promotes the reusability of each modules and cleanly separates each module's purpose.
The aspect of layering has been indirectly fulfilled by the aforementioned decentralization of the client, server and database ideas of LSA's architecture but this is further reinforced through the utilization of APIs on the server side, this results in applications and databases being independent of the chosen technology and fulfills the condition of separation of accelerator modeling and software engineering.

# 4. Fragmentation

This Ch. will give an overview about the nuclear fragmentation reaction, as it was used as the main instrument for the search of new neutron-rich isotopes towards the $N = 126$ line between rhenium and terbium. The basic principles of fragmentation, its benefits and disadvantages for isotope production, distinction from other reactions and theoretical predictability will be discussed.
Fragmentation as a reaction channel opens up for projectiles at energies above the Fermy energy $\sim 40\mathrm{AMeV}$ [66] because the projectile's energy is high enough to allow for a passing through the target's nuclei electric field and a collision becomes possible. This is one of the reactions channels that are used at the FRS [1] to produce wide variety of exotic nuclei as projectiles and study their properties via inverse kinematics. In the case of a central collision the transferred energy into the projectile nucleus can be high enough to cause a disintegration, in analogy to a liquid droplet overheating in a very short time ($t \sim 10^{-23}\mathrm{s}$)[9], followed by an immediate cooling down and restructuring of the disintegrated mass into smaller fragments and their deexcitation. In the case of a peripheral collision only the overlapping regions of target and projectile nuclei interact and a similar process takes place. At first, the overlapping region disintegrates and is abraded from both projectile and target. The remainder of the projectile nucleus is left in a highly excited localized state, where the interaction occurred [67, 68]. Now as the next step thermalization starts, in which the nucleons of the excited region dynamically interact with the rest of the nucleus. This can lead to the further removal of several nucleons and results in an homogeneous distribution of excitation energy among the constituents of the remaining nucleus. This resulting excited state is called the pre-fragment and de-excites via further statistical evaporation of nucleons and emission of gammas [69], see Fig. 4.1. It is important to note that the excitation energy of the nucleus after the abrasion depends on the number of constituents removed during the process, which has an influence on the shape of the momentum distribution.

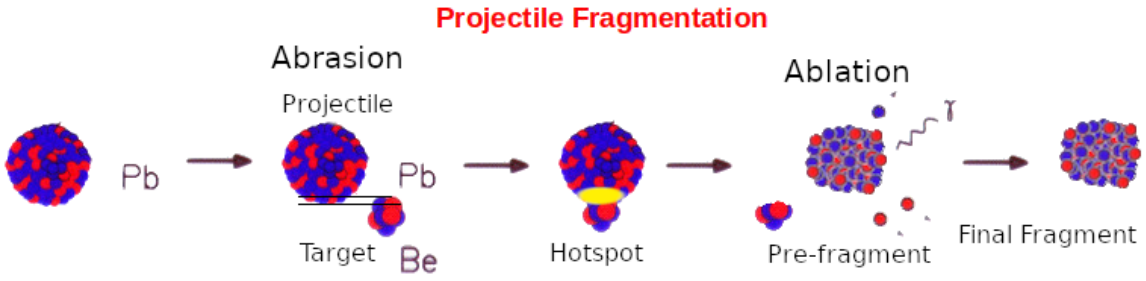


**Figure 4.1.:** Figure taken from [67]. Visual representation of a decentral collision between an exemplary lead nuclide and a beryllium nuclide (abrasion) resulting in a thermalized pre-fragment nuclide de-exciting (ablation or evaporation) into a final fragment. Copyright 2006, with permission from S. Pietri.

Due to the forward momentum of the projectile and its highly relativistic energy, the resulting fragments maintain most of the original momentum and stay forward focused, which allows for a very high transmission yield in combination with the FRS. Fragments far away from the initial projectile's mass possess an isotopic distribution which is independent of the original heavy-ion, since the isotopic distribution of fragments as a

result of relativistic heavy-ion collisions is dominated by the statistical evaporation of extremely excited pre-fragments, whereas fragments incurring a small mass loss have a narrow distribution similar to the projectile's distribution. The downside of this reaction channel as a production mechanism is that it requires high energies in the region of $\sim 100 A\mathrm{MeV}$ and more [66], which can only be achieved in bigger more sophisticated facilities.

## 4.1. Momentum Distribution

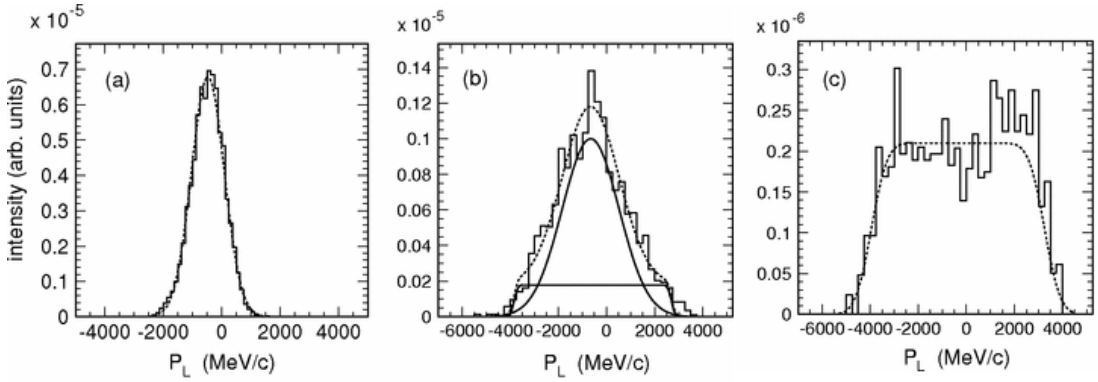


**Figure 4.2.:** Comparison of measured longitudinal momentum distributions in the projectile frame for a $^{238}$U beam impinging on a deuterium target at 1 $A\mathrm{GeV}$ [70]. The different plots are (a) $^{205}$At, (b) $^{156}$Dy and (c) $^{152}$Sm. From (a) to (c) the change from a Gaussian to a flat-top distribution takes place and can be attributed to the different reaction mechanisms involved, as (a) is the product of a pure spallation-evaporation reaction, (c) only spallation-fission and (b) a combination of both. Note that the zero point is defined as the momentum of the ion of interest in the respective FRS settigns and the momentum is a difference. Copyright 2006, with permission from American Physical Society.

A prominent feature of fragmentation reactions are their momentum distributions after the reaction[1]. It was already discussed that the resulting momentum has a dominating forward component close to the initial momentum. The width of the momentum distribution can be described by the Goldhaber model [71], which agrees well with experimental results. The Goldhaber model states that the width of the longitudinal momentum distribution can be described as such

$$\sigma_{||} = \sigma_0 \sqrt{\frac{A_F(A_P - A_F)}{A_P - 1}}, \tag{4.1}$$

where $\sigma_0$ is the mean width and could be experimentally determined to be $90\frac{\mathrm{MeV}}{c}$, $A_F$ and $A_P$ are the fragment's and projectile's mass number respectively. This assumes that a primary beam with a Gaussian-shaped longitudinal momentum distribution is provided by the accelerator and impinging on the target. In the next step the fragments enter the FRS and are separated due to the dispersive properties of the first dipole stage until S2, where the positions of the fragments are being measured via TPCs. A momentum distribution can be derived similarly to Eqs. (2.9) and (2.4) trough $B\rho$ and a position measurement as such

$$B\rho_{S2} = B\rho_0(1 - \frac{x_{S2}}{D_{TA-S2}}), \tag{4.2}$$

[1] Spallation-fission is also called abrasion-fission in LISE++ and spallation-evaporation corresponds to projectile fragmentation respectively.

where $x_{S2}$ is the horizontal positions inside the S2 focal plane, $D_{TA-S2}$ the dispersion coefficient and $B\rho_0$ the rigidity of a centered isotope. The resulting momentum distribution starts as a Gaussian-shaped distribution for fragments close to the initial beam and transforms to a broad flat-top distribution for fragments far away from the initial beam after the target. Through correct fitting, the exact number of isotopes produced via fragmentation can be determined. It will be shown later, that all measured isotopes during S468 were produced via fragmentation, as only the flat-top distribution was present in the measurement of the longitudinal momentum at S2 for all isotopes in the region of interest between rhenium and dysprosium.

## 4.2. EPAX

EPAX [72, 73, 74] stands for Empirical Parametrization of fragmentation cross sections and is a powerful tool used to calculate the fragmentation cross sections within LISE++ [75, 76] or MOCADI [77, 78], in order to estimate production rates of isotopes and experimental yields in the FRS or similar facilities. It is used in its currents version 3.1. The following assumptions are used within EPAX to model the fragmentation process:

1. Only the limiting fragmentation regime above $\sim 40\mathrm{AMeV}$ is considered. This is the energy range at which the projectile fragmentation cross section stays constant and holds true for typical SIS18 energies of (500-1000)$A\mathrm{MeV}$.
2. Only fragmentation is considered and other contributing channels like fission or nucleon knockout are omitted, meaning that the predictability is restricted to medium to heavy mass projectiles in the range of Argon to Lead.
3. Fragments far away from the initial projectile's mass possess an isotopic distribution which is independent of the original heavy ion, since the isotopic distribution of fragments as a result of relativistic heavy-ion collisions is dominated by the statistical evaporation of extremely excited prefragments.
4. Fragments incurring a small mass loss should have a narrow isotope distribution close to the projectile, which should smoothly transition into the distribution of assumption three.

With these assumptions in mind, the cross section function is then given by

$$\sigma(A,Z) = Y_A \sigma_z(Z_{prob} - Z) = Y_A n \exp\left(-R\left|Z_{prob} - Z\right|^U\right), \tag{4.3}$$

where $Y_A$ is the mass yield function, which is the sum of all cross sections with mass A, $\sigma_z$ is the charge dispersion distribution of cross section around the centroid $Z_{prob}$, $R$ is the width function that controls the shape of the distribution together with the exponent $U$ and $n$ is a normalization factor guaranteeing that the integral of $\sigma_z$ stays 1. All these functions depend on a total set of 29 Parameters, whose definitions and values can be found in Ref. [74]. The value of each Parameter was achieved by fitting the respective functions to experimental data of several fragmentation studies, whose references can be found in Ref. [72, 73, 74] as well.
In a previous isotope production experiment [79], a 1 $A\mathrm{GeV}$ $^{208}$Pb beam was impinging on a beryllium target to produce neutron-rich isotopes in the mass region of $A = 195$ via fragmentation. It was possible to show that the measured residues' fragmentation cross sections are in accordance to what EPAX was able to predict for heavy neutron-rich isotopes, see Fig. 4.3. With this result in mind, it was justified to rely on

EPAX to calculate the individual isotopic yields for experiment S468 and originally predict that 34 new isotopes should be seen [25]. Due to different reasons which will be discussed in Part IV of this dissertation, less new isotopes were observed but nonetheless identified as expected from EPAX and simulations.

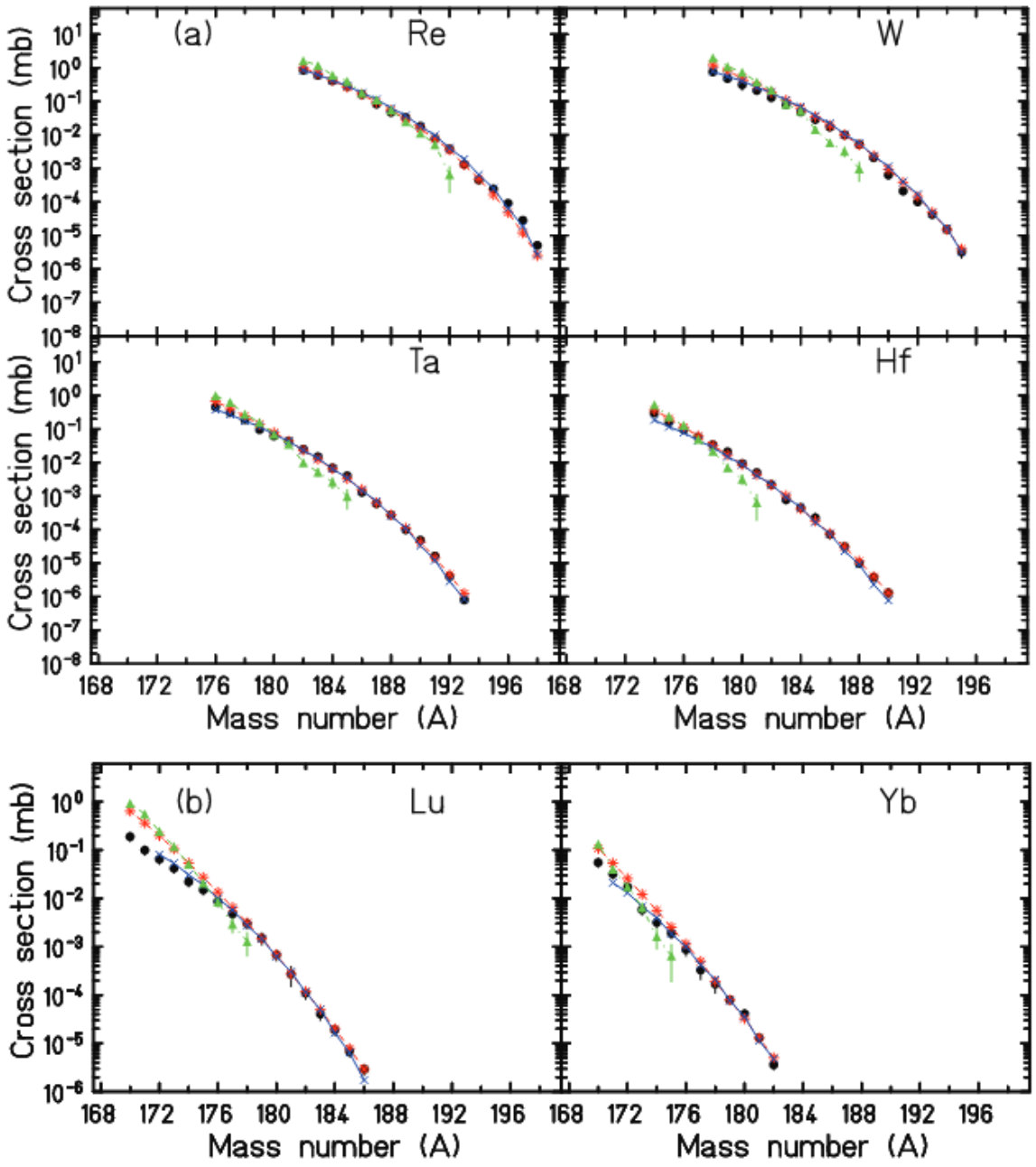


**Figure 4.3.:** Figure from [79], measured fragmentation cross sections (black circles) compared to different model predictions from EPAX (red stars), COFRA (blue crosses) [80] and ABRABLA (green triangles) [81]. For rhenium, tungsten, tantalum and hafnium EPAX shows very good agreement for the whole range of isotopes, whereas for lutetium and ytterbium it shows deviation from the experimental results for $\beta^+$-unstable isotopes. Copyright 2014, with permission from American Physical Society.

# Part II.

# Implementation

The following Chaps. treat of the realistic implementation of the FRS within the LSA control system framework. It is important to note that this Part does not provide an actual manual on how to work with the LSA framework or how to implement changes on different layers of the control system, this can be found in Reference [20]. Instead the following Chs. will focus on the changes being implemented since [20], which encompass an update of the general FRS target hierarchies, the introduction of slit and drive hierarchies as well as the implementation of functional hierarchies which allow the operators to manually overwrite the $B\rho$ of individual dipole sections and provide target alignment methods at the FRS target station. Additionally the most important Makerules, their structure and functionalities will be discussed in the second Ch. of this Part with specific code segments being shown.
The hierarchies, Makerules and code shown in this Part are from the current build of the LSA framework as it stands on 16.12.2021. Naming conventions for Parameters, Parameter types, methods or whole functionalities can change in the future, due to the dynamic nature of the LSA project and its many contributors within the GSI and from CERN.

# 5. Parameter Hierarchies

Before the individual hierarchies can be introduced it is important to briefly discuss the concept of an Accelerator Zone (short AZ), see Fig. 5.1 to better understand the decisions behind the design of the Parameter hierarchies.
An AZ is defined as a section of an accelerator or beam transfer line in which the properties of the beam, i.e. Beam Device, do not change. These inherent properties are the beam energy $E$, mass number $A$, elemental number $Z$ and charge number $Q$ and can be grouped into the set $T$, which stands for the transported beam properties. All other properties such as the magnetic rigidity $B\rho$, Lorentz factor $\gamma$, velocity $\beta$ or mass $m$ are derived from this set of properties. In order to follow the definition of an Accelerator Zone, all devices within the zone have to be arranged and connected in a particular way, where the block of all devices representing matter comes first and is then followed by the block of ion-optical elements. The connection between matter, magnets and different AZs is then established by the Beam Device, which represents the heavy-ion beam and all its properties.

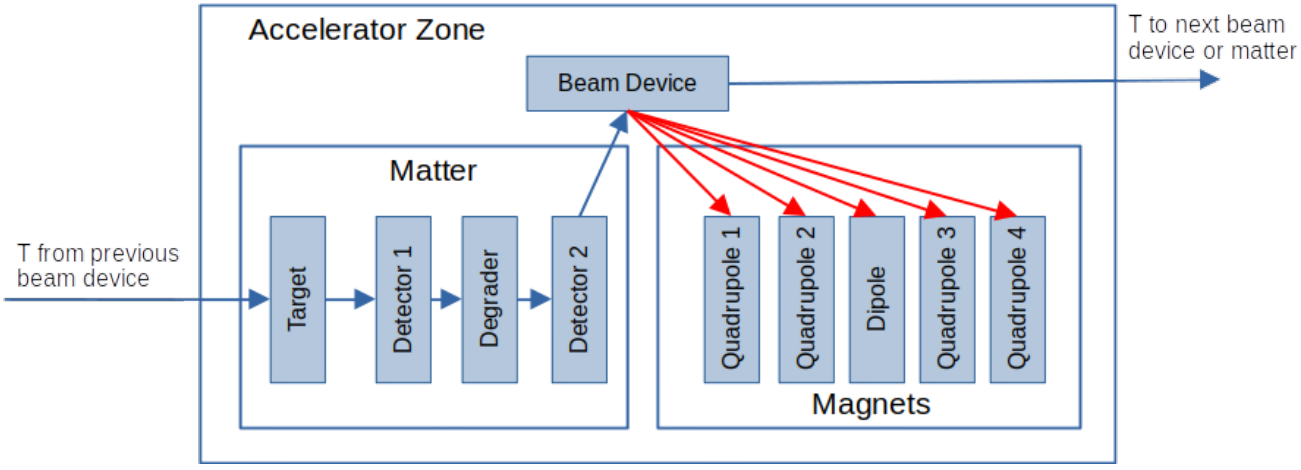


**Figure 5.1.:** Overview of devices being grouped inside an Accelerator Zone standard configuration. The blue arrows represent the Parameter set $T = \{E, A, Z, Q\}$ being transported from one device to another and the red arrows represent the $B\rho$ that the magnets receive from the Beam Device. The illustrated devices serve to visualize the process of Parameters being passed along the beam line and can vary depending on the real AZ in question.

The first device with matter within an AZ takes the set of properties $T$ from the Beam Device of the previous AZ, does its respective calculations and passes a possibly modified set $T$ to the next matter device until the last matter device is reached. This last device gives its resulting set $T$ to the Beam Device of the current AZ, where the derived properties are calculated and magnets are provided with a $B\rho$. The Beam Device passes its set $T$ now either to the first device with matter of the next AZ or if there is none then to the Beam Device of the next AZ. Implementing this design chose allows to fulfill the restriction, that beam

properties and therefore Beam Device Settings should not change within the same AZ, since the Beam Device only ever has one other device from which it receives its Parameter set, being either the previous AZ's Beam Device or the current AZ's last matter device. This process repeats until the final AZ and device along the Beam Production Chain is reached. The following Secs. will use the mathematical set notation and definition to describe collections of Parameters with their respective names in LSA.

## 5.1. FRS General Target Hierarchy

The first hierarchy to be introduced is the FRS General Target Hierarchy (shorthand GTH), see Fig. 5.2, which is used for all matter inside the FRS, where beam properties can change. It consists of one base target Parameter hierarchy, an extended target ladder hierarchy and an extended degrader hierarchy. The combination of these three hierarchies provides a minimal and generic approach to cover all possible forms of matter inside the FRS beam line, as will be discussed in this Sec.
The base target hierarchy has a set of incoming Parameters $I_P$, which either take their values from a Beam Device or the outgoing Parameters of a previous target device, and a set of outgoing Parameters $O_P$ which are passed to either a Beam Device or the next matter device. The two sets are as follows:

$$I_P = \{TARGET\_EIN\_S,\ ELEMENT\_IN\_S,\ ISOTOPE\_IN\_S,\ Q\_IN\_S\} \tag{5.1}$$

$$O_P = \{TARGET\_EOUT\_S,\ ELEMENT\_OUT\_S,\ ISOTOPE\_OUT\_S,\ Q\_OUT\_S\} \tag{5.2}$$

The sets $I_P$ and $O_P$, incoming and outgoing black arrows in Fig. 5.2, can be identical to the previously introduced set $T$. The prefix "TARGET_" denotes that a Parameter is used within a target hierarchy and the suffix "_S" denotes that it's a scalar type Parameter, i.e. it only holds one constant value at all times unless changed, like the input energy for a target. This distinction is important for Parameters, because time-dependent Parameter types exists as well, e.g. the current for SIS18 dipole magnets (AC called in LSA), in a Pattern (see B.1) compared to constant value Parameter types (called DC). "IN" or "OUT" denotes if the respective beam property is incoming or outgoing. "E" stands for the beam energy in $A\mathrm{MeV}$, "ELEMENT" for the elemental charge number, "ISOTOPE" for the mass number of the respective ion and "Q" for the charge-state.

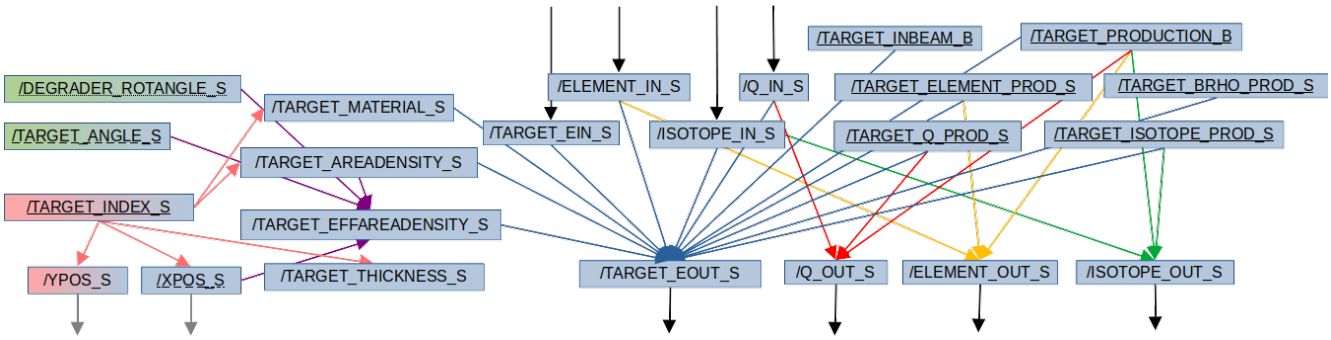


**Figure 5.2.:** Overview of Parameters and their connections inside the GTH. Incoming and outgoing Parameters have a black arrow, which shows that these values are either taken from or given to other devices within the machine-model. Grey arrows symbolize the transport of values to drives. All other colored arrows symbolize that a set of Parameters contributes to the determination of another Parameter via a Makerule. The red and green gradient Parameters belong to target ladders and degraders, which extend the GTH in those cases. Underlined Parameters are input Parameters.

The third set $M_P$ of Parameters are input Parameters, which require manual input from the operator, see Fig. 5.2 underlined Parameters. This set is defined as such:

$$\begin{aligned} M_P = \{&XPOS\_S,\, TARGET\_INBEAM\_B,\, TARGET\_PRODUCTION\_B,\\ &TARGET\_ELEMENT\_PROD\_S,\, TARGET\_Q\_PROD\_S\\ &TARGET\_ISOTOPE\_PROD\_S,\, TARGET\_BRHO\_PROD\_S\} \end{aligned} \tag{5.3}$$

The suffix "B" denotes a Boolean type Parameter, which can hold either true or false and is not time dependent. The Parameters "INBEAM" and "PRODUCTION" are important Booleans for determining if a matter device is inside the beam ($INBEAM = true$) or outside ($INBEAM = false$) or if the matter is specifically used to produce a different isotope or change the charge-state, in this case it would be $PRODUCTION = true$. These determining Booleans are important for the EOutMakerule (See 6.1) to decide if energy-loss occurs within the beam or other mechanisms do. The tag "PROD" denotes that a Parameter belongs to the group of properties necessary to produce different ions within matter. These are "ELEMENT", "Q", "ISOTOPE" and "BRHO" and fulfill similar roles to those within the sets $I$ and $O$. Only "BRHO" is different from the usual "E", since it was requested to preserve former FRS functionalities such as the usage of the magnetic rigidity instead of the energy for beam properties. The Parameter for the position of a matter device "XPOS" fulfills a special role in a sense that in some cases, a value doesn't necessarily have to be given but instead can be read out from a database, especially for devices that only have one well-defined end position inside the beam. As an example for a target ladder it stands for the horizontal position of the stepper motor and is inputted by the operator, whereas for a detector it stand for the pneumatic drive's position inside the beam, which is always the same and thus read out from a database.
The fourth set $D_P$ of Parameters are database Parameters that are read out from the FRS target database and is defined in the following way:

$$\begin{aligned} D_P = \{&TARGET\_MATERIAL\_S,\, TARGET\_AREADENSITY\_S,\\ &TARGET\_EFFAREADENSITY\_S,\, TARGET\_THICKNESS\_S\} \end{aligned} \tag{5.4}$$

"MATERIAL" denotes the material of the matter device as a string, "AREA-" and "EFFECTIVEAREADENSITY" denote the area or respectively the effictive area density of a material in $\mathrm{mg\,cm^{-2}}$, which is the most common unit in use at the FRS, all energy-loss calculations and for operation. The last Parameter "THICKNESS" describes the thickness of a target in $\mathrm{mm}$ and is not in use for any Makerules, but instead for redundancy as an additional control Parameter. With these 4 sets of Parameters simple matter devices like a target, a detector or a stripper foil can be described by the base target hierarchy, but are insufficient to describe more complex matter devices like a wedge degrader, disk degraders, target ladders, detector ladders or a degrader ladder. In order to include those devices as well, two more sets have to be introduced, which extend the base target hierarchy when necessary. These two sets $G_P$, the set of degrader Parameters, and $L_P$, the set of ladder Parameters, describe all matter devices completely and are defined in the following manner:

$$G_P = \{DEGRADER\_ROTANGLE\_S,\, TARGET\_ANGLE\_S\} \tag{5.5}$$

$$L_P = \{TARGET\_INDEX\_S,\, YPOS\_S\} \tag{5.6}$$

The prefix "DEGRADER" denotes that the Parameter belongs only to the group of degraders, specifically only degrader disks. "ROTANGLE" as a Parameter describes the rotational angle of a degrader disk setup in degrees, in contrast to "ANGLE" which describes the angle at which the heavy-ion beam hits the wedge degrader and influences the effective thickness. Both Parameters are used as manual input Parameters as

well. The ladder set $L_P$ is compromised of the two Parameters ”INDEX” and ”YPOS”. Target ladders are the only devices which have a horizontal and vertical drive to manipulate their positions in order to select one of up to 75 individual experimental targets that can be potentially held in a single ladder. ”YPOS” has to be introduced as a second position Parameter in units of $\mathrm{m}$ to account for this fact and in order to streamline and make the operation more intuitive the Parameter ”INDEX” exists. It’s a simple integer value with no units, which represents the respective targets within the ladder and selects the corresponding properties for further calculations, and has to be given manually.
Now that all Parameters have been properly introduced it is important to understand their connections with each other and which Makerules are involved. The Makerules themselves will be described in Ch. 6 in proper detail. The first and most important connections to be established are for the EOutMakerule (see Fig. 5.2 blue arrows), which mainly calculates the energy-loss of a heavy-ion beam passing through matter but also determines the outgoing energy of isotopes being produced inside a target. The set of Parameters contributing to $TARGET\_EOUT\_S$ can be summarized as the set $E_P$ and is the sum of $I_P$, $M_P$, $D_P$ without $XPOS\_S$ and $TARGET\_THICKNESS\_S$:

$$E_P = (I_P \cup M_P \cup D_P) \backslash \{XPOS\_S, TARGET\_THICKNESS\_S\} \tag{5.7}$$

The next important connections are for the determination of $Q\_OUT\_S$, $ELEMENT\_OUT\_S$ and $ISOTOPE\_OUT\_S$ via the same generic TargetProductionMakeRule (see 6.3 and Fig. 5.2 red, yellow and green arrows respectively). Contributing to this Makerule are the respective ”IN” and ”PROD” Parameters as well as the $TARGET\_PRODUCTION\_B$ Parameter.
Even though the base target hierarchy possesses the Parameters $XPOS\_S$ and $TARGET\_EFFAREADENSITY\_S$ for non-degraders, the connection exists, but due to the lack of $TARGET\_ANGLE\_S$ and $DEGRADER\_ROTANGLE\_S$ the calculation is skipped and instead the value of $TARGET\_AREADENSITY\_S$ is passed along the hierarchy. The corresponding Makerule to calculate $TARGET\_EFFAREADENSITY\_S$ from the Parameters $XPOS\_S$, $TARGET\_ANGLE\_S$, $DEGRADER\_ROTANGLE\_S$ and $TARGET\_EFFAREADENSITY\_S$ is EffectiveThicknessMakeRule (see 6.2) and Fig. 5.2 purple arrows.
The last connections are a total of five separate links which originate from the Parameter $TARGET\_INDEX\_S$ and determine $TARGET\_MATERIAL\_S$, $TARGET\_AREADENSITY\_S$, $TARGET\_THICKNESS\_S$, $XPOS\_S$ and $YPOS\_S$ separately. Each relationship has its own Makerule named ”IndexToNAMEMakeRule” (see Fig. 5.2 salmon arrows), where ”NAME” stands as a placeholder for the Parameter name, e.g. Material, XPos, etc.
These are all the connections and responsible Makerules within the FRS General Target Hierarchy. In order to ensure that Parameter values are properly propagated from one matter device to another or towards the beam device as well as towards their respective drives, a set of TakeBeamNAMEMakeRules and TakeTargetNAMEMakeRules (see Fig. 5.2 black arrows) together with the PropagateXPosMakeRule and PropagateYPosMakeRule (see Fig. 5.2 gray arrows) were implemented, where ”NAME” acts similarly as a placeholder, to ensure said features.

## 5.2. Slit Hierarchies

95% of all matter devices within the FRS can be covered with the introduction of the GTH and the only other important devices left are collimator slits and drives. Slits and drives can be treated very similarly and easily since they posess mostly only position information that needs to be propagated to their respective real drive. The special features lie within the details of the slits, in a sense that according

to the GSI/FAIR component list and naming convention slits are multi-layered devices, see Fig. 5.3, and horizontal slits can potentially change the $B\rho$ of a heavy-ion beam by cutting parts of it. The first aspect of being a multi-layered device can be exemplified with the device GTS3DS6, which is a group of slits at S2 consisting of two horizontal and two vertical slits. Following the GSI nomenclature this device consists in total of seven separate devices as well as their underlying four drives. The devices in question are GTS3DS6 the group of slits itself, GTS3DS6H and GTS3DS6V the horizontal and vertical pair of slits respectively as well as the individual left, right, upper and lower slits GTS3DS4HL, GTS3DS6HR, GTS3DS6VO and GTS3DS6VU . The resulting individual slits act as their own drives and don't have a separate drive device for position adjustment. This example as an extreme case shows that an introduction of seven new device types with their own hierarchies was necessary for slits. Therefore $GROUP\_SLITS$, $HORIZONTAL\_SLITS$, $VERTICAL\_SLITS$, $LEFT\_SLITS$, $RIGHT\_SLITS$, $UPPER\_SLITS$ and $LOWER\_SLITS$ were introduced as new device types within LSA. Compared to the previous GTH, the hierarchy for slits posssesses a much lower complexity, since all hierarchies only consist of position Parameters, whose unit is given in $\mathrm{mm}$. The only exception is the type

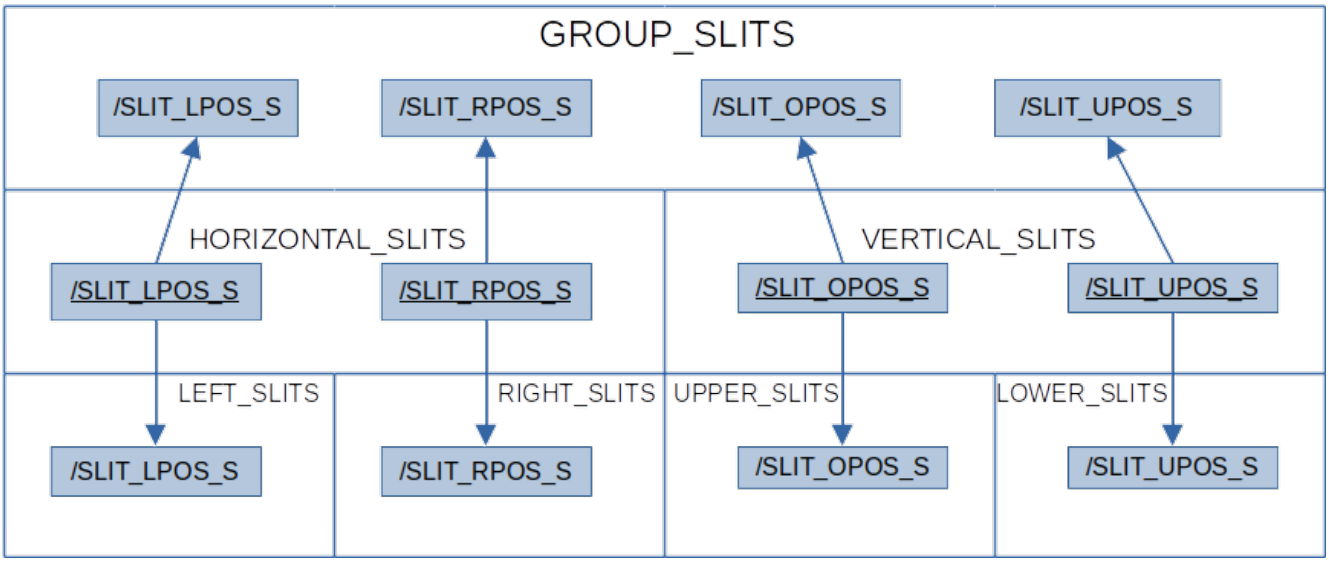


**Figure 5.3.:** Visualization of slit device types and the connection of their position Parameters. It is important to note that the middle layer acts as the manual input layer for the operators, hence the Parameter names are underlined. The Parameters are propagated by their respective Makerules symbolized by arrows. Additional Parameter of the $HORIZONTAL\_SLITS$ device type are not visualized.

$HORIZONTAL\_SLITS$, as these have the ability to potentially change the beam energy and the state of the machine.
The set $P_P$ of Parameters required to fully describe the $GROUP\_SLITS$ devices consists of the total of all position Parameters:

$$P_P = \{SLIT\_LPOS\_S,\ SLIT\_RPOS\_S,\ SLIT\_OPOS\_S,\ SLIT\_UPOS\_S\} \tag{5.8}$$

The prefix "SLIT" denotes that the Parameter belongs to the group of slit devices and the middle part "ZPOS", where Z stands for either L, R, O or U, denotes the left, right, upper or lower position. These names are derived from the devices original german designations links, rechts, oben and unten. Similarly the set $V_P$ of Parameters for $VERTICAL\_SLITS$ only contains the subset of vertical Parameters from P and the idividual slits are again a subset $P_Z$ of their respective groups, where $P_Z$ only contains the corresponding

position Parameter “ZPOS”. The only difference are devices of type $HORIZONTAL\_SLITS$, see Fig. 5.4, as these contain the subset $H_P$ of $P_P$ such that it contains only the horizontal position Parameters $SLIT\_LPOS\_S$ and $SLIT\_RPOS\_S$ together with the set $B_P$ of Parameters responsible for the beam $B\rho$ change and is defined as such:

$$H_P = \{SLIT\_LPOS\_S,\ SLIT\_RPOS\_S\} \cup B_P \tag{5.9}$$

$$B_P = \{TARGET\_EIN\_S,\ SLIT\_BRHOIN\_S,\ SLIT\_BRHODEVIATION\_S,\ TARGET\_EOUT\_S,\ SLIT\_BRHOOUT\_S\} \tag{5.10}$$

The new Parameters are here “BRHOIN”, “BRHOOUT” and “BRHODEVIATION” which denote respectively the incoming and outgoing $B\rho$ in $\mathrm{T\,m}$ of the particle beam as well as the deviation factor for the possible change as a dimensionless factor.
Since most slits at the FRS, six out of eight, are $HORIZONTAL\_SLITS$ devices, it was chosen that the position Parameters of the middle layer of $HORIZONTAL\_SLITS$ and $VERTICAL\_SLITS$ are used as manual input Parameters, contrary to the intuitive approach of using the $GROUP\_SLITS$ position Parameters as required manual input Parameters. Enforcing this choice was also the design decision to include the $B\rho$ deviation factor as a manual input Parameter in the middle layer. Figure 5.3 visualizes which device layer functions as an input and how the corresponding Parameters propagate inbetween the layers. The propagation of the different “ZPOS” position Parameters is guaranteed by the PropagateZPosMakeRule, where Z denotes either L, R, O or U. The $HORIZONTAL\_SLITS$ hierarchy contains two additional connections which are calculated by two different Makerules. The first one are the Parameters $TARGET\_EIN\_S$ and $SLIT\_BRHODEVIATION\_S$ contributing to $TARGET\_EOUT\_S$ via the same EOutMakeRule, see Fig. 5.4 red arrows, as with the GTH and the second connection exists between the pair $SLIT\_BRHOIN\_S$ and $SLIT\_BRHODEVIATION\_S$ and the single Parameter $SLIT\_BRHOOUT\_S$ via the SelectBrhoMakeRule (see Fig. 5.4 blue arrows). The redundancy in energy and magnetic rigidity exists as a special request to guarantee the former operational workflow of the FRS. Though it is recommended that the energy Parameters are utilized, since energy, elemental charge number, isotopic mass number and charge-state are the only beam properties that are propagated inbetween beam devices of different AZs. The $B\rho$ value as a lower laying Parameter within the beam device hierarchy should stay within an AZ since it is calculated from said properties, as can be seen in Fig. 5.5 in Sec. 5.3.

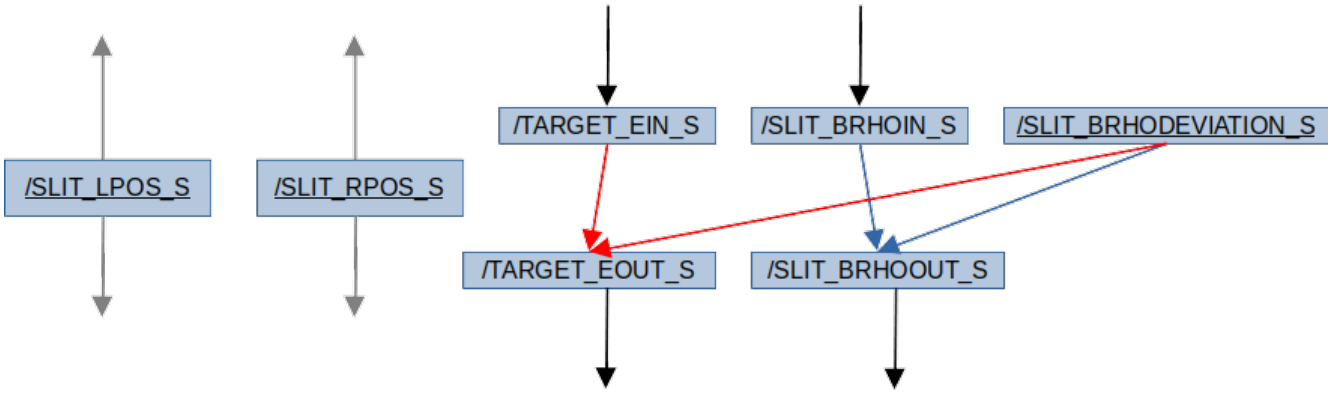


**Figure 5.4.:** Detailed visualization of the $HORIZONTAL\_SLITS$ type. The underlined Parameters act as manual input Parameters for the operators. Grey arrows symbolize the propagation towards other slit device types and black arrows symbolize similarly like the GTH that the respective Parameters are either taken from previous beam devices or matter devices and propagated to those as well.

## 5.3. Functional Hierarchies

The previously introduced hierarchies cover all of the potential devices within the current FRS and Super-FRS as well, that could lead to a change of beam properties and were always coupled to the development of new device types. It is also possible to introduce new functionalities to pre-existing devices without establishing new ones by simply extending the hierarchy of either individual certain devices or all devices of one type. The former approach was chosen to implement a manual $B\rho$ overwrite function for several complete dipole stages at the FRS and the possibility to align the primary beam on the main target station in the TA section of the FRS and will be referred to as a functional hierarchy, since they only fulfill one specific purpose in certain cases and are added either upon request or if the need arises without implementing a full new device type with its hierarchy.
Overwriting the magnetic rigidity of a dipole stage was made possible by introducing a set of Parameter $W_P$ defined as such:

$$W_P = \{OVERWRITE\_BRHO\_B,\ BRHO\_S,\ Q\_OUT\_S,\ ELEMENT\_OUT\_S,\ ISOTOPE\_OUT\_S\} \tag{5.11}$$

The “OUT” Parameters, which belong to the last matter device of an Accelerator Zone, are known from the previous definition of the target hierarchy and the two new Parameters are $OVERWRITE\_BRHO\_B$ and $BRHO\_S$, see Fig. 5.5. They are defined as a Boolean Parameter type, which represents the operators request to overwrite a section’s magnetic rigidity, and a scalar, that contains the requested magnetic rigidity in $\mathrm{T\,m}$ to which the dipole stage should be set to.

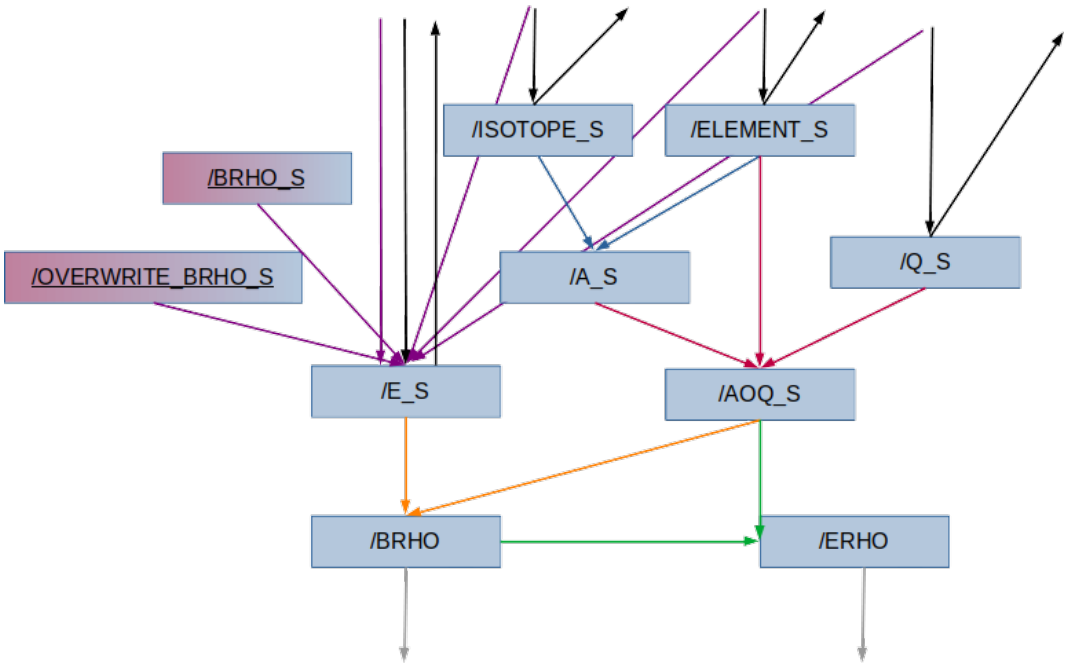


**Figure 5.5.:** Base Parameters of the Beam Device visualized with the extension required for overwriting the $B\rho$ of one dipole stage. The black arrows symbolize the same Makerules as used in the GTH, that are responsible for propagating beam Parameters to and from matter or beam devices. The red arrows stand for the connection between the beam device and ion-optical elements, either magnetic or electrostatic. The additinal Parameters of the extended functional hierarchy are marked with a purple gradient and connected via purple arrows.

This set of Parameters is then connected via the Give2BeamTargetEMakeRule, see Sec. 6.4 and Fig. 5.5 purple arrows, to the energy Parameter $E\_S$ of the beam device, which rests within the same AZ as the dipole stage. Connecting the set $W_P$ to the Parameter $E\_S$ allows the control system then to propagate the new energy to the next AZ, consequently setting all following magnets to the correct $B\rho$ as well.
In order to permit an alignment of the primary beam unto the target it is necessary that two horizontal and two vertical steerers are involved, which are positioned in front of the target as two separate pairs of one vertical and one horizontal steerer. This configuration was implemented for the beam line to transport the primary beam after the SIS18 to its destined experimental area but can also be used to adjust the angle and position on the target. The exact position on the target itself is not measured, instead the position and angle information is derived from the projection of a horizontal and vertical position measurement in two separate current grids, one before and one after the target, unto the respective target station. By knowing the optical matrix coefficients and exact distances of this setup (two horizontal steerers, two vertical steerers and one target station) the shift in $B\rho$ required to center the beam can be calculated. The responsible Makerule is named TargetAlignmentMakeRule and is explained in more detail in Sec. 6.5. In order to implement the hierarchy, see Fig. 5.6, five Parameters had to be introduced in the set $T_P$:

$$\begin{aligned} T_P = \{&OPTIC\_NAME\_S,\ XPOSITION\_CHANGE\_DET1\_S,\\ &XPOSITION\_CHANGE\_DET2\_S,\ YPOSITION\_CHANGE\_DET1\_S,\\ &YPOSITION\_CHANGE\_DET2\_S\} \end{aligned} \tag{5.12}$$

$OPTIC\_NAME\_S$ is a string based Parameter and represents the name of the optical file, that responds to the configuration in use. The files themselves are simple text files containing the ion-optical matrix Parameters, to allow the alignment on either target station at TA for different optical modes and are prepared via GICOSY [32]. $ZPOSITION\_CHANGE\_DETA\_S$ is the corresponding scalar position Parameter of position change required in the respective detector, $Z$ stands for either $X$ or $Y$ and $A$ denotes either detector 1 or detector 2. All of these introduced Parameters are required as manual input from the operator if a target alignment should be performed in the desired AZ. Two position Parameters of the same axis together with the optical name Parameter are connected to the $ZKICK\_TARGET$ kick Parameter of a steerer, the same notation for $Z$ applies here. A kick is defined as the change from the originally defined deflection angle of a magnet in $\mathrm{mrad}$. The ion-optical device's hierarchy, see Fig. C.1 in Appendix C, then calculates the resulting $B\rho$ and current $I$ automatically.

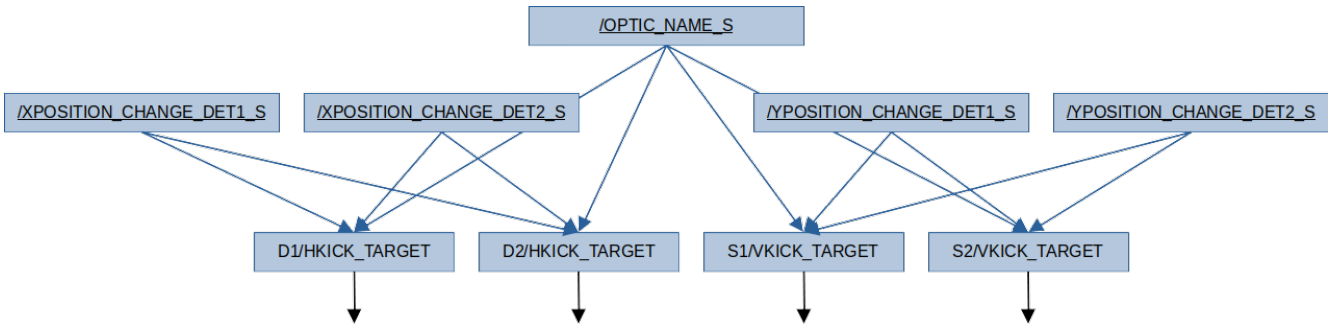


**Figure 5.6.:** Visualization of target alignment functional hierarchy. The respective position change Parameters are connected with the optic name Parameter to the kick adjustment Parameters via the TargetAlignment-MakeRule (blue arrow). $DA$ and $SA$ denote the involved horizontal main dipoles and vertical support steerers and $A$ denotes the either the first or second magnet. It is important to note that the rest of the ion-optical hierarchy below the kick Parameter is omitted but symbolized by the black arrow.

# 6. Makerules

As discussed in Sec. 3.1, a Makerule is a relation between two or more Parameter types. In the following sections, Parameter names will be omitted when they are not necessary. Note that the spelling of the names of each Makerule is attributed to the Java programming language naming convention for classes.

## 6.1. EoutMakeRule

The first iteration of this Makerule has already been implemented in [82] as a benchmark and proof of principle that a simplified machine-model for the FRS can be implemented with simple energy-loss calculation functionalities inside the LSA framework, which will then be later used for the Super-FRS. In its current iteration with its several subroutines the EoutMakeRule is capable of the following tasks:

- Calculating the energy-loss of a heavy-ion beam passing through matter devices, i.e. targets, strippers, target ladders, detectors, detector ladders, degraders, degrader disks and degrader ladders.
- Deciding whether production or propagation within matter occurs and outputting as well as converting the correct corresponding energy, given as a $B\rho$ value into an energy value.
- In the case of a pair of horizontal slits, it calculates the changed beam energy due to the applied cut in the phase space, if preferred to do so by the operator.

It acts as the connecting Makerule between the Parameter type set $A_T$ and the single Parameter type $SCALAR\_TARGET\_EOUT$, where $A_T$ is defined as such:

$$\begin{aligned} A_T = \{&SCALAR\_TARGET\_EIN,\ STRING\_TARGET\_MATERIAL,\\ &SCALAR\_TARGET\_AREADENSITY,\ SCALAR\_TARGET\_EFFAREADENSITY,\\ &SCALAR\_TARGET\_ISOTOPE,\ SCALAR\_TARGET\_Q,\\ &SCALAR\_TARGET\_ELEMENT,\ BOOLEAN\_TARGET\_INBEAM,\\ &BOOLEAN\_TARGET\_PROPAGATE,\ SCALAR\_TARGET\_BRHO\_PROD,\\ &SCALAR\_TARGET\_ELEMENT\_PROD,\ SCALAR\_TARGET\_ISOTOPE\_PROD,\\ &SCALAR\_TARGET\_Q\_PROD,\ SCALAR\_SLIT\_BRHODEVIATION\} \end{aligned} \tag{6.1}$$

The denomination for Parameter types is very similar to the one previously introduced for Parameter names. ”SCALAR” as a prefix denotes a scalar Parameter type, that has a time-independent static numerical value. ”BOOLEAN” stands for a Boolean Parameter type which only has two possible values, that are either ”TRUE” or ”FALSE” and ”STRING” stand for a string Parameter type that takes a string of characters as an input. The middle denomination ”TARGET” assigns Parameter types to the new common device group for targets and ”SLITS” to the device group of slits. And finally the suffix ”PROD” denotes a Parameter type

that belongs to the set of production type Parameters used within targets. Concerning the other middle denominations, these share the same names as their corresponding Parameter names, that were previously introduced.

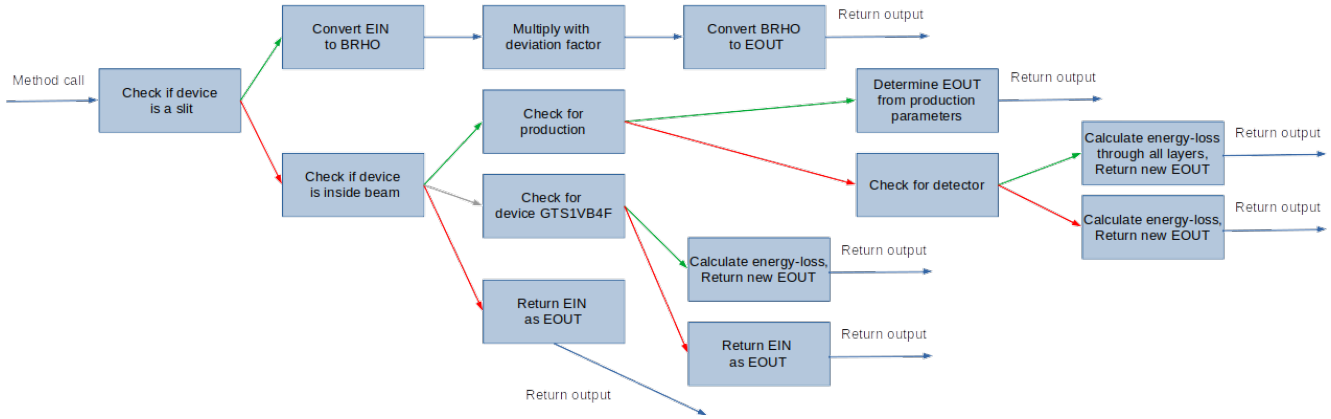


**Figure 6.1.:** Flowchart visualizing each major step taken in the EoutMakeRule. Green arrows symbolize true statements, whereas red arrows symbolize false statements. If a ”null” statement occurs, which can happen for non-initialized Parameters, then this case is symbolized by a gray arrow.

With these Parameter types in mind, the discussion of the EoutMakeRule program sequence can commence. Fig. 6.1 shows an abstract flowchart with the major steps happening within the EoutMakeRule. As any Java method, the EoutMakeRule starts with a method call, that has been triggered by a change in Setting values due to different circumstances. The method in question is makeValueGsiImpl(), see Lst. 6.1 and has to be implemented in each Makerule separately as each individual Makerule inherits from the LSA class called AbstractGsiMakeRule which defines the method makeValueGsiImpl() as abstract, i.e. it has to be implemented by its inheriting class. The method makeValueGsiImpl() takes one argument which is a full List of Parameters, that are the parents for which the Makerule is called. The argument is of type MakeRuleArguments and named mra. As a first step inside the Makerule it is checked if the parent Parameters belong to a slit device via the private method checkForSlit(). It takes the list of parent Parameters and checks if it contains a Parameter of type $SCALAR\_SLIT\_BRHODEVIATION$. If that is the case then the Setting value of the Parameter whose type is $SCALAR\_SLIT\_BRHODEVIATION$ is extracted and checked if it exists. If it is “null” then the incoming energy is given out as the output energy. If it exists it is transformed from a $B\rho$ changing factor to an energy changing factor and multiplied unto the incoming energy and the product is returned as the outgoing energy, see Lst. 6.2.

```
1  package de.gsi.lsa.ext.fair.rules.makerule.target;
2
3  public class EoutMakeRule extends AbstractTargetMakeRule {
4
5    @Override
6    protected ImmutableValue makeValueGsiImpl(final MakeRuleArguments mra)
7    throws TrimException {
8    final List<Parameter> parentParameters = mra.getParentParameters();
9    ...
10   }
11 }
```

**Listing 6.1:** EoutMakeRule head and definitions.

In the case that the arguments do not belong to a slit device, the Makerule continues regularly and extracts the Parameters of type $SCALAR\_TARGET\_EIN$ and $BOOLEAN\_TARGET\_INBEAM$. Afterwards it is checked if the Parameter corresponding to “INBEAM” exists. If it does not, the incoming energy is returned unchanged and if it does then the Setting value of the inbeam Parameter is extracted and checked if it exists. This can have three cases. In the first one the Setting value is “null”, which could either mean an undefined matter device status or one very specific device named “GTS1VB4F”, which is the SIS18 vacuum window and should never be moved. But it is still important to consider it for energy-loss calculations. If the EoutMakeRule is called for this device then its corresponding target text file is read out from the FRS target database via the TargetReader class and its properties, i.e. material and thickness, are used for the energy-loss calculation in the private method calculateEnergylossInTarget() within the Makerule class. If it is not the aforementioned device “GTS1VB4F” and the device status is undefined, then the incoming energy is simply passed along, 6.3. In the second case that the inbeam Setting exists but is “false”, meaning said device is not in the beam, then no calculation occurs and the incoming energy is propagated unchanged. At last in the third case, the inbeam Setting value exists and is “true”, then the next check occurs. Now the production Parameter and its Setting are extracted. In the cases that the production Setting is either “null” or “false” then the production part is skipped and the Makerule continues as per usual. If production occurs then the corresponding “PROD” type parent Parameters and their Settings are extracted from the main arguments. From these a new $A/Q$ value is calculated as well as a new energy from the given $B\rho$. This new energy is then returned as the outgoing energy, see Lst. 6.4.

```
final boolean slitCheck = checkForSlit(parentParameters);
if (slitCheck) {
  final ImmutableScalar einScalar = this.getParentValueAsTyped(mra, ''SCALAR_TARGET_EIN'');
  final Parameter brhodeviationParameter = Parameters.getParameterByTypeName(
    parentParameters, ''SCALAR_SLIT_BRHODEVIATION'');
  final Setting brhodeviationSetting = getSettingOrNull(mra, brhodeviationParameter);
  if (brhodeviationSetting == null) {
    return ValueFactory.createScalar(einScalar.getDouble());
  }
  final ImmutableScalar brhodeviation = this.getParentValueAsTyped(mra,
   ''SCALAR_SLIT_BRHODEVIATION'');
  final Double factor = Math.sqrt(Math.pow(BeamProperties.betaOfE(einScalar.getDouble())
   * BeamProperties.gammaOfE(einScalar.getDouble()) * brhodeviation.getDouble(), 2) + 1)
   / Math.sqrt(Math.pow(BeamProperties.betaOfE(einScalar.getDouble())
   * BeamProperties.gammaOfE(einScalar.getDouble()), 2) + 1);
  return ValueFactory.createScalar(einScalar.getDouble() * factor);
}
```

**Listing 6.2:** Code snippet for slit energy change

Back to the case when no production happens. In the next step the current device is checked via the private method checkDetector() by comparing its name against a predefined list of names of all detectors. If the list doesn’t contain the device’s name then it is treated as a target and the method calculateEnergylossInTarget() is called to calculate the simple one step energy-loss and returned. Whereas if a detector is present then the method detectorEoutCalculate() of the class DetectorEoutCalculate is initiated and called in order to calculate the energy-loss of the beam step-wise through all layers of matter of the detector and the final energy is returned as outgoing energy, see Lst. 6.5.
Several methods and classes were mentioned now, but only calculateEnergylossInTarget() and detectorEoutCalculate() will be further explained. The method calculateEnergylossInTarget uses 5 Parameters as input, which are the variables mra, parentParameters, targetReader, zBeamvalue and eIn, whose initialization can be found in the listings 6.1 and 6.3. The only exception is the variable targetReader which is is defined

by the class TargetReader and automatically initialized in the definition of AbstractTargetMakeRule for every call of the EoutMakeRule and whose task it is to read out the respective target's .csv-files and the properties saved therein, so that these are accessible to the EoutMakeRule. As a first step the area density, material, and charge-state para-

```
if (inbeamSetting == null) {
  final String devicename = extractDevicename(eInParameter);
  if (devicename.equals(''GTS1VB4F'')) {
    final TargetReader targetReader = readTargetFile(devicename);
    final ImmutableScalar zBeam = this.getParentValueAsTyped(mra, ''SCALAR_TARGET_ELEMENT'')
    ;
    final int zBeamvalue = zBeam.getInt();
    final double eIn = einScalar.getDouble() / 1000000;
    return calculateEnergylossInTarget(mra, parentParameters, targetReader,
     zBeamvalue, eIn);
  }
  return ValueFactory.createScalar(einScalar.getDouble());
}
```

**Listing 6.3:** SIS18 vacuum window GTS1VB4F special case.

meters are extracted from mra and parentParameters and the mass of the ion is determined from this information via the private method getIonMass(). Consecutively an instance of the class SplineFinder sf and EoutCalculate EC are initialized, which, respectively, are responsible to find the correct ATIMA spline file for the given combination of beam and material as well as calculating the energy-loss from the given information and the splines. The correct spline file is then saved in the String variable spline and all necessary target properties are read-out and saved in their corresponding variables for further processing.

```
if (productionSetting != null) {
  if (productionSetting.getScalarValue().getBoolean()) {
    final ImmutableScalar aBeamProd = this.getParentValueAsTyped(mra,
     ''SCALAR_TARGET_ISOTOPE_PROD'');
    final ImmutableScalar qBeamProd = this.getParentValueAsTyped(mra,
     ''SCALAR_TARGET_Q_PROD'');
    final ImmutableScalar zBeamProd = this.getParentValueAsTyped(mra,
     ''SCALAR_TARGET_ELEMENT_PROD'');
    final Parameter brhoprodParameter = Parameters.getParameterByTypeName(parentParameters,
    ''SCALAR_TARGET_BRHO_PROD'');
    final Setting brhoprodSetting = getSettingOrNull(mra, brhoprodParameter);
    final ImmutableScalar brhoprodScalar = brhoprodSetting.getScalarValue();
    final ChemicalElement element = ChemicalElements.getElementByAtomicNumber(
     zBeamProd.getInt());
    final Isotope isotope = element.getIsotopeByMassNumber(aBeamProd.getInt());
    final double atomicMass = isotope.getMass();
    final double eprod = BeamProperties.eOfBrhoAoq(brhoprodScalar.getDouble(),
     BeamProperties.aoqOfAZeroQ(atomicMass, qBeamProd.getInt()));
    return ValueFactory.createScalar(eprod);
  }
}
```

**Listing 6.4:** Code snippet handling the production case.

As a final step EC calls the method eoutCalculate() (see Lst. 6.5), which requires the variables eIn, spline, sr, areaDensity, ionMass and qBeam. This final method consists of six steps:

1. Read out the spline file, which corresponds to the String spline via the passed SplineReader variable sr, which also holds all spline information (i.e. beam, material, kinetic energy intervalls/knots,

coefficients for range, range straggling, angular straggling and time-of-flight).

2. Extract the range spline from sr and save all the knots, coefficients, number of coefficients and spline order inside the variable rangebs of class BSpline.
3. Determine the value of the BSpline rangebs for the given energy eIn via the ATIMA algorithm bvalue (mentioned in Sec. 2.4). The resulting double rangeValue will be given in units of $\mathrm{mg\,cm^{-2}}$.
4. Calculate the variable primaryIonMass from the mass number A given by the SplineReader sr and the beam charge-state qBeam. The corresponding ATIMA spline contains the respective atomic mass of the most common isotope, which has to be corrected for other charge-states.
5. Determine the value of the variable fraction by multiplying the ratio of the material thickness variable areaDensity and the beam's maximum range rangeValue with the ratio of the spline's primaryIonMass and the beam's ionMass from LSA. This is important since ATIMA only possesses the splines for the most abundant isotope of each element and all other isotopes are derived by multiplication with this ratio.
6. Calculate and return the resulting energy double variable eInter, which stands for intermediate energy, via the e_out method from ATIMA, which uses the previously determined variables rangeValue, eIn and fraction as input to find the root of the function $F_B = rangeValue - bvalue(b, 0) - rangeValue * fraction$, where $\{b \in \mathbb{R} \mid 0 \leq b < eIn\}$, via the one-dimensional Brent method [60] and return $b$ as eInter.

```
class EoutCalculate {

  private final double electronMass = 0.0005485799091; //given in units of u

  public double eoutCalculate(final double eIn, final String spline, final
   SplineReader sr, final double areaDensity, final double ionMass, final int qBeam) throws
    TrimException {
    try {
      sr.ReadSpline(''lsa/frs_spline_db/src/'' + spline);
    } catch (final IOException e) {
      throw new TrimException(e);
    }
    final BSpline rangebs = new BSpline(sr.getKinEn(1),sr.getBCoeff(1),
     sr.getCoeffNr(1), sr.getOrder(1));
    final double rangeValue = rangebs.bvalue(eIn, 0);
    final double primaryIonMass = sr.getMaxA() - electronMass * qBeam;
    final double fraction = (areaDensity / rangeValue) * (primaryIonMass / ionMass);
    final double eInter = rangebs.Eout(rangeValue, eIn, fraction);
    return eInter;
  }

}
```

**Listing 6.5:** Complete definition of EoutCalculate class.

Consequently all mentioned classes and methods in as well as around the EoutMakeRule, except for higher abstract classes like AbstractGSIMakeRule and other LSA provided dependencies, exist to feed information into the root-finding process and propagate the resulting root value b, which is equivalent to the outgoing beam energy, though all layers of abstraction constructed by the control system framework. The aforementioned method detectorEoutCalculate() of the same class DetectorEoutCalculate provides a very similar functionality. Since detectors are multi-layered matter devices, detectors are first read-out

layer by layer via the TargetReader class and in the next step the energy-loss is calculated by applying the eoutCalculate() method to each layer, where the output of the previous layer of matter serves as the output for the next layer until the final layer is reached and thefinal outgoing energy is outputted. This approach allows for less code redundancy and more utility in the application of generalized classes for several use cases.

## 6.2. EffectiveThicknessMakeRule

When a beam passes through a matter device like a wedge degrader or a setup of degrader disks, then the device-position-dependent thickness has to be calculated. The same applies if the heavy-ion beam passes through these devices at a residual different angle other than $0\ \mathrm{mrad}$ or the degrader is being put into the beam at an angle, since the energy-loss for an angled beam in such thick matter devices is non-negligible and can cause misalignment further down the transfer line, if not taken into account. This Makerule could also be applied to both thick targets or targets in general but utmost care is put into the centering and proper alignment of the heavy-ion beam through the FRS at the beginning of each operational cycle, i.e. at the beginning of an experiment, and thus reducing the beam angle to $0\ \mathrm{mrad}$ - in theory - and not necessary for such devices.
The EffectiveThicknessMakeRule is defined as the connecting relation between the set $D_T$ of Parameter types and the single Parameter type $SCALAR\_TARGET\_EFFAREADENSITY$, defined as such:

$$D_T = \{SCALAR\_TARGET\_ANGLE,\ SCALAR\_TARGET\_XPOS,\\ SCALAR\_DEGRADER\_ROTANGLE,\ SCALAR\_TARGET\_AREADENSITY\} \tag{6.2}$$

where ”DEGRADER” denotes a Parameter type belonging to the group of degrader devices and the respective suffixes denote the Parameter name as previously introduced. Furthermore is the Makerule an extension of the already discussed AbstractTargetMakeRule to gain access to the TargetReader class, which reads out all relevant matter information.
When the Makerule is called, see Lst. 6.6, a very similar program sequence takes place in which at first all parent Parameters of set $C_T$ are extracted as a list of Parameters and consequently each individual Parameter, their Setting and value is checked and extracted into different variables, as well. Once the variables are defined, an instance of the TargetReader class reads out the .csv-file of the corresponding device name and extract the minimum and maximum area density than can be reached by this degrader in units of $\mathrm{mg\,cm^{-2}}$ as well as the respective drive positions at which these thicknesses can be achieved. A similar readout occurs for devices whose area density depends on the rotational angle of the drives. This has the advantage that a private method can be implemented inside the Makerule class, which can be

```
1 public class EffectiveThicknessMakeRule extends AbstractTargetMakeRule {
2
3   @Override
4   protected ImmutableValue makeValueGsiImpl(final MakeRuleArguments mra) throws
5   TrimException {
6     final List<Parameter> parentParameters = mra.getParentParameters();
7     ...
8   }
9 }
```

**Listing 6.6:** Head and definition of EffectiveThicknessMakeRule class.

called for both aforementioned cases and sets of variables. The name of the method is effAD() and it takes the variables xmax, which is the drive Setting (position or rotational angle) at which the thickness is maximal, xmin, the drive Setting at which the thickness is minimal, maxad, the maximum thickness at xmax, minad, the minimum thickness at xmin, xpos, which is the currentdrive position, and angle, which is the previously described angle at the degrader. In the case that there is no angle present the calculation simplifies into a linear interpolation inbetween the maximum and minimum thickness:

$$effad = \frac{maxad - minad}{xmax - xmin} * xpos + (minad - \frac{maxad - minad}{xmax - xmin} * xmin) \tag{6.3}$$

In the case that an angle occurs it changes to

$$effad = \frac{maxad + minad}{xmax - xmin} * \frac{(-offset - \cot angle)}{slope - \cot angle} * xpos, \tag{6.4}$$

with slope and offset defined as

$$offset = minad - \arctan(slope) * xmin, \tag{6.5}$$

$$slope = \frac{maxad - minad}{xmax - xmin}. \tag{6.6}$$

These equations have been implemented in the code as can be seen in Lst. 6.7. After the calculation the value for effad is returned inside the EffectiveThicknessMakeRule and from there given to the respective Parameter of type $SCALAR\_TARGET\_EFFAREADENSITY$ from the method makeValueGsiImpl().

```
private static ImmutableScalar effAD(final double xmax, final double xmin, final double
    maxad, final double minad, final ImmutableScalar angle, final ImmutableScalar xpos) {
  if (xpos.getDouble() == 0) {
    return ValueFactory.createScalar(minad);
  }
  if (angle.getDouble() == 0) {
    final double slope = (maxad - minad) / (xmax - xmin);
    final double offset = minad - slope * xmin;
    final double effAD = slope * xpos.getDouble() / 1000 + offset;
    return ValueFactory.createScalar(effAD);
  }
  final double slope = (maxad - minad) / (xmax - xmin);
  final double offset = minad - Math.atan(slope) * xmin;
  final double xposneu = (-offset - Math.cot(angle.getDouble()) * (xpos.getDouble() / 1000))
     / (slope - Math.cot(angle.getDouble()));
  final double effAD1 = (maxad + minad) * (xposneu / xmax - xmin);
  return ValueFactory.createScalar(effAD1);
}
```

**Listing 6.7:** Implementation of method effad().

## 6.3. TargetProductionMakeRule

Beyond calculating the energy-loss, other mechanisms that could alter the main beam's properties such as the charge-state $Q$, isotopic mass number $A$ or elemental charge number $Z$ have to be taken into account. In order to calculate these properties for a beam impinging on a target, stripper or any other piece of

matter within the beam line, a myriad of algorithms exists to predict the change in both nuclear and atomic properties of the aforementioned attributes via numerous reaction mechanisms and theoretical models. This leads to the conclusion that implementing all these algorithms into the control system would be deemed highly unfeasible as on one hand it would take a wasteful amount of work hours to translate the existing algorithms from their original language into Java and consequently implement them into LSA as well as on the other hand it would completely overwhelm the LSA server network as most performance would be taken up by calculations for these algorithms and not be utilized for communication in between devices, timing and data supply. It was decided for these reasons that production within matter devices should be triggered by an experienced and expert operator for specialized machines, like the FRS or later Super-FRS, as well as manually input. This means that all the corresponding calculations have to be done via an external application in advance and the resulting properties are used via the previously introduced production Parameters of the FRS General Target Hierarchy, see Sec. 5.1. The Makerule which builds this relation is called the TargetProductionMakeRule and acts upon the input Parameter type set

$$P_T = \{SCALAR\_TARGET\_NAME,\ SCALAR\_TARGET\_NAME\_PROD,\ BOOLEAN\_TARGET\_PRODUCTION\} \tag{6.7}$$

and the output Parameter type $SCALAR\_TARGET\_NAME\_OUT$, where ”NAME” can stand for one of the following Parameters $ELEMENT$, $ISOTOPE$ or $Q$.
In order to minimize code and enable a more abstract and generalized use for this case, the implementation for this Makerule is less specific than the previous ones. Contrary to the previous two Makerules, this Makerule extends the AbstractGsiMakeRule, which omits the possibility to use the TargetReader class, since no matter device information has to be read out from the FRS target database, see Lst. 6.8. Furthermore three private attributes are defined in the beginning of the class. The first is a String named Parameter_TYPE_PRODUCTION containing the Parameter type name as a String variable and is to be unchanged. The two others are the String variables defaultParameterType and productionParameterType, which contain the default Parameter type name if no production occurs and the production Parameter type name if production occurs. These names correspond to the two scalar types in set F. The attributes are then followed by the definition of two usual set methods, which require another String variable as an input and set the respective private attribute accordingly. This is followed by the implementation of the method makeValueGsiImpl(), which now contains a very simple body. It begins with the extraction of the value of the parent Parameter with type $BOOLEAN\_TARGET\_PRODUCTION$. Consecutively, this value is checked if it is ”null”. In the case that the value does not exist, a new Boolean variable isProduction gets the assignment ”false” otherwise the respective value is assigned to isProduction. According to the value of this variable the new variable dependentValue is either - true - assigned the value of the corresponding Parameter from productionParameterType or - false - assigned the value from defaultParameterType and returned. In order for LSA to know which Parameter types are available for the method call, the Spring

```
1  public class TargetProductionMakeRule extends AbstractGsiMakeRule {
2
3    private static final String PARAMETER_TYPE_PRODUCTION ''BOOLEAN_TARGET_PRODUCTION'';
4    private String defaultParameterType;
5    private String productionParameterType;
6
7    public void setDefaultParameterType(final String defaultParameterType) {
8      this.defaultParameterType = defaultParameterType;
9    }
10
11   public void setProductionParameterType(final String productionParameterType) {
12     this.productionParameterType = productionParameterType;
13   }
```

```
14   @Override
15   protected ImmutableValue makeValueGsiImpl(final MakeRuleArguments mra) throws
       TrimException {
16     final ImmutableValue parameterProductionValue = getParentValueOrNull(mra,
       PARAMETER_TYPE_PRODUCTION);
17     final boolean isProduction;
18     if (parameterProductionValue == null) {
19       isProduction = false;
20     } else {
21       isProduction = ((ImmutableScalar) parameterProductionValue).getBoolean();
22     }
23     final ImmutableValue dependentValue;
24     if (isProduction) {
25       dependentValue = getParentValue(mra, productionParameterType);
26     } else {
27       dependentValue = getParentValue(mra, defaultParameterType);
28     }
29     return dependentValue;
30   }
31 }
```

**Listing 6.8:** Full definition and implementation of TargetProductionMakeRule

framework [83] is used to inject the respective Parameter types into the method call by utilizing a concept called ”Beans” which are defined by the following code example in Lst. 6.9.

```
1 @Bean
2 public TargetProductionMakeRule SCALAR_PRODUCEELEMENTMR() {
3 final TargetProductionMakeRule rule = configureMakeRule(new TargetProductionMakeRule());
4 rule.setDefaultParameterType(''SCALAR_TARGET_ELEMENT'');
5 rule.setProductionParameterType(''SCALAR_TARGET_ELEMENT_PROD'');
6 return rule;
7 }
```

**Listing 6.9:** Bean example for TargetProductionMakeRule in the case for $ELEMENT$

This Bean defines that whenever the TargetProductionMakeRule gets called for their respective case, the previously defined set methods are called with the corresponding Parameter type names to instantiate the correct version of TargetProductionMakeRule.

## 6.4. Give2BeamTargetEMakeRule

Since its inception, the basic mode of operation for the FRS has been to segment the machine into its nine different main foci and define the magnetic rigidity of the six main dipole stages together with their quadrupoles and sextupoles as the basic input. This would prove to be sufficient to manipulate a heavy-ion beam’s phase space within the FRS. These $B\rho$ were calculated by LISE++ and input into the now obsolete former control system. Technically this functionality persists with the introduction of LSA and its concept of Trims, which are defined as permanent changes to a Parameter’s Setting, but are not easily accessible within the current GUI. Instead of a $B\rho$ value the operator would have to input an energy Trim. In order to ensure the former functionality of applying a $B\rho$ in $\mathrm{T\,m}$ directly from pre-calculated values to a dipole stage, guarantee simple and intuitive accessibility for the operator and streamline the operation process the Give2BeamTargetEMakeRule has been introduced together with its respective functional Parameter

hierarchy. This Makerule fulfills the two purposes that it allows for the outgoing energy after the last matter device of one Accelerator Zone to be propagated to the Beam Device of the same AZ if no $B\rho$ overwrite is requested. However, if it is, then the Makerule processes the given overwrite $B\rho$ value into the correct energy value for the Beam Device. The following set of Parameter types is defined as its parent Parameters:

$$W_T = \{SCALAR\_TARGET\_EOUT,\ BOOLEAN\_OVERWRITE\_BRHO,\ SCALAR\_BRHO,\ SCALAR\_TARGET\_Q,\ SCALAR\_TARGET\_ISOTOPE,\ SCALAR\_TARGET\_ELEMENT\} \tag{6.8}$$

This set is connected via the Makerule to the Parameter type $SCALAR\_E$. As per standard, Give2BeamTargetEMakeRule inherits from AbstractGsiMakeRule and implements the makeValueGsiImpl() method, see Lst. 6.10.

```
public class Give2BeamTargetEMakeRule extends AbstractGsiMakeRule {

  @Override
  protected ImmutableValue makeValueGsiImpl(final MakeRuleArguments mra) throws
    TrimException {
    final ImmutableScalar e = this.getParentValueAsTyped(mra, ''SCALAR_TARGET_EOUT'');
    final List<Parameter> parentParameters = mra.getParentParameters();
    for (final Parameter parameter : parentParameters) {
      if (parameter.getParameterType().getName().equals(''BOOLEAN_OVERWRITE_BRHO'')) {
        ...
        if (overwriteSetting == null || userBrhoSetting == null) {
          return e;
        }
        if (overwrite) {
          ...
          final ChemicalElement element = ChemicalElements.getElementByAtomicNumber(
           atomicNumber);
          if (element == null) {
            throw new TrimException(''Cannot find an element for a given atomic number ''
             + atomicNumber);
          }
          final Isotope isotope = element.getIsotopeByMassNumber(massNumber);
          if (isotope == null) {
            throw new TrimException(''Cannot find an isotope for the element '''
             + element.getSymbol() + ''' and the given mass number '' + massNumber);
          }
          final double atomicMass = isotope.getMass();
          final Double AoverQ = BeamProperties.aoqOfAZeroQ(atomicMass, charge);
          final Double userEnergy = BeamProperties.eOfBrhoAoq(userBrho, AoverQ);
          return ValueFactory.createScalar(userEnergy);
        }
      }
    }
    return e;
  }

}
```

**Listing 6.10:** Full definition and implementation of Give2BeamTargetEMakeRule. "..." symbolizes parts of the code where Parameters and Settings are extracted similar to previous listings.

The beginning of the method sequence is characterized by the extraction of parent Parameters, which in the next step are checked if they contain the type $BOOLEAN\_OVERWRITE\_BRHO$. If not then

the whole sequence is skipped and the outgoing energy from the last target is returned unchanged. If it contains said type, then further the Boolean overwrite Parameter and the user $B\rho$ are extracted and checked for existence. If either of them is not defined then the unchanged energy value is propagated. In the case that both of them have a value and the operator wishes to overwrite the current $B\rho$ of a dipole stage the classes ChemicalElements and Isotope are instantiated to get related beam properties, i.e. the exact atomic mass, to further derive the corresponding $A/Q$-value and the new energy for the beam via the class BeamProperties. This energy is then returned as the new Beam Device energy. The classes ChemicalElements, Isotope and BeamProperties are provided by the LSA framework.

## 6.5. TargetAlignmentMakeRule

Another important aspect of the old operation mode of the FRS was the ability to align the primary heavy-ion beam unto one of the target stations situated in the target area TA. This alignment meant that the two dipole magnets GTS1MU1 and GTS1MU2 for horizontal angular and position correction together with the vertical dipole steerers GTE1KY1 and GTS1KY1 for vertical angular and position correction such that the beam is centered with no angle on the target. The current grids GTS1DG5 and GTS2DG2 are utilized for this purpose by measuring the horizontal and vertical beam position. With the help of an ion-optical matrix describing the setup, the beam spot on the target can be calculated. The difference in necessary position change within the detectors is used as input for this calculation. This calculation was heretofore carried out with the ion-optical program MIRKO [84] and the magnets were set to their corrected values via the function ”Gerade legen”. As of today, MIRKO is being worked on to be ported into Java, under the name jMIRKO, and provide the same functionalities as previously and be compatible with LSA. As an intermediate solution, the target alignment hierarchy from Sec. 5.3 has been implemented to fulfill the same purpose and allow for a very similar style of operation with the LSA control system framework with the help of the TargetAlignmentMakeRule. As such it builds the relation between the set $T_T$ of parent Parameter types responsible for the target alignment and the set $K_T$ of ion-optical kick Parameter types, with the following definitions:

$$T_T = \{STRING\_OPTIC\_NAME,\ SCALAR\_TARGET\_XPOS,\\ SCALAR\_TARGET\_YPOS,\ STRING\_TARGET\_MATERIAL\} \tag{6.9}$$

$$K_T = \{HKICK\_TARGET,\ VKICK\_TARGET\} \tag{6.10}$$

The special relation here is that every element of $T_T$ is a parent of every element of $K_T$ except for the types with the suffixes ”XPOS” and ”YPOS”. These are only parents to one element of $K_T$, which are the types with the prefixes ”HKICK” and ”VKICK” respectively. One might notice that the string Parameter type used here is called $STRING\_TARGET\_MATERIAL$ instead of the expected $STRING\_TARGET\_OPTICNAME$ for the name of the file containing the ion-optical coefficients. This was simply to avoid introducing another string Parameter type when the other one already exists and can be used for the same purpose, while still establishing a unique relation between Parameter types. Another specialty of this Makerule is that it the calculation of the new kick value depends on the current kick value, which differs from all other introduced Makerules so far as they all were either unidirectional calculations or propagations.
The Makerule definition begins with the standard class definition that TargetAlignmentMakeRule extends AbstractGsiMakeRule. Eighteen private string variables are subsequently introduced to cover the name of all involved matrix coefficients and detector distances, followed by the definition of four more string variables for the respective device names of the magnets. An additional private enum for Mode with the

two states ”X_MODE” and ”Y_MODE” is defined (see Appendix C). After this the definition of the main method makeValueGsiImpl() begins by extracting the Beam Process and the dependent Parameter via the arguments. From these variables the Setting of the dependent Parameter is checked if it was initialized. If not then the Makerule returns a corresponding zero function for the length of the whole Beam Process, see Lst. 6.11.

```
1  final BeamProcess beamProcess = mra.getBeamProcess();
2  final Parameter depParameter = mra.getParameter();
3  final Setting depSetting = getSettingOrNull(mra, depParameter);
4  if (depSetting == null) {
5    return ValueFactory.createZeroFunction(beamProcess.getLength());
6  }
```

**Listing 6.11:** Initial extraction and check for depSetting.

Otherwise the sequence continues and the current kick value, parent Parameters, optics name and magnet device name are extracted. Followed by a check if opticNameValue has a value different from null and resulting in the same procedure as with the previous check, see Lst. 6.12.

```
1  final ImmutableValue K0LKickCurrentValue = depSetting.getValue();
2  final List<Parameter> parentParameters = mra.getParentParameters();
3  final String deviceName = depParameter.getDevice().getName();
4  final ImmutableValue opticNameValue = getParentValueOrNull(mra,
5   PARAMETER_TYPE_STRING_TARGET_MATERIAL);
6  if (opticNameValue == null) {
7    return ValueFactory.createZeroFunction(beamProcess.getLength());
8  }
```

**Listing 6.12:** Continued extraction and check for opticNameValue.

After this check the actual string of the variable opticNameValue is extracted and it is decided which mode, ”X_MODE” or ”Y_MODE”, is assigned to the current device via the private method getModeForDevice(deviceName) (see Appendix C). This decision is done by checking the name string for the respective device, where the main horizontal dipoles are assigned ”X_MODE” and the vertical steerers are assigned ”Y_MODE”, see Lst. 6.13. Depending on the previously determined mode, a Pair of two immutable scalars is instantiated via a call to the method getChangeValuesForMode(). The purpose of this method is to extract the pair of values for the Settings belonging to the Parameters ”ZPOSITION_CHANGE_DELTA”, where Z is either X or Y and corresponds to the chosen mode and A is a placeholder for 1 or 2, that describe the needed change towards the center in either horizontal or vertical position in $\mathrm{mm}$ in the two current grids at TA. Once all these variable are instantiated and it is ensured that the pair changeValues is not null the actual calculation takes place in the method doAlignmentCalculation().

```
1  final String opticName = opticNameValue.getString();
2  final Mode mode = getModeForDevice(deviceName);
3  final Pair<ImmutableScalar, ImmutableScalar> changeValues =  getChangeValuesForMode(mra,
     mode, parentParameters);
4  if ((mode.equals(Mode.X_MODE) || mode.equals(Mode.Y_MODE)) && changeValues ==  null) {
5    return ValueFactory.createZeroFunction(beamProcess.getLength());
6  }
7  final ImmutableValue K0LKickNewValue = doAlignmentCalculation(deviceName,
8   changeValues, opticMode, mode, K0LKickCurrentValue);
9  return K0LKickNewValue;
```

**Listing 6.13:** Continued extraction and check for opticNameValue.

This method utilizes the OpticsReader class (see Appendix C) to produce a HashMap that contains the strings defined in the head as keys and the extracted coefficient values as double values for instantaneous access to each coefficient.
The new kick value is then calculated according to the following set of formulae and returned as the new kick value to the corresponding magnet:

$$\Delta\theta_i = \frac{\Delta s_{1i} - \Delta s_{2i}}{d_1 - d_2}, \quad \Delta s_i = \Delta s_{1i} + d_1 * \Delta\theta_i \tag{6.11}$$

Here, $\Delta\theta_i$ and $\Delta s_i$ stand for the angular and positional change of the beam on the target. Respectively the index $i$ denotes either $x$ or $y$ for the horizontal or vertical direction. The quantity $\Delta s_{ji}$ denotes the positional change within detector $j$ in direction $i$, with $j$ being either 1 or 2. Finally, $d_j$ denotes the distance of detector $j$ from the target.

$$A_x = (x,x)_2 * (x,\delta)_1 + (x,a)_2 * (a,\delta)_1, \quad B_x = (a,x)_2 * (x,\delta)_1 + (a,a)_2 * (a,\delta)_1 \tag{6.12}$$
$$A_y = (y,y)_2 * (y,d)_1 + (y,b)_2 * (b,\delta)_1, \quad B_y = (b,y)_2 * (y,\delta)_1 + (b,b)_2 * (b,\delta)_1 \tag{6.13}$$
$$C_x = A_x * (a,\delta)_2 - B_x * (x,\delta)_2, \qquad C_y = A_y * (b,\delta)_2 - B_x * (y,\delta)_2 \tag{6.14}$$

The ion-optical matrix coefficients are denoted in the style $(c_k, c_m)_n$, where $k$ and $m$ are the matrix indices going from 1 to 6 and $n$ being the magnet index which is either 1 or 2. The general symbols $c_k$ and $c_m$ were then substituted by the more intuitive representation $x$, $a$, $y$, $b$ and $\delta$, which stand for the horizontal position and angle, vertical position and angle as well as the momentum deviation respectively. The abbreviations $A_i$, $B_i$ and $C_i$ are introduced for easier visibility. From these equations one obtains the kick deviation $\Delta p_{ni}$

$$\Delta p_{1x} = \frac{(a,\delta)_2 * \Delta s_x - (x,\delta)_2 * \Delta\theta_x}{C_x}, \qquad \Delta p_{2x} = \frac{-B_x * \Delta s_x + A_x * \Delta\theta_x}{C_x} \tag{6.15}$$
$$\Delta p_{1y} = \frac{(b,\delta)_2 * \Delta s_y - (y,\delta)_2 * \Delta\theta_y}{C_y}, \quad \Delta p_{2y} = \frac{-(b,\delta)_1 * \Delta s_y + (y,\delta)_1 * \Delta\theta_y}{C_y} \tag{6.16}$$

and can calculate the final kick value $k_{fni}$

$$k_{fnx} = (k_{0nx} - \theta_n) * (1 - \Delta p_{nx}) + \theta_n, \quad k_{fny} = k_{0ny} - \Delta p_{ny}, \tag{6.17}$$

where $k_{0ni}$ is the initial kick value and $\theta_n$ the mechanical deflection angle of $7.5^o$ of the main dipoles. This set of equations can be obtained with the help of the ion-optical transfer matrix $T$ for the system such that it describes the initial deviation on the target. The linear system of equations can then be solved for the requirement that the beam is centered on the targets, under the assumption that no quadrupoles change and only kicks are applied to the horizontal dipoles and vertical steerers, i.e. a deviation on the deflection angle.

# Part III.

# Benchmark

After the previous description and discussion of the FRS machine-model, the following Chs. deal with a thorough assessment and benchmark of the implemented model. Chapter 7 starts with a comparison of the two ATIMA versions in use, which are the methods and functions translated from Fortran to Java and used within LSA, named LSA ATIMA or ATIMA light, and the current ATIMAPy build [22, 50]. Their accuracy and differences will be discussed.
Chapter 8 compares the predictive power of the machine-model by utilizing the implemented energy-loss methods and different setups with the FRS GTH, from Sec. 5.1, to calculate magnetic rigidities as well as currents for power supplies that are then compared to past experiments and discussed.
Chapter 9 treats machine experiments run during the engineering runs from 2019, which were used as the very first machine-operated runs with actual heavy-ion beams to test the functionalities of the LSA control system and the full capabilities of the FRS machine-model in different primary and secondary beam setups.
Finally, Ch. 10 describes the final experimental benchmark of the implemented machine-model with a current experiment from spring 2020 that utilized the full LSA control system framework. Similar comparison methods from Ch. 8 are applied here.

# 7. Numerical Comparison and Accuracy of Original ATIMA Versus ATIMA in LSA

In order to show the equivalence, both numerically and physically, of the translated ATIMA routines inside LSA (short LSA ATIMA) and the original ATIMA version [50], it was chosen to compare the calculated output energy from LSA ATIMA with the calculated output energy of the current ATIMAPy [22] build, a version of ATIMA, which utilizes the full FORTRAN libraries wrapped in a Python interface, that allows for easy-to-program multi-array calculations for several beam-target combinations at once. A total of 180 beam-target combinations were chosen for the most common interactions at the FRS, see Tab. 7.1.

| Beams | $^{1}$H , $^{6}$Li , $^{12}$C , $^{16}$O , $^{40}$Ar , $^{48}$Ca , $^{56}$Fe , $^{58}$Ni , $^{136}$Xe , $^{197}$Au , $^{208}$Pb , $^{238}$U |
|---|---|
| Targets / $[\mathrm{mg\,cm^{-2}}]$ | Nb 117, 223; Be 400, 1035, 2513, 4014, 6346; Cu 89; Ta 4020; |
| | Pb 3910; $C_9H_{10}$ 517, 301, 107; P10 gas 10.9, 124.9 |

**Table 7.1.:** Most common beam and target combinations for energy-loss calculations at the FRS. Every beam was combined with every target for the purpose of this comparison and assumed to be fully stripped ranging in input energy from 1 to 1000 $A\mathrm{MeV}$. $C_9H_{10}$ is also called BC420 or simply plastic. P10 gas is a mixture of 90% Ar and 10% CH4.

Further observables are then calculated by the respective output energies. For a simple comparison, the difference $\Delta E_O$ is calculated

$$\Delta E_O = E_{O,LSA} - E_{O,ATIMA}, \tag{7.1}$$

where $E_{O,LSA/ATIMA}$ is the LSA ATIMA (LSA) and ATIMAPy (ATIMA) calculated output energy, respectively. The next observable calculated is the relative difference $\Delta E_{rel,0}$

$$\Delta E_{rel,O} = \Delta E_O / E_{O,ATIMA}, \tag{7.2}$$

With this relative difference it is especially interesting to see how close $\Delta E_{rel,0}$ can be to 0, with 0 resulting if and only if $E_{O,LSA}(E_i) = E_{O,ATIMA}(E_i)$ for the same input energy $E_i$.
The discussion in this Ch. will only be held for combinations of a $^{208}$Pb beam and the respective targets, since this was the primary beam that was used for the S468 new isotope search experiment. Figures for other beam-target combinations can be found in the Appendix D.
Figures 7.1 and 7.2 show the results for $\Delta E_O$ and $\Delta E_{rel,0}$ plotted, respectively, for the input energy range of 1 to 1000 $A\mathrm{MeV}$. As a good example the target Be 2513 $\mathrm{mg\,cm^{-2}}$ has been singled out. For input energies below the material thickness equivalent of the stopping power, in this case it would be below $\sim$ 338 $A\mathrm{MeV}$, $\Delta E_O$ assumes values between 800 and 340 $A\mathrm{eV}$, these values are cut out from the plots since they are physically wrong, as the beam should be stopped and therefore 0 $A\mathrm{eV}$ is expected. Even though the input energy is not high enough for the beam to pass the matter, ATIMAPy outputs values differing from 0 $A\mathrm{MeV}$ in the same range as mentioned before. LSA ATIMA on the other hand outputs beam output energy values in the range of $2{\cdot}10^{-31} A\mathrm{MeV}$, which for a double floating precision variable, as used in

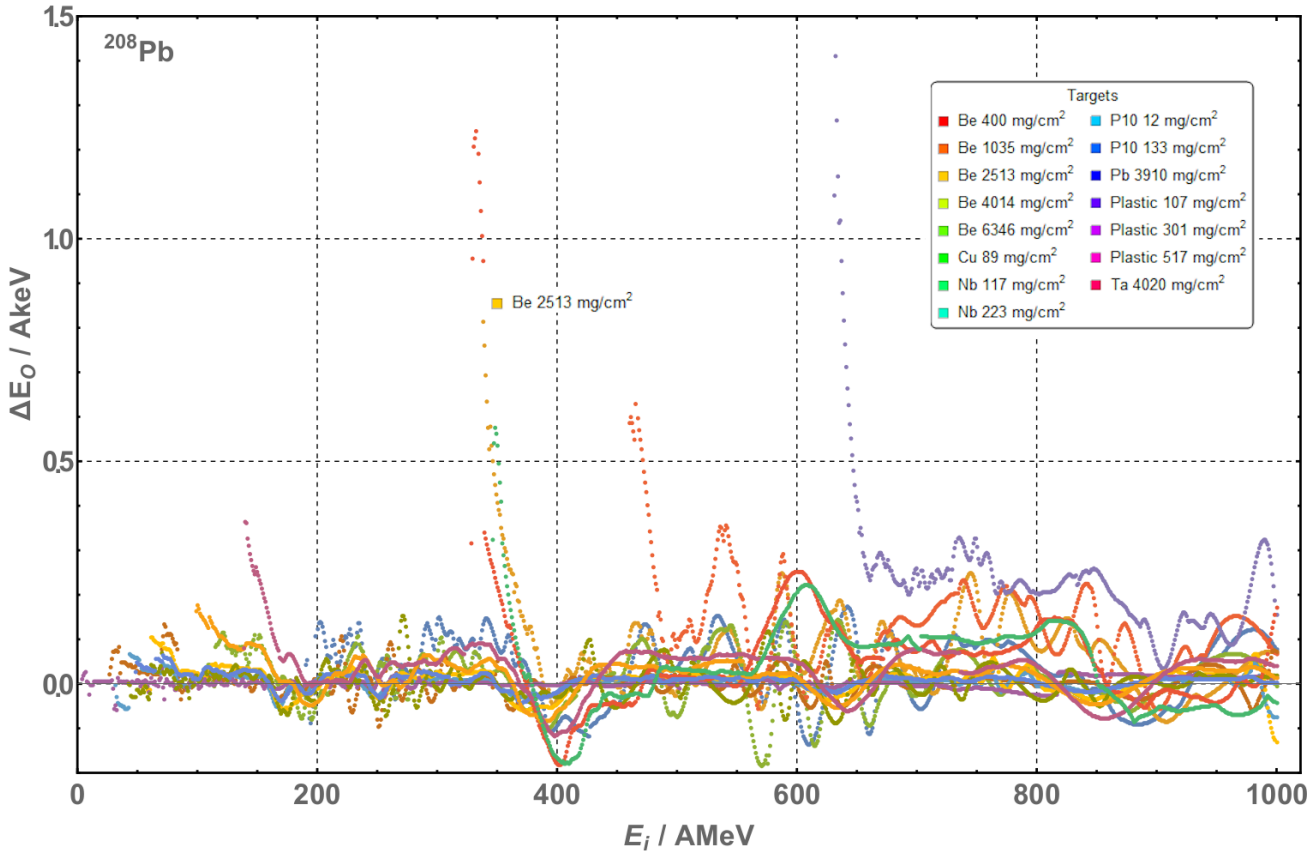


**Figure 7.1.:** $\Delta E_o$ plotted over the incoming energy $E_i$. Even though fluctuations occur, the trend is visible, that the difference diminishes for higher energies and stays within a tight band around 0 $A$eV.

LSA ATIMA, see code in Lst. 6.5, corresponds to a numerical 0, as expected. For input energies above $\sim$ 338 $A$MeV, the output energies of LSA ATIMA and ATIMAPy start to approach each other, whereby the difference never exceeds the values of the previous upper limit of 800 $A$eV, and for high enough input energies stays within a band of $\pm$ 100 $A$eV.
The observable accuracy $\Delta E_{rel,0}$ shows a very similar behaviour to the previously described function of $\Delta E_0$, but what is especially noteworthy is that the relative accuracy values do not exceed $10^{-5}$ and for input energies higher than the material's stopping power the accuracy is better than $10^{-6}$. For gaseous targets and thin materials the accuracy reaches values of down to $10^{-7}$. These trends and behaviours can be seen for all considered targets. A difference in behaviour for different targets can be seen when different thicknesses for the same material is considered, where thicker targets have a higher threshold for the input energy and vice versa. The same is valid for denser materials and materials with higher proton numbers. From these observations it can be deduced that even though the calculated output energies differ on the level of up to several $A$keV, depending on the beam and target combinations as well as how close the input energy is to the passing threshold, the energy-loss calculations can achieve accuracies of up to $10^{-7}$ or better for certain combinations and the typical operational energies of the FRS. This already provides a higher accuracy than can be achieved in the adjustment of the magnetic rigidity of the FRS dipole stages, which lies in the region of $10^{-4}$ T m by utilizing Hall-probe measurements.
An important critique point is the systematic inaccuracy of ATIMAPy calculating output energies in the range of 300 $A$eV to 800 $A$eV for a beam that should be stopped within a target. Even though LSA ATIMA and ATIMAPy are based of the same FORTRAN libraries and the code is functionally identical, it is important

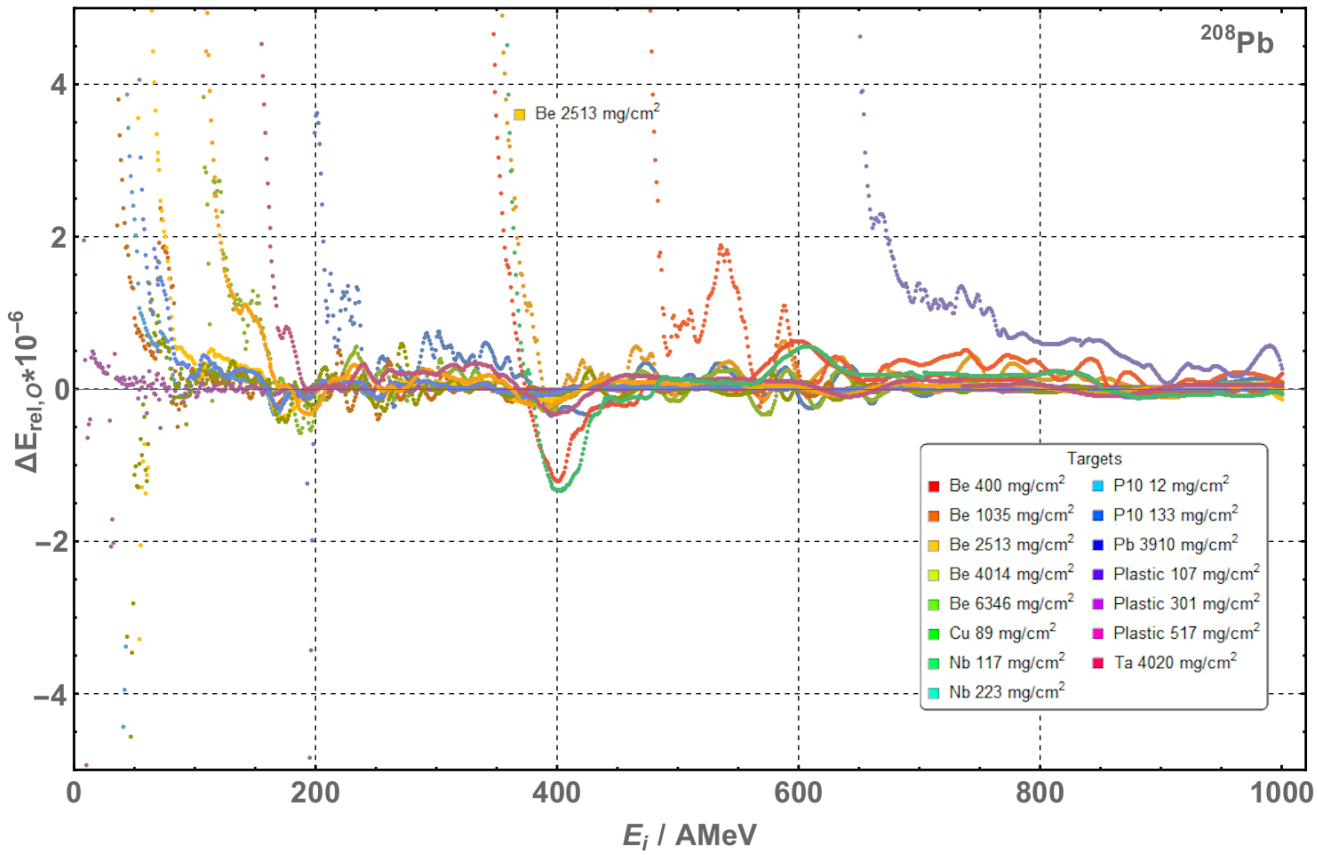


**Figure 7.2.:** The relative accuracy $\Delta E_{rel}$ plotted over the incoming energy. A similar beheavior as Fig. 7.1 can be seen for the different targets. For energies higher than the passing threshold energy of each material the output energies of both version approach each other and become physically as well as numerically identical, considering the systematic issues of ATIMAPy. Fluctuations in the accuracy down to $10^{-8}$ exist, which are considerably below the measureable accuracy of the FRS' magnetic rigidity of $10^{-4}$ T m.

to note that both versions differ in how the energy-loss in matter is actually calculated. In its core, LSA ATIMA just reads out precalculated range splines from the current FORTRAN version of ATIMA in use, which is 1.41, and calculates the energy-loss from those splines. ATIMAPy on the other hand does every single calculation step, as described in Sec. 2.4, for every energy step. It is unclear, though, what causes the systematic discrepancy of ATIMAPy's output energie for a stopped beam and could either be an issue of utilizing float variables which possess a lower precision than LSA ATIMA's double variables or rounding errors might be causing inaccuracies in the numerical integration methods of ATIMAPy. This is simply conjecture and requires further investigation [59]. In order to further cement LSA ATIMA's accuracy it has been compared to CATIMA [22, 85], whose FORTRAN libraries were wrapped in a C interface and possesses the same core functionality of utilizing and reading out precalculated range splines as LSA ATIMA. The disadvantage is that CATIMA only calculates the energy-loss for one input energy at a time and requires manual input. Therefore, only a few selected energies per target where chosen. Additionally, CATIMA was used during the Engineering Runs in 2019 to debug and fine-tune LSA ATIMA in such a way, that the results were identical. Therefore, CATIMA delivers the same identical results for the current comparison, and LSA ATIMA can be used as a reliable source for automated, repeatable and exact energy-loss calculations for any beam and target combinations at the FRS and upcoming Super-FRS.

# 8. Comparison Simulation and Experiment

After it was shown that LSA ATIMA and ATIMAPy as well as CATIMA are numerically equivalent, it will now be shown that LSA can reproduce rigidity $B\rho$ and current $I$ Settings by comparing LSA machine-model predictions with experimental settings from 2016. Two experimental settings are being considered, the first one is a $^{124}$Xe primary beam at 600 $A\mathrm{MeV}$ and the second one is a secondary $^{111}$Sn beam produced via projectile fragmentation. This requires the utilization of the relative deviation, in order to compare the settings, defined as such

$$\Delta x_{rel} = \frac{x_{Exp} - x_{Pred}}{x_{Pred}}, \tag{8.1}$$

where $x$ denotes either the magnetic rigidity $B\rho$ or the current $I$. Different matter configurations are used within each setting and can be seen in Tab. 8.1.

| Setting | SIS Vacuum Window | Be Target / $[\mathrm{mg\,cm^{-2}}]$ | SEETRAM | S2 Scintillator | S2 Degrader / $[\mathrm{mg\,cm^{-2}}]$ |
|---|---|---|---|---|---|
| $^{124}$Xe | ✓ | 1612.3 | ✓ | ✓ | 0 |
| $^{111}$Sn | ✓ | 1622 | ✓ | ✓ | 737 |

**Table 8.1.:** Experimental settings and matter configurations used for the comparison of LSA setting generation to experimental settings. The thickness of the beryllium target changes since it was recalibrated inbetween settings. And the S2 scintillator matter is 1 $\mathrm{mm}$ of BC420. The material of the S2 degrader is $AlMg_3$

### 8.0.1. Power-Supply Fluctuations

Concerning the discussion of uncertainties within the next sections, settings were only available as a simple snapshot without continuous logging prior to the implementation of MagStat [86]. Using this new functionality, to log all power supply settings every three minutes and store them, it is possible to evaluate extended periods of time to analyze the offset of the actual current and its fluctuation over time for each individual power supply. This was done for the four FRS main dipoles and can be seen in Tab. 8.2. These results can then be applied to all settings utilizing the same calibration functions as the engineering run and Phase-0 experimental period in 2019/2020.

| | GTS3MU1 | GTS3MU2 | GTS4MU1 | GHFSMU1 |
|---|---|---|---|---|
| Variance $I$ /[A] | 0.055 | 0.110 | 0.275 | 0.175 |
| Offset $I$ / [A] | 0.287 | -0.087 | 0.011 | 0.165 |
| $B\rho$ fluctuation / $[\mathrm{T\,m}]$ | 2.9(5)·$10^{-4}$ | -0.9(11)·$10^{-4}$ | 0.1(27)·$10^{-4}$ | 1.6(17)·$10^{-4}$ |

**Table 8.2.:** Resulting offset and variance in actual current compared to set current for the power supplies of the four FRS main dipoles. The stability of the current is then also translated into a fluctuation of the magnetic rigidity in $\mathrm{T\,m}$. It is important to note, that the theoretical set $B\rho$ value does not fluctuate.

Since no other similar data was available for experiments performed before the engineering run, the same offset and variance is assumed to be applicable to previous power supply settings to be aware of the order of magnitude of current fluctuations and accuracy over time.

## 8.1. Magnetic Rigidity $B\rho$

At first the set experimental magnetic rigidity settings are compared to LSA's predictions. These are given for the transfers TA-S2 and S2-S4, meaning that the two main dipoles in each transfer are set to the same value. Table 8.3 shows the experimental set values compared to the machine-model predictions as well as the corresponding relative deviation for each isotope setting and Fig. 8.1 shows the visualization. It is important to note, that both $B\rho$ set values of LSA and the experiment are theoretical input values and as such do not possess an uncertainty.

| $^{124}$Xe | TA-S2 $B\rho$ / [T m] | S2-S4 $B\rho$ / [T m] | $^{111}$Sn | TA-S2 $B\rho$ / [T m] | S2-S4 $B\rho$ / [T m] |
|---|---|---|---|---|---|
| Exp. | 8.4667 | 8.3991 | Exp. | 8.1836 | 7.7489 |
| LSA | 8.4668 | 8.3989 | LSA | 8.1836 | 7.7481 |
| $\Delta B\rho_{rel}$ | $1.18{\cdot}10^{-5}$ | $-2.38{\cdot}10^{-5}$ | $\Delta B\rho_{rel}$ | 0.0 | $-1.03{\cdot}10^{-4}$ |

**Table 8.3.:** $B\rho$ comparison of experimental settings and calculated values from LSA for $^{124}$Xe and $^{111}$Sn.

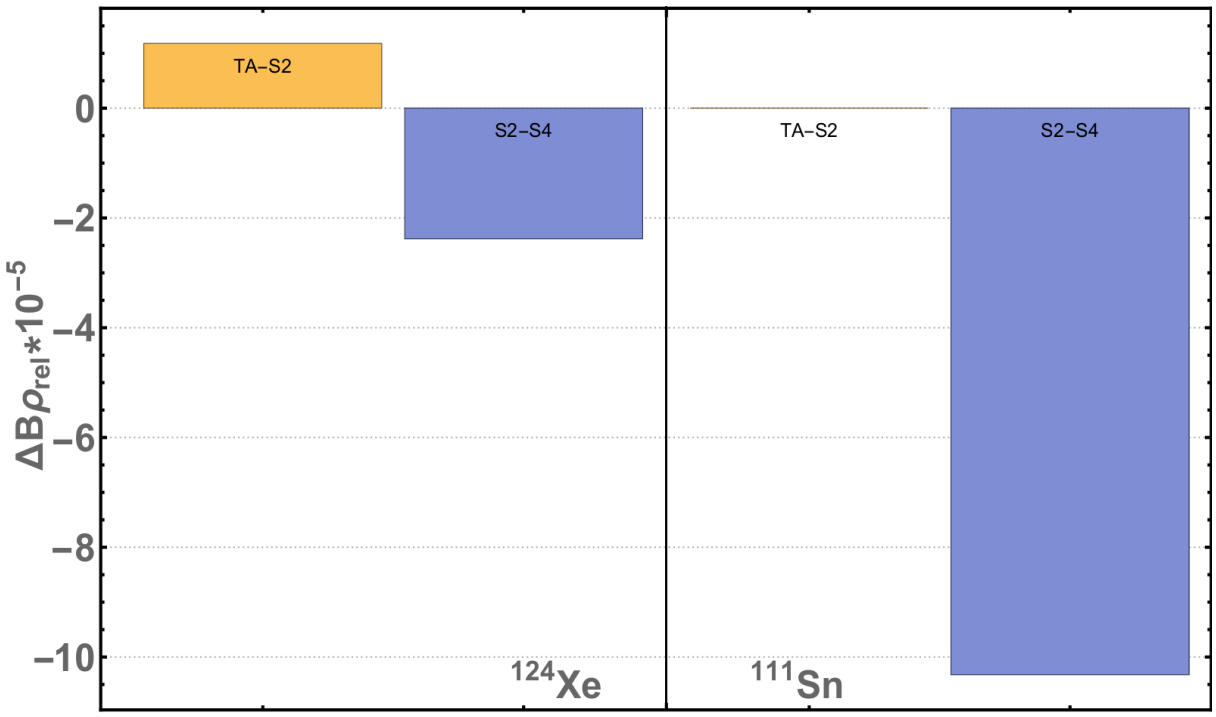


**Figure 8.1.:** Comparison of the deviation in magnetic rigidity for the transfers TA-S2 and S2-S4 in the respective isotope settings $^{124}$Xe as well as $^{111}$Sn.

It can be seen that for the primary $^{124}$Xe setting the deviation in $B\rho$ is in the order of $10^{-5}$, which lies within the $B\rho$ fluctuation of a dipole caused by the fluctuation in current of its corresponding power supply and

can therefore be considered as identical. This is discussed in Subsec. 8.0.1. For the secondary $^{111}$Sn setting it is important to note that the TA-S2 value shows no deviation from each other as LSA requires the LISE++ calculated $B\rho$ value as input, since LSA itself does not calculate the outgoing energy of the resulting ejectiles from projectile fragmentation. For the transfer S2-S4 it results in a deviation of -1.03·$10^{-4}$, which would lie outside of the fluctuation range, discussed in Subsec. 8.0.1, and would cause a miniscule shift in position. In this case, the deviation comes from a different version of ATIMA being used in 2016. A quick calculation for the exact same configuration gives a rigidity of 7.7489 $\mathrm{T\,m}$ for ATIMA version 1.2, opposed to 7.7481 $\mathrm{T\,m}$ from LSA ATIMA, which utilizes version 1.41 resulting in a slightly increased energy loss. Figure 8.1 visualizes the data from the previous table.
In conclusion, LSA is able to reproduce older $B\rho$ settings with an accuracy that lies within the power supplies' current fluctuation levels and persisting differences in the energy loss and therefore deviation in magnetic rigidity can be attributed to different versions of ATIMA being used and have to be considered when comparing older settings to current LSA predictions.

## 8.2. Current

The second comparable observable is the dipoles current in each section. This one is especially interesting as it is distinguished by the set current $I_{set}$ that is sent to the power supply and the actual current $I_{act}$ that is measured and delivered by the power supply. Furthermore, the current is derived via a calibration function which converts the integral field strength of a dipole into the required current. They are usually measured when a dipole is commissioned and subsequently saved in a database. Thus, they can potentially vary every few years depending on the maintenance status of the respective dipole and is important to consider when comparing current LSA predictions with older experimental settings, since LSA only utilizes the most current calibration functions from the GSI OperDB and selecting older ones is not possible.
Similar to the magnetic rigidity in the previous Sec., the deviation was calculated for both the set and actual current values of each dipole's power supply and can be found in Tab. 8.4 for the $^{124}$Xe and Tab. 8.3 for the $^{111}$Sn setting. On first glance it is interesting to see that the deviation of the actual current values is smaller than for the set values. Here GTS3MU1 shows the minimum in deviation for the set values with 9.75·$10^{-4}$ and GTS4MU1 shows the absolute maximum with -5.21·$10^{-3}$.

| $^{124}$Xe | GTS3MU1 I / [A] | GTS3MU2 I / [A] | GTS4MU1 I / [A] | GHFSMU1 I / [A] |
|---|---|---|---|---|
| Set | 388.158 | 386.884 | 384.258 | 384.081 |
| Actual | 388.543(55) | 387.555(110) | 386.456(275) | 384.314(175) |
| LSA | 387.78 | 387.98 | 386.27 | 384.87 |
| $\Delta I_{rel,set}$ | 9.75·$10^{-4}$ | -2.82·$10^{-3}$ | -5.21·$10^{-3}$ | -2.05·$10^{-3}$ |
| $\Delta I_{rel,actual}$ | 1.97(14)·$10^{-3}$ | -1.10(28)·$10^{-3}$ | -4.82(7.12)·$10^{-4}$ | -1.44(45)·$10^{-3}$ |

**Table 8.4.:** Comparison of different experimental currents with the predicted values of LSA for the $^{124}$Xe setting. Uncertainties for actual values are taken from Tab. 8.2.

Since the rigidity values are accurate in the order of $10^{-5}$, it would be expected that the current set values would deviate in the same order of magnitude. Instead a deviation in the order of $10^{-3}$ is observed and can be easily understood with the previously explained field-to-current calibration functions that were different in 2016, when the experiment was conducted, and 2022, when LSA was used to simulate the setup and predict the currents. The dipole's calibration functions were remeasured in 2019 when all four

main dipoles were disassembled and remounted after maintenance. It would have been possible to map old calibration function values to new ones and vice versa, but the old functions are not available anymore. Nonetheless, it shows appropriate agreement even though different calibration functions were used, as will be discussed.

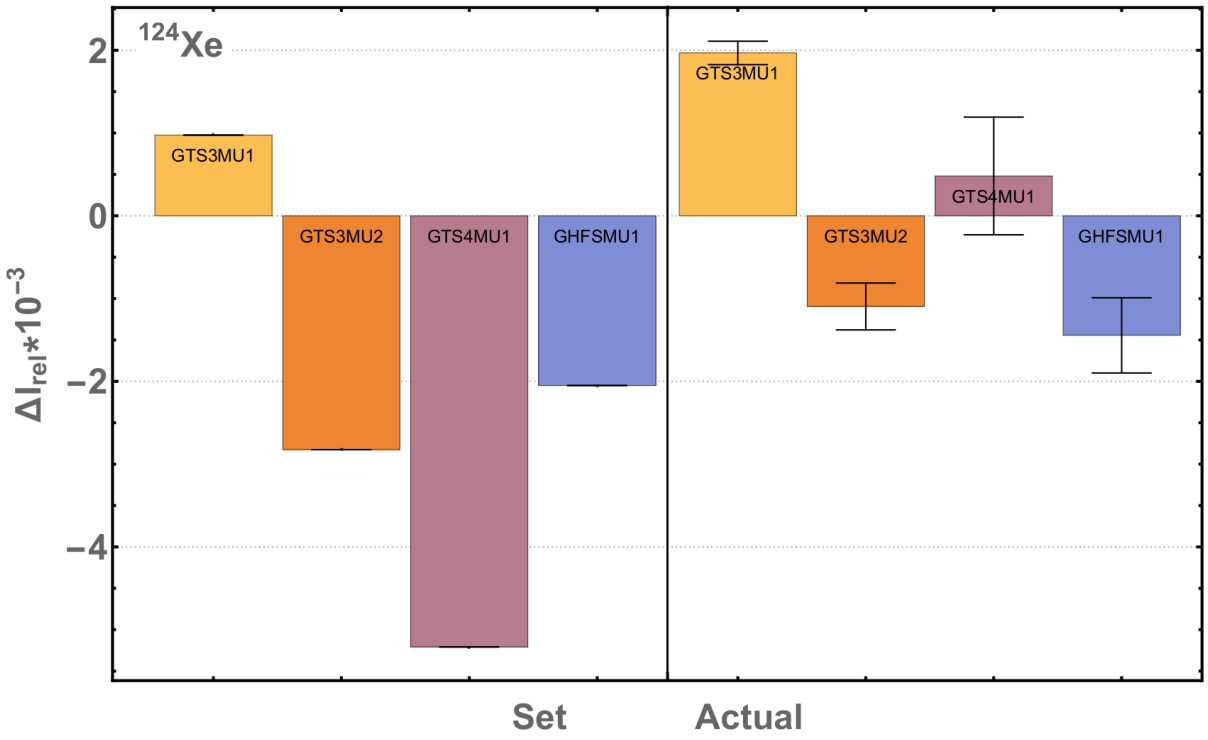


**Figure 8.2.:** Comparison of the deviation in set (left) and actual (right) current for the individual dipole's power supplies in the isotope setting $^{124}$Xe.

In the case of the actual current value it can be seen that the deviation tends to be lower, especially for GTS4MU1, which deviates the least with -4.82·$10^{-4}$, whereas GTS3MU1 shows the opposite with the largest deviation of 1.97·$10^{-3}$. Additionally, an error can be determined for the actual current, which is derived from the power supplies offset and fluctuation in time, see Subsec. 8.0.1. Even though data was available for 2016, the fluctuation and offset from current experiments from 2020 was used and are discussed in the following subsection. Figure 8.2 visualizes the respective deviations and errors as mentioned before.

| $^{111}$Sn | GTS3MU1 I / [A] | GTS3MU2 I / [A] | GTS4MU1 I / [A] | GHFSMU1 I / [A] |
|---|---|---|---|---|
| Set | 375.204 | 373.924 | 354.579 | 354.369 |
| Actual | 375.552(55) | 374.563(110) | 356.38(275) | 354.622(175) |
| LSA | 374.84 | 374.99 | 356.40 | 355.07 |
| $\Delta I_{rel,set}$ | 9.71·$10^{-4}$ | -2.84·$10^{-3}$ | -5.11·$10^{-3}$ | -1.97·$10^{-3}$ |
| $\Delta I_{rel,actual}$ | 1.90(15)·$10^{-3}$ | -1.14(29)·$10^{-3}$ | -5.61(77.0)·$10^{-5}$ | -1.26(49)·$10^{-3}$ |

**Table 8.5.:** Comparison of different experimental currents with the predicted values of LSA for the $^{111}$Sn setting. Uncertainties for actual values are taken from Tab. 8.2.

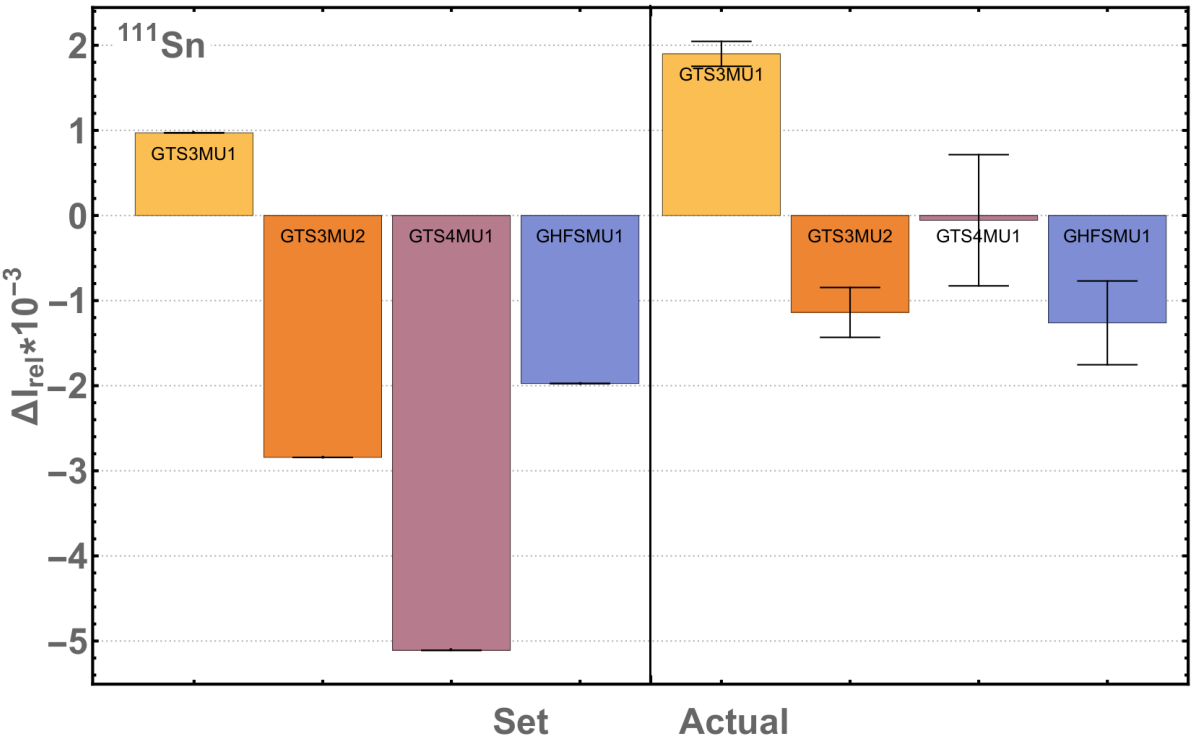


**Figure 8.3.:** Comparison of the deviation in set (left) and actual (right) current for the individual dipole's power supplies in the isotope setting $^{111}$Sn.

For the $^{111}$Sn setting the deviation of the set and actual current show similar results, as can be seen in Tab. 8.4, where GTS3MU1 shows the least deviation in the set current but the highest in the actual current. In contrary to GTS4MU1 which again shows the highest deviation in the set current values but the lowest in the actual values. It can as well be seen in Fig. 8.3. This concludes that within the confines of systematic deviation in currents due to different calibration functions being in use, it is still possible to reproduce settings of older experiments at the FRS, before the LSA control system was implemented, with a high accuracy in the order of $10^{-5}$ for the magnetic rigidity, but a lower accuracy for both the actual and set currents of the power supplies in the order of $10^{-3}$. Only by coincidence can a higher accuracy of $10^{-5}$ be achieved. Consequently, in order to prove the new framework's accuracy appropriately, it has to be firstly utilized within the scope of an extensive testing arrangement with actual heavy-beam and secondly as the basis for a nuclear-physical experiment. The prior requirement will be fulfilled in the following Ch. 9 and the latter requirement in Ch. 10.

# 9. Results Engineering Run

This Ch. is using terminology introduced in Sec. 3.1 and additionally explained in App. B.1. The main test and proof of full functionality for the machine-model and the new control system for the FRS was its use with the first heavy-ion beam in November 2019 as part of the GSI/FAIR-Phase 0 commissioning period for experimental beam time in 2020. In order to achieve this goal the following test strategy was devised:

Test 1: Use an FRS Pattern with no Trims, see App. B.1. Revert Trims if there are any, and test how far and well a primary beam can be tuned through the FRS without modifications. Use current grids for position measurement and beam confirmation. Check when tuning/scaling, meaning a $B\rho$ overwrite, see Sec. 6.4, has to be used to ensure beam can be transported to S4. When using $B\rho$ overwrite, check if Precycling, see paragraph below, has to be performed.

Test 2: Reset the Pattern and use the TargetAlignmentMakeRule to center the beam on a target at TA.

Test 3: Use the machine-model's automated energy-loss calculation for detectors/targets/degraders in combination with the Precycling sequence to tune the beam through the FRS to S4. Use current grids and detectors for position measurement as well as beam confirmation.

Test 4: Reset drives and use the automated energy-loss calculation in combination with the Precycling and SetAllDrives sequence, which automatically sets all drives to their respective positions using the Sequencer [87].

Test 5: Use an FRS Pattern with no Trims and revert Trims if necessary. After that use the TargetAlignmentMakeRule to center the beam on TA and set the production in target to a fragment setting. Test how far and well beam can be transported through the FRS without tuning. Use current grids for position measurement and beam confirmation. Check when scaling, i.e. $B\rho$ overwrite, has to be used to ensure beam can be transported to S4. When using $B\rho$ overwrite, consider Precycling. Use degraders at S2 and check automated drive setting together with the usage of detectors at S4 for identification, depending on availability.

In parallel: Use Magstat [86] and Drivestat [88] for monitoring and FMGSKAL [89] for Precycling the magnets. Drivestat will be used additionally for the SetAllDrives sequence while all settings are done by ParamModi [90].

These tests were conducted for a primary beam of $^{40}$Ar with 550 $A\mathrm{MeV}$ and $^{238}$U with 850 $A\mathrm{MeV}$, respectively. The primary beam intensities were adjusted to be around $10^4$ pps to guarantee that no detector damage would be sustained.
The aforementioned Precycling is a sequence that was implemented inside the Sequencer [87], a test and automation framework for the GSI and FAIR facilities. The goal of the Precycling is to remove hysteresis effects when ramping the FRS dipole magnets to new current settings which would incur a change in $B\rho$ by more than 0.1 %. This is achieved in four steps, firstly by ramping the affected magnet to its maximum current and waiting for saturation, then ramping to its minimum current and waiting for 0 A. Ramping up

and waiting with an additional ramping down and waiting are repeated and the procedure is finalized by ramping to the new current value.

## 9.1. $^{40}$Ar Primary Beam

### Test 1

Test No. 1 had two intentions in mind, first to show that the new control system framework alone is capable to deliver beam into and through the FRS to an experimental station without any matter to consider and no dipole tuning applied, second to see the quality of alignment at different foci. As a first step, all slits except for the slits at TA were closed and it was confirmed that the primary beam could reach the target area via current-grid readout [35]. It was confirmed that the current grids themselves were properly centered and calibrated, and it was possible to see the beam at TA. The measured positions can be seen in Table 9.1.

| Current Grid | X Position / [mm] | Y Position / [mm] |
|---|---|---|
| CG01 | 4(1) | -2(1) |
| CG02 | -14(1) | -3(1) |

**Table 9.1.:** Measured positions at TA from CG01 and CG02. The measured position is the mean value of an assumed Gaussian distribution and the sign of the coordinate system is chosen such that the observer travels with the beam. A properly centered beam would show 0 $\mathrm{mm}$ in all positions resulting in an angle of 0 $\mathrm{mrad}$. Given the distance of 1126 $\mathrm{mm}$ the horizontal angle is -15.9(1.8) $\mathrm{mrad}$.

Since the current grids are not integrated into the FRS MBS data acquisition systems and no offline information is stored, their values can only be given in tables from online readouts. Furthermore, large off-centered positions on the current grids can be explained since no alignment on the FRS target station was performed and therefore no fine tuning on the TA dipole magnets was executed and additionally no

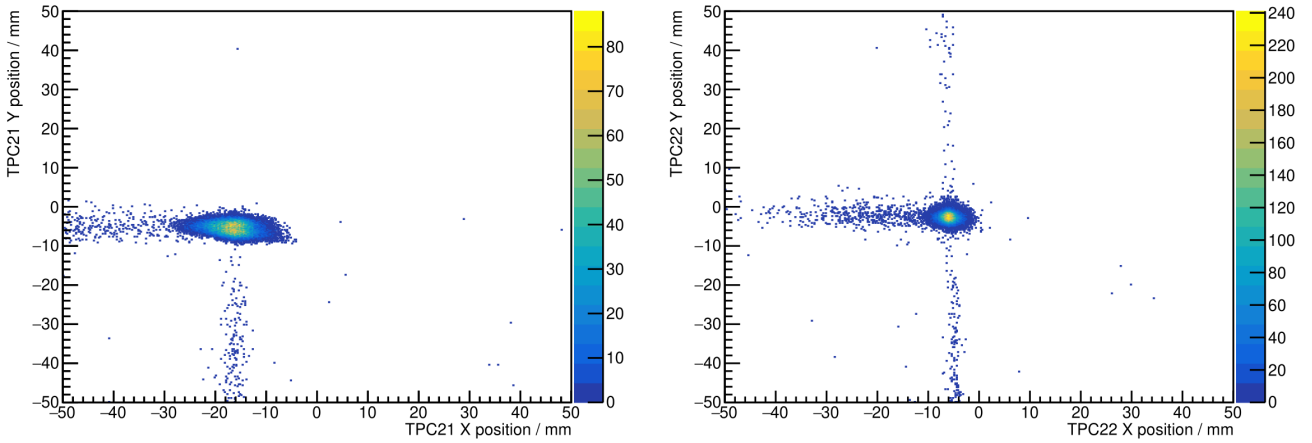


**Figure 9.1.:** Measured position spectra at S2 from TPC21 (left plot) and TPC22 (right plot). The vertical axis shows the vertical position in mm and the horizontal axis shows the horizontal position in mm. The sign of the axes is chosen such that the observer travels with the beam.

SIS18 beam extraction optimization was performed. Nonetheless, LSA and the machine-model with default settings alone was sufficient to deliver beam to TA.
In the second step, the current grids at TA were moved out of the beam, protective slits at S1 and S2 were opened and the time-projection chambers [36] at S2 were moved into the beam together with a plastic scintillator, which was used as a trigger for the readout. Figure 9.1 shows the position measurement at S2 via the TPC21/22 time-projection chambers, which were previously calibrated. The whole setup at S2 was in vacuum. The calibration method for the TPCs will be discussed in more detail in Sec. 12.3. The peak positions for each TPC's two-dimensional position distribution was determined via a fit to a two-dimensional Gaussian probability-density function, and the resulting values can be found in Tab. 9.2.

| TPC | $C$ | $\mu_x$ / [mm] | $\sigma_x$ / [mm] | $\mu_y$ / [mm] | $\sigma_y$ / [mm] |
|---|---|---|---|---|---|
| TPC21 | 161.7(104) | -17.02(100) | 2.91(200) | -5.32(100) | 1.35(140) |
| TPC22 | 199.8(180) | -5.898(3) | 1.307(7) | -2.562(6) | 1.067(5) |
| Angle / [mrad] | - | 9.4(16) | - | 2.3(11) | - |

**Table 9.2.:** Measured positions at S2 from TPC21 and TPC22. The measured positions are determined via a fit to a two-dimensional Gaussian distribution, with $C$ being the constant, $\mu_i$ the mean position in its respective direction and $\sigma_i^2$ the variance. All fit parameters are given with their respective uncertainties.

It can be seen that the primary beam successfully reaches S2, although the previously noted offset at the target area persists at S2 and is still quite significant, as is expected without any kind of adjustment. Knowing that the primary beam was able to reach S2, the TPCs and plastic scintillator were moved out and the subsequent slits at S3 and S4 were opened to allow the beam to propagate towards its destination at S4 with the regular fixed detector setup, as can be seen in Fig. A.5 of App. A. The trigger was changed to the S4 plastic scintillator and the beam position was determined in a similar manner with TPC41/42, see Fig. 9.2, and the same fitting method was utilized, see Tab. 9.3. It presents the determined values from the S4 position measurement and shows a drastic offset with a strong angle at S4. Since no target at TA or other matter was present in the beamline until S4, it can be determined with very high confidence that the provided primary beam of $^{40}Ar^{18+}$ did not change and propagated to S4. Therefore, charge and mass identification via energy-loss measurements was not necessary for this test.

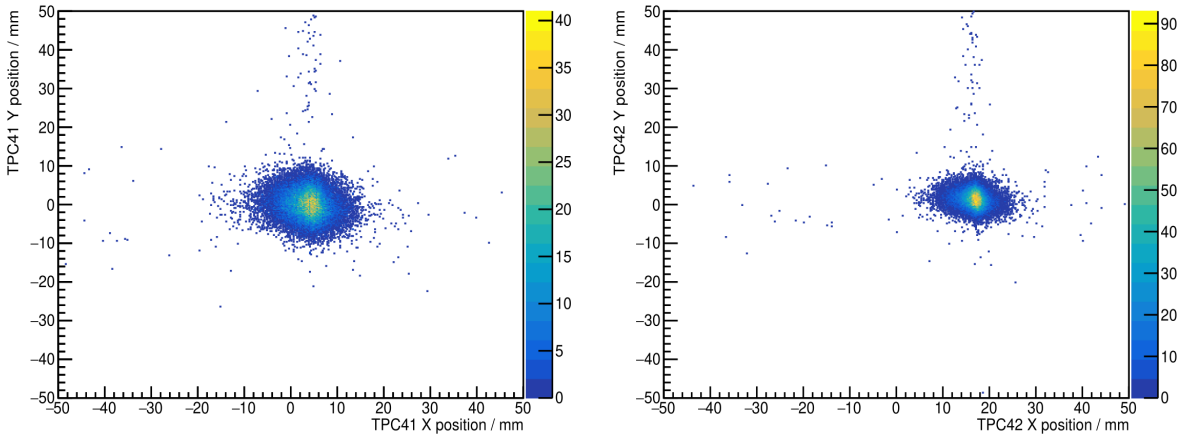


**Figure 9.2.:** Measured position spectra at S4 from TPC41 (left plot) and TPC42 (right plot). The vertical axis shows the vertical position in mm and the horizontal axis shows the horizontal position in mm. The sign of the axes is chosen such that the observer travels with the beam.

| TPC | C | $\mu_x$ / [mm] | $\sigma_x$ / [mm] | $\mu_y$ / [mm] | $\sigma_y$ / [mm] |
|---|---|---|---|---|---|
| TPC41 | 21.52(26) | 3.79(2) | 3.20(3) | -0.21(2) | 3.35(2) |
| TPC42 | 64.25(75) | 16.89(1) | 1.83(2) | 1.53(1) | 1.96(1) |
| Angle / [mrad] | - | 11.5(15) | - | 1.5(16) | - |

**Table 9.3.:** Measured positions at S4 from TPC41 and TPC42. The measured positions are determined via a fit to a two-dimensional Gaussian distribution, with $C$ being the constant, $\mu_i$ the mean position in its respective direction and $\sigma_i^2$ the variance. All fit parameters are given with their respective uncertainties.

This concludes that test No. 1 was successful, which intended to show that LSA as the new control system framework is capable to deliver beam into and through the FRS to an experimental station if there is no matter present to consider and no dipole tuning applied, albeit centering at the different focal planes is not guaranteed and would require additional tuning, either manually by the operator or automatically with the help of different MakeRules to prevent extreme angles and off-center positioning from occurring. The $B\rho$ settings required for this test were automatically calculated by LSA from the information present in the beam device to be 8.5269 $\mathrm{T\,m}$ for all dipole stages TA-S4.

### Test 2

Test No. 2 focuses on the functionality and correctness of the TargetAlignmentMakeRule applied at the target area TA. For this purpose, the beam was stopped, all slits except for the TA slits were closed to prevent the beam from spilling into other parts of the FRS. The corresponding Pattern, see App. B.1, was reset to revert any unwanted changes, and the current grids CG01/02 were moved into the beam and beam delivery was resumed. The corresponding primary-beam positions on the respective current grids before application of the target alignment can be found in Tab. 9.4. From this readout it is possible to use the difference of the respective position measurement towards the supposed center at 0 $\mathrm{mm}$ as input.

| Current Grid | X Position / [mm] | Y Position / [mm] |
|---|---|---|
| CG01 | 3(1) | -2(1) |
| CG02 | -12.5(10) | -2.5(10) |

**Table 9.4.:** Measured positions at TA from CG01 and CG02 before TargetAlignmentMakeRule was applied. The measured position is the mean value of an assumed Gaussian distribution and the sign of the coordinate system is chosen such that the observer travels with the beam. A properly centered beam would show 0 $\mathrm{mm}$ in all positions resulting in an angle of 0 $\mathrm{mrad}$. Given the distance of 1126 $\mathrm{mm}$ the horizontal angle is -13.8(1.8) $\mathrm{mrad}$.

| Current Grid | X Position / [mm] | Y Position / [mm] |
|---|---|---|
| CG01 | -0.5(10) | -1(1) |
| CG02 | 0(1) | -1(1) |

**Table 9.5.:** Measured aligned positions at TA from CG01 and CG02. The measured position is the mean value of an assumed Gaussian distribution and the sign of the coordinate system is chosen such that the observer travels with the beam. A properly centered beam would show 0 $\mathrm{mm}$ in all positions resulting in an angle of 0 $\mathrm{mrad}$. Given the distance of 1126 $\mathrm{mm}$ the horizontal angle is -0.4(18) $\mathrm{mrad}$.

Even though no real target was in use, it was assumed that target station 1 (GTS1ET5) was to be centered on and therefore the corresponding optics file ”SISTA2019_TA1_LO.txt”, see Lst. D.1 in App. D, was loaded. The TargetAlignmentMakeRule calculation resulted in the current grid positions seen in Tab. 9.5. Considering that the maximum position measurement accuracy that can be achieved with the current grids is 1 $\mathrm{mm}$, the final alignment can be regarded as centered on the target station. Additionally interesting

| Magnet | HKICK / [mrad] | VKICK / [mrad] |
|---|---|---|
| GTS1MU1 | -7.9(3) | - |
| GTS1MU2 | -2.0(3) | - |
| GTE1KY1 | - | -0.2(3) |
| GTS1KY1 | - | 0.1(3) |

**Table 9.6.:** Resulting kick values for the magnets responsible for the alignment on the respective target station. These kick values were calculated by the TargetAlignmentMakeRule, see 6.5 and are added unto the deflection angle of the individual magnets that lead to a change in power-supply current.

to see are the kick values that have to be added to the deflection angle of the corresponding correctional magnets, which can be seen in Tab. 9.6. GTS1MU1/2 are horizontal dipoles which have a positive deflection angle of 7.5°, and as a result from the alignment calculation GTS1MU1 needs to decrease its deflection strength by 7.9 $\mathrm{mrad}$ whereas GTS1MU2 needs to decrease its deflection strength by 2.0 $\mathrm{mrad}$ in order to compensate the horizontal angle at target station 1 and shift the beam parallel accordingly. For the vertical correction dipoles GTE/S1KY1, which have a default deflection angle of 0°, the VKICK Settings of -0.2 and 0.1 $\mathrm{mrad}$ have to be added to correct for the flat vertical angle and parallel shift on the target station. As a quick sanity check, a Mirko [84] calculation has been performed in parallel and showed the same results. Given how the current grids can only resolve position measurements with a maximum accuracy of 1 $\mathrm{mm}$, the resulting kicks can then be calculated within a maximum accuracy of 0.3 $\mathrm{mrad}$.
With the previous results in mind, it can be concluded that test No. 2 was successful. It was possible to show that the TargetAlignmentMakeRule, as implemented in Sec. 6.5, works as intended and produces results for the correction of ion-optical deflection angles such that a heavy-ion primary beam can be centered and aligned unto the target stations within the experimental accuracy provided by the current grids.

### Test 3

The third test utilizes the automated energy-loss calculation with actual matter in the beam to achieve primary beam-propagation through the FRS to S4. Additionally, the TargetAlignmentMakeRule will be used to ensure beam centering on the target. All this is done with a Pattern reverted to its initial default state. As the first step, all slits except for the TA slits were closed and the current grids together with the SEETRAM intensity monitor were moved into the beam. According to our expectations, the beam position on the current grids and resulting angle, were similar to what was seen in test 2, and the subsequent target alignment calculation yielded the similar results. For the next step, the current grids were moved out and the S2 TPCs and plastic scintillator were moved in and the respective ”INBEAM” flag of the devices was set to true to allow for energy-loss calculation. Including the current matter, the stages were automatically set to 8.5269 $\mathrm{T\,m}$ for TA-S2 and 8.3516 $\mathrm{T\,m}$ for S2-S4 by the LSA machine-model. All dipoles were precycled, and subsequently the slits were opened. The measured position spectra within the different TPCs can be found in Fig. 9.3. The same method as in test 1 was applied to this measurement to determine the peak

position in the individual TPCs and the results can be found in Tab. 9.7.
It is interesting to see that after the performed alignment on the target, LSA ATIMA correctly calculates the energy-loss within the SIS18 vacuum window and the SEETRAM intensity monitor and the beam reaches S2. However, the beam arrives at S2 off-centered with a steep horizontal and vertical angle. After the

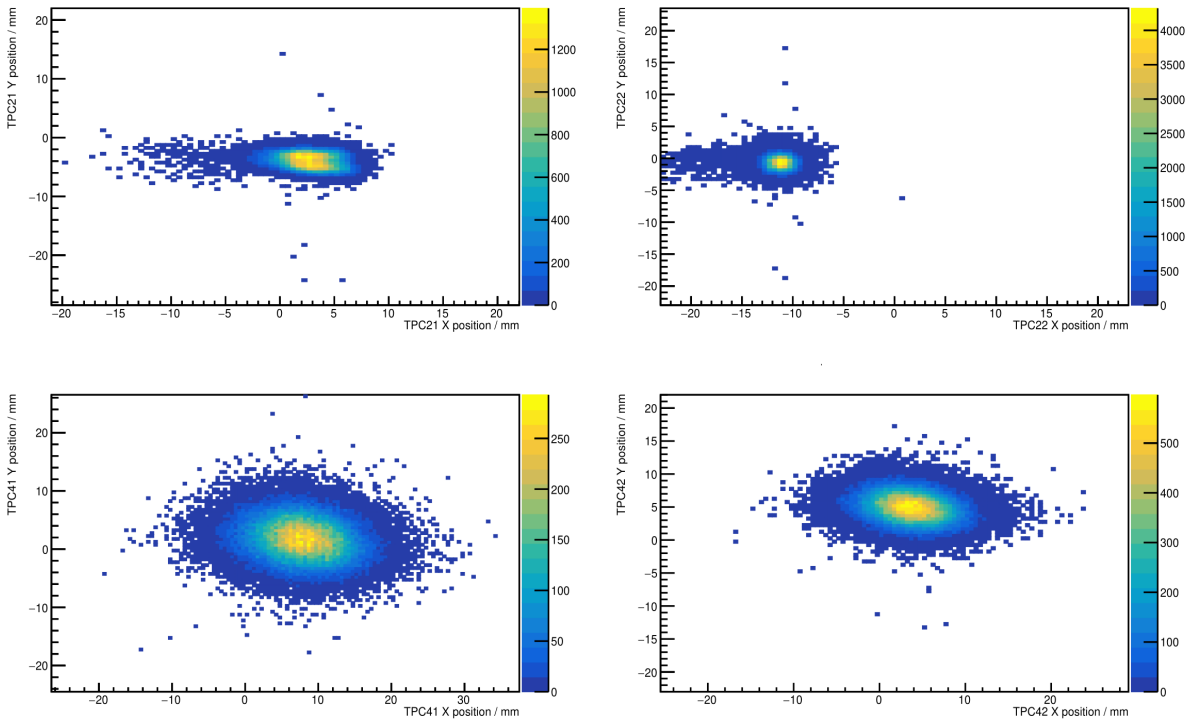


**Figure 9.3.:** Measured position spectra at S2 (top) from TPC21 (left plot) and TPC22 (right plot) and S4 (bottom) from TPC41 (left plot) and TPC42 (right plot). The vertical axis shows the vertical position in mm and the horizontal axis shows the horizontal position in mm. The sign of the axes is chosen such that the observer travels with the beam.

| TPC | C | $\mu_x$ / [mm] | $\sigma_x$ / [mm] | $\mu_y$ / [mm] | $\sigma_y$ / [mm] |
|---|---|---|---|---|---|
| TPC21 | 1652(8) | 2.694(7) | 1.851(4) | -3.808(4) | 1.089(2) |
| TPC22 | 4374(21) | -11.164(3) | 0.940(2) | -0.625(3) | 0.909(2) |
| Angle / [mrad] | - | -11.8(16) | - | 2.7(10) | - |
| TPC41 | 262(1) | 7.80(2) | 4.47(1) | 1.78(1) | 3.051(8) |
| TPC42 | 588(3) | 3.68(1) | 3.248(8) | 4.961(7) | 1.870(5) |
| Angle / [mrad] | - | -3.6(16) | - | 2.8(16) | - |

**Table 9.7.:** Measured TPC positions. The measured positions are determined via a fit to a two-dimensional Gaussian distribution, with $C$ being the constant, $\mu_i$ the mean position in its respective direction and $\sigma_i^2$ the variance. All fit parameters are given with their respective uncertainties.

energy-loss calculation at S2, within the two TPCs and one plastic scintillator, the beam is then successfully transmitted to S4, where both the beam angle and off-center positioning is less pronounced than at S2 and during the previously discussed test 1, since the target alignment was applied. In order to confirm that

the energy-loss calculation was correct and the off-centering does not come from a miscalculation, the setup was simulated in LISE++, which delivered identical $B\rho$ for TA-S2 and S2-S4. This leaves mechanical misalignment of detectors and ion-optical elements as the main contributors to the resulting intermediate and final positions of the argon beam, especially since the four main dipole magnets from TA to S4 had to be dismantled and reassembled for repairs shortly before the engineering run. Additionally it was confirmed at a later stage of the engineering run that the matter in use was not properly calibrated, and the thicknesses had to be updated as well. This was done for the uranium beam setting.
It was tested to propagate the heavy-ion beam from S2 to S4 without precycling the dipole magnets beforehand, which resulted in a beam-loss before S4. Thus it is standard procedure that whenever a relative $B\rho$ change of more than $0.1\%$ is incurred, that the Precycling sequence is executed on the affected dipoles. In conclusion, it was possible to align the primary argon beam unto the target with minimal angle and off-centering and utilize the FRS machine-model with LSA to automatically and correctly calculate the energy-loss online for matter that is being put into the beam, resulting in a successful propagation of the primary beam from TA through several devices with matter into the experimental station S4, while also relying on the precycling sequence, to correct the hysteresis deviation of ion-optical elements when an magnetic rigidity change of more than $0.1\%$ occurs.

### Test 4

It was intended for the fourth test to use the Drive Sequence from within DriveStat [88]. DriveStat was developed as a graphical monitoring solution for the FRS, displaying the status of all FRS drives in a tabular manner. Within DriveStat, the operator has the possibility to use the Drive Sequence which enables automated parallel readout from the LSA machine-model and ParamModi [90], checking the drives parameters if their are supposed to be in the beam and their corresponding positions and then setting all drives in parallel. Thus avoiding individual manual manipulation via DeviceControl [91], saving time and streamlining the operation process.
Tests during the Dry-Run in April 2019 have proven that the Drive Sequence as well as its functionalities and sub-routines are operational and drives could be manipulated via ParamModi, but due to a short notice roll-out of a new production version of LSA, Maven [92] version control dependencies changed and rendered the Drive Sequence unusable for the Engineering run in November 2019. Functionality could only be restored after the run, due to its lower priority, so that test 4 was skipped for the entirety of the Engineering run.

### Test 5

Building up to be the final test, it was intended for test 5 to incorporate all previously tested functionalities and use the FRS machine-model's production capabilities to simulate an experiment producing lighter secondary fragments and transmitting them to the S4 experimental focal plane. Two settings were chosen for this purpose and calculated via LSA. The energy of the primary beam energy was changed to 300 $A\mathrm{MeV}$, to show that the energy-loss calculation also holds true for other energies than just 550 $A\mathrm{MeV}$, see Tab. 9.8. For detection and identification at S2, the previous setup of 1 plastic scintillator with a thickness of 1.04 $\mathrm{mm}$ and the 2 TPCs were used. Additionally, the SEETRAM and SIS18 vacuum window at TA had to be considered. The procedure was then similar to test 3, all slits were closed and at first the beam had to be centered on the target, then the detectors were moved in and the FRS slits were opened.

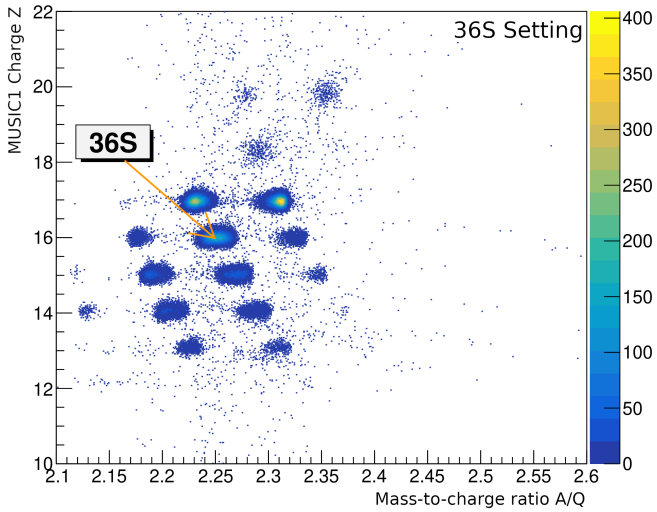


**Figure 9.4.:** ID plot for the first setting. Marked with the centered position of the isotope of interest $^{36}$S.

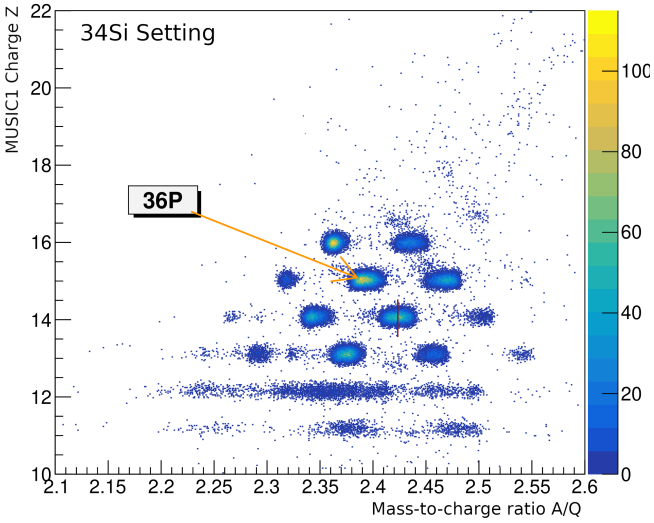


**Figure 9.5.:** ID plot for the second setting. Marked with the centered position of $^{36}$P even though the ion of interest was $^{34}$Si (red line).

| IOI | TA-S1 $B\rho$ / [Tm] | S1-S2 $B\rho$ / [Tm] | S2-S3 $B\rho$ / [Tm] | S3-S4 $B\rho$ / [Tm] |
|---|---|---|---|---|
| 1. $^{36}S^{16+}$ | 5.3234 | 5.3234 | 5.1852 | 5.1852 |
| 2. $^{34}Si^{14+}$ | 5.8085 | 5.8085 | 5.5658 | 5.5658 |

**Table 9.8.:** $B\rho$ settings for the different ions of interest and dipole stages as calculated by LSA. The rigidity for TA-S2 was chosen by calculating the energy of the IOI via LISE++ after projectile fragmentation, see Ch. 4, occurs in the target. As previously discussed, see Ch. 8, LSA does not provide accuracies for $B\rho$ values.

It was immediately possible to detect the beam at S4 and utilizing one MUSIC detector and time-of-flight measurement between SC21-SC41 the fragments could be identified. Figures 9.4 and 9.5 show the resulting identification plots, where the measured element charge Z is plotted over the $A/Q$ value. It is important to note that since MUSIC2 was not working at that time, a clean-up due to charge-changing reactions in the MUSICs could not be applied as well as other charge-state clean-ups where omitted, which is sufficient to show the functionalities of the machine-model. For the new isotope search in part IV, it is imperative to consider such clean-ups. The isotopes marked in the identification plots denote the respective isotope, which was experimentally measured to be considered as close as possible to the center position at S2 and S4. In the case of the first $^{36}$S setting it is $^{36}$S, whereas in the case of the $^{34}$Si setting it ended up being $^{36}$P. This shift in centered isotopes can be attributed to the previously mentioned uncentered beam at S2 and S4 during test 3. The same effect plays a role during this test while producing a secondary heavy-ion beam as result of projectile fragmentation from the primary argon beam.
It can be concluded that the TargetProductionMakeRule successfully and correctly produces the desired ion of interest, by utilizing the predicted energy/magnetic rigidity and isotope information from LISE++ and subsequently propagating the secondary beam throughout the machine-model, while also applying automatic energy-loss calculations.

## 9.2. $^{238}$U Primary Beam

The machine-model test with the argon beam was conducted on the 21.11.2019 and 22.11.2019, while the test with a uranium beam was conducted on the 12.12.2019 and 13.12.2019. This time in between beam changes was used to debug, update and optimize the control system together with its procedures.

### Tests 1, 2 and 3

Since the capabilities of the machine-model were already shown extensively for an argon beam, it was decided to skip the separate tests 1, 2 and 4, instead do only test 3, which incorporates all previously introduced functionalities as well as test 5 afterwards for a specific fragment setup.
The testing procedure was as follows: At first all FRS slits were closed to protect detectors from sustaining damage from a high-intensity primary uranium beam. The current grids were moved in to align the beam on a copper stripper foil with a thickness of 89 $\mathrm{mg\,cm^{-2}}$ to produce fully stripped uranium-238 ions. After the alignment, the following dipole stages were precycled and then set to the rigidity values that can be found in Tab. 9.9 together with their respective kick values to center the beam at S2 as well as S4. The two TPCs at S2 and one plastic scintillator were moved into the beam line.

| IOI | TA-S1 | S1-S2 | S2-S3 | S3-S4 |
|---|---|---|---|---|
| $^{238}U^{92+}$ $B\rho$ / [Tm] | 13.0370 | 13.0370 | 12.7731 | 12.7731 |
| HKICK / [mrad] | 2.6(3) | -0.2(3) | -2.2(3) | 2.2(3) |

**Table 9.9.:** $B\rho$ for $^{238}U^{92+}$ at 850 $A\mathrm{MeV}$. The rigidity for TA-S2 was chosen by calculating the energy-loss with the machine-model for the SIS18 vacuum window, SEETRAM and copper stripper and S2-S4 incorporated the energy-loss inside two TPCs and one plastic scintillator with updated calibrated thicknesses. As previously discussed, see Ch. 8, LSA does not provide accuracies for $B\rho$ set values.

After decreasing the intensity of the primary beam to acceptable levels, the slits were opened, and the beam was immediately registered at S2 and S4. Table 9.10 shows the measured positions in the individual TPCs and the angles that can be derived from the measurement. In comparison to test 3 that was conducted for the argon beam configuration, the angles and positions at the respective focal planes are much more improved now. At S2 both the horizontal as well es vertical angle stay within experimentally acceptable ranges and the centering of the beam is much less off-center than previously measured. Surprisingly at, S4 the beam has a stronger horizontal angle than before and appears to be off-centered.

| TPC | C | $\mu_x$ / [mm] | $\sigma_x$ / [mm] | $\mu_y$ / [mm] | $\sigma_y$ / [mm] |
|---|---|---|---|---|---|
| TPC21 | 86.7(1.7) | 2.03(3) | 1.82(2) | -0.49(2) | 1.41(1) |
| TPC22 | 194(4) | -0.42(1) | 1.07(1) | 1.53(2) | 1.17(1) |
| Angle / [mrad] | - | -2.0(10) | - | 1.7(8) | - |
| TPC41 | 26.0(6) | -8.82(3) | 3.91(5) | -0.03(2) | 1.83(2) |
| TPC42 | 45(1) | -3.3(1) | 3.08(6) | 0.96(4) | 1.18(2) |
| Angle / [mrad] | - | -4.7(9) | - | 0.8(10) | - |

**Table 9.10.:** Measured TPC positions. The measured positions are determined via a fit to a two-dimensional Gaussian distribution, with $C$ being the constant, $\mu_i$ the mean position in its respective direction and $\sigma_i^2$ the variance.

However, when projecting the beam into the supposed focal point at a distance of 2930 $\mathrm{mm}$ after the last quadrupole, it is centered at 0 $\mathrm{mm}$. For reference in App. A.5, the focal point would be positioned between SC42 and Ion C Disk. Figure 9.6 shows the position spectra from the respective TPCs, from which the positions in Tab. 9.10 were derived.

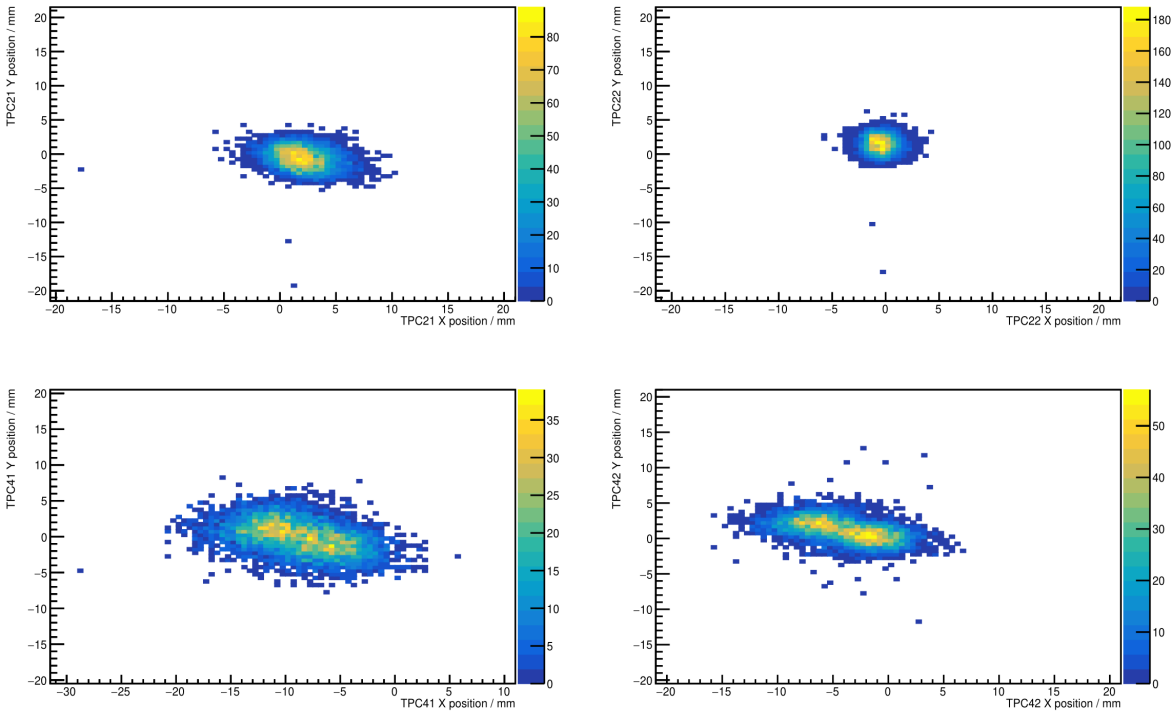


**Figure 9.6.:** Measured position spectra at S2 (top) from TPC21 (left plot) and TPC22 (right plot) and S4 (bottom) from TPC41 (left plot) and TPC42 (right plot). The vertical axis shows the vertical position in mm and the horizontal axis shows the horizontal position in mm. The sign of the axes is chosen such that the observer travels with the beam.

Therefore the combined tests for the primary uranium beam show promising results and can be considered successful. It was possible to propagate a uranium beam from the target area TA into the experimental area S4 with matter at several stations, automated energy-loss calculation and $B\rho$ setting via LSA and the FRS machine-model. Beam positions and angles at the different focal planes could further be improved by providing more exact information about the present matter by previous thickness calibrations, database updates and alignment via dipoles. Experimentally acceptable position and angle ranges could be achieved, although mechanical misalignment persists and cannot be fully corrected.

### Test 5

As the final test for the experimental machine-model benchmark a fragment setting was chosen with $^{165}\mathrm{W}^{74+}$ as the isotope of interest being produced with a $^{238}\mathrm{U}^{92+}$ beam impinging on a Be target with a thickness of 1624 $\mathrm{mg\,cm^{-2}}$ and a Nb stripper foil backing of 223 $\mathrm{mg\,cm^{-2}}$ thickness at 850 $A\mathrm{MeV}$. The target area consists additionally of the SIS18 vacuum window and the SEETRAM intensity monitor. Afterwards, the FRS slits are fully closed, all HKICKs from before remain and S2 consists of two TPCs, one plastic scintillator as well as the S2 $\mathrm{AlMg_3}$ degrader wedges at a thickness of 2350.7 $\mathrm{mg\,cm^{-2}}$. The

machine-model was set to this configuration and the magnet settings were calculated. After a precycle sequence, the dipoles were ramped to their set values, as can be seen in Tab. 9.11 and the FRS slits were opened.

| IOI | TA-S1 $B\rho$ / [Tm] | S1-S2 $B\rho$ / [Tm] | S2-S3 $B\rho$ / [Tm] | S3-S4 $B\rho$ / [Tm] |
|---|---|---|---|---|
| $^{165}W^{74+}$ | 10.1204 | 10.1204 | 8.3074 | 8.3074 |

**Table 9.11.:** $B\rho$ settings for the ion of interest and dipole stages. The rigidity for TA-S2 was chosen by calculating the energy of the IOI via LISE++ after projectile fragmentation, see Ch. 4, occurs in the target. As previously discussed, see Ch. 8, LSA does not provide accuracies for $B\rho$ set values. The same HKICKs are applied as before.

The secondary fragment cocktail could be propagated to the experimental area in S4 and identification via energy-loss measurement in one MUSIC, time-of-flight measurement between S2 and S4 as well as position measurement with the TPCs at S2 and S4. The resulting identification plot can be seen in Fig. 9.7 and shows clearly distinguished $^{165}W^{74+}$, which was also centered at S2 and S4.
As the final experimental benchmark, this test shows that it is possible to run a mock-up experiment with a secondary cocktail beam by fully utilizing all previously introduced functionalities of the FRS machine-model with its implemented Parameter hierarchies (Ch. 5) and Makerules (Ch. 6). Therefore the only test left, is to show that the FRS machine-model is able to reproduce contemporary experimental settings, that were calculated via LISE++ and then set via the $B\rho$ overwrite methodology, with just the EoutMakeRule.

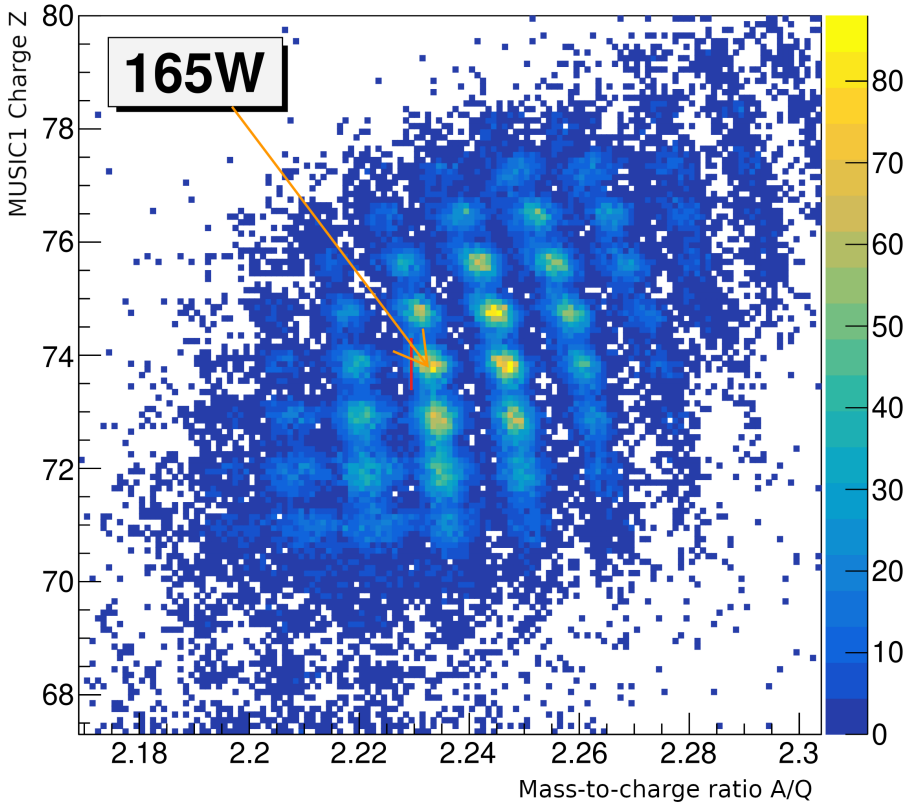


**Figure 9.7.:** ID plot for the $^{165}W$ setting marked with theoretical (red line) and real position of the the ion of interest.

# 10. Comparison with S468

After it was shown that the machine-model in LSA is capable of delivering a primary heavy-ion as well as a secondary fragment beam to the FRS experimental areas with the help of the automated energy-loss calculation by LSA ATIMA, it will now be shown that LSA can reproduce rigidity $B\rho$ and current $I$ settings by comparing LSA machine-model predictions with experimental settings from 2020. Two experimental settings are being considered, the first one is a $^{208}$Pb primary beam at 1050 $A\mathrm{MeV}$ and the second one is a secondary $^{205}$Au beam produced via projectile fragmentation of the primary lead beam. The same definition of the deviation as introduced in Sec. 8 will be used for this purpose.
Different matter configurations are used within each setting. The lead setting starts with the SIS18 vacuum window and the SEETRAM at TA, which is then followed by a 1.04 $\mathrm{mm}$ thick BC420 plastic scintillator at S2, a total degrader thickness of 2000 $\mathrm{mg^2\,cm^{-1}}$ for the wedges and disks, as well as two vacuum windows, two TPCs in air, an additional 1.15 $\mathrm{mm}$ plastic scintillator and a total of 133 $\mathrm{cm}$ of air. In contrast the gold setting uses an additional Be target with a thickness of 4000 $\mathrm{mg^2\,cm^{-1}}$ at TA for secondary-beam production via fragmentation.

## 10.1. Magnetic Rigidity

At first the experimental magnetic rigidity settings that were calculated by LISE++ and input into the machine-model's $B\rho$ overwrite functionality, see Sec. 6.4, are compared to LSA's automated energy-loss predictions. These are given for the transfers TA-S2 and S2-S4, meaning that the two main dipoles in each transfer are set to the same value. Table 10.1 shows the experimental values compared to the machine-model predictions as well as the corresponding relative deviation for each isotope setting. It can be seen, that for the primary $^{208}$Pb setting the deviation in $B\rho$ is in the order of $10^{-6}$ to 0.0, which lies within the $B\rho$ fluctuation of a dipole caused by the fluctuation in current of its corresponding power supply and can therefore be considered as identical. This is already discussed in Subsec. 8.0.1. For the secondary $^{205}$Au setting it is important to note that the TA-S2 value shows no deviation from each other as LSA requires the LISE++ calculated $B\rho$ value as input, since LSA itself does not calculated the outgoing energy of the resulting ejectiles from projectile fragmentation.

| $^{208}$Pb | TA-S2 $B\rho$ / [Tm] | S2-S4 $B\rho$ / [Tm] | $^{205}$Au | TA-S2 $B\rho$ / [Tm] | S2-S4 $B\rho$ / [Tm] |
|---|---|---|---|---|---|
| Exp. | 15.1539 | 13.1338 | Exp. | 12.5380 | 10.7348 |
| LSA | 15.1539 | 13.1339 | LSA | 12.5380 | 10.7352 |
| $\Delta B\rho_{rel}$ | 0.0 | $7.61{\cdot}10^{-6}$ | $\Delta B\rho_{rel}$ | 0.0 | $3.73{\cdot}10^{-5}$ |

**Table 10.1.:** Comparison of experimental $B\rho$ set values and calculated values from LSA for $^{208}$Pb and $^{205}$Au. It is important to note, that both $B\rho$ set values of LSA and the experiment are theoretical input values and as such do not possess an uncertainty.

For the transfer S2-S4 it results in a deviation of $3.73{\cdot}10^{-5}$, which would lie inside of the fluctuation range and would not cause any shift in position. In this case, the deviation comes from LISE++ using a slightly different density for $AlMg_3$ than the LSA ATIMA splines. Figure 8.1 visualizes the data from the previous table.

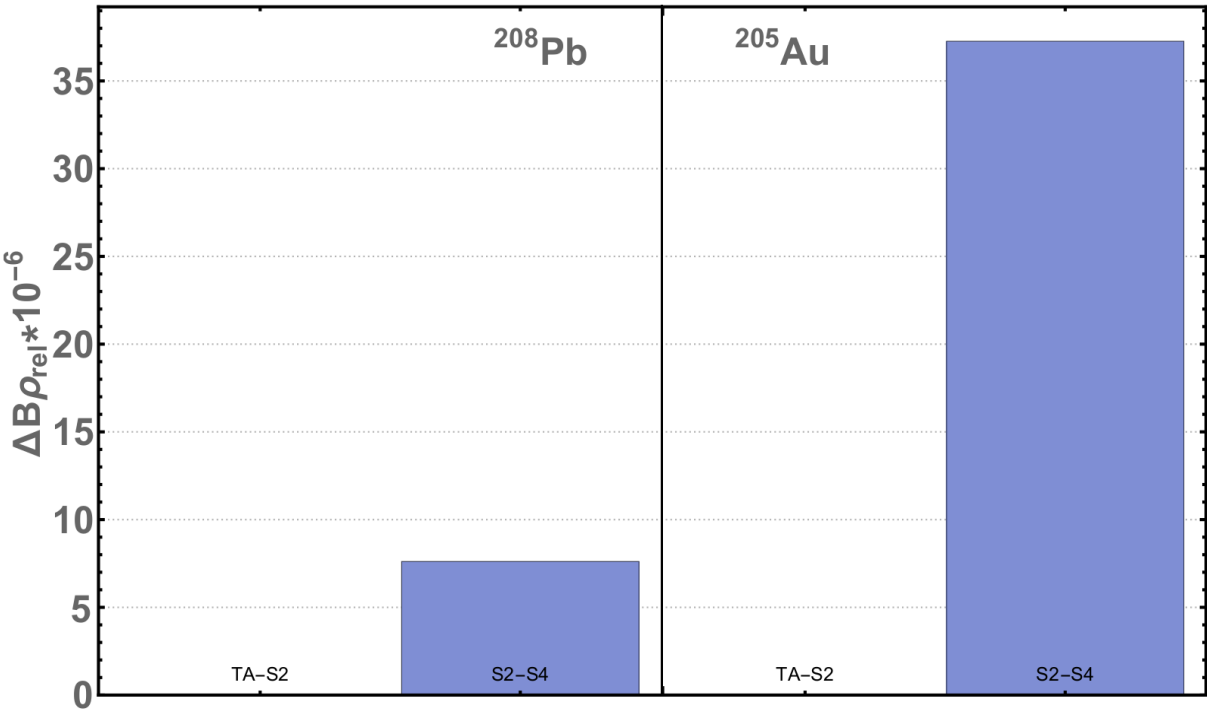


**Figure 10.1.:** Comparison of the deviation in magnetic rigidity for the transfers TA-S2 and S2-S4 in the respective isotope settings $^{208}$Pb as well as $^{205}$Au.

In conclusion, it can be said that LSA is able to reproduce contemporary $B\rho$ settings with an accuracy that lies within the FRS Hall-probe measurement accuracy of $10^{-4}$ T m and can therefore be considered as identical. Any persisting differences in the energy loss and therefore deviation in magnetic rigidity can be attributed to slightly differing beam or material characteristics, e.g. density, mass, ionisation potential, being used in LSA ATIMA and other versions of ATIMA and have to be considered when comparing contemporary experimental settings with LSA predictions.

## 10.2. Current

The second comparable observable is the dipoles current in each section. As discussed in Sec. 8.1, the calibration functions are stored in the GSI OperDB, that determine the current from the integrated field strength. In the case of all S468 settings, the currents were derived from the same calibration functions that are in currently in use for the FRS machine-model and therefore potentially provide the highest precision in predictive power.
Similar to the magnetic rigidity in the previous Sec., the deviation was calculated for both the set and actual current values of each dipole's power supply and can be found in Tab. 10.2 for the $^{208}$Pb and Tab. 10.3 for the $^{205}$Au setting. It becomes apparent that the deviation of the set current values is smaller than

| $^{208}$Pb | GTS3MU1 $I$ / [A] | GTS3MU2 $I$ / [A] | GTS4MU1 $I$ / [A] | GHFSMU1 $I$ / [A] |
|---|---|---|---|---|
| Set | 694.35 | 697.61 | 602.73 | 601.09 |
| Actual | 694.630(55) | 697.46(11) | 602.700(275) | 601.220(175) |
| LSA | 694.35 | 697.61 | 602.74 | 601.1 |
| $\Delta I_{rel,set}$ | 0.0 | 0.0 | -1.66·10$^{-5}$ | -1.66·10$^{-5}$ |
| $\Delta I_{rel,actual}$ | 4.03(79)·10$^{-4}$ | -2.15(158)·10$^{-4}$ | -0.66(456)·10$^{-4}$ | 1.99(291)·10$^{-4}$ |

**Table 10.2.:** Comparison of different experimental currents with the predicted values of LSA for the $^{208}$Pb setting. Uncertainties for actual values are taken from Tab. 8.2.

for the actual values. Here GTS3MU1 and GTS3MU2 show no deviation for the set values, whereas GTS4MU1 and GHFSMU1 show the the same deviation with -1.66·10$^{-5}$. Since the rigidity values are accurate in the order of $10^{-6}$ for the primary beam setting, it would be expected that the current set values would deviate in the same order of magnitude. Indeed, a slightly increased deviation in the order of $10^{-5}$ is observed and can be easily understood with the previously explained calibration functions, which are obtained by utilizing Hall-probes to measure the dipole's field strength $BL$ with an accuracy of up to $10^{-5}$ T m. Since the calibration functions in use for both the experiment and prediction are identical, the resulting set values can be considered identical within the measurement accuracy. Figure 10.2 visualizes the respective deviations and errors as discussed earlier.

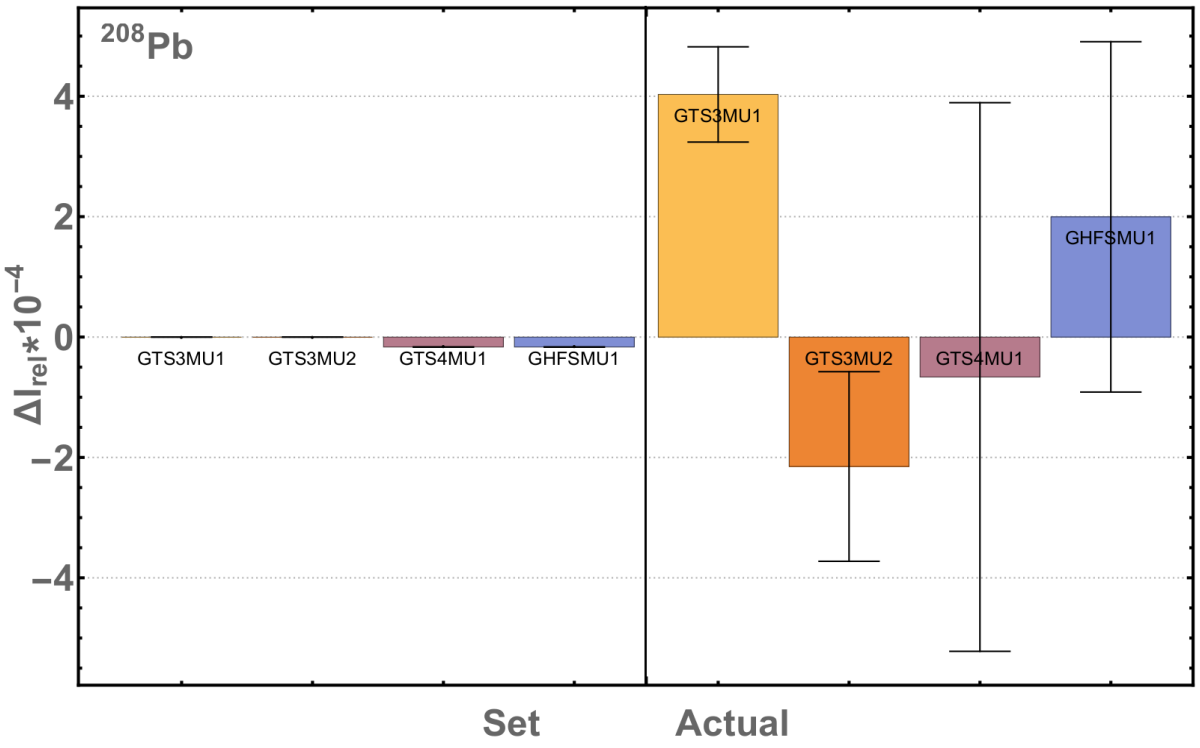


**Figure 10.2.:** Comparison of the deviation in set (left) and actual (right) current for the individual dipole's power supplies in the isotope setting $^{208}$Pb.

In the case of the actual current value it can be seen that the deviation tends to be higher, especially for GTS3MU1, which deviates the most with 4.03·10$^{-4}$, whereas GTS4MU1 shows the opposite with the least

deviation of -6.64·$10^{-5}$. It is now interesting to note that the remaining deviation from the actual current and the given error bars agree very well with what could be determined for the offset and fluctuation of each power supply, since those were derived during the same time the experiment S468 was conducted. For the $^{205}$Au setting the deviation of the set and actual current show similar results as for the $^{208}$Pb setting, where GTS3MU1 and GTS3MU2 show the least deviation in the set current, but GTS3MU1 shows the highest offset in the actual current. GTS4MU1 and GHFSMU1 show the highest deviation in the set current values and the highest fluctuation in the actual values. It can be seen in Fig. 10.3 as well.

| $^{205}$Au | GTS3MU1 I / [A] | GTS3MU2 I / [A] | GTS4MU1 I / [A] | GHFSMU1 I / [A] |
|---|---|---|---|---|
| Set | 573.3 | 574.46 | 492.08 | 490.50 |
| Actual | 573.560(55) | 574.38(11) | 492.200(275) | 490.64(175) |
| LSA | 573.3 | 574.46 | 492.09 | 490.52 |
| $\Delta I_{rel,set}$ | 0.0 | 0.0 | -2.03·$10^{-5}$ | -4.08·$10^{-5}$ |
| $\Delta I_{rel,actual}$ | 4.53(96)·$10^{-4}$ | -1.39(191)·$10^{-4}$ | 2.24(559)·$10^{-4}$ | 2.45(357)·$10^{-4}$ |

**Table 10.3.:** Comparison of different experimental currents with the predicted values of LSA for the $^{205}$Au setting. Uncertainties for actual values are taken from Tab. 8.2.

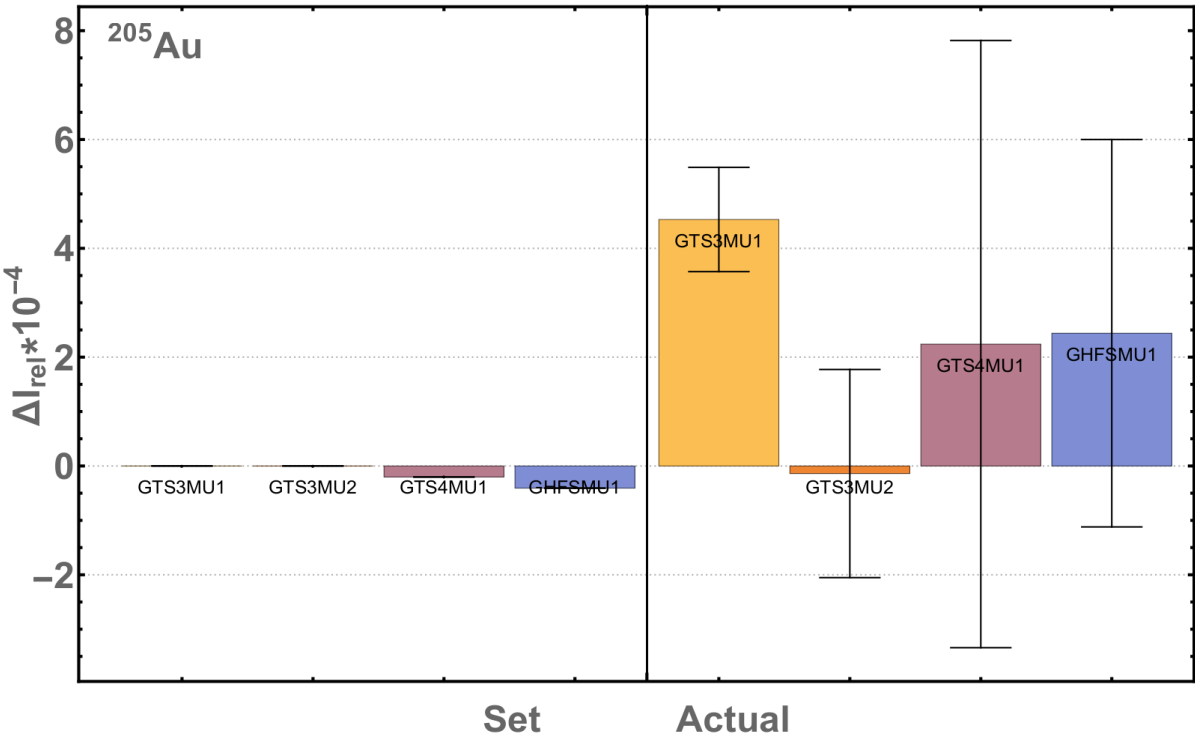


**Figure 10.3.:** Comparison of the deviation in set (left) and actual (right) current for the individual dipole's power supplies in the isotope setting $^{205}$Au.

Within the inherent inaccuracies in currents, given by the FRS' main dipole power supplies, it is easily possible to reproduce settings of contemporary experiments at the FRS, that utilize the LSA control system, with a high accuracy in the order of $10^{-6}$ for the magnetic rigidity and a slightly lower accuracy for the set currents of the power supplies in the order of $10^{-5}$. Both observables can therefore be considered identical, whereas for the actual currents a higher inaccuracy in the order of $10^{-4}$ is determined to be

true. Nonetheless, the predicted currents are more precise when reproducing contemporary experiments compared to older experiments, since the same calibration functions are in use. Consequently, it shows that the calculation of experimental settings, solely by using the FRS machine-model, delivers the same accuracy as can be achieved by previously utilizing LISE++ and is therefore equivalent.

# Part IV.

# New Isotope Search S468

The following part is linked to the experiment ”Search for new neutron-rich isotopes and exploratory studies in the element range from terbium to rhenium” S468 [25] conducted by the Super-FRS Experimental Collaboration [26] as part of its Physics Topic 1 program to produce new isotopes and study their basic properties during the FAIR-Phase 0 experimental beam time in 2020. This thesis emphasizes on the identification of new isotopes and the analysis of fragmentation production cross-sections of said isotopes. The lifetime analysis will be part of the PhD work of H. Rösch-Kabadayi [27] and M. Luoma [28]. The analysis of new masses will be part of the PhD work of D. Amanbayev [29]. It is structured into the following Chs.: Goal and Motivation, Experimental Setup, Analysis, Conclusion and Outlook. In the Ch. Goal, the general goal and physics case of the experiment will be discussed. This is followed by the Experimental Setup Chapter, which introduces at first the utilized Hardware during the runs and their respective DAQ setups. Then the Setting Simulations, which encompasses the necessary simulations that were calculated to derive the settings to run the experiment in its second Section. Afterwards, in the third Sec., the calibration of the individual detector systems, which are responsible for the general particle identification at the FRS, are discussed and presented.
Chapter 13 Analysis is subdivided into two Sections. It begins with the Sec. Particle Identification, in which the underlying analysis methods for particle identification and counting are presented and explained step-by-step. In the second Sec. AoQ and Position Spectra of $^{190}$Lu Setting, an in-depth comparison of experimental position spectra compared to theoretical position is conducted for each indvidual isotope of the elements osmium, rhenium, tungsten, tantalum, hafnium, lutetium, ytterbium, thulium, erbium, holmium and dysprosium such that a preliminary count can be determined. Followed by a in-depth conclusion in Ch. 14, the results are being put into context of the current state of nuclear structure physics and nuclear astrophysics.

# 11. Goal and Motivation

Since the inception of the NUSTAR collaboration in 2003 [93], one of the main areas of interest is the production and study of new exotic isotopes to advance the field of nuclear physics in its understanding of nuclear structures, nuclear astrophysics and limits of nuclear stability [94]. Of particular interest is the heavy neutron-rich region in between rhenium and erbium due to its close vicinity to the N=126 shell closure and its missing information relating to nuclear properties, which can now be reached by utilizing the unique properties of the upgraded SIS18 ring accelerator with its increased beam intensity (up to $2 \cdot 10^9$ pps for lead) in combination with the FRS and modern equipment intended for use at FAIR and Super-FRS, like the AIDA (Advanced Implantation Detector Array) [95], FATIMA (Fast TIMing Array) [96] and FRS Ion Catcher systems [97]. It is intended to produce and identify novel neutron-rich isotopes by utilizing projectile fragmentation and the FRS separation capabilities, derive the production cross-sections and longitudinal momentum distributions via the FRS standard equipment and measure new as well as increase precision of already known nuclear masses, half-lives and decay-spectroscopic data, see Fig. 11.1.

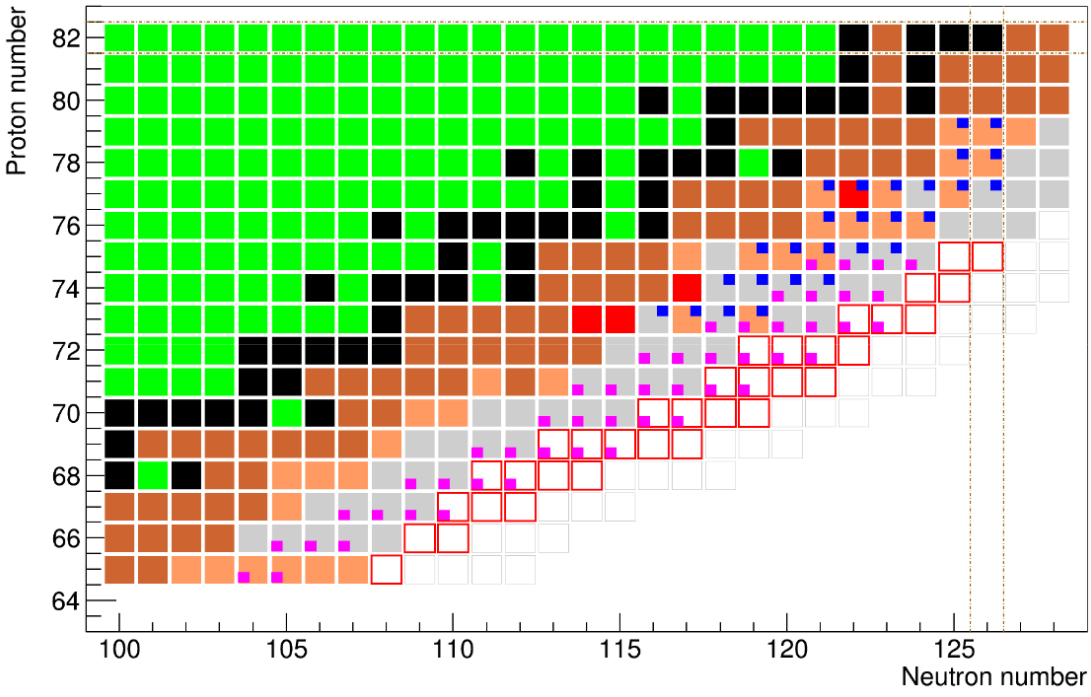


**Figure 11.1.:** Predicted new isotopes and intended measurements, taken from [25]. Black squares symbolize stable nuclei. Green squares are neutron deficient nuclei. Dark brown squares show nuclei with known half-lives and masses whereas light brown squares show nuclei with known half-lives. Red Squares depict nuclei with known masses. Grey squares are discovered but not measured nuclei. Red-bordered squares show potential new isotopes. Pink- and blue-squared markings signal possible half-live and mass measurements.

The data is shared within the Super-FRS Experimental Collaboration such that the isotopic identification is part of this dissertation. Half-lives are part of the PhD work of H. Rösch-Kabadayi [27] and M. Luoma [28] and the nuclear masses are part of the PhD work of D. Amanbayev [29]. These findings can contribute to multiple nuclear physical fields of study in accordance with NUSTAR's motivations. By synthesizing new isotopes, the known region on the chart of nuclides can be expanded towards the neutron dripline, even though still far away it allows to probe into terra incognita and opens the possibility for potential future experiments at Super-FRS with similar but adapted setups. Secondly, high accuracy mass and decay-spectroscopy measurements allow the derivation of mass excess, binding energy and transition properties which in turn give insights into the nuclear structure and shells around the magic numbers $Z = 82$ and $N = 126$. Additionally, the evolution of nuclear shells and shell models far-off from stability or devolution thereof into deformed shell models can not only be experimentally tested, but new experimental data will provide necessary input for theoretical model calculations of nuclear many-body systems. Especially since exact models are highly challenging to compute in this region and mean-field approaches have to be relied upon to try and understand the strong interaction. Lastly, for nuclear astrophysics it would aid the better understanding of the stellar r-process and its synthesis of heavy elements [98]. By experimentally determining masses together with $\beta$-decay half-lives, extensive value can be gained in the constraint of theoretical reaction network calculations to determine the r-process path, which highly relies on such data far-off from stability and in most cases can only be supported by theoretical values. Even though isotopes directly on the r-process path can not be produced in this experiment, the advance into the unknown neutron-rich isotopes of this region, nonetheless provides a gain in accuracy for the aforementioned network calculations and prediction of the third r-process abundance peak.

# 12. Experimental Setup

In order to produce new neutron-rich exotic isotopes between rhenium and erbium by making use of projectile fragmentation of lead nuclei, a $^{208}Pb^{67+}$ beam at highest intensities of up to $1.5 \cdot 10^9$ particles per spill (short pps) on the target with a beam energy of 1050 $A\mathrm{MeV}$ was chosen to impinge on a thick 4 $\mathrm{g\,cm^{-2}}$ beryllium target with a 223 $\mathrm{mg\,cm^{-2}}$ niobium backing. The high beam energy guarantees that the lead primary beam passes through the SIS18 vacuum window mostly fully ionized into the target and that produced fragments stay fully ionized with a probability of around 90% until they reach the scintillator at S4 for counting, according to LISE++ [76]. The thick beryllium target allows to increase the production yield through secondary fragmentation reactions, as suggested by [99], but introduces additional angular and energy-loss straggling. Additionally, the beam energy was increased over its initially proposed energy of 1000 $A\mathrm{MeV}$ [25] to 1050 $A\mathrm{MeV}$, in order to run at the maximum achievable $B\rho$ in the SIS18 and FRS beam line. The additional niobium backing of the target acts as a further ionisation stage and allows for all fragments to be ca. 95% fully ionized, according to GLOBAL [45]. Figure 12.1 shows the final detector configuration of the FRS for the new isotope search experiment.
Due to the very high primary beam intensity and short extraction time of down to 0.5 $\mathrm{s}$, it is expected that secondary beam intensities in the order of $10^5$ pps will be present at the second focal plane S2. As such the equipment was chosen to withstand these intensities and will be discussed in more detail in the next Section 12.1. On the other hand the expected beam intensity at the final focal plane is expected to be in the order of 100 pps, which poses no threat to the equipment and should not cause any efficiency losses. This is discussed in more detail for the individual settings in Sec. 12.2.

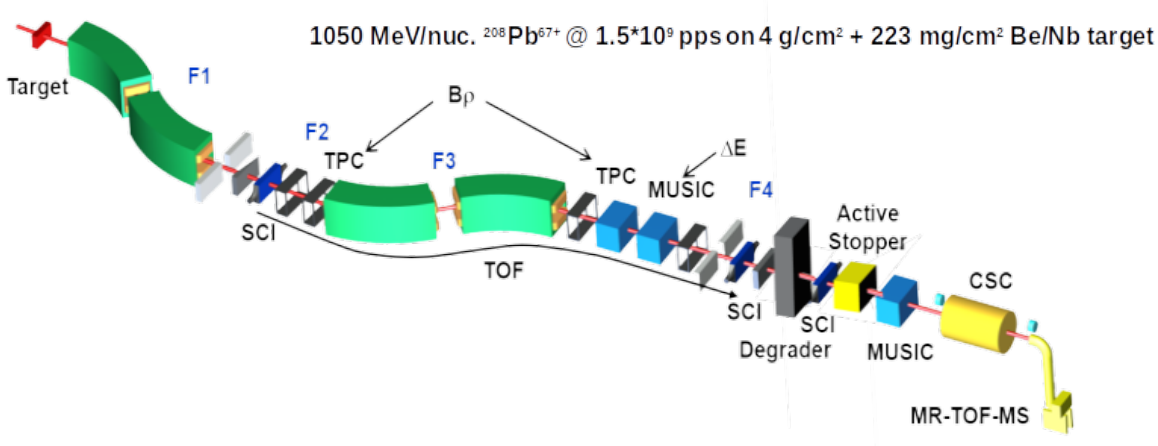


**Figure 12.1.:** Experimental Setup of the FRS as used for S468. Marked in the graphic are the plastic scintillators used for the time-of-flight measurement, the TPCs for the position and $B\rho$ determination, the MUSIC detectors for the energy-loss measurement, the Active Stopper with its 6 DSSSDs [100] and $LaBr_3$ array for implantation and $\beta$-decay measurement and lastly the FRS Ion Catcher [97] with its cryogenic stopping cell (CSC) and MR-TOF mass spectrometer.

## 12.1. Hardware

The following section will give an overview about the necessary detector setup at the FRS including its implementation into the data acquisition system, in order to allow unambiguous particle identification, production yield measurements and longitudinal momentum distribution evaluation as well as total production cross-section determination for projectile fragmentation.

### Scintillator

Four plastic scintillators (short SC21/22, SC41/42) were in use during the experiment in order to provide a high accuracy Time-of-Flight measurement and additional fallback measurements, in case there should be a failure. Two were used at S2 (SC21/22) and another two at S4 (SC41/42), their respective positions in the beamline can be seen in Figs. A.3. and A.5. in App. A. There was a third scintillator at S4 (SC43) as well, but this one was only in use as a veto counter for the active stopper implantation setup. With the utilization of four platic scintillators, it was possible to conduct four different TOF measurements, which are 21-41, 21-42, 22-41 and 22-42 respectively. The specialty here was, that SC22 was positioned behind the degrader system at S2 in air, as close as possible to the vacuum chamber. Thus by calculating the difference in TOF between 21-41 and 22-41, it would provide additional information should pileup occur due to high rates at S2, thus events appearing to have a velocity faster than the speed of light. The two plastic scintillators in use at S2 were one 1.04 $\mathrm{mm}$ BC420 and one 1.15 $\mathrm{mm}$ BC420 plastic scintillator. The two at S4 were quite similar with 1.0 $\mathrm{mm}$ BC420 each. The left and right side of each plastic scintillator were respectively connected to a photo-multiplier tube (PMT), at S2 [101] and at S4 [102]. Figure 12.2 shows how the scintillators were connected to the FRS data acquisition system.

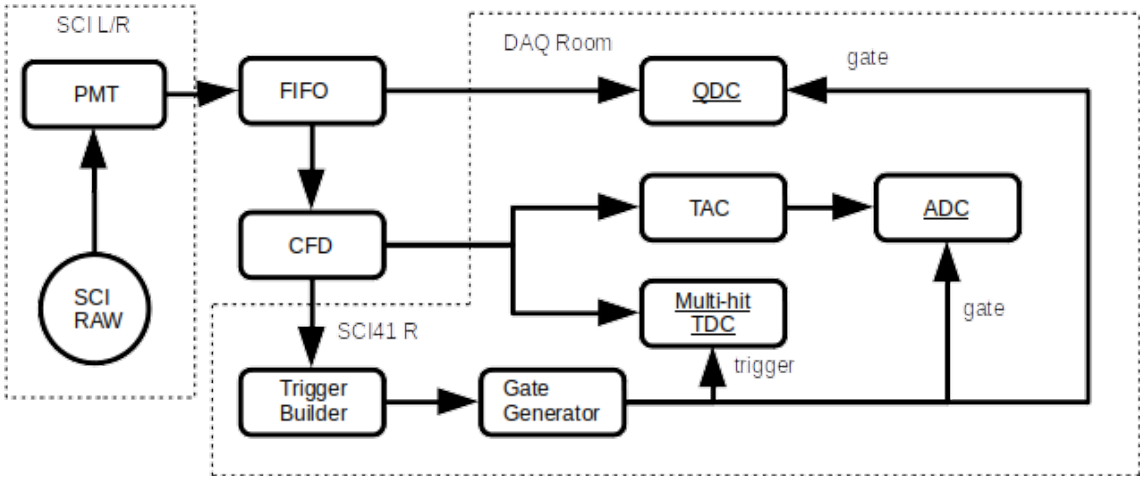


**Figure 12.2.:** Overview of the electronic setup for scintillators during the experiment. The scintillator light is first converted by a respective PMT into and electric signal, which is then split via a linear Fan-in/Fan-out (FIFO) element to both a Constant-Fraction-Discriminator (CFD), to produce a timing signal, and a Charge-to-Digital-Converter (QDC), for energy-deposition measurement. The signal of the right side of SCI41 is then used for the trigger building process, whose accepted triggers are fed into the gate generation and subsequently trigger the readout of the Multihit Time-to-Digital-Converters and open the gate for the QDC and Analog-to-Digital-Converter (ADC) readout of the Time-to-Amplitude-Converter after the CFD. The TAC and mhTDC systems are used in combination as a redundancy mechanism and for pileup detection in the MUSIC.

### TPC

For the position measurement at S2 and S4, two time-projection chambers TPC23/24 were in use at S2 after SC22 in air, standing ca. 1130 $\mathrm{mm}$ apart, as well as two TPCs TPC41/42 at S4 at a distance of 1140 $\mathrm{mm}$ to eachother. Each TPC provides four drift-time measurements for vertical position determination, via four anodes embedded individually in a shielded C-shaped cathode pad operated as a proportional chamber. The back and front provide a horizontal position measurement via a time difference measurement through metallized mylar strips, with the drift volume being 240 $\mathrm{mm}$ wide, 70 $\mathrm{mm}$ long and 120 $\mathrm{mm}$ high, filled with P10 gas (90% Ar and 10% $CH_4$). The connection of each TPC to the FRS DAQ can be seen in Fig. 12.3.

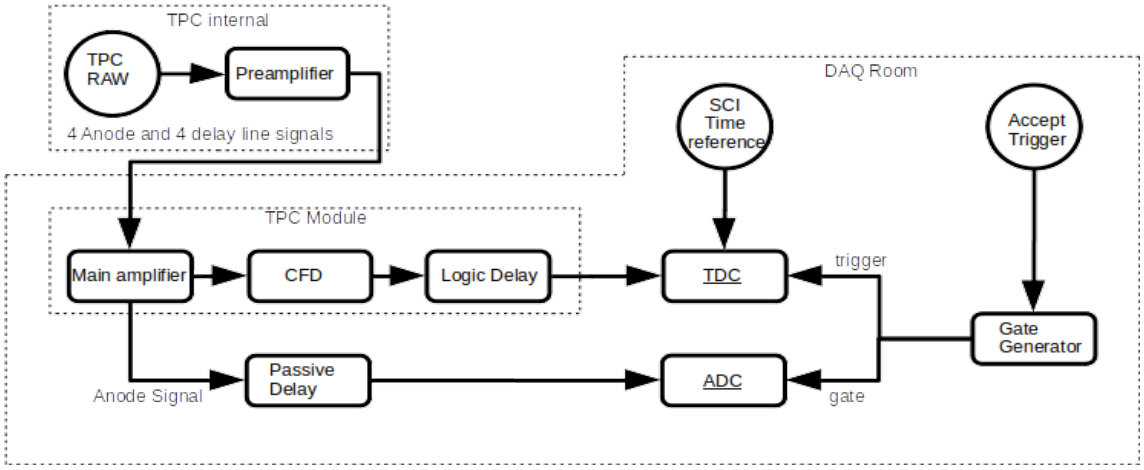


**Figure 12.3.:** Overview of the electronic setup for TPCs during the experiment. Each anode and delay-line signal is first internally preamplified before it is transported into the special TPC module. It consists of a main amplifier, that feeds into the CFD and a logic delay, which then connects to a TDC, whose readout is triggered by the same gate generator that relies on the accepted triggers provided by the SC41R signal. The scintillator at the respective focal plane provides a time reference signal for TPC drift-time measurements into the TDC. From the main amplifier the anode signals are split into a passive delay and then transported to an ADC for readout of energy-deposition measurements.

### MUSIC

Energy-loss measurements and nuclear charge determination according to Sec. 2.2 are facilitated by the use of the MUSIC detectors at S4. As a charged particle passes through the gaseous drift volume in the detector, it ionizes the argon atoms and methane molecules along its path due to electromagnetic atomic interactions. The produced free electrons and ions drift towards the cathode and anodes respectively because of the applied voltage and produce a voltage signal in turn. This voltage signal depends on the produced charge, which sequentially is proportional to the lost energy of the initial particle transversing the drift volume. Each MUSIC possesses eight anodes that are shielded via a Frisch-grid and the final signal is determined as the geometric mean of all anode signals, in order to improve the signal-to-noise ratio. Both MUSICs were filled with P10 gas and operated within proportional range. The active geometry of the MUSIC detector is 200 $\mathrm{mm}$ wide, 80 $\mathrm{mm}$ high and 400 $\mathrm{mm}$ long.
In order to detect any electron pick-up or loss reactions inside of the drift length of one MUSIC, a second MUSIC is installed immediately after the first one. By correlating the deposited energies in both MUSICs

and picking the maximum of each individually determined charge, it is possible to filter out atomic charge-changing processes and fully determine the nuclear charge Z. Figures 12.4 and 12.5 give an overview of the music detector and its DAQ setup respectively.

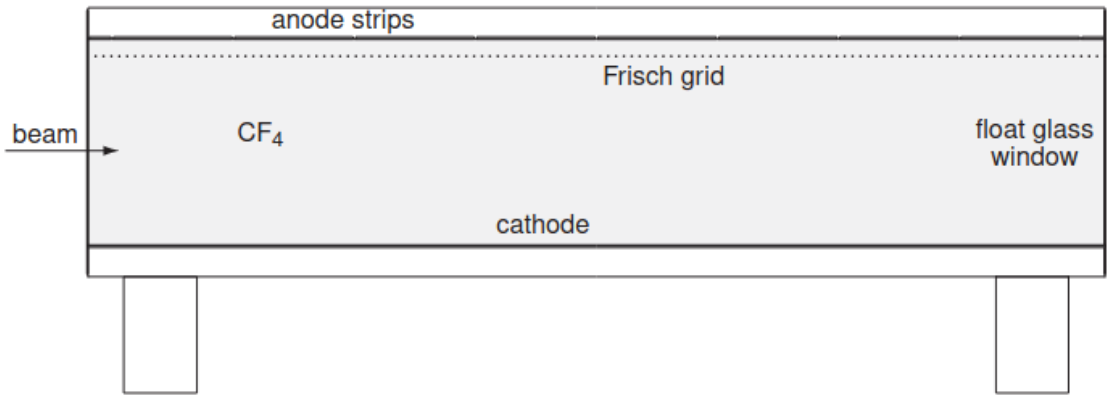


**Figure 12.4.:** Schematic overview of MUSIC detector [38]. Even though $CF_4$ is shown to be the detection gas, P10 was used during the experiment.

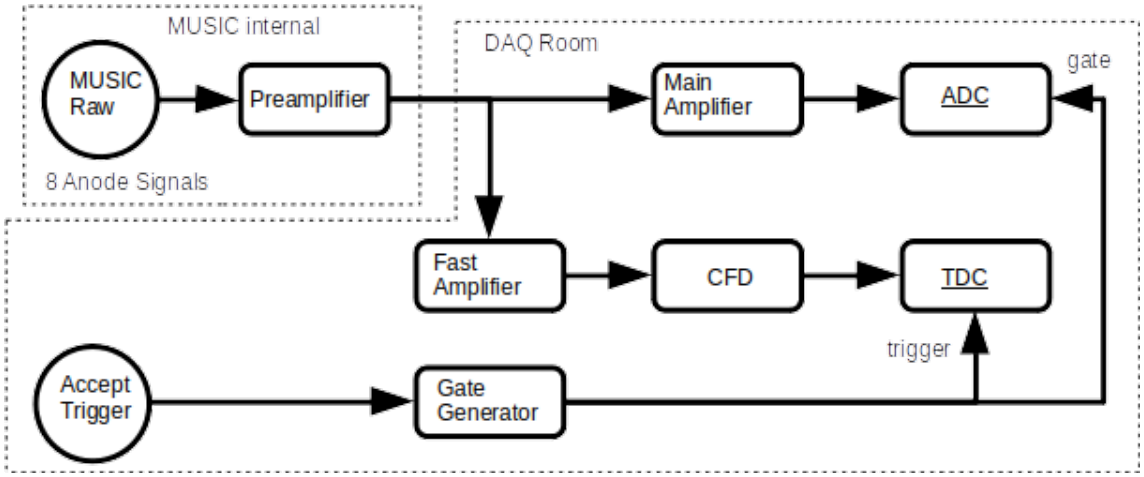


**Figure 12.5.:** Overview of the DAQ setup for MUSICs during the experiment. The raw signal of each anode is first internally preamplified and then split into a main as well as fast amplifier module for amplification and shaping purposes. The fast amplifier signal is used by a CFD to produce a timing signal for drift-time measurement within the MUSIC. The signal is given to a TDC, whose readout is triggered by a gate generated from an accepted trigger, as previously mentioned for scintillators. Another generated gate triggers the ADC readout from the main amplifier for the energy-loss measurement.

It will be shown in the next Sec. that the expected heavy-ion rates at S2 and S4 for the respective ion-optical settings were within the acceptable limits of operation for the detectors described in this Section.

## 12.2. Setting Simulations

It was discussed that the previous settings from [25] could be optimized to allow for minimal detector setup changes and maximized effective beam-time utilization by finding a single exotic open setting, that allowed for the maximum number of new species to be produced and transmitted, as suggested by [99]. This had to be simulated with the goal in mind to measure as many new masses, $\beta$-decay lifetimes and new isotope counts as possible. For this purpose, LISE++ [76] version 12.1.2 in combination with MOCADI [78] version 4.2 were used to simulate the predicted transmissions and yields for the FRS.
The FRS was rebuilt inside LISE++ and MOCADI according to the specifications given in the experimental proposal [25] and showcased earlier in Ch. 10. In order to maximize isotopic yields the optimal target thicknesses, optical modes and beam energy were investigated in addition to the minimization of settings. The starting configuration was a 2512 $\mathrm{mg\,cm^{-2}}$ beryllium target with a 223 $\mathrm{mg\,cm^{-2}}$ niobium backing, with a 1000 $A\mathrm{MeV}$ lead beam and the FRS in achromatic mode. The target thickness was quickly determined via LISE++ "Optimum Target" calculation for a given beam and fragment combination of the previously mentioned lead beam and $^{191}$Lu as the fragment. $^{191}$Lu was chosen, since it was originally predicted to be produced and acted as the middle-ground between osmium ($Z = 75$) and terbium ($Z = 65$). The resulting thickness of 2806 $\mathrm{mg\,cm^{-2}}$ was closest to the aforementioned existing FRS target. Variations in fragments all resulted in similar thicknesses such that 2512 $\mathrm{mg\,cm^{-2}}$ was chosen, as it was the only existing one in this thickness region. As starting optical mode the achromatic mode, see Sec. 2.1, was chosen, since it allowed for the transmission of more isotopes than the mono-energetic mode, and was further compared to the newly developed high-transmission mode [103].
This starting configuration was used to determine an optimal setting[1], as described in the previous paragraph, by calculating the transmission and yield of many different settings in parallel and comparing the number of potentially newly found isotopes with each other. This calculation was assuming for the projectile fragmentation that the reaction cross sections were given by EPAX 3.1a [74], which was shown in [79] to hold true for heavy neutron-rich isotopes in this region, furthermore it was assumed that the fragment momentum distribution was according to [71], a quick comparison with the Morrissey [104] distribution did not yield any differences for transmission or yields. The fragment velocity distribution was assumed to be according to Goldhaber [71]. charge-state calculations, according to GLOBAL [45], and secondary reaction calculations, with EPAX cross sections, were conducted in parallel for the main beryllium target, its niobium stripper and the aluminium degrader wedge at S2. With all these considerations in mind, it resulted in $^{190}$Lu as the isotope of interest setting, such that the highest number of new isotopes can be discovered in a single setting during a continuous time of 12 allotted shifts. In order to allow for unambiguous identification by counting down the isotopes from the primary beam towards the new isotopes, in case mass tagging via the FRS Ion Catcher fails, three more settings were found to be necessary to provide momentum overlap to measure longitudinal momentum distributions, use the FRS Ion Catcher [97] to determine new masses and mass tag isotopes as well as the Active Stopper [100] to determine new lifetimes. This resulted in the additional $^{205}$Au, $^{193}$W and $^{193}$Ta settings as well as the primary beam lead setting, for calibrating and setting up the FRS.
In the next step, the influence of different target thicknesses, optical modes and beam energies will be simulated. A limiting factor for the experiment was that fragments reaching S4 should have an energy of around 600 $A\mathrm{MeV}$ or more, in order to minimize charge-state changing reactions at S4 in the MUSICs, i.e. electron pickup or loss, and maximize correct z identification efficiency. This limited the target thicknesses not to be too thick and primary beam energies not to go lower than 1000 $A\mathrm{MeV}$.

[1] By setting it is implied that only the $B\rho$ values of each dipole stage are changed to center a given isotope of interest in LISE++.

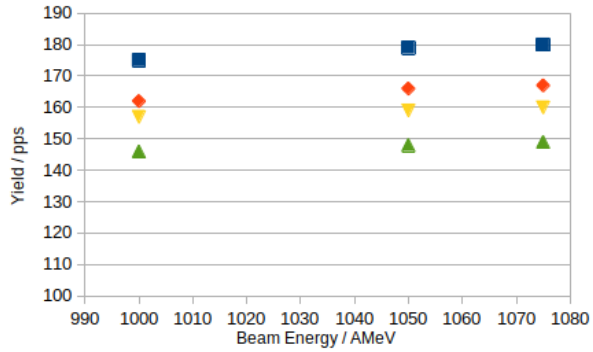


**(a)** $^{205}$Au in $^{205}$Au setting

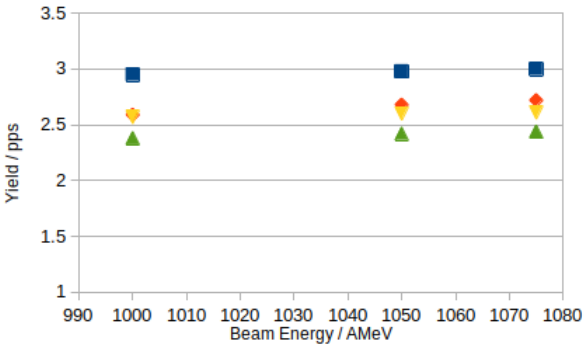


**(b)** $^{193}$W in $^{193}$W setting

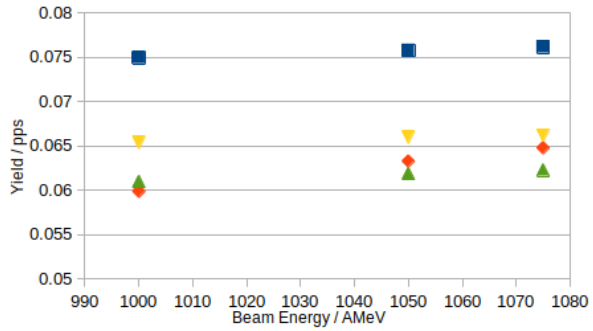


**(c)** $^{193}$Ta in $^{193}$Ta setting

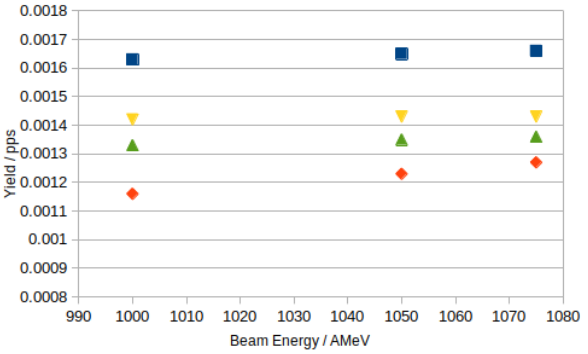


**(d)** $^{190}$Lu in $^{190}$Lu setting

**Figure 12.6.:** Yield, given in particles per spill (pps), comparison for the isotopes of interest in its respective setting for varying beam energies in $A$MeV, target thicknesses and optical modes. The colours represent the different combinations of 2512 $\mathrm{mg\,cm^{-2}}$ with the achromatic mode (green, combination 1), 2512 $\mathrm{mg\,cm^{-2}}$ with high-transmission mode (yellow, combination 2), 3991 $\mathrm{mg\,cm^{-2}}$ with achromatic mode (red, combination 3) and 3991 $\mathrm{mg\,cm^{-2}}$ with high-transmission mode (blue, combination 4). The primary beam intensity for the calculation was $1{\cdot}10^9$ pps.

Additionally a very thick target would introduce too much angular straggling as well as particle loss inside the target such that the gain from secondary reactions would be negated and the transmission negatively impacted. The yield comparison for the isotope of interest in the respective settings for varying primary beam energies, target thicknesses and optical modes can be found in Fig. 12.6. It becomes apparent in all settings that a higher primary beam energy results in a higher yield due to better focussing, although the gain is only marginally increased in most cases ($\sim 1\%$), in the cases of the $^{190}$Lu and $^{193}$Ta settings there is a yield gain by $6\%$ and $5.7\%$ respectively for an increase of 50 $A$MeV for combination 3. Thus making 1075 $\mathrm{A\,MeV}$ the preferred energy, which corresponds to 18.3980 $\mathrm{T\,m}$ for the dipoles before the FRS target station and lies theoretically below the maximum limit of 18.5 $\mathrm{T\,m}$ for the power supplies. It was experimentally proven that 1075 $\mathrm{A\,MeV}$ was not possible to achieve and instead 1050 $\mathrm{A\,MeV}$ was used. Now comparing the different thicknesses, one can see that for the combinations 1 and 3 with an energy of 1050 $A$MeV the gains in yield ranged from $12.2\%$ for the gold setting down to $-8.9\%$ for the lutetium setting, leading to the conclusion that the yield of less exotic already discovered nuclei increased whereas the yield for highly exotic, yet undiscovered isotopes, tends to decrease. This would be an undesirable outcome but a deeper look into the yield of further exotic isotopes in the lutetium settings shows that

even more exotic nuclei than $^{190}$Lu show a yield loss of only $\sim -2\%$, which is only a slight effect on the final statistics. Thus in order to promote the statistics of known isotopes and the measurement of their masses, lifetimes and cross sections it is beneficial to use a thicker target. This is further proven to be correct by considering combination 2 and 4, which show an overall increase in yield by $12.6\%$ for the gold setting up to $15.4\%$ for the lutetium setting. Therefore the 3991 $\mathrm{mg\,cm^{-2}}$ beryllium target was chosen. When considering the different possible optical modes, it becomes immediately apparent that the newly developed high-transmission mode lends itself a substantial increase in both combinations 2 and 4 across all settings. For the thinner target the yield increases by $7.4\%$ down to $5.9\%$ for the gold and lutetium settings respectively, which in itself is already good, but can be further increased by utilizing the thicker target and resulting in a gain of $7.8\%$ up to $34.1\%$ for the gold and lutetium settings respectively. Nonetheless, since the high-transmission mode was not yet tested in a nuclear physical experiment at that point in time and experience with it was lacking, it was deemed too high a risk and thus the standard achromatic mode was ultimately chosen. Thus the final setup used a primary beam energy of 1050 $A\mathrm{MeV}$ with a 3991 $\mathrm{mg\,cm^{-2}}$ beryllium target and the achromatic mode. The final settings with their respective setups, expected lifetimes, masses and new isotopes can be found in Tab. 12.1 and Tab. 12.2.

| Setting Centered Fragment | Active Stopper | Ion Catcher | New Lifetimes | New Masses | New Isotopes | Shifts |
|---|---|---|---|---|---|---|
| $^{205}$Au$^{79+}$ A | | x | - | - | - | 1 |
| $^{205}$Au$^{79+}$ B | x | | - | - | - | 1 |
| $^{193}$W$^{74+}$ A | | x | - | 27 | - | 0.5 |
| $^{193}$W$^{74+}$ B | x | | 24 | - | - | 0.5 |
| $^{193}$Ta$^{73+}$ | x | | - | - | - | 1 |
| $^{190}$Lu$^{71+}$ | x | | 28 | - | 33 | 12 |
| Total | - | - | 44 | 27 | 33 | 16 |

**Table 12.1.:** Final settings and setups for the experiment together with predicted new lifetimes, mass and isotopes per setting. The tungsten and lutetium settings were intended as the main measurement settings, whereas the gold and tantalum settings were intended as quick intermediate settings to allow for momentum overlap with the other settings. The active stopper could be quickly mounted and dismounted. The threshold for discovery was 3 counts in total and the threshold for a mass or lifetime measurement was 10 counts in total.

| Setting Centered Fragment | $B\rho$ TA-S2 | $B\rho$ S2-S4 |
|---|---|---|
| $^{205}$Au$^{79+}$ | 12.5518 T m | 10.7378 T m |
| $^{193}$W$^{74+}$ | 12.7006 T m | 11.0257 T m |
| $^{193}$Ta$^{73+}$ | 12.9112 T m | 11.2668 T m |
| $^{190}$Lu$^{71+}$ | 13.1174 T m | 11.5294 T m |

**Table 12.2.:** Predicted $B\rho$ settings for the individual settings considering combination 3 and a primary beam energy of 1050 $A\mathrm{MeV}$. It is important to note that these rigidities were calculated and initially used for the experiment before the thicknesses of all matter devices were experimentally calibrated. The actual final experimental $B\rho$ values differ slightly and can be found in Sec. 10.

When considering the final count of each new isotopes, LISE++ takes into account the efficiency from spatial and angular transmission, reaction probability in matter or survivability of one isotope separated

into unreacted and unstopped particles, the charge-state ratio of fully-stripped ions at scintillator SC42 and the contribution of secondary reactions. Not taken into account by LISE++ is the detection probability for each detector, event-loss due to DAQ dead-time or pile-up occurring for higher particle rates. Assuming an additional flat reduction of events by a factor of 10 from these contributions, a final count of 19 new isotopes, 13 new masses and 30 new lifetimes could still be achieved.
Finally, it is important to determine from the simulations that the particle rates at S2 and S4 stay within the operational limits of FRS detectors. For this purpose the fragmentation and fission rate of all isotopes from lead to hydrogen together with their charge-states and secondary reactions for each individual setting were calculated and summed up. A primary beam intensity of $10^9$ pps was used for these calculations, in order to be as close as possible to the SIS18 maximum intensity of $1.5{\cdot}10^9$ pps. The results can be seen in Tab. 12.3 for each setting. For the gold setting it is immediately clear that the rate at such a primary beam intensity would be too high and thus has to be adjusted to be acceptable, which can be quickly done online with the benefit that the calculated rates scale linearly with the primary beam intensity. For the tungsten setting, the same statement holds true. Additionally, high intense $^{208}Pb^{80+}$ and $^{208}Pb^{79+}$ spatially narrow charge-states would impinge on the S2 scintillator and have to be cut away by moving the S1 slits into the position -10/100 $\mathrm{mm}$ and by decreasing the primary beam intensity to acceptable levels. For the last two tantalum and lutetium settings, it is important that maximum beam intensity is utilized during the experiment, thus spill length and beam intensity adjustment have to be avoided and instead S1 slit positions can contribute to improve rate conditions at S2 and S4. This leads for the tantalum setting to a decrease to a total rate at S2 of $1.53{\cdot}10^5$ pps and $3.05{\cdot}10^1$ pps at S4. For the lutetium setting a total rate of $7.91{\cdot}10^4$ pps and $1.42{\cdot}10^1$ pps at S2 and S4 respectively would be expected. With these considerations in mind, it would be possible to run the experiment within the operational limit of the FRS detectors, albeit very close to the maximum sustainable particle rate and some event losses due to high particle rates might be expected. Even though not explicitly mentioned here, MOCADI was used in parallel to simulate the settings, cross-check and confirm the findings from LISE++.

| Setting Centered Fragment | Fragmentation Rate S2 | Fragmentation Rate S4 | Fission Rate S2 | Fission Rate S4 | Total Rate S2 | Total Rate S4 |
|---|---|---|---|---|---|---|
| $^{205}Au^{79+}$ | $5.76{\cdot}10^6$ | $8.95{\cdot}10^4$ | $7.97{\cdot}10^6$ | $4.90{\cdot}10^4$ | $1.37{\cdot}10^7$ | $1.38{\cdot}10^5$ |
| $^{193}W^{74+}$ | $2.80{\cdot}10^5$ | $1.64{\cdot}10^3$ | $1.08{\cdot}10^6$ | $6.30{\cdot}10^3$ | $1.36{\cdot}10^6$ | $7.94{\cdot}10^3$ |
| $^{193}Ta^{73+}$ | $5.55{\cdot}10^4$ | $9.35{\cdot}10^1$ | $2.04{\cdot}10^5$ | $2.84{\cdot}10^0$ | $2.60{\cdot}10^5$ | $9.63{\cdot}10^1$ |
| $^{190}Lu^{71+}$ | $3.39{\cdot}10^5$ | $2.85{\cdot}10^1$ | $9.75{\cdot}10^4$ | $1.68{\cdot}10^0$ | $1.31{\cdot}10^5$ | $3.02{\cdot}10^1$ |

**Table 12.3.:** Predicted particle rates for projectile fragmentation and coulomb fission from LISE++, with cross-sections from ABRABLA [81, 105]. Even though ABRABLA produces cross-sections for abrassion-fission reactions, these were loaded into LISE++ via the coulomb fission mechanism and calculated for the individual settings in combination 3 with a primary beam intensity of $10^9$ pps. For comparison, calculating abrassion-fission yields directly through LISE++ by adjusting low, middle and high excitation energy regions yields a total fission rate of $\sim 10^{-4}$ pps. The rates are given in particles per spill (pps), assuming a spill length of 1 $\mathrm{s}$. Rate optimisations are discussed in the paragraph above.

## 12.3. Calibration

### TPC Calibration

The first important calibration to perform is the one of the Time-Projection-Chambers (TPCs), in order to allow the primary beam to be centered at all focal planes of the FRS. This calibration lays the foundation of all subsequent calibrations, i.e. matter, time-of-flight, MUSIC velocity and position corrections, and ultimately particle identification. Each TPC is outfitted with a scintillating fibre mask possessing three horizontal and vertical fibres each, positioned at (-12 $\mathrm{mm}$, 0 $\mathrm{mm}$, 12 $\mathrm{mm}$) horizontally and (-6 $\mathrm{mm}$, 0 $\mathrm{mm}$, 6 $\mathrm{mm}$) vertically. Additionally, each mask can act as the trigger for the readout of every TPCs four drift-time and two delay-line measurements. In order to illuminate the scintillator mask and calibrate each TPC, the primary beam is transported to the respective focal plane with no other matter before the TPC via LISE++ calculated $B\rho$ values and consequently defocused. The resulting position spectra in raw TDC channel numbers can be seen in Fig. 12.7 and 12.8 exemplary for the drift-time of cathode 1 and the time difference of delay-line 1 of TPC42 respectively.

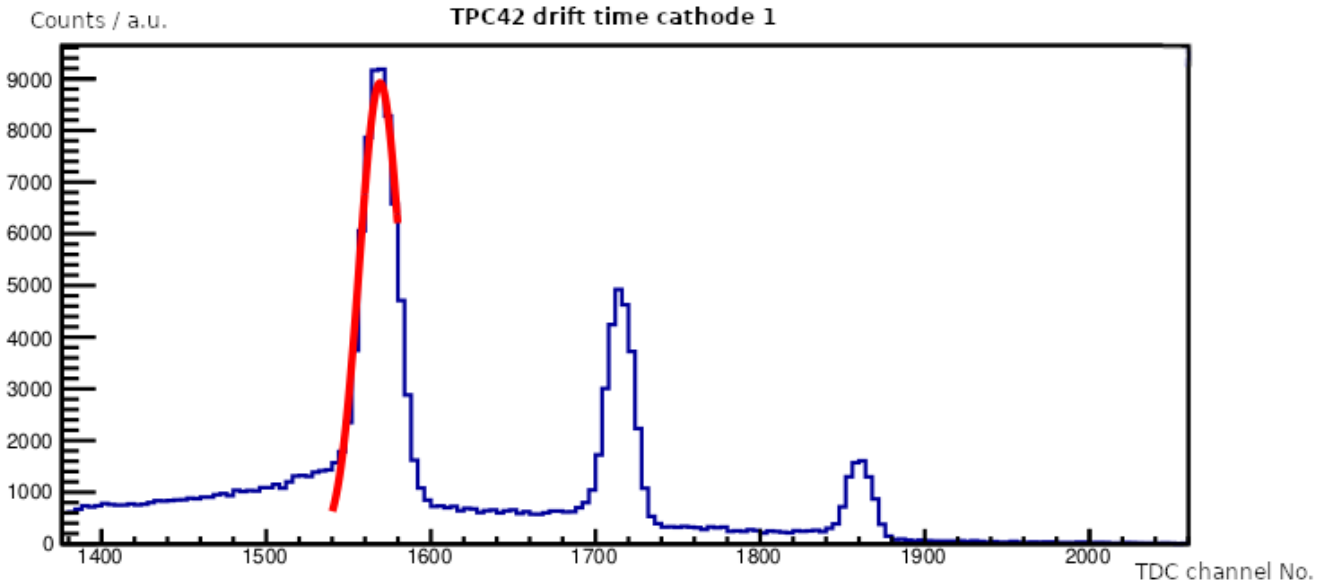


**Figure 12.7.:** Drift-time measurement for the first cathode of TPC42. It is important to note that a low channel number corresponds to a low drift-time and therefore a high vertical position. The peaks from left to right correspond to the positions (6 $\mathrm{mm}$, 0 $\mathrm{mm}$, -6 $\mathrm{mm}$) and are fitted via a Gaussian distribution, indicated by the red curve in the plot.

By fitting a Gaussian distribution to each peak, the positions can be associated to the channel numbers and a linear calibration function can be derived. A full table of all TPC calibration functions in use can be found in Appendix E.0.1.
It is important to note, that the calibration grids were used for TPCs 21,22,31,41 and 42, whereas the TPCs 23 and 24 were calibrated by utilizing the projection of the grid position spectrum from TPC 22 unto 23 and 24 for which the same Gauss fitting method was applied to derive the linear calibration function.

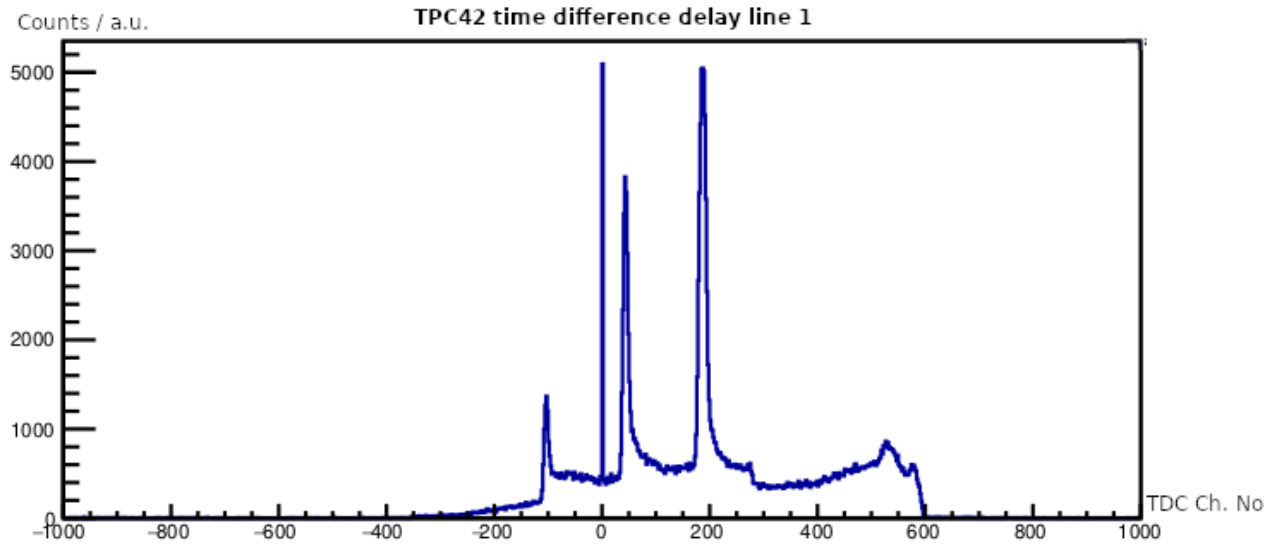


**Figure 12.8.:** Time difference measurement for the first delay-line of TPC42. Per definition, a negative channel number corresponds to a negative position and a positive channel number to a positive position. Thus the peaks can be associated with horizontal positions (-12 $\mathrm{mm}$, 0 $\mathrm{mm}$, 12 $\mathrm{mm}$) from left to right. The same fitting method is applied to this measurement as well. The peak at channel 0 corresponds to events, whose triggers did not receive any TPC information.

### TOF Calibration

After the TPC calibration, it was possible to first center the primary beam at all focal planes of the FRS by adjusting the dipole stages kick values, such that the beam goes trough the 0 $\mathrm{mm}$ position at an angle of 0 $\mathrm{mrad}$. As a next step, the relevant matter devices were put into the beam individually and the primary beam's deviation from the center position was observed and the $B\rho$ values of the respective dipole stages were adjusted. These preparatory steps allow to facilitate the time-of-flight calibration between S2 and S4 with all plastic scintillators by changing the primary beam's energy and utilizing the S2 degrader wedge. The five variations were:

1. Primary beam energy of 600 $A\mathrm{MeV}$ ($\widehat{=}$ 0.7770931 c from S2-S4).
2. Primary beam energy of 670 $A\mathrm{MeV}$ ($\widehat{=}$ 0.7997628 c from S2-S4).
3. Primary beam energy of 750 $A\mathrm{MeV}$ ($\widehat{=}$ 0.8215097 c from S2-S4).
4. Primary beam energy of 1050 $A\mathrm{MeV}$ ($\widehat{=}$ 0.8768016 c from S2-S4).
5. Primary beam energy of 1050 $A\mathrm{MeV}$ with the S2 aluminium degrader wedge set to 2 $\mathrm{g\,cm^{-2}}$ ($\widehat{=}$ 0.8575317 c from S2-S4).

All these settings were considering the SIS18 vacuum window, SEETRAM at TA and SCI21/22 as well as TPC23/24 at S2. The time-of-flight is then calculated in the following way

$$\delta t_{ll} = t_{41l} - t_{21l}, \qquad \delta t_{rr} = t_{41r} - t_{21r}, \tag{12.1}$$

$$tof_{ll} = \delta t_{ll} * m_{ll} + n_{ll}, \qquad tof_{rr} = \delta t_{rr} * m_{rr} + nrr, \tag{12.2}$$

$$tof(21-41) = (tof_{ll} + tof_{rr})/2, \quad tof(21-41, calib) = tof_{off} - tof(21-41), \tag{12.3}$$

where $t_{x,y}$ is the time determined for scintillator x (21,22,41,42) on side y (left l, right r) and $\delta t_{yy}$ the time difference of the same side of two different scintillators. From that the uncalibrated time-of-flight $tof_{yy}$ for each side is calculated via $\delta t_{yy}$ and the TAC calibration factors $m_{yy}$ and offsets $n_{yy}$, which are separately determined. In the next step, the uncalibrated time-of-flights from both sides are averaged into $tof(a-b)$ and calibrated via $tof(a-b, calib)$ and the time-of-flight offset $tof_{off}$. This method can be used for all scintillator combinations between S2 and S4. From these formulas $\beta$ is derived as such

$$\beta = \frac{path(21-41)}{tof(21-41, calib)}, \tag{12.4}$$

where $path(a-b)$ is the path length in ps between scintillator a and b. Plotting the calibrated time-of-flight over the inverse $\beta$ value gives the path length and offset. For the distance 21-41 the factors are $path(21-41) = 123304.0$ ps and $tof_{off} = 174620.0$ ps for the given energies. The TAC and other time-of-flight calibration factors in use can be found in App. E.0.2. It is important to note that when using the S4 scintillator for triggering purposes, the start and stop signals are swapped. Meaning SC41 signals start the TAC, whereas SC21 signals stop it again after passing through a delay-line. As a result, faster isotopes have a higher tof(21-41) value than slower ones.

### $B\rho$ Calibration

The particle mass identification has been derived and discussed in detail in Ch. 2.2 under Mass Identification. Especially formula 2.9 plays a significant role in determining the particle mass. Since it was already introduced how the position information is derived from the TPC calibrations it will be quickly presented how $B\rho_0$ for the dipole stages S2-S4 is determined. $B\rho_0$ is simply calculated as the average value of two dipole stages. These values are manually inputted by the operator via LSA and calculated for TA-S2 and S2-S4 by taking the mean $B\rho$ values of GTS3MU1 and GTS3MU2 as well as GTS4MU1 and GHFSMU1. Such an example can be seen in Sec. 10.1 Tab. 10.1 for the respective $B\rho_0$ values.

### MUSIC Calibration

The last important calibration necessary in order to perform particle identification is for the energy-loss measurement inside the MUSIC detectors, which were equipped with the internal preamplifiers A, which according to the MUSIC manual [38] are suitable for Z ranges between 92 and 25. Next the energy-loss is calibrated in two ways, which is a correction of the energy-loss inside each MUSIC depending on the charge collection deficit close to the walls and the second correction is a velocity dependent energy-loss correction depending on the $\beta$ of the passing particle. The energy-loss and charge Z are calculated in the following way including all mentioned corrections for each MUSIC individually

$$dE_{xc} = dE * \frac{a_0}{a_0 + a_1 * x + a_2 * x^2 + a_3 * x^3 + a_4 * x^4 + a_5 * x^5 + a_6 * x^6}, \tag{12.5}$$

$$c_v = b_0 + b_1 * \beta + b_2 * \beta^2 + b_3 * \beta^3 + b_4 * \beta^4, \tag{12.6}$$

$$Z = Z_{prim} * \sqrt{\frac{dE_{xc}}{c_v}} + Z_{off}, \tag{12.7}$$

$dE$ is the energy-loss determined by the geometric mean of all eight anodes, $a_i$ are the coefficients of the position-dependent correctional sixth order polynomial and x the position inside the MUSIC. The velocity correction is calculated by applying a fourth-order polynomial with the coefficients $b_i$ and the $beta$ value

from the time-of-flight measurement. Assuming a square dependency of Z for the energy-loss, Eq. 12.7 follows with $dE_c$ and $v_c$ from previous corrections and $Z_{prim}$ the charge of the primary beam ($Z_{prim} = 82$) and an offset $Z_{off}$ to make the charge spectrum fit better.
In order to perform the position correction, two methods can be utilized. The first one uses the primary beam to sweep across the face of the MUSIC detector to cover the full horizontal space whereas the second method uses fragments of one Z such that the full horizontal width of the detector is covered. In both cases, the resulting energy-loss $dE$ can be plotted over the position in the respective MUSIC and fitted with a sixth-order polynomial. For the velocity correction, the primary beam is used at different energies and the energy-loss $dE$ is plotted over the given $\beta$ values of the TOF calibration and fitted via a fourth-order polynomial. All used position and velocity calibration coefficients can be found in App. E.0.3.
With all these calibrations in mind, it is possible to unambiguously identify different isotopes inside the FRS and lay the foundation to count and determine the fragmentation cross-sections for the production of the individual isotopes.

# 13. Analysis

In the previous chapter, it was shown which new isotopes were expected to be produced via projectile fragmentation, what the experimental setup of the FRS is composed of, how a simulation of new settings can achieve an optimal yield given the difficult situation and how the calibration of each detector subsystem was performed in order to achieve unambiguous particle identification.
This Chapter will discuss in great detail the analysis method that was utilized to precisely determine the isotopes that were seen in the experiment, how they were identified and how their individual count was established, using the $^{190}$Lu setting as an example. It will go into detail how the AoQ path-length correction influences the resolution of the particle identification plot, how the MUSIC maximum charge selection cleans up any electron-loss or -pickup within the MUSIC detectors, how the degrader 0e0e charge-state selection removes fragment contaminants and how the TPCs check-sum can be utilized to clean up events with incorrect position information and ultimately leading to the correct anchoring of the identification matrix for each setting. This is followed by a discussion and analysis of each isotopes individual AoQ and position spectra at S2/S4, to determine the final count of newly discovered isotopes.

## 13.1. Particle Identification and New Isotopes

As previously introduced in Sec.2.2, an unambiguous particle identification can be achieved by determining the nuclear charge Z via energy-loss measurements inside the MUSICs and mass-to-charge ratio A/Q via $B\rho$ measurements derived from time-of-flight and position evaluations. When first looking at the particle identification plot (short ID-plot from now), which is the charge Z plotted over the $A/Q$ value (AoQ from now), several aspects become apparent. Without application of any corrections, selections and clean-up methods applied, there are several contributions, which lead to a pollution of the ID plot and prevent the unambiguous identification of new isotopes, see Fig. 13.1 for the $^{190}$Lu setting.

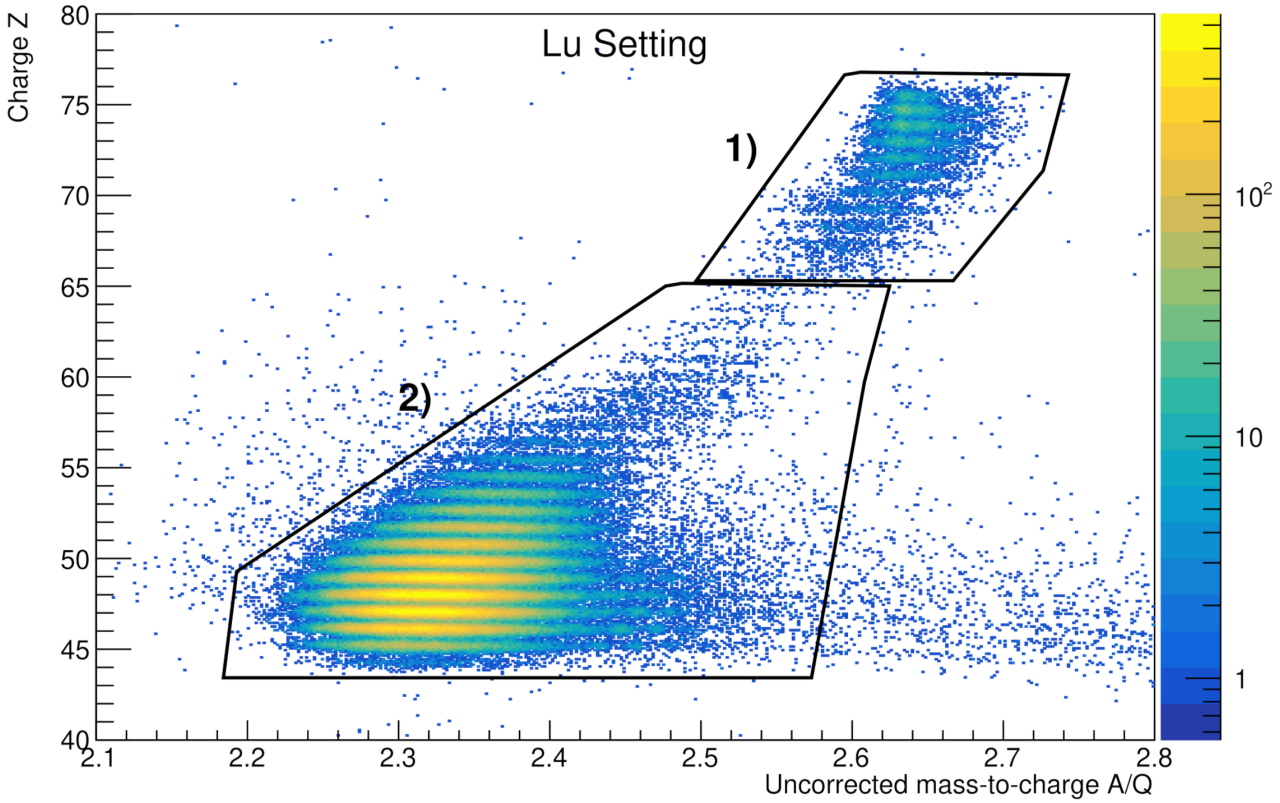


**Figure 13.1.:** Identification plot of the $^{190}$Lu setting without any clean-up applied. Two areas can be immediately identified, the area of projectile fragmentation 1) and abrasion-fission in 2). When comparing the intensities of area 1) and 2) a ratio of 50 to 1 can be observed, which seems to contradict the expectation from Tab. 12.3. The fragmentation rate at S4 from said table does not differentiate the different regions of interest. When comparing the fragmentation rate at S4 for only the isotopes of interest to the combined fragmentation rate and abrassion-fission rate at S4 of all other isotopes, then the ratio results in 103 to 1, with a fragmentation rate of 0.29 $\mathrm{s}^{-1}$ for the isotopes of interest. A reduction from 103 to 1 down to 50 to 1 could be achieved by closing the TA slits to (-8.6 $\mathrm{mm}$, 8.6 $\mathrm{mm}$) horizontally and (4 $\mathrm{mm}$, -5 $\mathrm{mm}$) vertically.

Two regions are visible: The first one is the region of interest between $65 < Z < 77$ and $2.5 < AoQ < 2.75$. Projectile fragments and new isotopes are expected to lie in this region, but a differentiation of isotopes can not be achieved by the default AoQ calculation alone, as presented in Sec. 2.2, and additional corrections are required. Furthermore, a significant admixture from other charge-states, originating mainly from

either the target station, the S2 degrader wedge or charge-changes within the MUSIC detectors, contribute to the pollution in this region. Another contribution to background in this area stems from the TPCs, especially those at S2 due to the particle intensities. The second region below $Z < 76$ and $AoQ < 2.5$ are fragments produced by varying mechanisms, the main contributors expected to be abrassion-fission, projectile fragmentation and secondary reaction fragments, as calculated and shown in Sec. 12.2.

### 13.1.1. AoQ Path-Length Correction

From the FRS ion-optical matrices, which are used to describe particle propagation throughout the machine into the experimental cave S4 and are obtained by GICOSY [32, 106] calculations, it can be seen that the individual particle's path-length dependence from S2 to S4 can be reduced to the horizontal position $x_{S2}$, angle $\alpha_{S2}$, momentum deviation $\delta_{S2-S4}$ and centered trajectory path-length $l_{S2-S4,0}$, since the corresponding coefficients of the ion-optical transport matrix from S2 to S4 do not vanish for these observables, see App. F and Lst. F.3 S2-S4. Thus the following expressions emerge for the corrected path-length $l_{S2-S4,cor}$ and other derived observables such as the corrected velocity $\beta$ and Lorentz-factor $\gamma$ values $\beta_{cor}$ and $\gamma_{cor}$ respectively

$$\begin{aligned} l_{S2-S4,cor} &= l_{S2-S4,0} + (l_{S2-S4,0}|\delta_{S2-S4}) \cdot \delta_{S2-S4} + (l_{S2-S4,0}|x_{S2}) \cdot (-x_{S2}/1000) + \\ &\quad (l_{S2-S4,0}|\alpha_{S2}) \cdot (-\alpha_{S2}/1000), \end{aligned} \tag{13.1}$$

$$\beta_{cor} = \frac{l_{S2-S4,cor}}{tof(21-41,calib) \cdot c \cdot 10^{-12}},\ \gamma_{cor} = \frac{1}{\sqrt{1-\beta_{cor}^2}}, \tag{13.2}$$

$$f = \frac{\beta \cdot \gamma}{\beta_{cor} \cdot \gamma_{cor}},\ \left(\frac{A}{Q}\right)_{cor} = \frac{A}{Q} \cdot f, \tag{13.3}$$

where the bracketed variables (a|b) correspond to their respective ion-optical matrix coefficients, given in units of either $\mathrm{m}^{-1}$ or $\mathrm{rad}^{-1}$. The centered path-length $l_{S2-S4,0}$ corresponds to its respective TOF calibration factor $path(21-41)$, which is the FRS path-length from scintillator SC21 to SC41 given as a time in picoseconds for the speed of light. It has the value $path(21-41) = 123304.0\ \mathrm{ps}$, see Sec. 12.3. The factor 1000 has to be introduced in order to account for correct unit conversions from $\mathrm{mm}$ to $\mathrm{m}$ and $\mathrm{mrad}$ to $\mathrm{rad}$ for the measured values $\alpha_{S2}$ and $x_{S2}$. Additionally, the factor $10^{-12}$ is used for the unit conversion of c from $\mathrm{m\,s}^{-1}$ to $\mathrm{m\,ps}^{-1}$. Thus resulting in the final correction function $f$ that is multiplied with the measured AoQ values in order to gain the corrected AoQ values.
Other correlations of AoQ with observables were studied as well, such as the measured vertical position $y_i$ and angle $\beta_i$ for i being either S2 or S4, the S4 position and angle $x_{S4}$ and $\alpha_{S4}$, the time-of-flight from SC21 to SC41 and SC22 to SC41, the momentum deviation from S2 to S4 $\delta_{S2-S4}$ as well as the velocity $\beta$, but once the path-length correction was introduced and the correlation of all the mentioned observables was cross-examined with the path-length corrected AoQ values, no further correlations could be found.

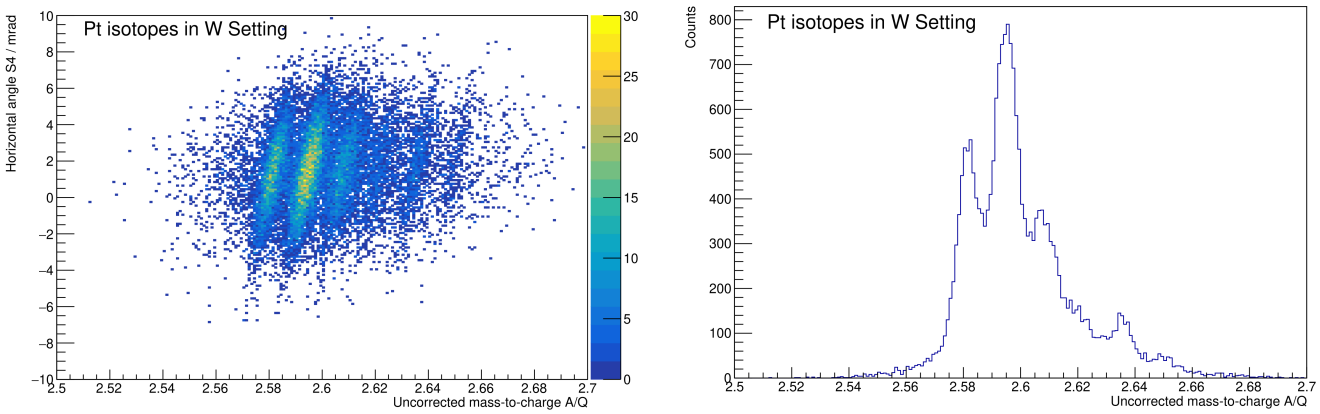


**Figure 13.2.:** Horizontal angle at S4 plotted over the uncorrected AoQ measured values (left plot) and AoQ measurement (right plot). These measurements are for platinum isotopes inside the $^{193}$W setting and no assignment of isotopes to peaks has been conducted at this point.

It can be seen in Fig. 13.2 (left plot) how the horizontal angle at S2 and uncorrected AoQ measurement are correlated with each other, and when projected unto the horizontal axis, the individual peaks start to overlap (right plot) such that a distinction between different isotopes becomes difficult. When applying the correction function, it is evident, that it the improves the identification as Fig. 13.3 (left plot) shows no correlation between the horizontal angle and AoQ values anymore and drastically reduces the overlap of individual isotopic peaks when projecting unto the horizontal axis. Consequently, the path-length correction method is applied to all AoQ measurements in all settings to improve the isotopic peak resolution.

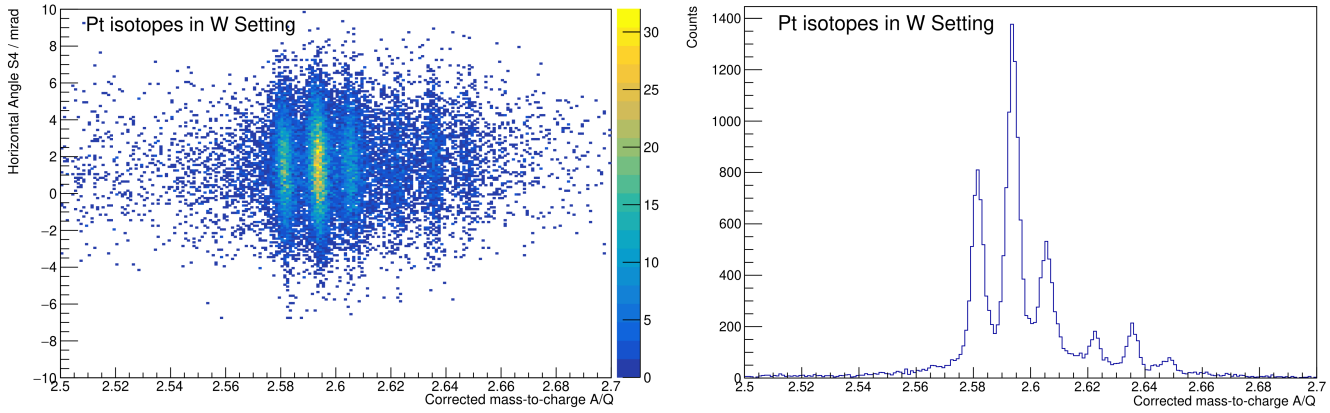


**Figure 13.3.:** Horizontal angle at S4 plotted over the corrected AoQ measured values (left plot) and AoQ measurement (right plot). These measurements are for platinum isotopes inside the $^{193}$W setting and no assignment of isotopes to peaks has been conducted at this point.

### 13.1.2. MUSIC Maximum Q Selection

Section 2.2 introduced the concept of charge identification by measuring the secondary fragment's energy-loss inside the gas-filled MUSIC detector, and Sec. 12.3 showed how the nuclear charge $Z$ is determined in the data analysis. So far the assumptions have been that the fragments are always fully stripped and that no charge-changing reactions occur. This only holds true for very high primary beam energies at the FRS as shown in Fig. 2.5. Realistically, as the $^{208}Pb^{+67}$ primary beam passes the SIS18 vacuum window, main target and stripper backing, its charge-state composition changes to 89.78% fully-stripped, 9.92% hydrogen-like and 0.3% others, according to GLOBAL. As projectile fragmentation occurs in parallel in the main target, secondary fragments populate several charge-states, other than the fully-stripped one ($\sim$ 94%), and as the fragments pass even more matter at S2, especially the thick aluminium degrader, the populations of other charge-states besides the fully-stripped one increases. As this particle cocktail is being transported towards the final focal plane S4 and deposit their energy-loss inside the MUSICs, the fragments are identified by their charge-state $Q$ instead of their nuclear charge $Z$. Furthermore electron-pickup or –loss can occur within the MUSICs, thus leading to an admixture of more charge-states. In order to prevent this reaction channel from happening within the MUSICs, the primary beam energy and thus secondary fragment energy can be increased and additionally a stripper foil inbetween the two MUSICs can be used. The choice of settings was already discussed in Sec. 12.2. Figure 13.4 shows the position-corrected

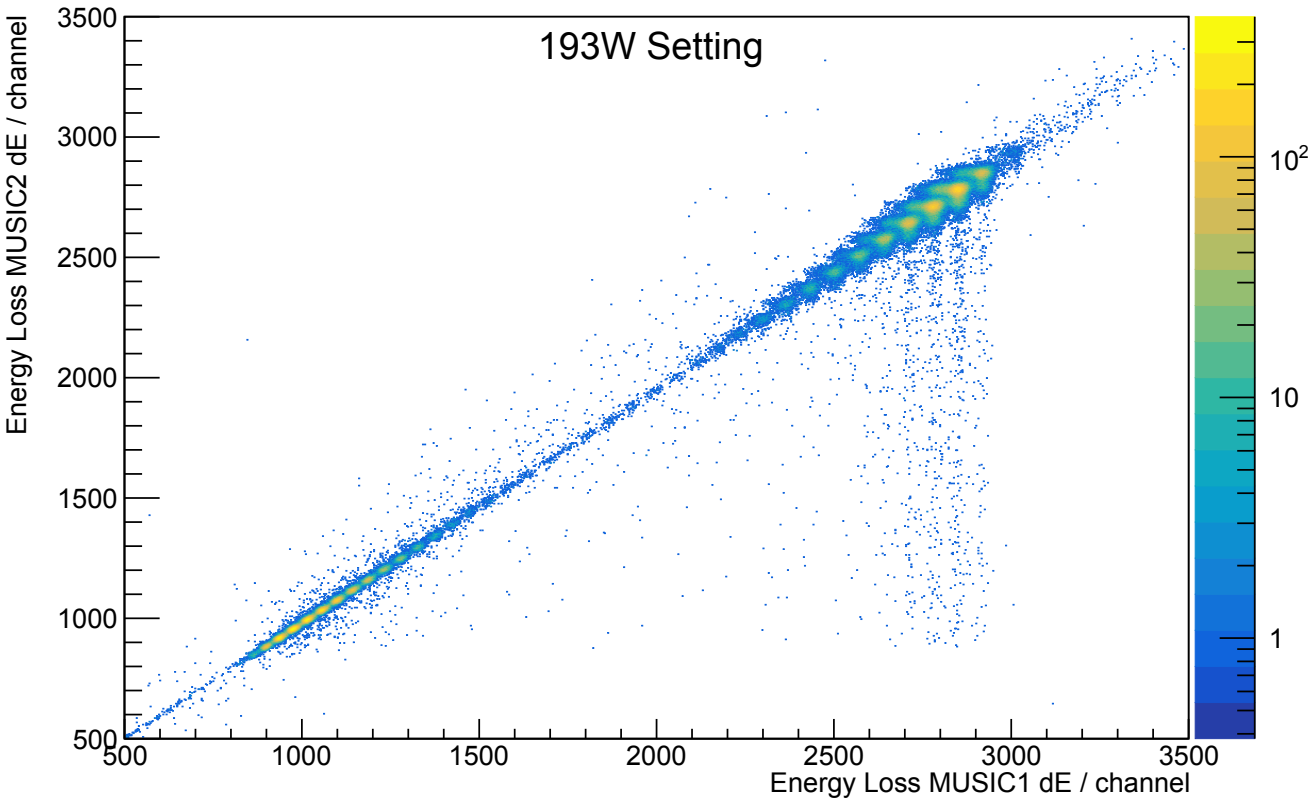


**Figure 13.4.:** Plot of $dE_{xc}$(MUSIC2) over $dE_{xc}$(MUSIC1) for the $^{193}$W setting. The two separate regions corresponding to fission and projectile fragments are visible here. The ejectiles produced primarily in fragmentation can be found for energy-depositions above channel number 2000 inside both MUSICs.

energy-loss $dE_{xc}$(MUSIC2) of MUSIC2, see Sec. 12.3, over the same observable $dE_{xc}$(MUSIC1) of MUSIC1, it becomes apparent that fragments, which do not change their electron configuration within one of the MUSICs are situated along the main line and show a very similar energy-deposition in both MUSICs. Fragments which change their charge-state show a different energy-deposition in one of the MUSIC detectors, depending on where the change occurred, and are situated next to the main line. Thus, in order to clean up charge-changing processes in the MUSIC detectors from the ID plot, a selection can be defined, which encapsulates all these events (see Fig. 13.5) and in order to assign the correct charge-state. The maximum charge $Q_{max}$ of one fragment in either MUSIC detector is now introduced, instead of Z, from now on, which is the charge determined by the maximum energy-loss of one fragment within both MUSICs. As such Eq. (12.7) changes to

$$Q_{max} = max(Z(MUSIC1), Z(MUSIC2)), \tag{13.4}$$

Where $Z(MUSIC1)$ and $Z(MUSIC)$ remain defined as previously established in Sec. 12.3. It can be seen in Fig. 13.6, how the redefinition from $Z(MUSIC1)$ to $Q_{max}$ improves the quality of the ID plot.

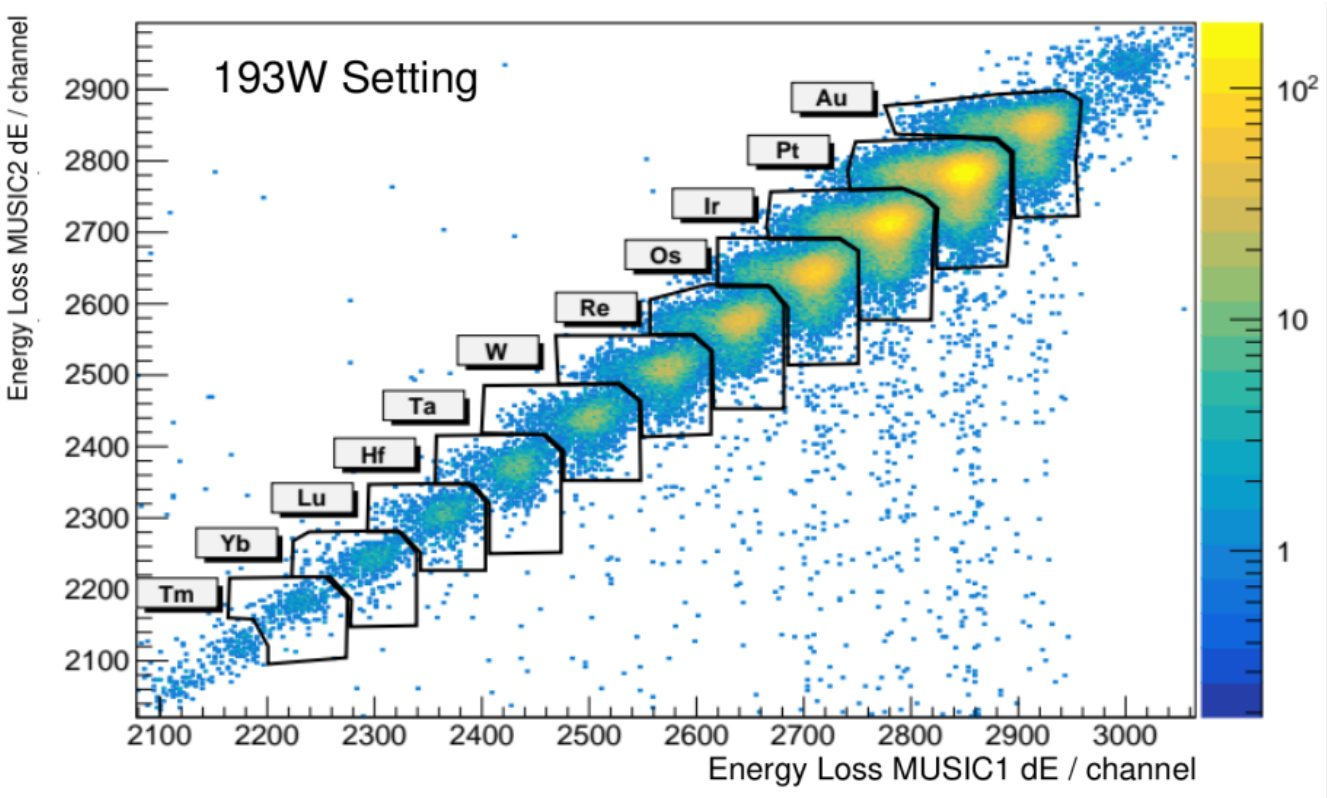


**Figure 13.5.:** Plot of the position-corrected energy-losses in MUSIC2 over MUSIC1 for the $^{193}$W setting, zoomed into the projectile fragments. The black line shows how each selection was defined for each element. It becomes apparent, that the more intense one elemental peak is the more charge-changing reactions occur.

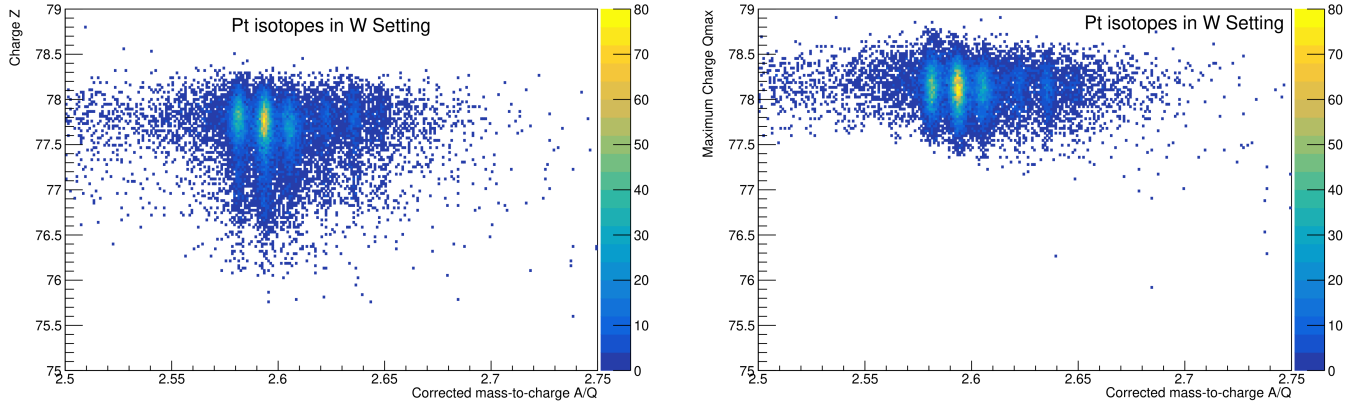


**Figure 13.6.:** MUSIC1 Z plotted over AoQ corrected (left plot) compared to $Q_{max}$ plotted over AoQ corrected with the selection from Fig. 13.5 applied (right plot) for platinum. On one hand $Q_{max}$ is shifted slightly above 78 whereas the original definition was slightly below 78, due to different calibration coefficients for each detector, and on the other hand 77+ and 76+ charge-states get correctly assigned to 78+ in (right plot).

### 13.1.3. Degrader 0e0e Charge State Selection

The selection of the maximum charge measured by both MUSIC detectors helps to produce a cleaner identification of isotopes. But it does not yet remove charge-states that were previously produced, mainly in either the target or der degrader wedge. In order to identify unwanted charge-states and only select fully stripped ions, the energy-loss inside the S2 degrader wedge can be measured and utilized to differentiate between different charge-states passing through this matter. This observable can be calculated in the following way

$$B\rho_{TA-S2} = B\rho_{TA-S2,0} \cdot \left(1 - \frac{x_{S2}}{(D_{TA-S2})}\right), \tag{13.5}$$

$$\gamma_{TA-S2} = \sqrt{1 + \left(\frac{c}{u \cdot 10^6} \cdot \frac{B\rho_{TA-S2} \cdot Q}{A}\right)^2}, \tag{13.6}$$

$$dE_{deg} = (\gamma_{TA-S2} - \gamma_{S2-S4}) \cdot \frac{A}{Q} \cdot Q_{max}, \tag{13.7}$$

where $dE_{deg}$ is the energy-loss inside the degrader, which is determined by the difference in $\gamma$ between the stages TA-S2 and S2-S4, as well as AoQ and $Q_{max}$ as determined earlier. Using either the corrected or uncorrected mass-to-charge ratio does not yield a difference that is significant enough, therefore the uncorrected one is being used. The Lorentz factor $\gamma_{TA-S2}$ can be derived from the general $B\rho$ expression, see 2.4. Similarly to 2.9, $B\rho_{TA-S2}$ can be derived from the ion-optical transfer matrix as it depends on the horizontal position at S2 $x_{S2}$ and the corresponding dispersion coefficient $D_{TA-S2}$, introduced in 4.2. Figure 13.7 shows the plot of the observable $dE_{deg}$ over the maximum charge $Q_{max}$.

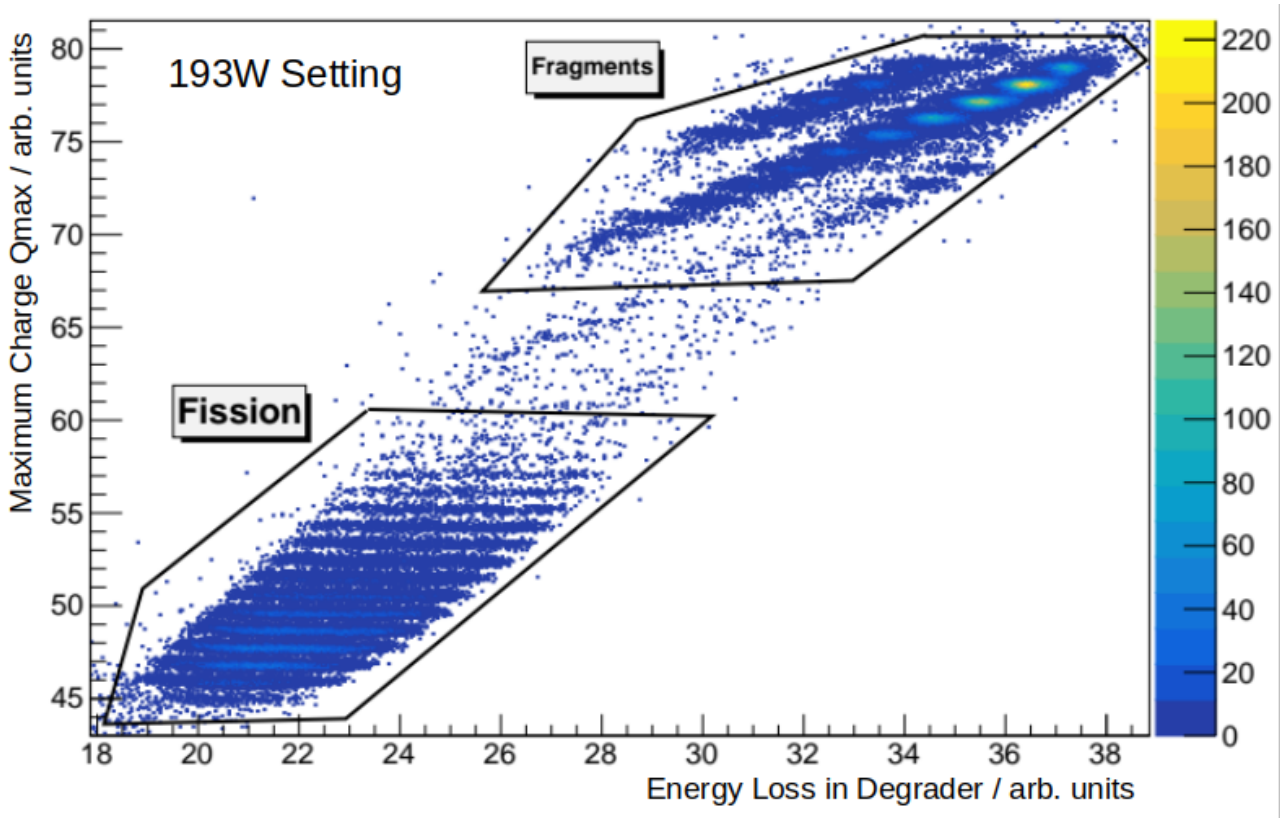


**Figure 13.7.:** Maximum MUSIC charge-state $Q_{max}$ plotted over the energy-loss in the degrader $dE_{deg}$ for the $^{193}$W Setting. Similar to Fig. 13.1, the two regions corresponding to fission and projectile fragments are visible in this setting, as well, but contrary to Fig. 13.1 there are three separate distributions corresponding to different charge-states of fragments.

A new nomenclature to denote charge-states in the different stages of the FRS will be introduced now in the notation NeMe, where N and M stand for the number of electrons in the stage TA-S2 and S2-S4 respectively. According to this nomenclature, fully stripped isotopes throughout the whole FRS are denoted as 0e0e, hydrogen-like in TA-S2 and fully-stripped in S2-S4 as 1e0e and vice-versa, with higher charge-states, helium-like 2eMe or Ne2e, et cetera being possible. Figure 13.8 shows three main regions that can be identified. The main region in the middle covers the greatest range $69 \leq Z \leq 79$ and is attributed to the fully-stripped isotopes in both stages as well as 1e1e isotopes, whose distribution overlaps with the 0e0e nuclei. A better separation could have been achieved in this case with the use of a thicker S2 degrader setup, but it would have also increased the population of undesired 0e1e and 1e0e charge-states and the probability of unwanted charge-changing reactions inside the MUSIC detectors.
It will be shown in 13.2, that it is possible to distinguish between 0e0e and 1e1e isotopes by comparing the S2 and S4 position spectra of each isotope and using GLOBAL and LISE++/MOCADI to calculate the 1e1e admixture and transport. In the given plot the relative abundance in each region is 0.8829(70) in (0e0e+1e1e), 0.1036(16) in (0e1e) and 0.0111(1) in (1e0e). This agrees with GLOBAL and LISE++ expectations for platinum in this setting with 0.8824 in (0e0e+1e1e), 0.1175 in (0e1e) and an admixture of 0.0249 (1e1e) in (0e0e+1e1e), but changes for lower $Z$ isotopes like tantalum to 0.9952 in (0e0e+1e1e), 0.0048 in (1e0e) and 0.0113 (1e1e) in (0e0e+1e1e).

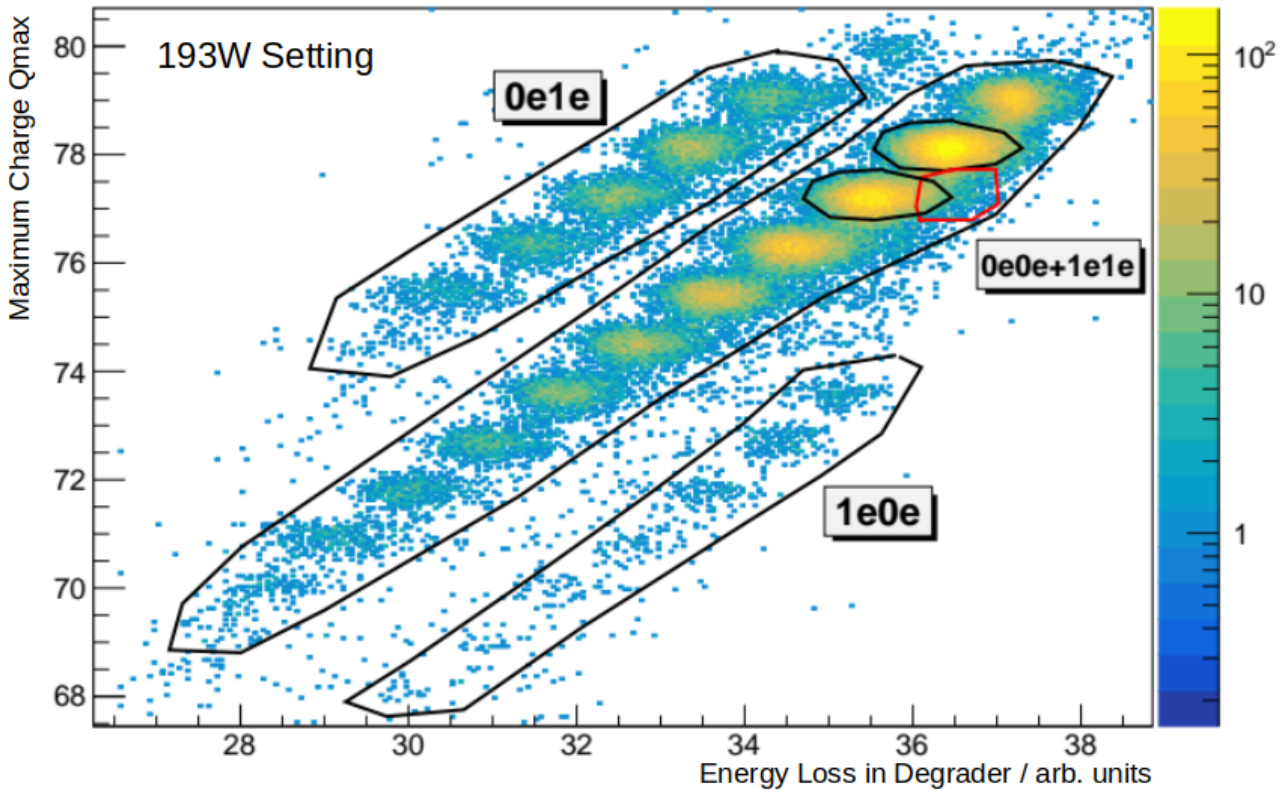


**Figure 13.8.:** Maximum MUSIC charge-state $Q_{max}$ plotted over the energy-loss in the degrader $dE_{deg}$ for the $^{193}$W setting. The main regions (0e0e+1e1e), (0e1e) and (1e0e) are immediately visible and cleanly separated. Separating the 1e1e and 0e0e events requires an additional separation step via position spectra comparison. The black circles correspond examplarily to 0e0e platinum and 0e0e iridium and the red circle to 1e1e platinum.

The previous Fig. 13.8 utilized $dE_{deg}$ without AoQ path-length corrections or $Q_{max}$ applied. Fig. 13.9 shows a comparison of both $dE_{deg}$ without and $dE_{deg,cor}$ using corrected observables in Eqs. 13.7 and 13.6 respectively. In (right plot) the peaks are slightly shifted towards lower $dE_{deg,cor}$ with a positive skewness but no apparent separation of 0e0e and 1e1e charge-states. Thus, method (left plot) will be continued to be used for analysis purposes. In order to improve the ID plot, a selection according to regions is introduced. Of special interest is the (0e0e+1e1e) region, since it has the highest statistics for all charge-states. Applying this selection to the ID plot produces Fig. 13.10 (right plot), where peaks around the points ($AoQ = 2.62$, $Z = 77$) as well as (2.52,72) are removed, that could be mistaken for new isotopes. All further ID plots will have the (0e0e+1e1e) selection or a selection on the individual 0e0e peak in Fig. 13.8 applied without further mention. The next step is to improve the isotope peak-to-background ratio in the ID plots, in order to allow the unambiguous identification of new isotopes with high AoQ values and very low count production rates.

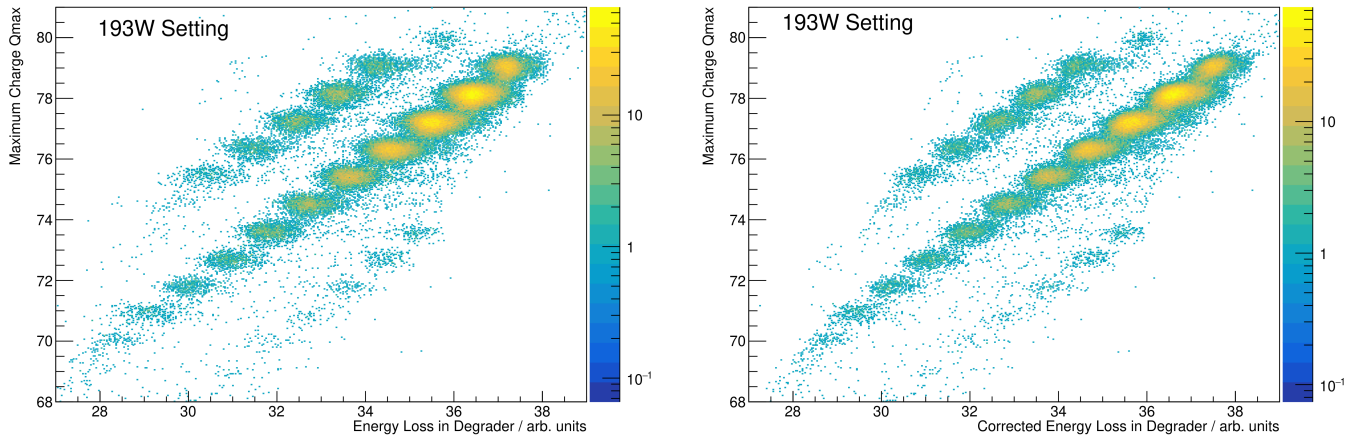


**Figure 13.9.:** Maximum MUSIC charge-state $Q_{max}$ plotted over the energy-loss in the degrader $dE_{deg}$ (left plot) and $Q_{max}$ plotted over $dE_{deg,cor}$ for the $^{193}$W setting (right plot), for $68 \leq Q_{max} \leq 80$. Utilizing $dE_{deg,cor}$ does not provide any additional separation of 0e0e and 1e1e isotopes.

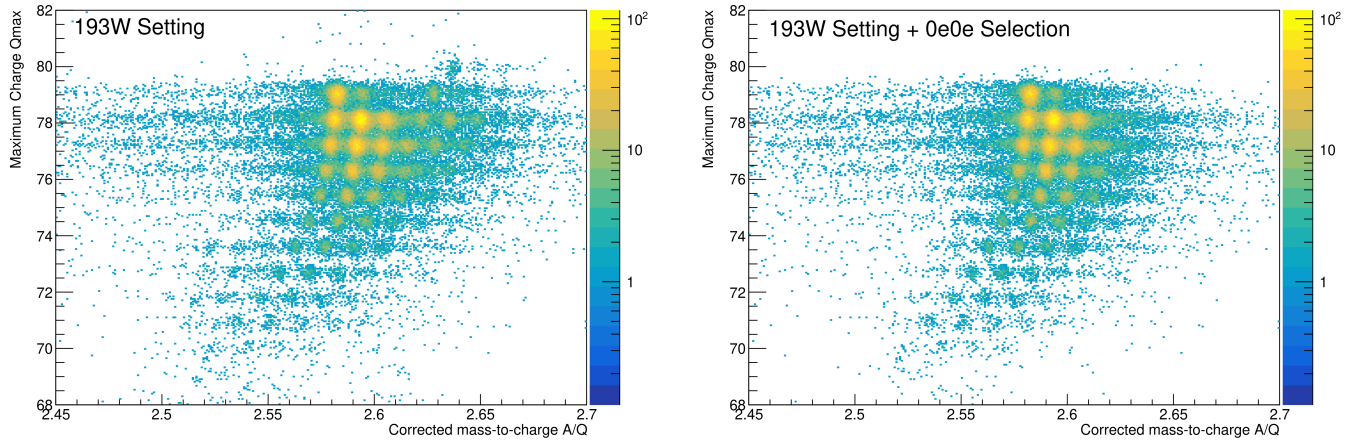


**Figure 13.10.:** ID plot with no (left plot) and ID plot with 0e0e selection (right plot) for the $^{193}$W setting, for $68 \leq Q_{max} \leq 80$.

### 13.1.4. TPC Event Clean-Up

One method to identify faulty events and reduce the background in the ID plot is via the checksum calculated for each TPC. Since each TPC performs four vertical drift-time measurements and two horizontal time difference measurements, each TPC possesses four checksums that are calculated in the following way

$$CSUM_{i,j} = lt_{i,1} + rt_{i,1} - 2dt_{i,j} \quad \text{for } (j = 0, 1), \tag{13.8}$$

$$CSUM_{i,j} = lt_{i,2} + rt_{i,2} - 2dt_{i,j} \quad \text{for } (j = 2, 3), \tag{13.9}$$

where $CSUM_{i,j}$ is the checksum of TPC i and drift-time channel j, where $0 \leq i \leq 3$ stands for TPC23/24/41/42 in the experiment and $0 \leq j \leq 3$. The quantities $lt_{i,1}$ and $rt_{i,1}$ are the left and right delay-line time of the front face of each TPC, whereas $lt_{i,2}$ and $rt_{i,2}$ represent the back face. Finally, $dt_{i,j}$ is the drift-time channel j of TPC i. By definition, the checksum clusters correctly assigned and processed events from the DAQ and Go4 together such that a clear peak appears. Should the rate at one of the TPCs have been too high, the electronics setup incorrect or the detector damaged, then events would have checksum values outside of said peak. This can be understood, when considering a well centered (0 $\mathrm{mm}$), aligned (0 $\mathrm{mrad}$), focused and low-intensity ($<$ 100 $\mathrm{kHz}$) primary beam inside the FRS. The resulting left and right delay-line as well as the drift-time channels will show a narrow Gaussian-shaped distribution, which results in a similarly narrow distribution for the checksums. When moving the primary beam horizontally, vertically or changing its angle, the resulting distribution moves or distorts respectively in the checksum space. Should the beam be defocused or a setting be used that produces a plethora of secondary fragments covering the whole TPC aperture, then the resulting checksum distribution widens according to the introduced individual particle's angles.

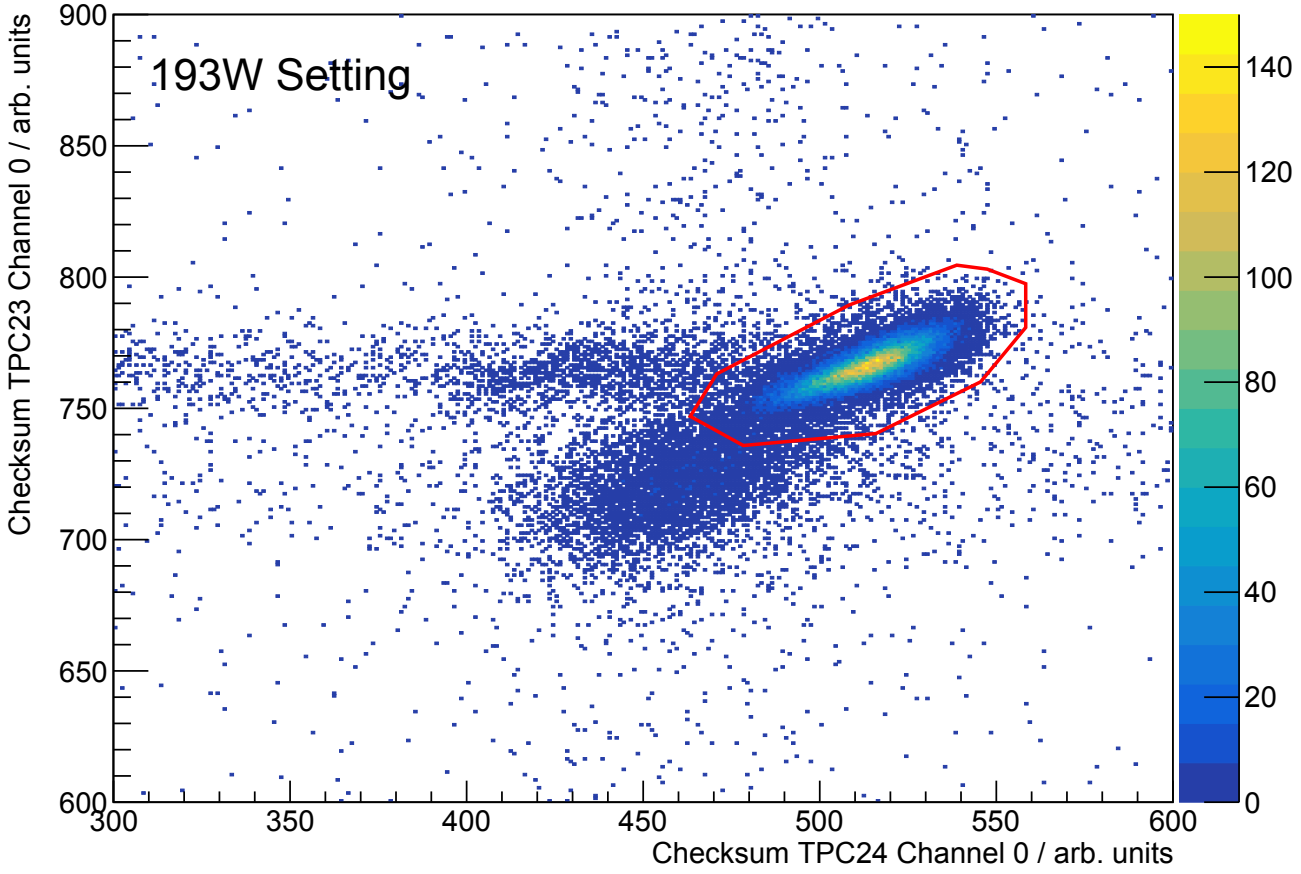


**Figure 13.11.:** Exemplary checksum plot for TPC23 checksum plotted over TPC24 checksum for channel 0. The peak is clearly visible in the spectrum, but also invalid events outside of it occur. All events inside the red selection are chosen for further identification.

If the incident particle intensity is low enough, then trajectories can be correctly assigned to its corresponding event. As the beam intensity rises, events can receive misassigned TPC timing information from other heavy-ions, thus checksum events outside of the main peak start to occur. Figure 13.11 shows an exemplary

checksum spectrum. All events from within the main peak are chosen for further analysis. This process can be repeated for all other TPCs and their checksums, 16 in total, to refine the selection of valid events suitable for identification. The Final ID plot can be seen in Fig. 13.12, which shows a significant reduction in background events for the given setting.

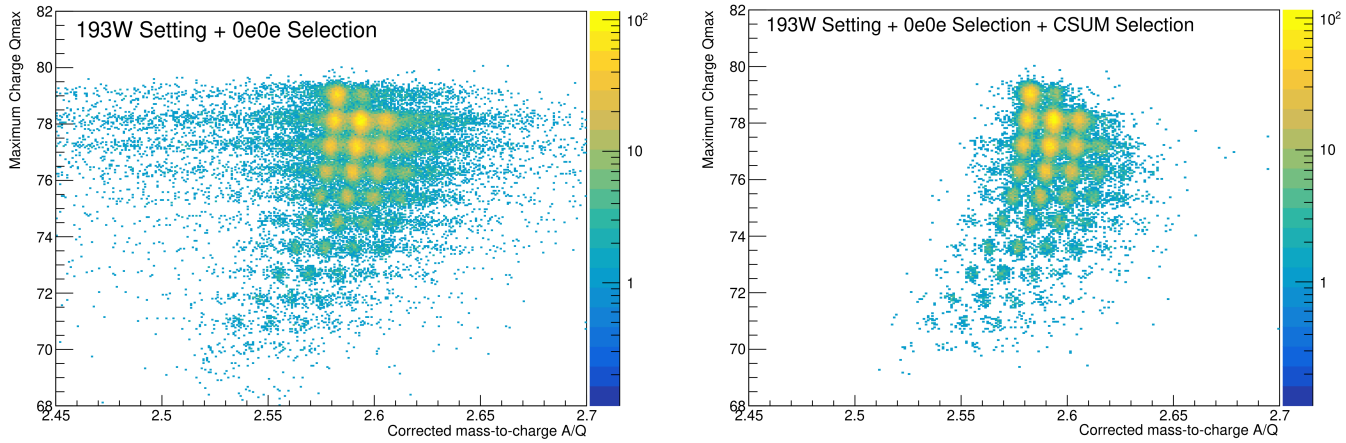


**Figure 13.12.:** ID plot with previous selections (left plot) and ID plot with additional checksum selections (right plot) for the $^{193}$W setting, zoomed into the projectile fragments. A visible reduction of background events can be achieved by applying checksum cuts. This is paired with a reduction of events from 61318 to 35876 with the aforementioned selections for this subset of data.

### 13.1.5. ID Anchoring and Repositioning

It can occur for time-of-flight and AoQ measurements that the ID plot shows a bend in the spectrum of identified isotopes, even though a linear grid-like structure is expected. This is due to the plastic scintillators, which depending on age and sustained radiation damage change their light collection properties depending on the position at which the isotopes hit the material. This is expected to lead to an asymmetric light output and non-linear light dispersion throughout the material to such a degree, that the time-of-flight measurement deviates from the theoretically expected values. Additionally the PMTs play also a role in such a way that when the incident particle is asymmetrically distributed along the face of the scintillator, one side can produce wrong timing information, due to high-rate saturation. For more information see App. G. This issue can be easily corrected by properly anchoring and assigning the isotopes in the ID plot, by mass-tagging cross measurements from the FRS Ion Catcher [97], comparison with LISE++/MOCADI simulations and identifying the crossing of the $N = 126$ line, which should not be possible for isotopes produced via projectile fragmentation. However, quasi-elastic charge-exchange nucleon-nucleon collisions at these energies primarily proceeding via $\Delta$-excitations [107, 108] may contribute to the creation of $N = 127$ isotones. It can be estimated using an INCL+ABLA [109, 110] implementation in Geant 4 [111, 112] that the cross section for said reaction in the specific channel of $Pb^{208}$ to $Re^{202}$ is 80 $\mathrm{nb}$.
The first setting to anchor is a lead setting. For this purpose, setting number five from the TOF calibration, see Sec. 12.3, is chosen, which utilizes the S2 degrader energy-loss to provide an additional time-of-flight calibration point, but also acts as a secondary fragmentation target for the primary beam. Instead of focusing on the fragmentation ejectiles, the lead charge-states $Pb^{82+}$, $Pb^{81+}$ and $Pb^{80+}$ are considered due to their high abundance. Fragments are cut out, and the previously discussed selection methods are

applied. The resulting lead charge-state peaks are then shifted via an offset in $Q_{max}$ and AoQ into their correct theoretical positions AoQ and $Q_{max}$ repositioned. The resulting ID plot can be seen in Fig. 13.13 and the corresponding reposition coefficients can be found in App. I.1.

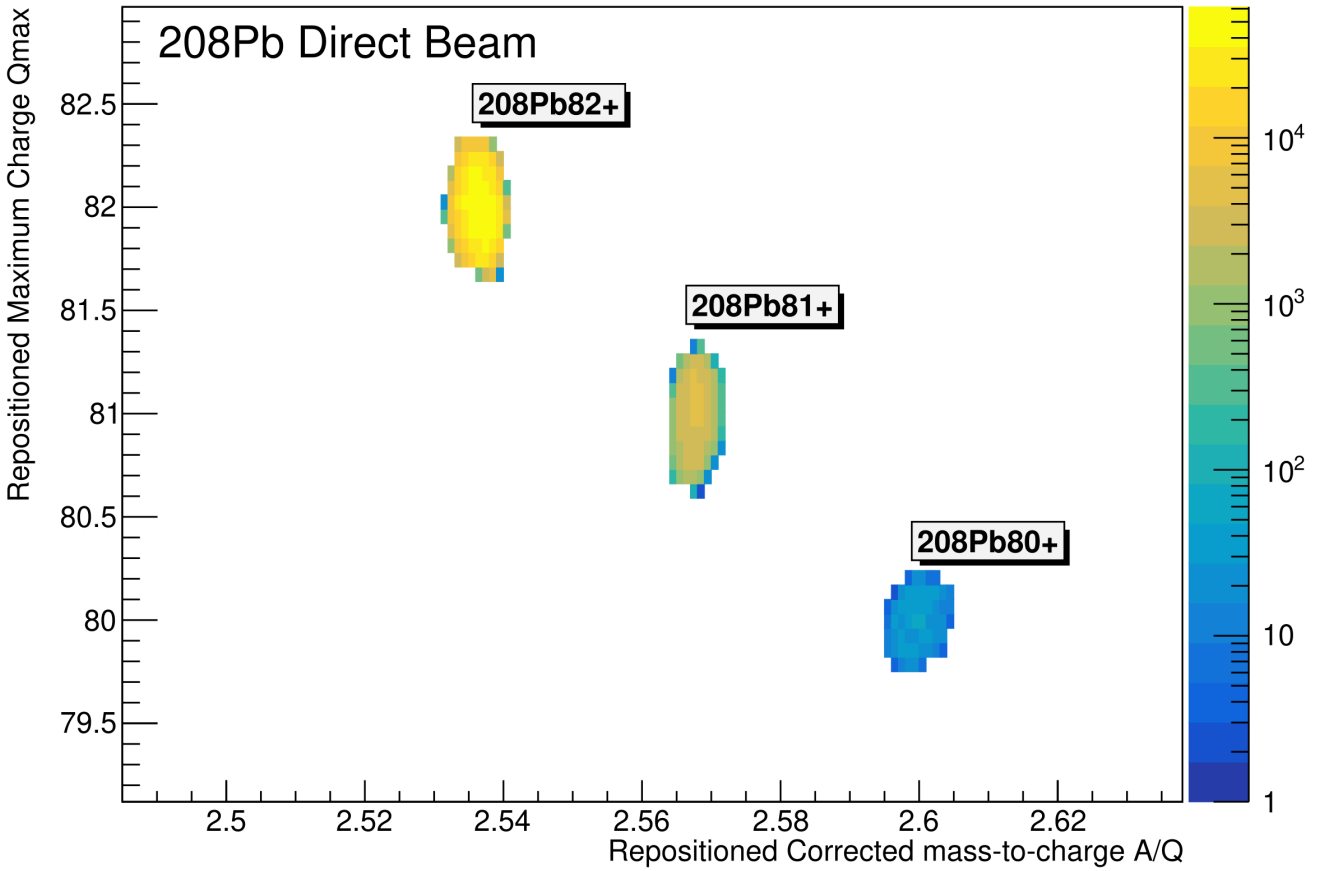


**Figure 13.13.:** Repositioned identification plot for $^{208}$Pb charge-states $82+$, $81+$ and $80+$. The repositioning was achieved by simply adding an offset unto the $Q_{max}$ and AoQ values.

### $^{205}$Au Setting

The $^{205}$Au setting is considered next. In order to determine which peak corresponds to which isotope in this case, mass-tagging with the FRS Ion Catcher will be used together with LISE++ predictions. An ID plot without assigned isotopes can be seen in Fig. 13.14. It is visible that the $Q_{max}$ for all isotopes is slightly increased and stems from the FRS MUSIC charge calibration, see Eq. (12.7), which only incorporates a simple square-root dependency, unlike the Bethe-Bloch equation, see Eq. (2.10). Thus only the charge of the primary beam $Z_{primary}$ is exactly determined and all other charges are identified by counting down and their measured values tend to be higher can their actual values the bigger $\Delta Z$ is. Due to this, it is safe to say that the row of isotopes between $79 \leq Z \leq 80$ belongs to gold. When comparing the transmission simulation for $^{204}$Au and $^{205}$Au with the assumptions from Sec. 12.2, both fully-stripped, LISE++ calculates a yield at S4 of 29.1 pps for $^{204}$Au and 20.3 pps for $^{205}$Au, which corresponds to an increased yield of factor 1.4335 for $^{204}$Au. When comparing to the peaks in Fig. 13.14, the strongest peak in the gold line shows a total count of 43039(207) and the one next to it 30022(173). Thus an increased yield for the strongest

peak of 1.434(15) can be deduced, which corresponds to the predicted ratio of LISE++. This gives one indication for the anchoring such that the strongest peak correlates to $^{204}$Au and the second strongest to $^{205}$Au, but as mentioned before, the mass-tagging was also utilized. For this method, the S4 aluminium wedge was set to a thickness such that mean-range bunching occurs and the gold isotopes are stopped

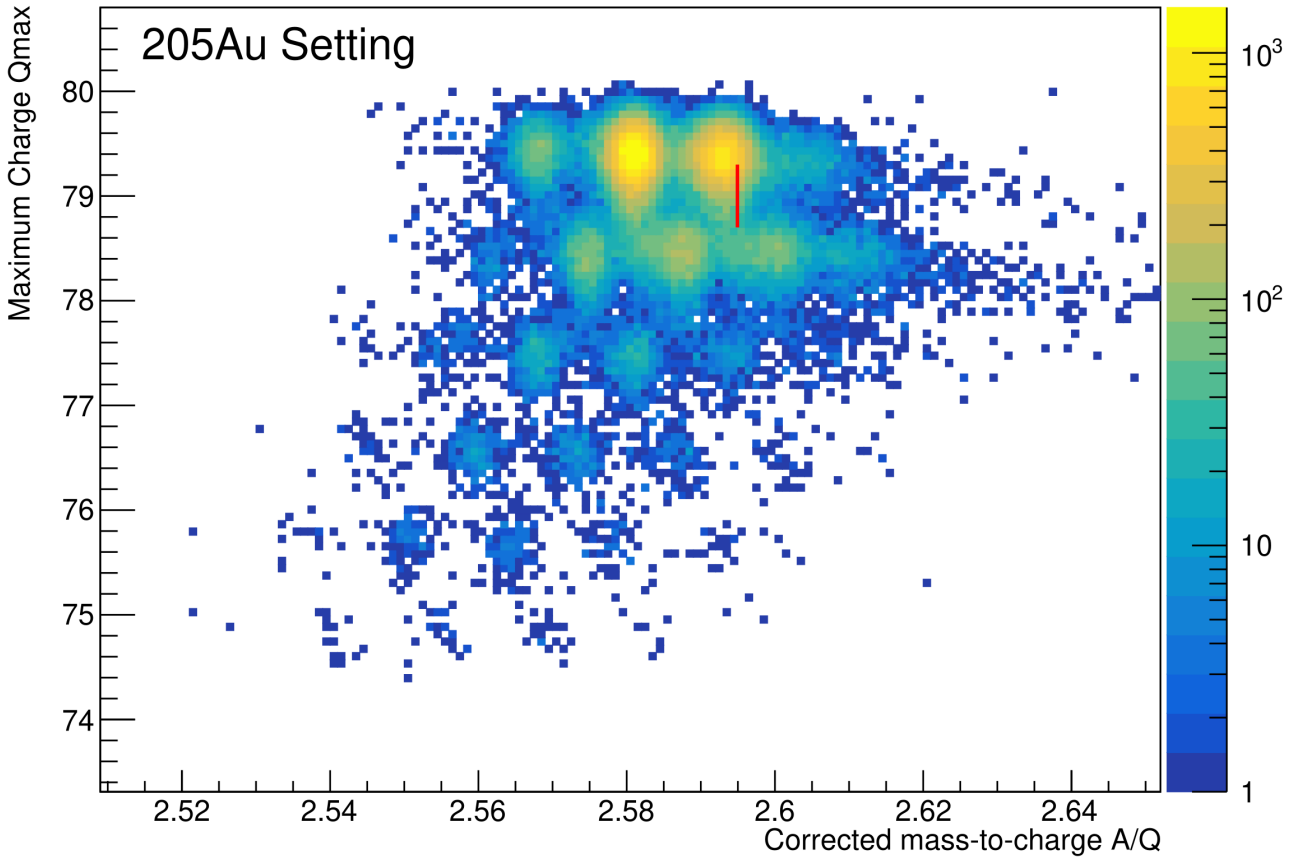


**Figure 13.14.:** ID plot for the $^{205}$Au setting with all previously introduced concepts for correction and clean-up applied. A positive shift in $Q_{max}$ together with a compression can be seen that needs to be repositioned. Peaks have not yet been assigned to isotopes. The isotope of interest for the $^{205}$Au setting is marked with a red line.

within the cryogenic stopping cell. Additionally, the S4 slits were closed according to the expected positions of gold isotopes at S4, see Fig. 13.15, the stopped isotopes masses were measured. It was possible to clearly measure $^{204}$Au masses and tag the correct isotope, see Fig. 13.16, that belongs to the peak of highest intensity. All other isotopes can then be identified by moving left $(A-1)$, right $(A+1)$, down-left $(Z-1,A-3)$ or up-right $(Z+1,A+3)$ within the ID plot. With this method, all other isotopes can be identified and their positions can be repositioned. For repositioning a second-order polynomial is utilized to reposition the $Q_{max}$ values and for each row a linear repositioning function is applied to shift the respective row into the correct positions. The final result can be seen in Fig. 13.17 and the corresponding repositioning function coefficients can be found in App. I.2. The remaining background in the ID plot as a result of the TPC event clean-up method, see Sec. 13.1.4, can not be fully removed due to the immense intensity of the secondary beam at S2, see discussion in App. H.

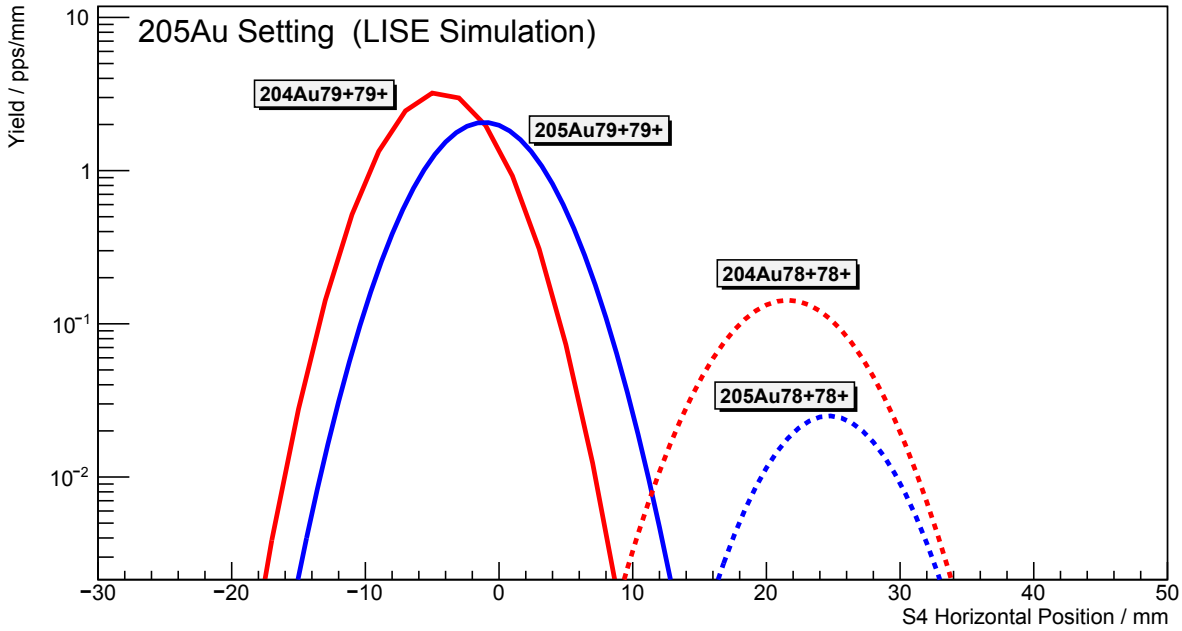


**Figure 13.15.:** Calculated yield by LISE++ for $^{205}$Au (blue) and $^{204}$Au (red) at the focal plane S4 as a function of position for both fully-stripped (solid line) and hydrogen-like (dashed line) isotopes.

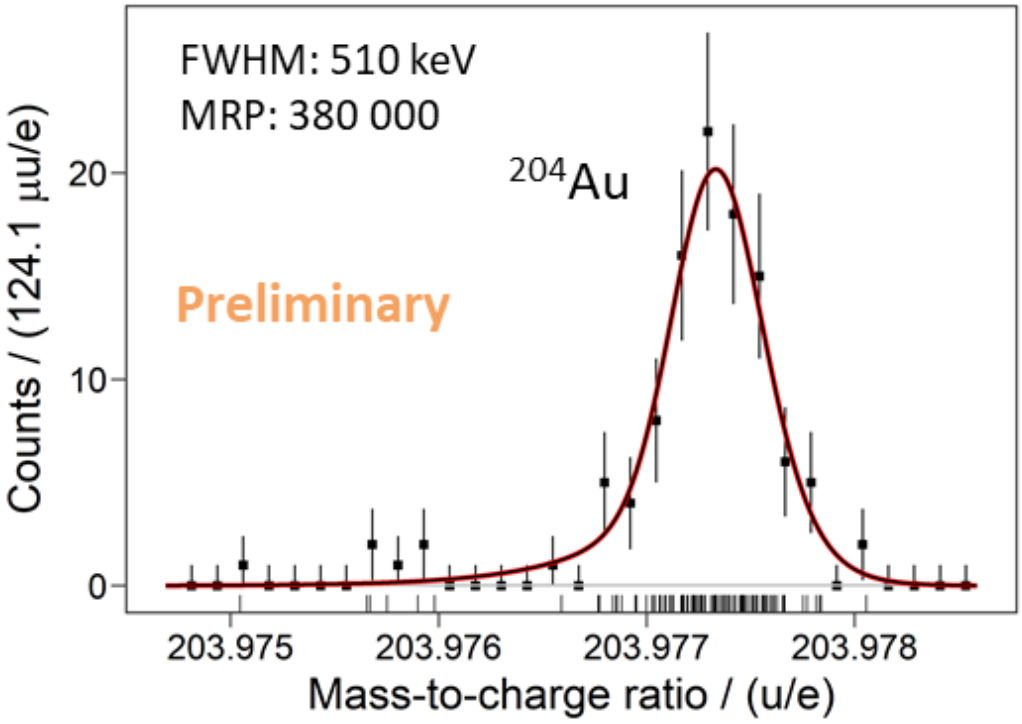


**Figure 13.16.:** Mass measurement inside the Ion Catcher's MR-TOF-MS, taken from [29, 113], which shows the mass-to-charge ratio on the x-axis and the counts on the y-axis. The $^{204}$Au isotope could be clearly identified by closing the S4 slits to -8 mm and 12 mm.

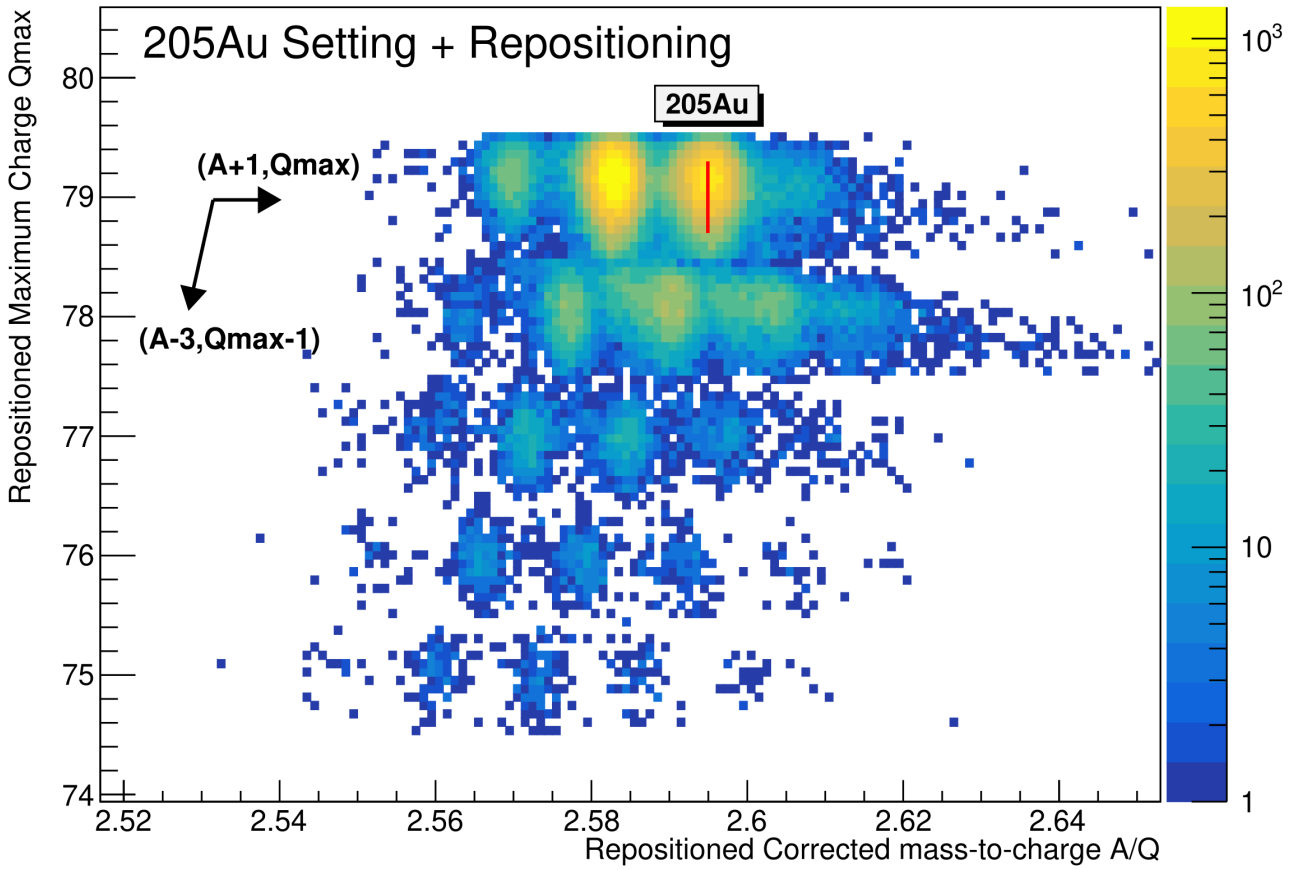


**Figure 13.17.:** Repositioned ID plot for the $^{205}$Au setting with the peak of strongest intensity correcty assigned to $^{204}$Au. The isotope of interest for the $^{205}$Au setting is marked with a red line.

**$^{193}$W Setting**

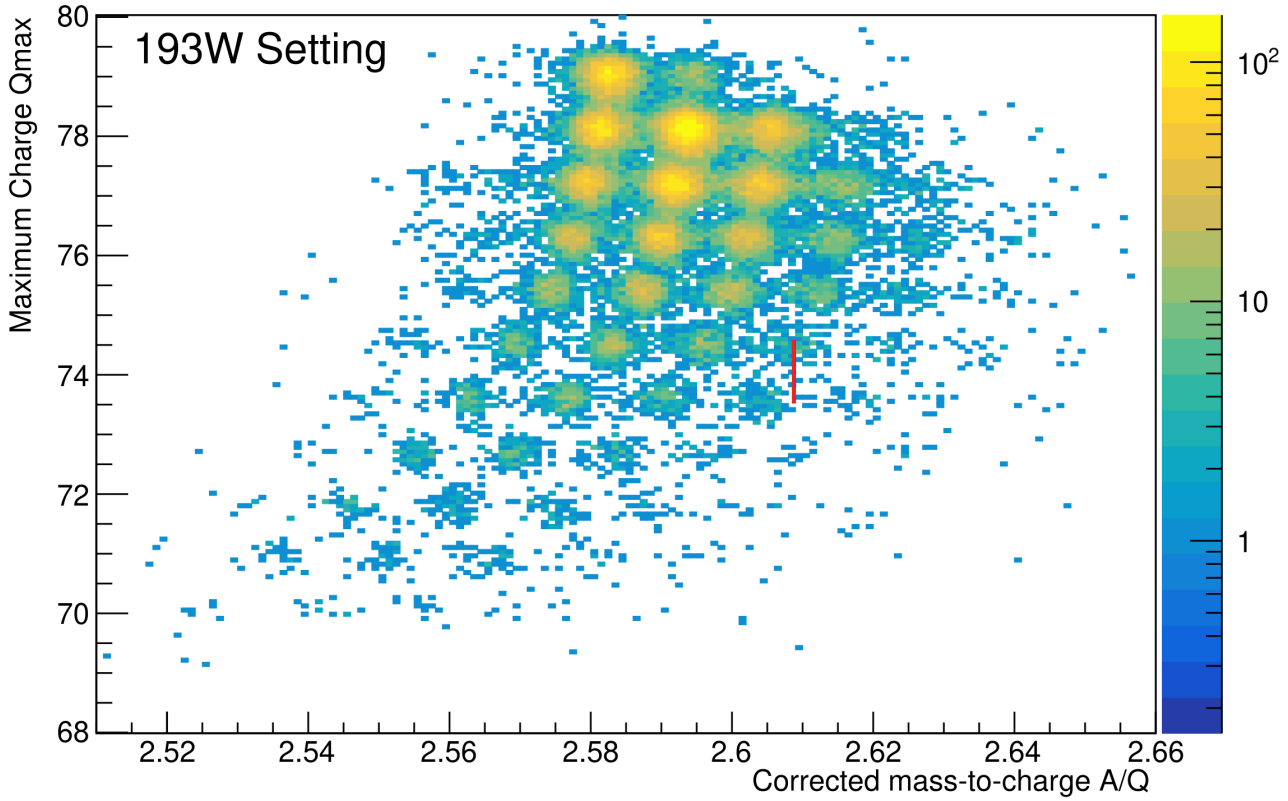


**Figure 13.18.:** ID plot for the $^{193}$W setting with all previously introduced concepts for correction and clean-up applied. A positive shift in $Q_{max}$ together with a compression can be seen that needs to be repositioned. Additionally, a bend along the AoQ axis can be observed. This is discussed in App. G. Peaks have not yet been assigned to isotopes. The isotope of interest for the $^{193}$W setting is marked with a red line.

The same method will be applied for the anchoring of the ID plot in the $^{193}$W setting. Assuming that the isotopic peak in the tungsten line closest to the theoretical position of the isotope of interest corresponds to $^{193}$W, see Fig. 13.18, which is derived from the previously described calibration methods, see Sec. 12.3, the same method of counting isotopes can be applied as previously in the $^{205}$Au setting. In this case, it results that the strongest peak in the line of iridium isotopes would correspond to $^{200}$Ir. This was confirmed by mass-tagging with FRS Ion Catcher and iridium can be easily identified by applying the dE selection from Fig. 13.5. The corresponding mass measurement with the FRS Ion Catcher shows a yield of 4 counts for $^{200}$Ir as the only iridium isotope [29]. Furthermore, LISE++ calculations result in a yield of 8.05 pps for $^{200}$Ir, 1.9 pps for $^{199}$Ir and 4.02 pps for $^{201}$Ir as well as a subsequent reduced yield ratio of 0.236 for $^{199}$Ir and 0.499 for $^{201}$Ir. From the ID it is possible to derive 2104(46) counts for $^{199}$Ir, 3868(62) counts for $^{200}$Ir and 2318(48) counts for $^{201}$Ir, resulting in yield ratios of 0.544(21) for $^{199}$Ir and 0.599(22) for $^{201}$Ir compared to $^{200}$Ir. Even though the yield ratios are deviating from their predicted values it is possible to recognize the trend that $^{199}$Ir and $^{201}$Ir have lower yields than $^{200}$Ir as well as $^{201}$Ir showing a higher yield compared to $^{199}$Ir. Thus, $^{200}$Ir can be identified as the highest peak inside the iridium line, and all other peaks can be assigned to their respective isotopes via repositioning functions, see App. I.3, and resulting in

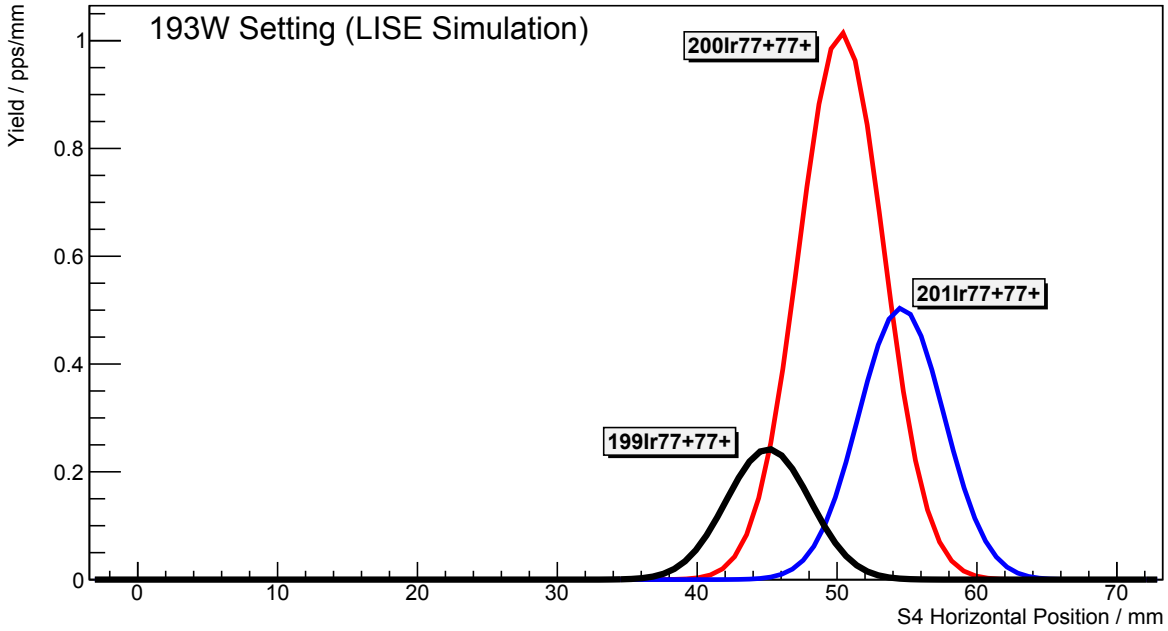


**Figure 13.19.:** Calculated yield by LISE++ for fully-stripped $^{199}$Ir (black), $^{200}$Ir (red) and $^{201}$Ir ions (blue) at the final focal plane S4 as a function of position.

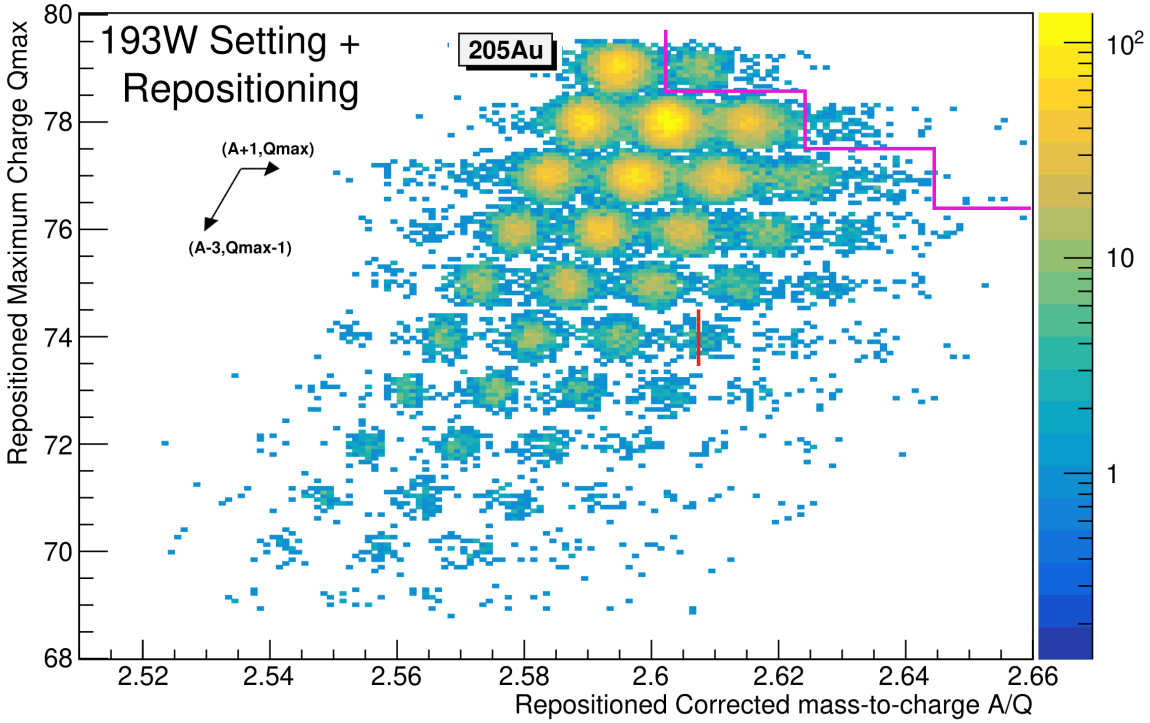


**Figure 13.20.:** Repositioned ID plot for the $^{193}$W setting with the peak of strongest intensity for iridium correctly assigned to $^{200}$Ir and the strong peak in gold assigned to $^{205}$Au. The isotope of interest for the $^{193}$W setting is marked with a red line and the crossing of the $N = 126$ line is represented with a fuchsia line.

Fig. 13.20. An additional hint is provided by the gold line of isotopes. Here, only two isotopes are visible, with one peak containing 3457(59) counts and the other 513(23) counts. This is a strong indication for the crossing of the $N = 126$ line from $^{205}$Au to $^{206}$Au, since it should not be possible to produce isotopes beyond the $N = 126$ from shear projectile fragmentation alone when using a $^{208}$Pb primary beam. Other processes are involved in the production of said isotopes and thus a sudden drop-off in yield is expected.

### $^{193}$Ta Setting

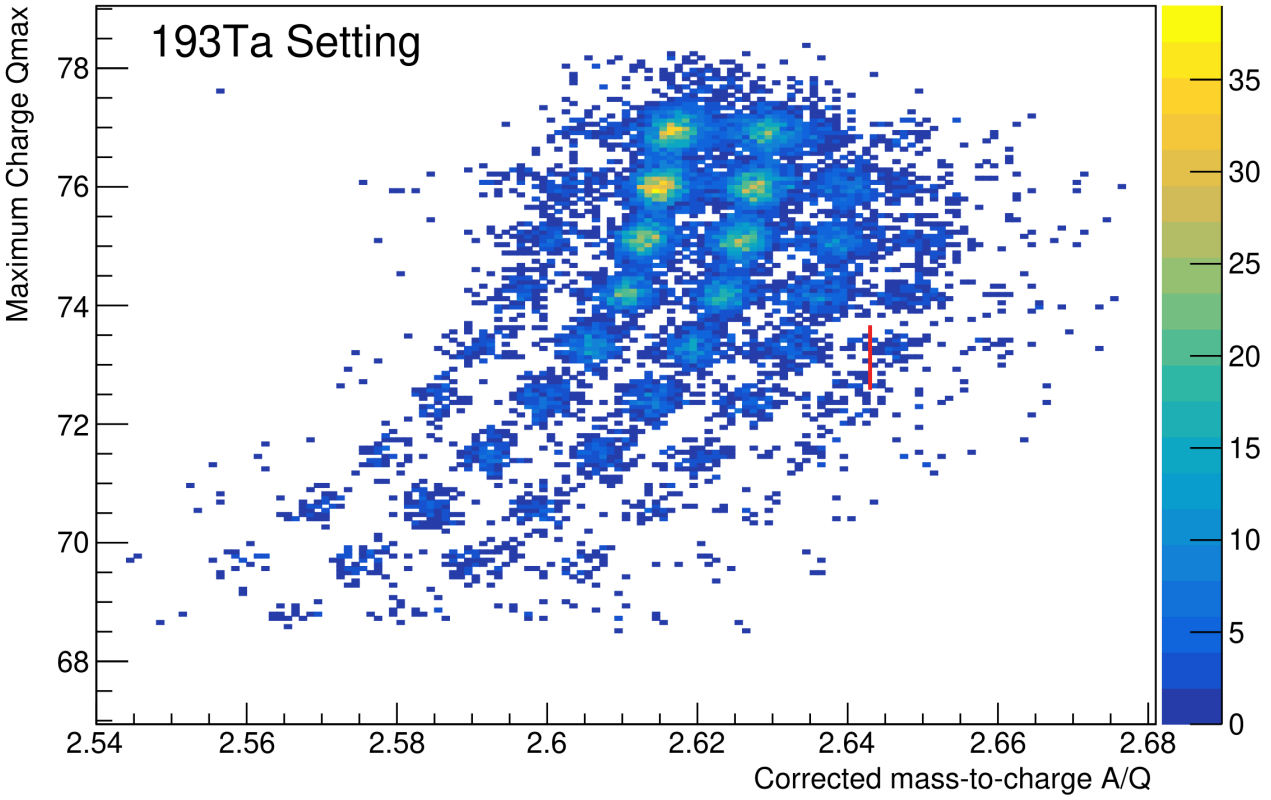


**Figure 13.21.:** ID plot for the $^{193}$Ta setting with all previously introduced concepts for correction and clean-up applied. A positive shift in $Q_{max}$ together with a compression can be seen that needs to be repositioned. Additionally, a bend along the AoQ axis can be observed. This is discussed in App. G. The isotope of interest for the $^{193}$Ta setting is marked with a red line.

For the tantalum setting, the FRS Ion Catcher was not available for mass-tagging due to technical issues. Instead the anchoring has to rely on the calibration and comparisons with estimated isotopic yields from LISE++ and the identification of the crossing of the $N = 126$ line. Figure 13.21 shows the corresponding ID plot for the $^{193}$Ta setting and similar to previous ID plots Fig. 13.14 and 13.18 a cutoff in isotope production for the highest $Q_{max}$ isotopes, 77 in this case, can be observed towards higher AoQ values. Counting from the presumed isotope of interest $^{193}$Ta towards iridium isotopes, shows that the two strong iridium peaks correspond to $^{202}$Ir and $^{203}$Ir, respectively. Counts upwards of $AoQ > 2.636$ are drastically reduced, which indicates the crossing of the $N = 126$ line from $^{203}$Ir to $^{204}$Ir. Comparing this to the LISE++ yield estimate at S4 for iridium in Fig. 13.22, the two strong peaks for iridium can be confirmed and assigned to $^{202}$Ir and $^{203}$Ir. This assignment is further supported by the measured counts which are 117(11) for the left-most peak, 1170(34) for the strongest peak, 820(29) for the second strongest peak and 109(10) for the remaining area upwards of $AoQ > 2.636$, where a clear peak is hard to make out and it has to be assumed that 1e1e charge-states are strongly mixed into this region. This assumption will be thoroughly investigated in the next Sec. 13.2 for the $^{190}$Lu Setting. From those counts the following yield ratios in relation to the strongest peak can be calculated, which are from left to right 0.10(13) (presumed $^{201}$Ir), 0.70(47) (presumed $^{203}$Ir) and 0.093(12) (presumed $^{204}$Ir). In comparison, LISE++ produces the following yields:

$4.61{\cdot}10^{-5}$ pps for $^{201}$Ir, $5.43{\cdot}10^{-2}$ pps for $^{202}$Ir, $5.3{\cdot}10^{-2}$ pps for $^{203}$Ir and $9.44{\cdot}10^{-4}$ pps for $^{204}$Ir[1], all isotopes fully-stripped. The corresponding ratios in relation to $^{202}$Ir are as such, $8.49{\cdot}10^{-4}$ for $^{201}$Ir, 0.976 for $^{203}$Ir and $1.74{\cdot}10^{-2}$ for $^{204}$Ir. A similar result, as to what can be seen in the $^{193}$W setting for the iridium isotopes, meaning that the general trend of yield ratios can be reproduced qualitatively, but they differ quantitatively from the experimental counts. A reason for this is that in this simple consideration of counts, no distinction between 0e0e and 1e1e charge-states has been made when measuring the peak intensity in the ID plots, compared to LISE++, which simulated the transport for all charge-states through the FRS and at S4 only the fully-stripped yield was then picked. The EPAX 3.1 cross-sections that were used for yield calculations via LISE++ could also be differing from the experimental cross-sections and therefore lead to different yield ratios. Though it is reasonable to trust EPAX in this region of the chart of nuclides from [79]. Additionally, there can be an influence by the TPC event selection method, which can remove events outside of the predefined valid checksum range, even though such events show correct S4 charge-state and position measurements, leading to a reduced count of isotopes, which are situated at the edges of the checksum range. This method alone would be insufficient for cross-section calculations or counting of new isotopes, but can be considered appropriate for the anchoring and assignment of peaks to isotopes, especially with identifying the $N = 126$ line by association. With all these considerations in mind, it is safe to assign the strongest peak in the line of iridium isotopes to $^{202}$Ir and the second strongest to $^{203}$Ir. This allows the repositioning of $Q_{max}$ and the AoQ for each isotope, whose repositioning coefficients can be found in App. I.4 and the resulting ID plot can be seen in Fig. 13.23.

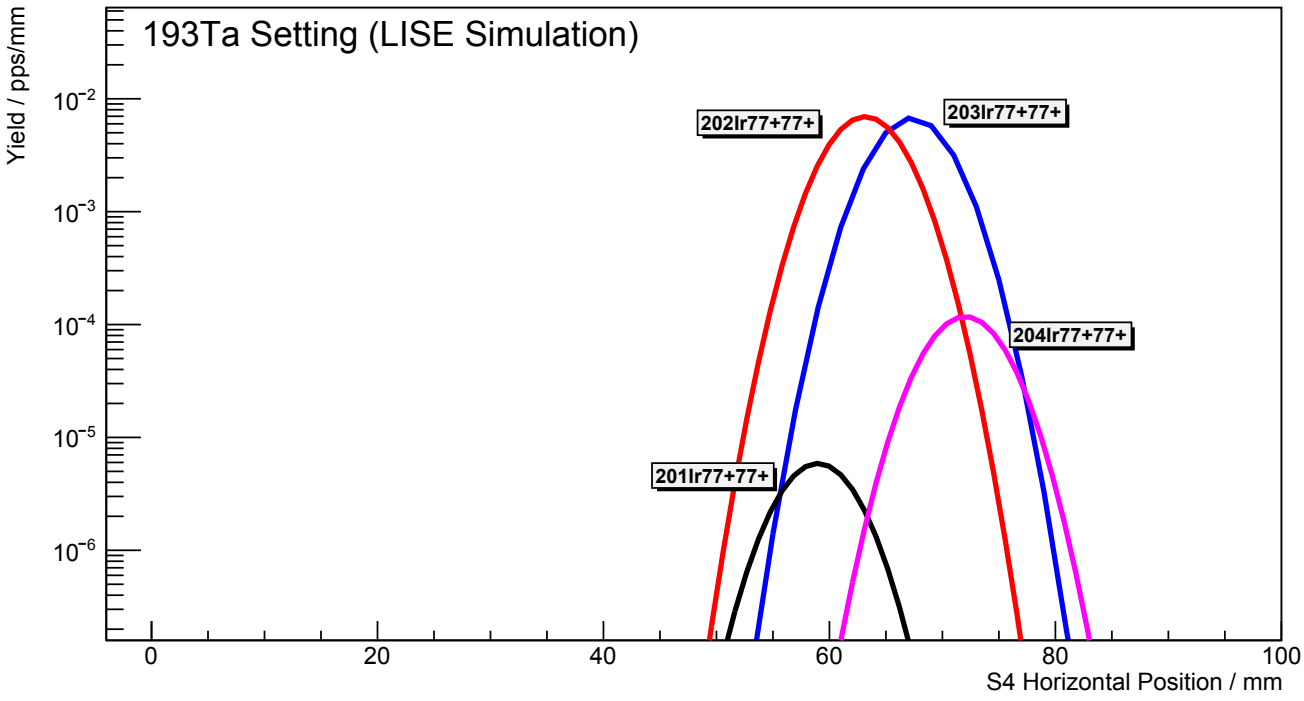


**Figure 13.22.:** LISE++ yield simulation for fully-stripped iridium isotopes in $^{193}$Ta setting at the final focal plane S4. The lowest intensity is expected for $^{201}$Ir (black), whereas $^{202}$Ir (red) and $^{203}$Ir (blue) have a very similar intensity at S4. Even though non-sensical $^{204}$Ir (fuchsia) can be calculated with EPAX.

[1]This yield was calculated with EPAX 3.1 in LISE++, assuming projectile fragmentation.

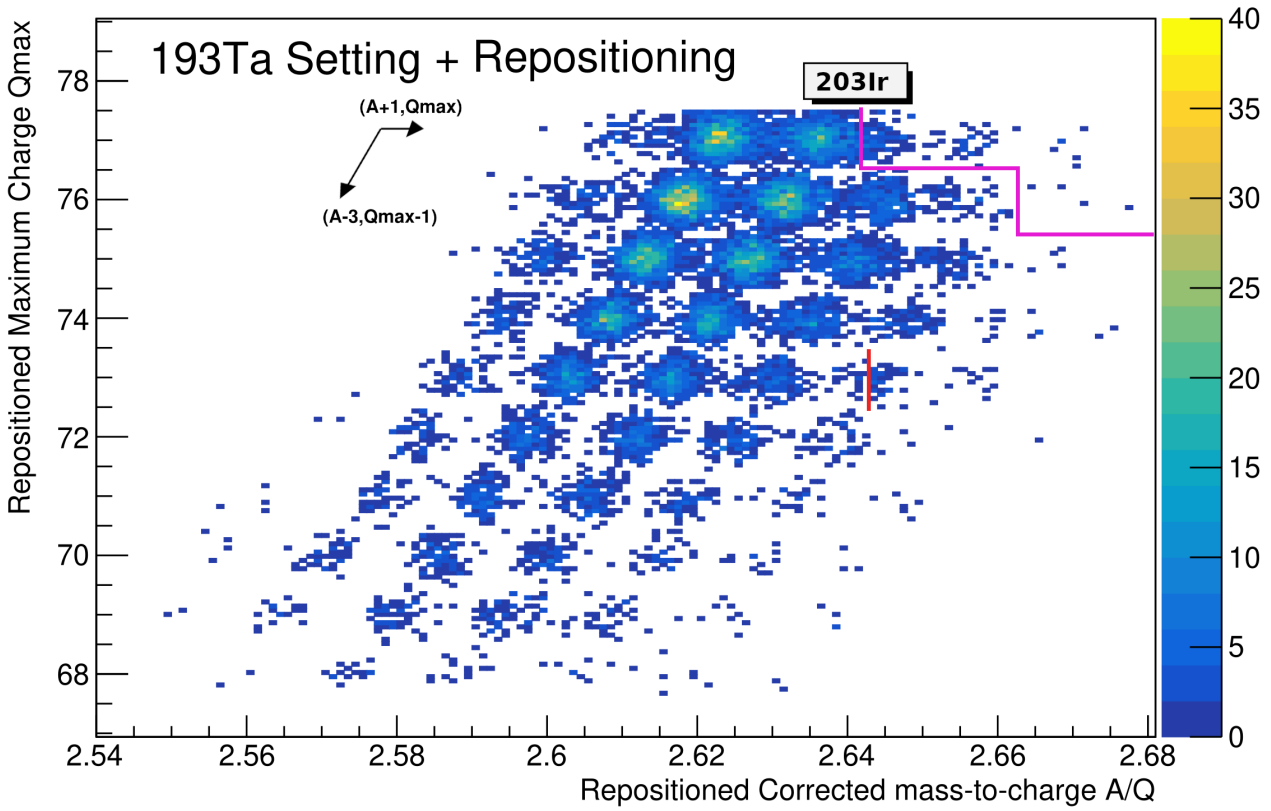


**Figure 13.23.:** Repositioned ID plot for the $^{193}$Ta setting with the peak of strongest intensity for iridium correctly assigned to $^{202}$Ir and the second strongest peak to $^{203}$Ir. The isotope of interest for the $^{193}$Ta setting is marked with a red line and the crossing of the $N = 126$ line is represented with a fuchsia line.

### $^{190}$Lu Setting

Finally, the lutetium setting, which holds all the information about potential new isotopes. Again, for this setting the FRS Ion Catcher was not available to provide mass-tagging information. Therefore the same method as before with tantalum setting has to be utilized to anchor and assign peaks to their respective isotopes. Figure 13.24 shows the ID plot for the $^{190}$Lu setting with all of the data gathered for this particular setting within four days of uninterrupted beamtime. The TPC checksum selection, introduced in Subsec. 13.1.4, is purposefully not applied in the following ID plots and therefore more background is visible. This is discussed in more detail in App. H as to why it is important. In this setting the osmium isotopes at $Q_{max} = 75.95$ are used to identify the crossing of the $N = 126$ line with the three visible peaks in the ID plot. The respective counts are 118(11) for the left peak, 530(23) for the middle peak and 245(16) for the right peak as well as a sharp cutoff in counts past $AoQ > 2.66$, indicating the $N = 126$ line. The count ratios in relation to the middle peak are 0.223(32) for the left one and 0.462(52) for the right one. When comparing to the LISE++ yield calculation for osmium in the lutetium setting, see Fig. 13.25, the respective osmium isotopes each have a yield of $1.14{\cdot}10^{-6}$ pps for $^{200}$Os, $4.22{\cdot}10^{-3}$ pps for $^{201}$Os and $1.82{\cdot}10^{-3}$ pps for $^{202}$Os. This results in the following yield ratios in relation to $^{201}$Os: $2.70{\cdot}10^{-4}$ for $^{200}$Os and 0.431 for $^{202}$Os. Interestingly, the left peak shows a major discrepancy with the LISE++ yield ratios, whereas the right peak agrees quite well with the simulated yield ratios. This can be

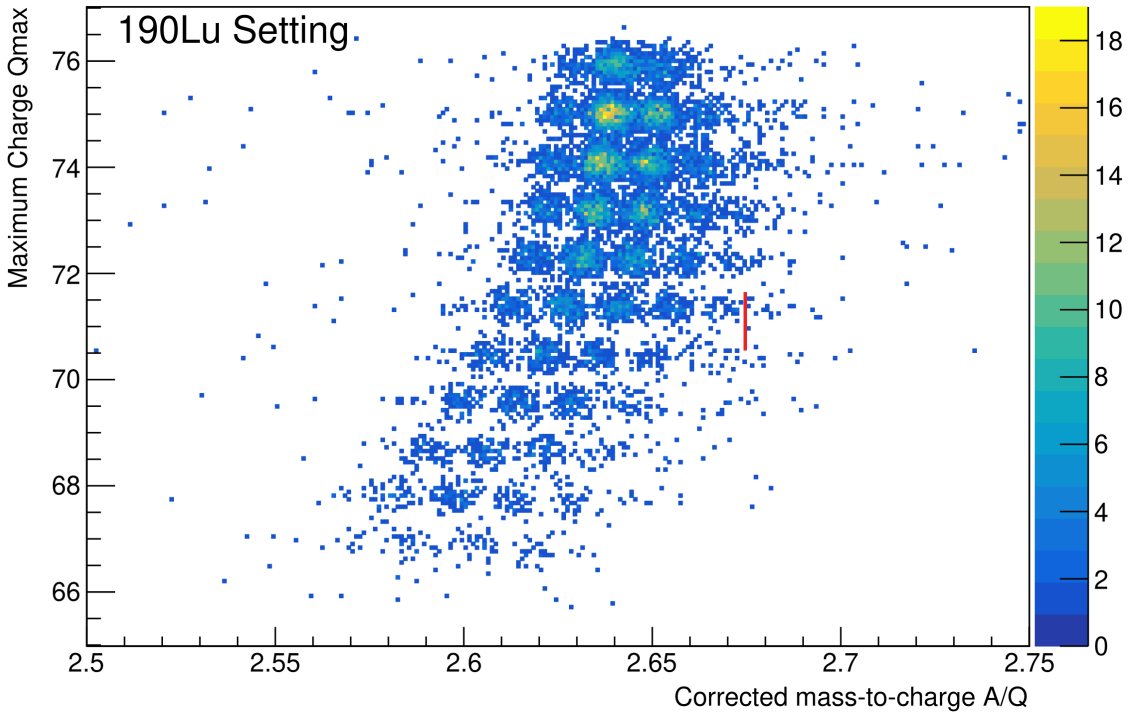


**Figure 13.24.:** ID plot for the $^{190}$Lu setting with all previously introduced concepts for correction and clean-up applied, except for TPC checksum clean-up. A positive shift in $Q_{max}$ together with a compression can be seen that needs to be repositioned. Additionally, a bend along the AoQ axis can be observed. This is discussed in App. G. The isotope of interest for the $^{190}$Lu setting is marked with a red line.

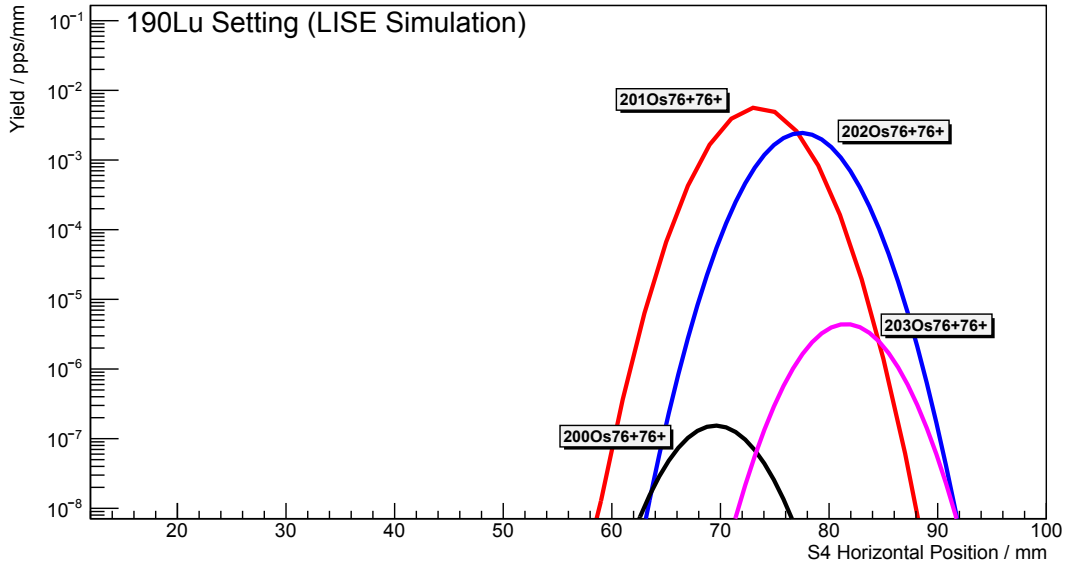


**Figure 13.25.:** LISE++ yield simulation for fully-stripped osmium isotopes in $^{190}$Lu setting at the final focal plane S4. The lowest intensity is expected for $^{200}$Os (black), $^{201}$Os (red) is supposed to have the highest yield and followed by $^{202}$Os (blue). Even though non-sensical $^{203}$Os (pink) can be calculated with EPAX.

understood to some extent, when changing the S1 slit configuration slightly. For the lutetium setting a configuration of (-100/20) mm was used for the left and right slit drive respectively at S1. When changing the right slit drive to 21 mm within LISE++, the yield of $^{200}$Os jumps to $9.75{\cdot}10^{-6}$ pps. Thus making it difficult to properly estimate the yield of isotopes that are significantly cut away by the S1 slits or other apertures. Nonetheless, it is possible to assign the strongest peak in the line of osmium isotopes to $^{201}$Os and the right one to $^{202}$Os, which also agrees with the significant drop in counts according to the crossing of the $N = 126$ line. This anchoring is further supported by the strong agreement of measured isotope position spectra in comparison to MOCADI calculations, as will be presented in great detail in the next Sec. 13.2. This enabled the the ID plot to be repositioned, which can be seen in Fig. 13.26 and the coefficients can be found in App. I.5.

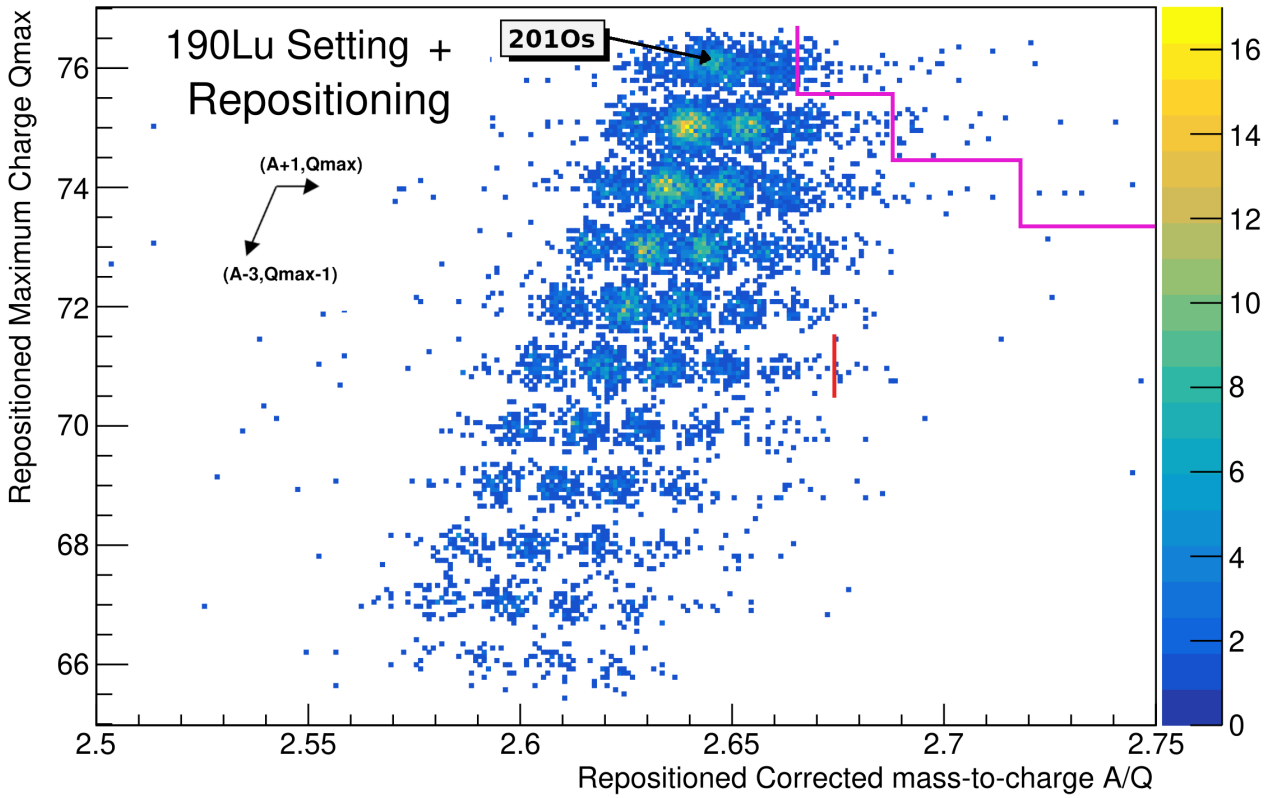


**Figure 13.26.:** Repositioned ID plot for the $^{190}$Lu setting with the peak of strongest intensity for osmium correctly assigned to $^{201}$Os and the second strongest peak to $^{202}$Os. The isotope of interest for the $^{190}$Lu setting is marked with a red line and the crossing of the $N = 126$ line is represented with a fuchsia line.

## 13.2. AoQ and Position Spectra of $^{190}$Lu Setting

The following analysis of isotope counts relies on the previously introduced concepts of MUSIC $Q_{max}$ and degrader 0e0e charge-state selections for the $^{190}$Lu setting, see Subsec. 13.1.2 and 13.1.3, in order to identify the available isotopes per element in the recalibrated ID plot. Following this, the recalibrated AoQ spectra are produced for each element and theoretical AoQ isotope values together with an interval of $(\frac{A-0.5}{Q_{max}}|\frac{A+0.5}{Q_{max}})$ are identified for each isotope A and used as isotope selections. In order to distinguish the different isotopic components in each interval the experimentally measured horizontal position spectra at S2 and S4 are plotted over each other and compared to similar spectra from MOCADI calculations, which are set up identical to the experimental configuration and assuming production cross sections from EPAX 3 [74] and Goldhaber momentum distribution of fragments [71]. In cases, for which MOCADI can not be used, LISE++ is used as an alternative with identical assumptions. In the next step, the experimental position spectra are projected unto the S4 position axis and 3 Gaussian distributions are fitted into the spectrum. One representing the main peak and isotope A under consideration, one representing isotope A-1 remains inside the interval and one representing isotope A+1. Isotopes A-1 and A+1 can be identified slightly left and right of the center position of A respectively. Other peaks further away can be either assigned to 1e1e charge-states of isotopes with $Q_{max}+1$, since they remain inside the predefined 0e0e+1e1e selection, or higher charge-states 2e1e or 1e2e, although rare. Another interesting case are isotopes above the isotope $(A|Q_{max})$ in question, i.e. $(A+3|Q_{max}+1)$, which remain fully-stripped 0e0e throughout the FRS and only pick-up an electron at S4 before the MUSIC detectors and remain hydrogen-like during the charge measurement. Thus, being measured as $Q_{max}$ instead of $Q_{max}+1$ but sharing the same position distribution as their fully-stripped counterpart $(A+3|Q_{max}+1)$. It can be seen for isotopes of higher intensity. This fitting method is suitable for isotopes with high statistics but starts to break down for low statistics isotopes. In this case an event by event decision has to be performed.
Another important aspect is the accuracy of the position measurement. Each TPC and their distances to each other are assumed to be accurate within a $1\ \mathrm{mm}$ level. The position inside a focal plane is determined as the projection of the TPC closest to the focal plane with the measured angle and respective distance. From this assumption an accuracy in position measurement at the respective focal plane can be derived to be $1.73\ \mathrm{mm}$ and is implicitly assumed from this point on for all position measurements. Any errors given from this point on are statistical fitting errors.

### 13.2.1. Os Isotopes

Figure 13.27 shows the previously described AoQ plot for the osmium isotopes together with theoretical isotopic AoQ values and predefined selection intervals. It can be seen that the individual peaks show an overlap with each other, which can be disentangled through appropriate fitting of Gaussian distributions, although other hidden components such as invading charge-states would remain hidden. Figure 13.28 (a) shows the previously described position spectra for what is assumed to be $^{200}$Os and (b) shows the corresponding predicted MOCADI positions. From the peak analysis the position of the main peak in Fig. 13.28 (a) can be determined to be 70.97(31) $\mathrm{mm}$, as compared to 71.95(29) $\mathrm{mm}$ from MOCADI (b) or LISE++ 69.55 $\mathrm{mm}$. Since LISE++ calculations involve a convolution method to determine the particle transport, all positions are given as exact by exactly determined functions, whereas MOCADI relies on an initial Monte-Carlo simulation to propagate each individual particle. Given the previously discussed accuracy of the position measurement, the experimental distribution agrees with both simulations, thus confirming the assumption that the first peak on the left of Fig. 13.27 can be assigned as the known isotope $^{200}$Os. The next two isotopes $^{201}$Os and $^{202}$Os can be determined similarly.

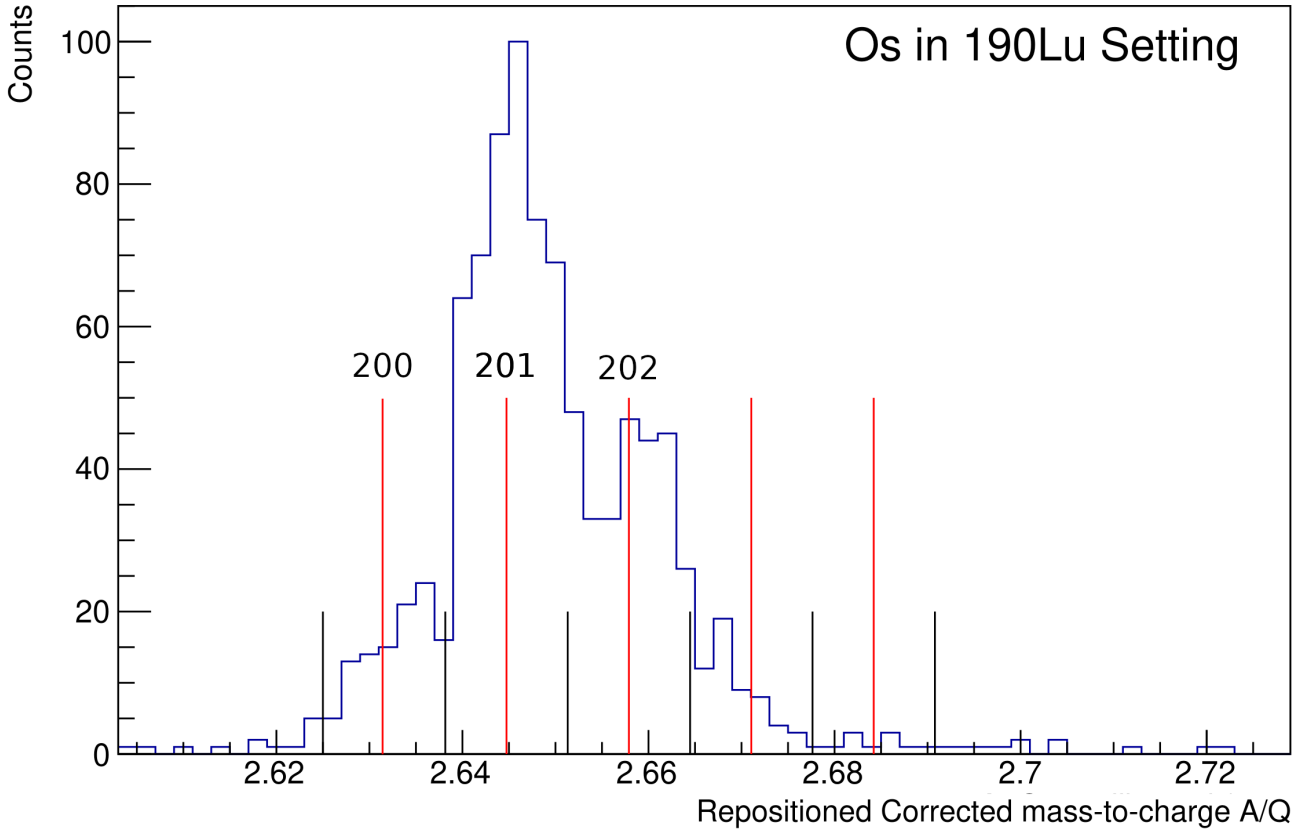


**Figure 13.27.:** AoQ spectrum for osmium isotopes in the $^{190}$Lu setting together with theoretical isotopic AoQ values (red lines) and predefined selection intervals (black lines). The strongest peak in this distribution corresponds to $^{201}$Os, which can be additionally confirmed by Fig. 13.29.

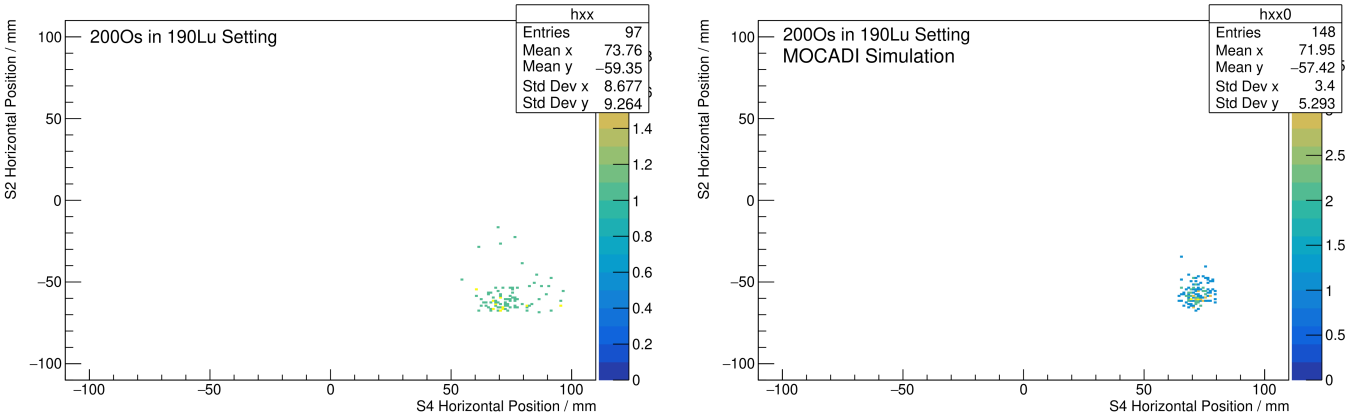


**Figure 13.28.:** S2 horizontal position plotted over S4 horizontal position for experimentally measured (left) and simulated (right) spectra. The experimental position of 70.97(31) mm at S4 agrees with both MOCADI and LISE simulations (69.55 mm).

Figure 13.29 and 13.30 show the respective measurements and simulations. In both cases a better agreement

with MOCADI can be achieved than with LISE++. This is understandable since FRS LISE++ simulation files don't take into account vacuum and gas-filled drift-lengths, thus differing from experimental measurements and MOCADI simulations regularly on the level of several $\mathrm{mm}$. Such a strong agreement with MOCADI additionally confirms the previously introduced anchoring and repositioning for the $^{190}$Lu setting.

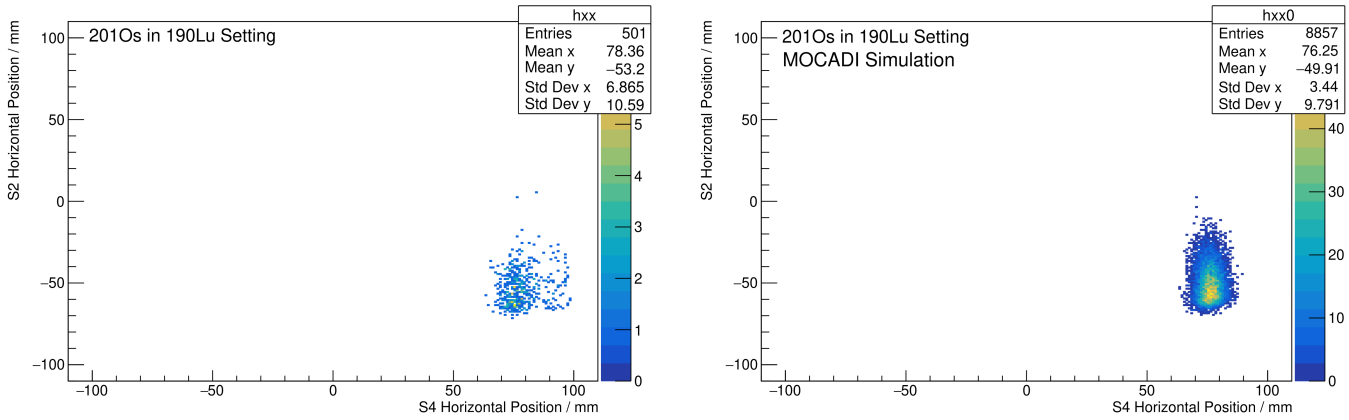


**Figure 13.29.:** S2 horizontal position plotted over S4 horizontal position for experimentally measured (left) and simulated (right) spectra. The experimental position of 75.94(27) $\mathrm{mm}$ at S4 agrees more with MOCADI (right) and less with LISE simulations (73.44 $\mathrm{mm}$).

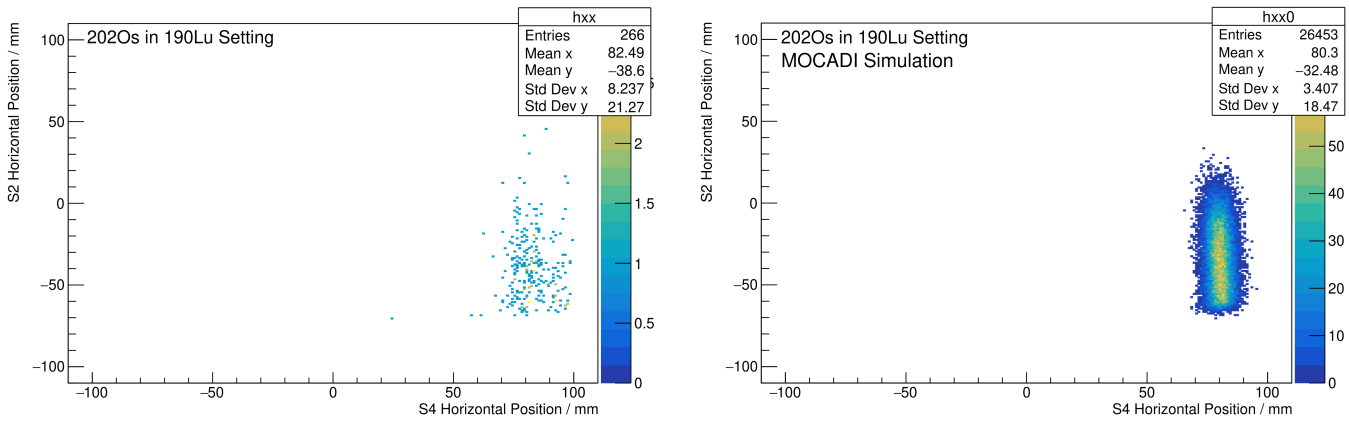


**Figure 13.30.:** S2 horizontal position plotted over S4 horizontal position for experimentally measured (left) and simulated (right) spectra. The experimental position of 80.34(49) $\mathrm{mm}$ at S4 agrees more with MOCADI (right) and less with LISE simulations (77.45 $\mathrm{mm}$).

The next isotope in line is $^{203}$Os, which was discovered at the FRS in a similar experiment utilizing a uranium beam and projectile fragmentation [114]. In this case, it is impossible for MOCADI to simulate the production and transport of $^{203}$Os since the framework does not allow the production of isotopes with a higher neutron number than the initial primary beam. At the same time, LISE++ and EPAX 3.1 allow the simulation of such fragments. Furthermore, EPAX 3.1 shows the highest possible yield out of available

reaction mechanisms in LISE, with an estimated $3.28{\cdot}10^{-5}$ pps. Given the total runtime of the experiment, this means an estimated total count of 3 isotopes, which is overproduced in Fig. 13.31. Another possible reaction to consider would be a two-body reaction of $^{208}$Pb into $^{209}$Pb and subsequent fragmentation into $^{203}$Os inside the beryllium target. This channel can be estimated to yield $7.38{\cdot}10^{-8}$ pps via LISE++.

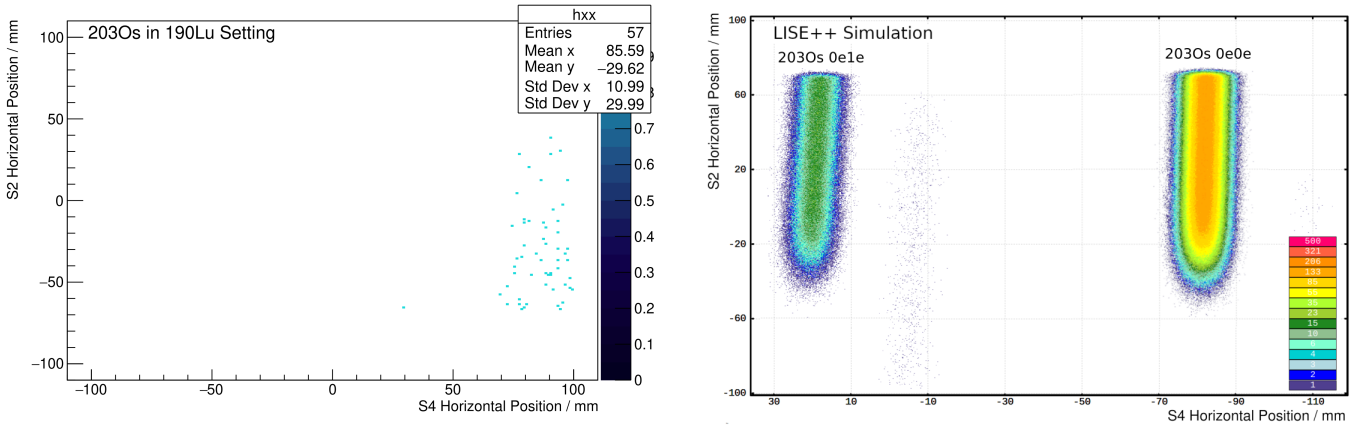


**Figure 13.31.:** S2 horizontal position plotted over S4 horizontal position for experimentally measured (left) and simulated (right) spectra. The experimental position of 85.59 mm at S4 compared to LISE simulations (81.54 mm) is higher but follows the systematic deviation of previous LISE++ simulations such that a shift of 3 mm can be safely applied to the LISE distribution. The LISE++ Y-Axis has to be flipped, due to the left-handedness of the coordinate system.

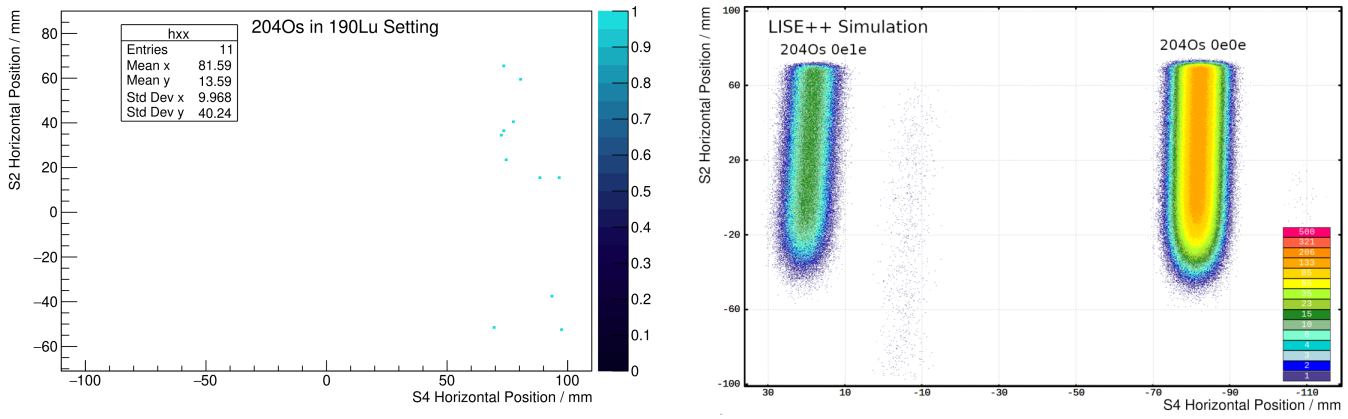


**Figure 13.32.:** S2 horizontal position plotted over S4 horizontal position for experimentally measured (left) and simulated (right) spectra. The experimental position of 81.59 mm at S4 compared to LISE simulations (85.96 mm) is higher but follows the systematic deviation of previous LISE++ simulations such that a shift of 3 mm can be safely applied to the LISE distribution. The LISE++ Y-Axis has to be flipped, due to the left-handedness of the coordinate system.

Thus making it highly unlikely. Therefore the reaction channel remains unclear, even though an agreement with LISE++ simulations can be seen for projectile fragmentation. It has to be assumed that most counts

are from $^{202}$Os and uncorrelated background, which appears constant past $^{202}$Os, due to the nature of the selection as shown in 13.27. Therefore no counts can be confirmed for $^{203}$Os. The same argumentation can be applied to Fig. 13.32 with the consequence that no new $^{204}$Os has been discovered.

### 13.2.2. Re Isotopes

Figure 13.34, 13.35 and 13.36 show the measured position spectra in comparison to MOCADI simulations, according to the defined selections in Fig. 13.33 for $^{197}$Re, $^{198}$Re and $^{199}$Re. The same analysis method was applied as for the osmium isotopes and the resulting positions for the respective isotopes show good agreement with the MOCADI simulations. As was shown previously, LISE++ calculations deviate significantly from the measured positions and were thus not used unless MOCADI could not simulate the required isotope. It can also be seen, that the rhenium isotopes possess a better separation compared to the osmium isotopes, especially in the position spectra, there is less overlap with neighboring isotopes and other charge-states are less intrusive.

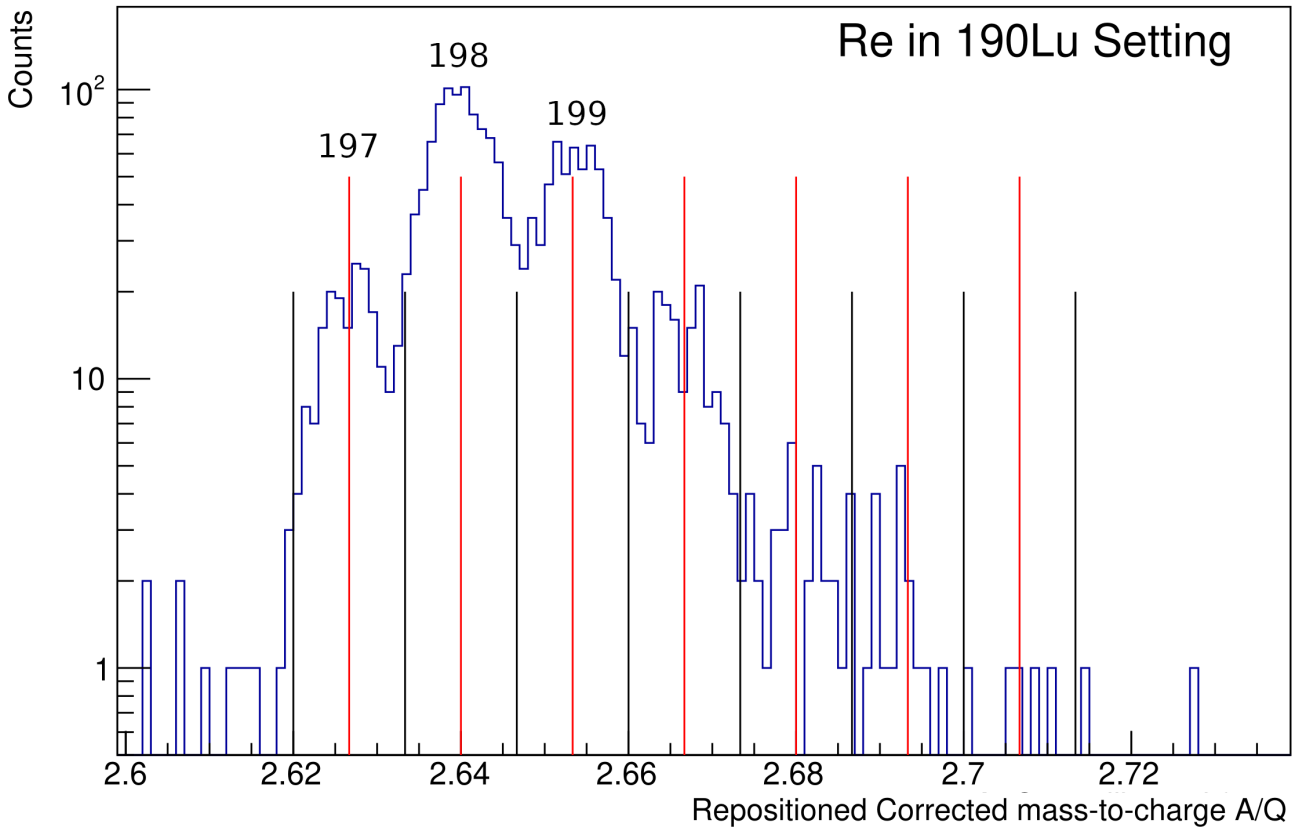


**Figure 13.33.:** AoQ spectrum for rhenium isotopes in the $^{190}$Lu setting together with theoretical isotopic AoQ values (red lines) and predefined selection intervals (black lines). The strongest peak in this distribution corresponds to $^{198}$Re, which can be additionally confirmed by Fig. 13.35.

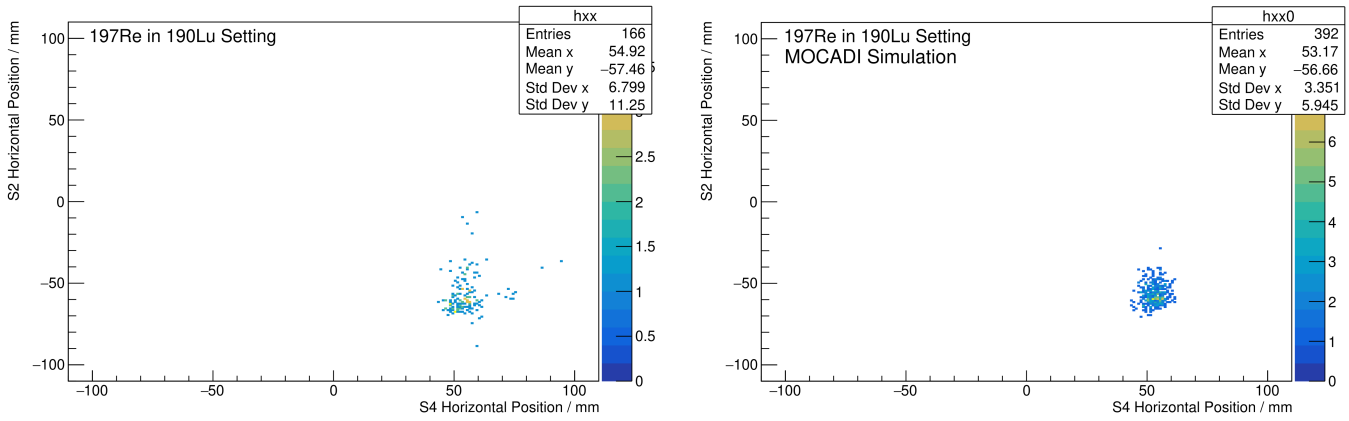


**Figure 13.34.:** S2 horizontal position plotted over S4 horizontal position for experimentally measured (left) and simulated (right) spectra. The experimental position of 53.53(36) mm at S4 agrees quite well with MOCADI.

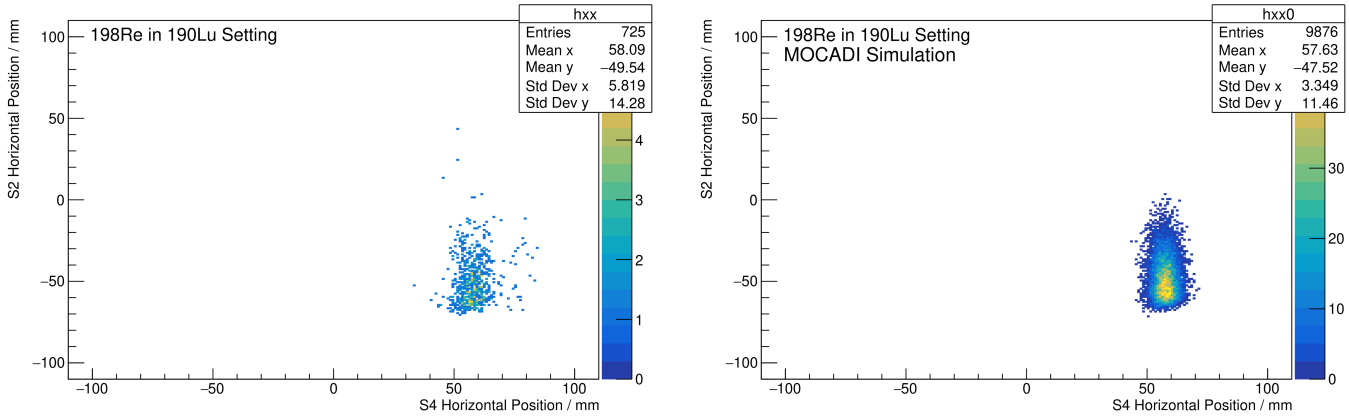


**Figure 13.35.:** S2 horizontal position plotted over S4 horizontal position for experimentally measured (left) and simulated (right) spectra. The experimental position of 57.53(19) mm at S4 agrees quite well with MOCADI.

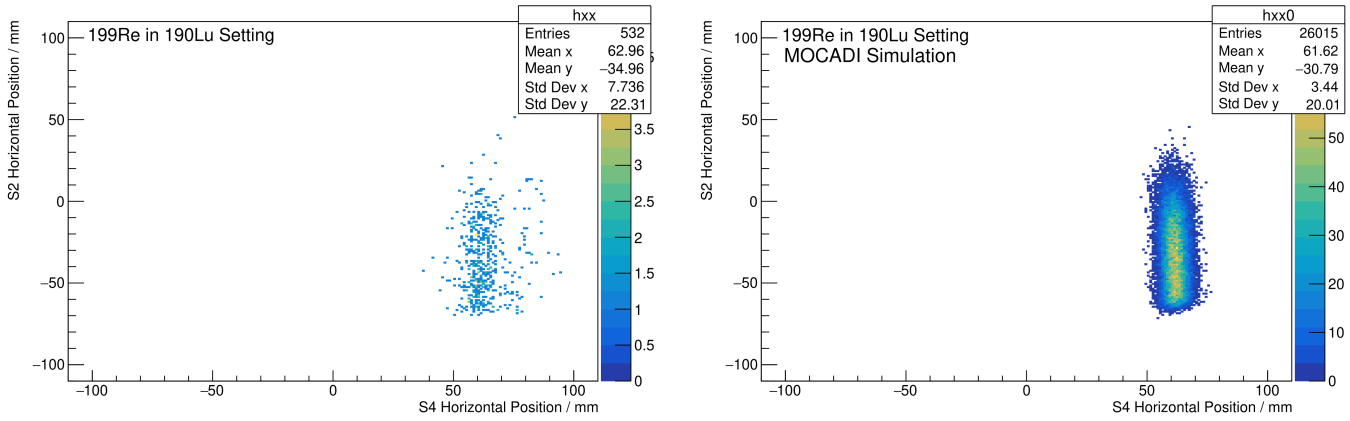


**Figure 13.36.:** S2 horizontal position plotted over S4 horizontal position for experimentally measured (left) and simulated (right) spectra. The experimental position of 61.52(26) $\mathrm{mm}$ at S4 agrees quite well with MOCADI.

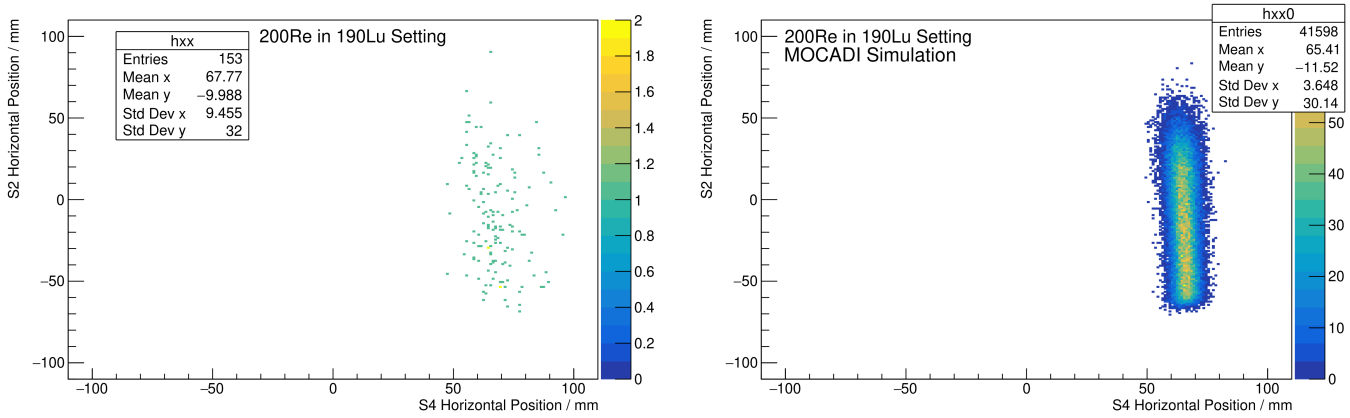


**Figure 13.37.:** S2 horizontal position plotted over S4 horizontal position for experimentally measured (left) and simulated (right) spectra. The experimental position of 65.01(71) $\mathrm{mm}$ at S4 agrees quite well with MOCADI.

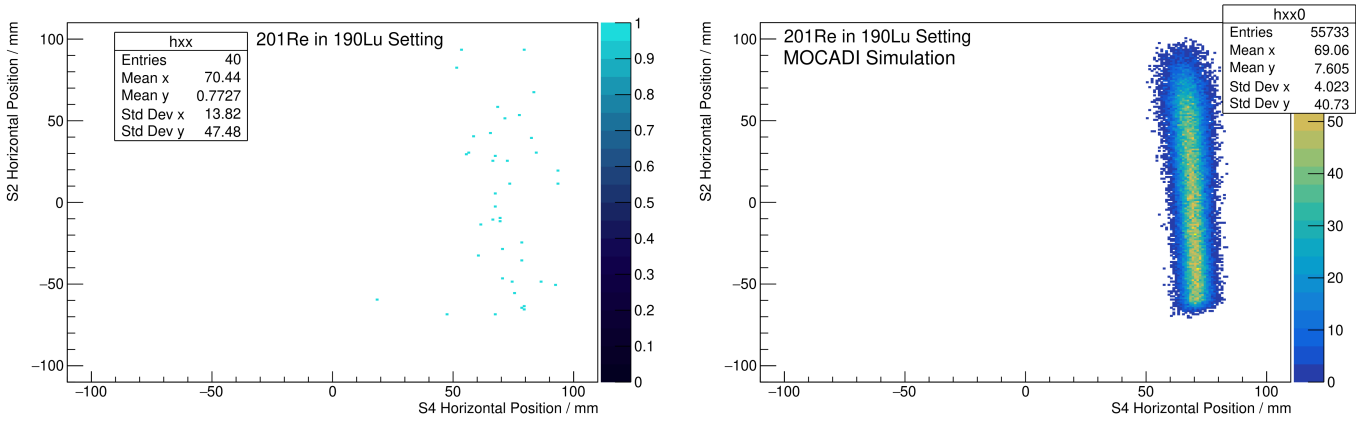


**Figure 13.38.:** S2 horizontal position plotted over S4 horizontal position for experimentally measured (left) and simulated (right) spectra. The experimental position of 70.84(1210) $\mathrm{mm}$ at S4 agrees quite well with MOCADI.

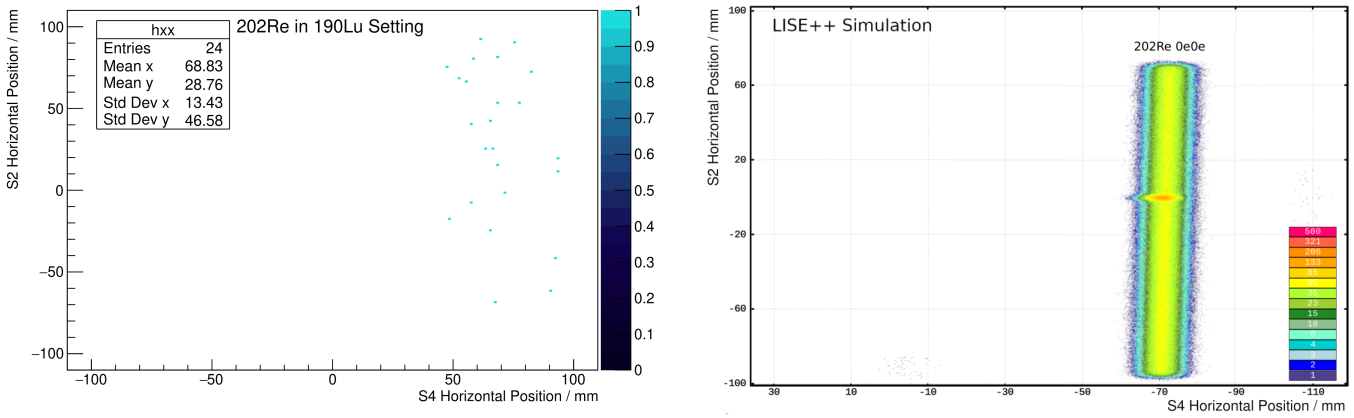


**Figure 13.39.:** S2 horizontal position plotted over S4 horizontal position for experimentally measured (left) and simulated (right) spectra. The LISE++ position is 71.68 $\mathrm{mm}$ at S4.

.

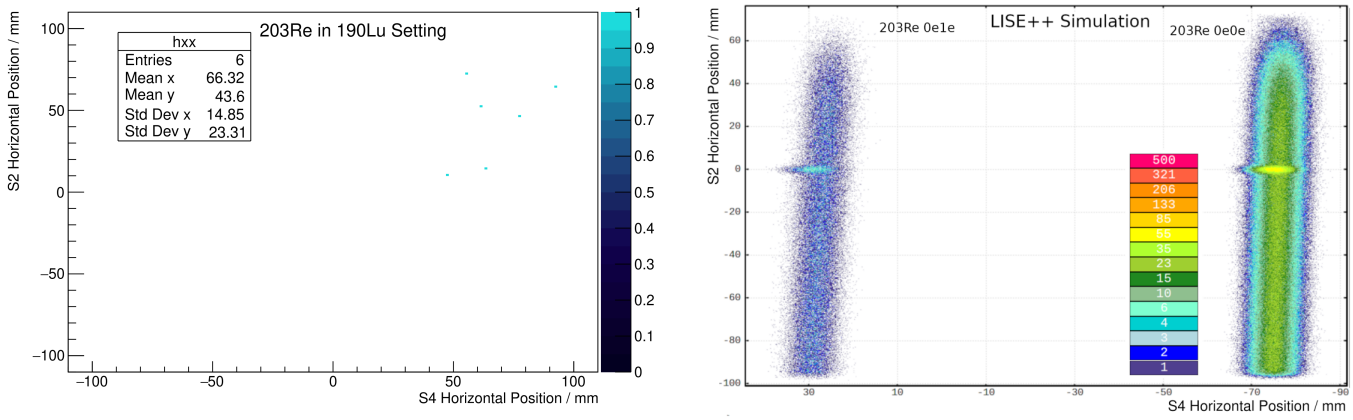


**Figure 13.40.:** S2 horizontal position plotted over S4 horizontal position for experimentally measured (left) and simulated (right) spectra. The LISE++ position is 75.91 mm at S4.

The rhenium isotopes show the first counts of the undiscovered isotope $^{200}$Re in Fig. 13.37. From previous considerations, only events are counted towards a new isotope which are situated within a $3\sigma$ region of the MOCADI distribution. Additionally, a background estimate is applied by averaging out the counts outside of the predefined isotopic intervals for each element and deducing it from the final count. The resulting number of counts can be found in Tab. 13.1.

| Isotope | $^{200}$Re | $^{201}$Re | $^{202}$Re |
|---|---|---|---|
| Counts | 121(11) | 21(5) | 8(3) |

**Table 13.1.:** Final counts for the new discovered $^{200}$Re, $^{201}$Re and $^{202}$Re isotopes. With an estimated background count of 8 counts per isotopes, $^{203}$Re is deemed as not discovered.

Without further comment, the previously introduced methods are applied to all other elements and isotopes and their corresponding results can be found in their respective spectra and tables.

### 13.2.3. W Isotopes

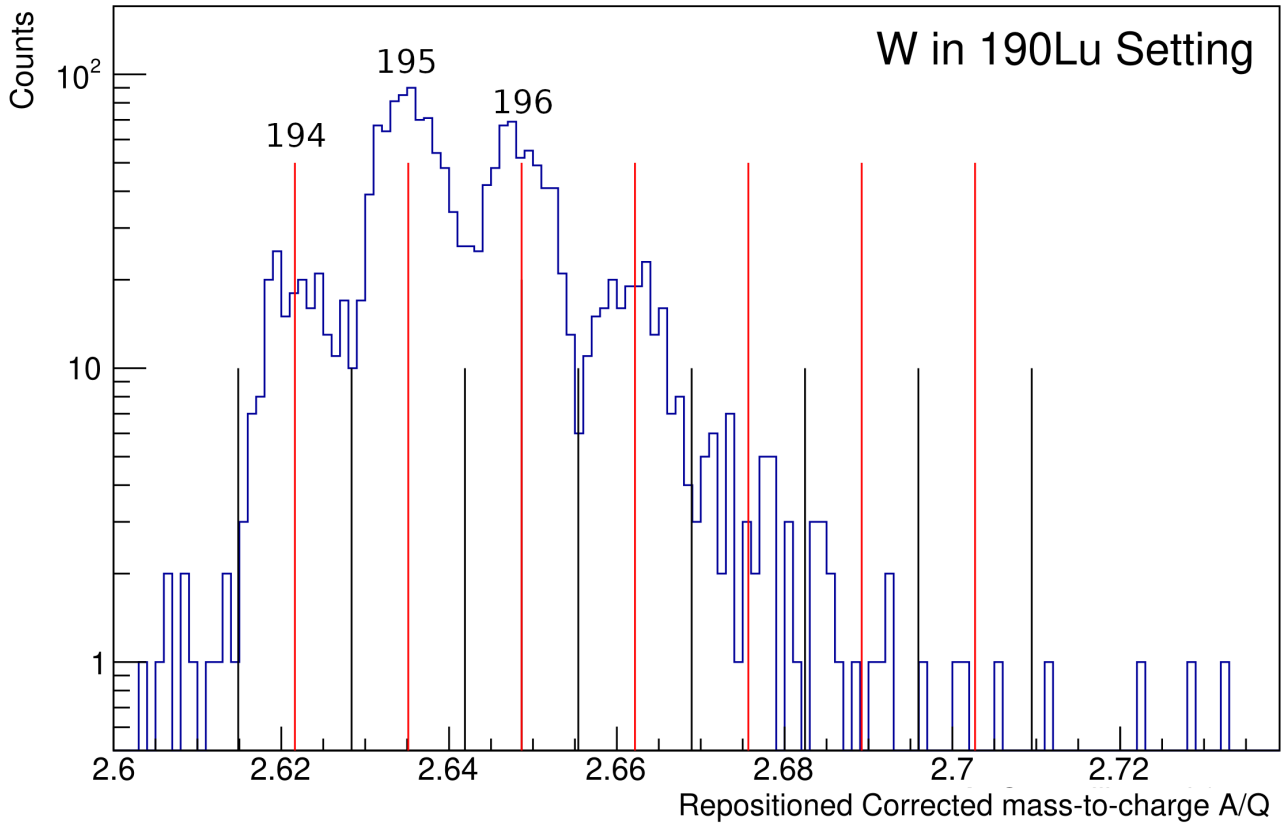


**Figure 13.41.:** AoQ spectrum for tungsten isotopes in the $^{190}$Lu setting together with theoretical isotopic AoQ values (red lines) and predefined selection intervals (black lines). The strongest peak in this distribution corresponds to $^{195}$W, which can be additionally confirmed by Fig. 13.43.

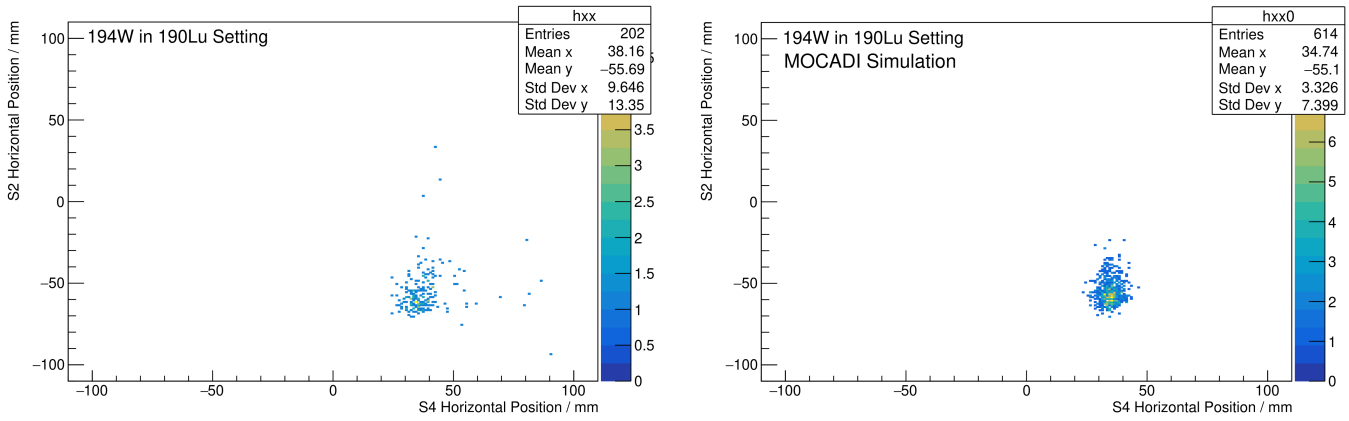


**Figure 13.42.:** S2 horizontal position plotted over S4 horizontal position for experimentally measured (left) and simulated (right) spectra. The experimental position of 35.48(34) $\mathrm{mm}$ at S4 agrees quite well with MOCADI.

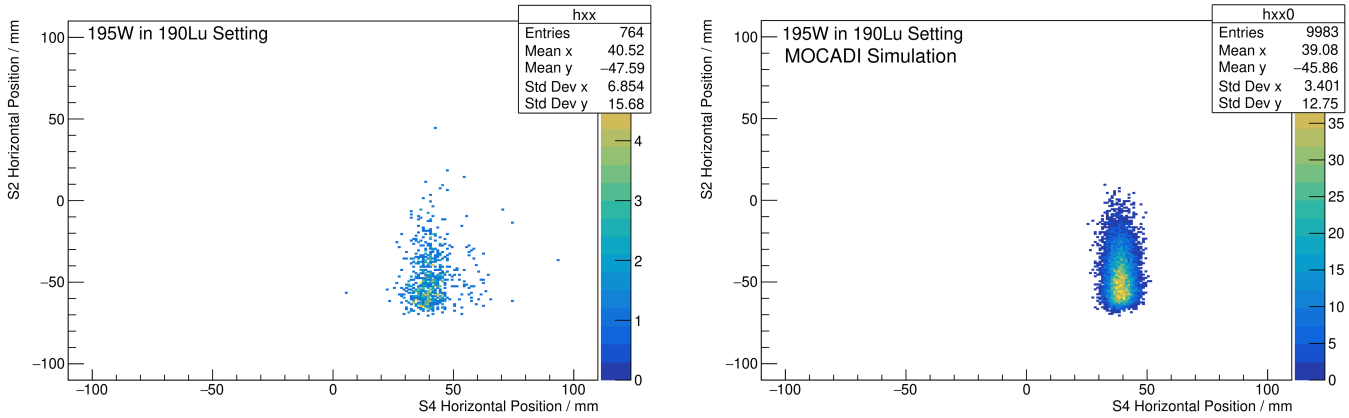


**Figure 13.43.:** S2 horizontal position plotted over S4 horizontal position for experimentally measured (left) and simulated (right) spectra. The experimental position of 39.45(17) $\mathrm{mm}$ at S4 agrees quite well with MOCADI.

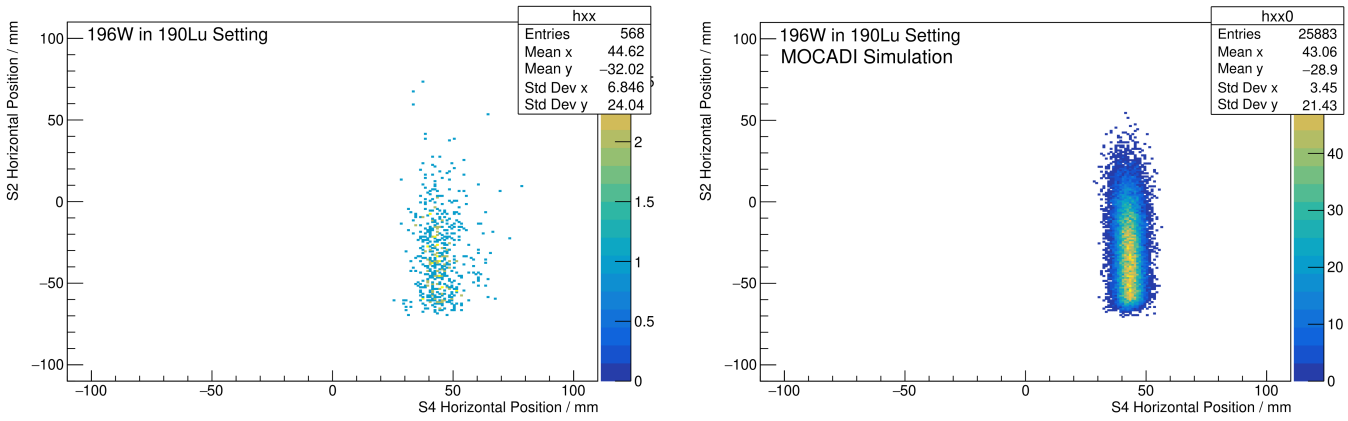


**Figure 13.44.:** S2 horizontal position plotted over S4 horizontal position for experimentally measured (left) and simulated (right) spectra. The experimental position of 43.18(28) mm at S4 agrees quite well with MOCADI.

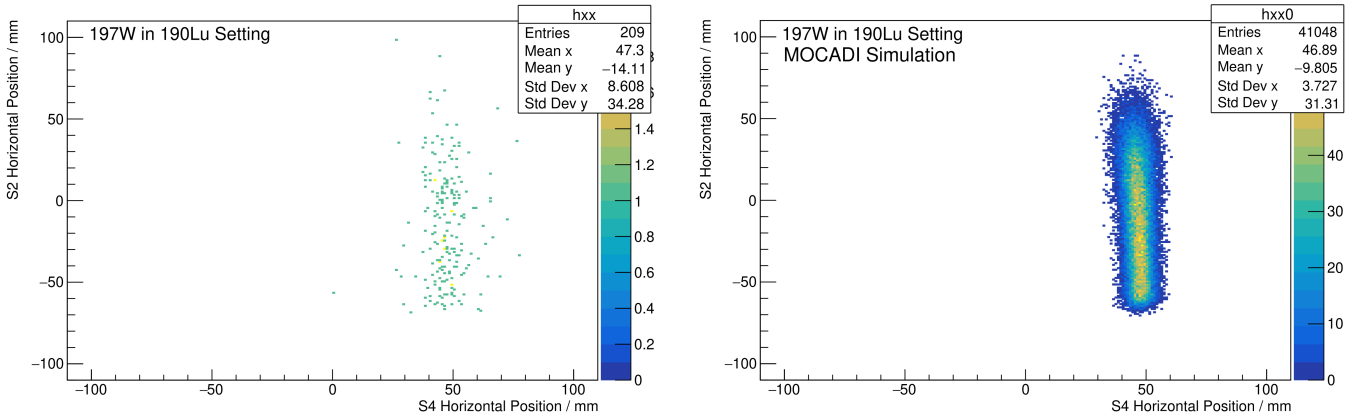


**Figure 13.45.:** S2 horizontal position plotted over S4 horizontal position for experimentally measured (left) and simulated (right) spectra. The experimental position of 46.90(52) mm at S4 agrees quite well with MOCADI.

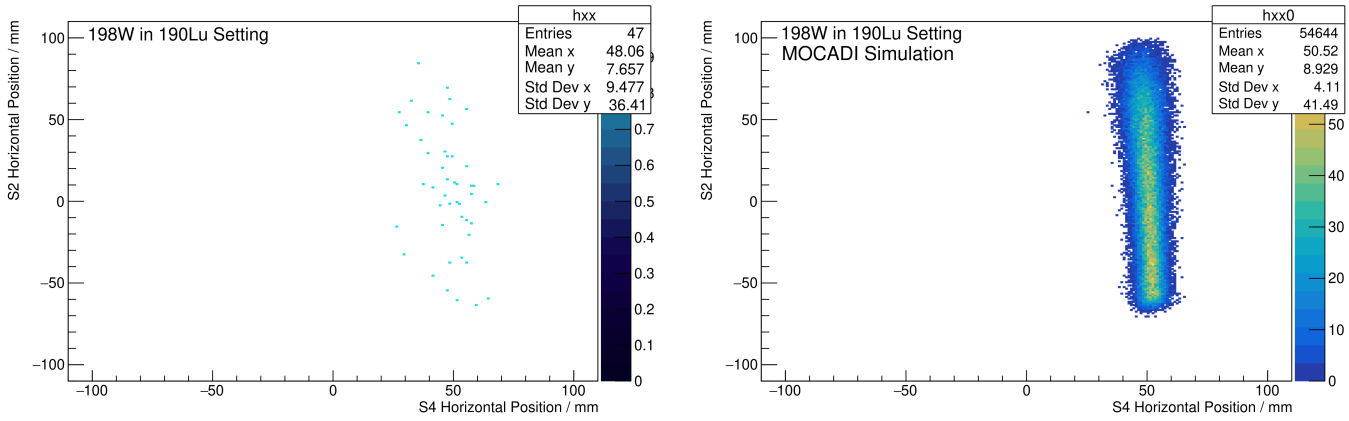


**Figure 13.46.:** S2 horizontal position plotted over S4 horizontal position for experimentally measured (left) and simulated (right) spectra. The experimental position of 48.95(380) mm at S4 agrees with MOCADI but the statistics start to break down.

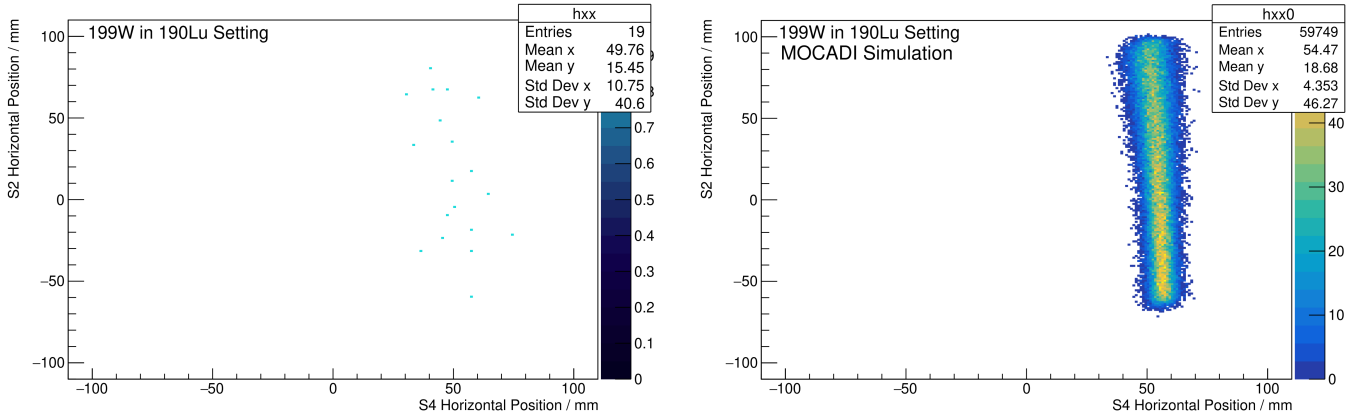


**Figure 13.47.:** S2 horizontal position plotted over S4 horizontal position for experimentally measured (left) and simulated (right) spectra. The experimental position of 54.59(1410) mm at S4 agrees with MOCADI but is highly inaccurate due to the low statistics.

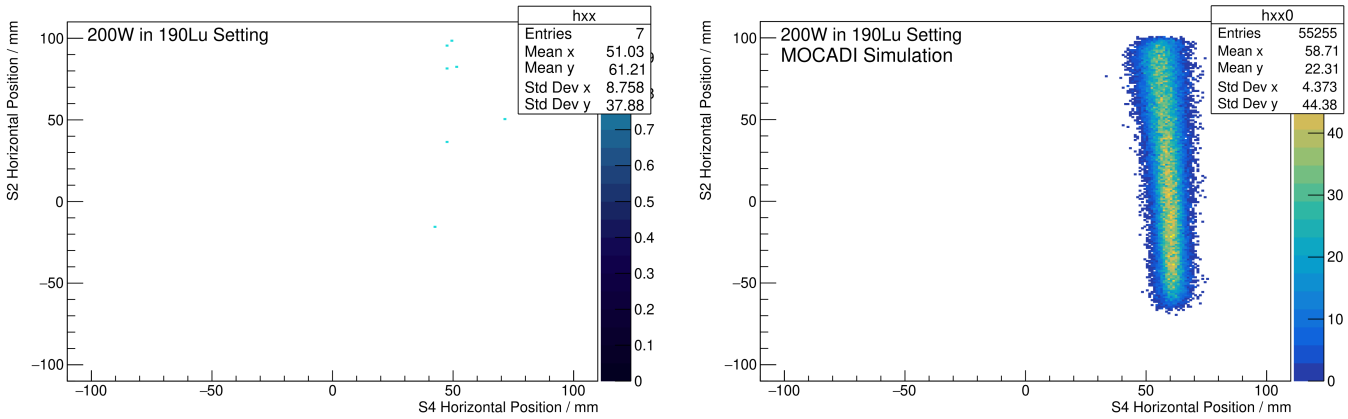


**Figure 13.48.:** S2 horizontal position plotted over S4 horizontal position for experimentally measured (left) and simulated (right) spectra. The experimental positioning at S4 (left) can not be determined via fitting due to the low statistics.

| Isotope | $^{198}$W | $^{199}$W | $^{200}$W |
|---|---|---|---|
| Counts | 41(6) | 12(3) | 0 |

**Table 13.2.:** Final counts for the new discovered $^{198}$W and $^{199}$W isotopes. With an estimated background count of 7 counts per isotopes $^{200}$W is deemed as not discovered.

### 13.2.4. Ta Isotopes

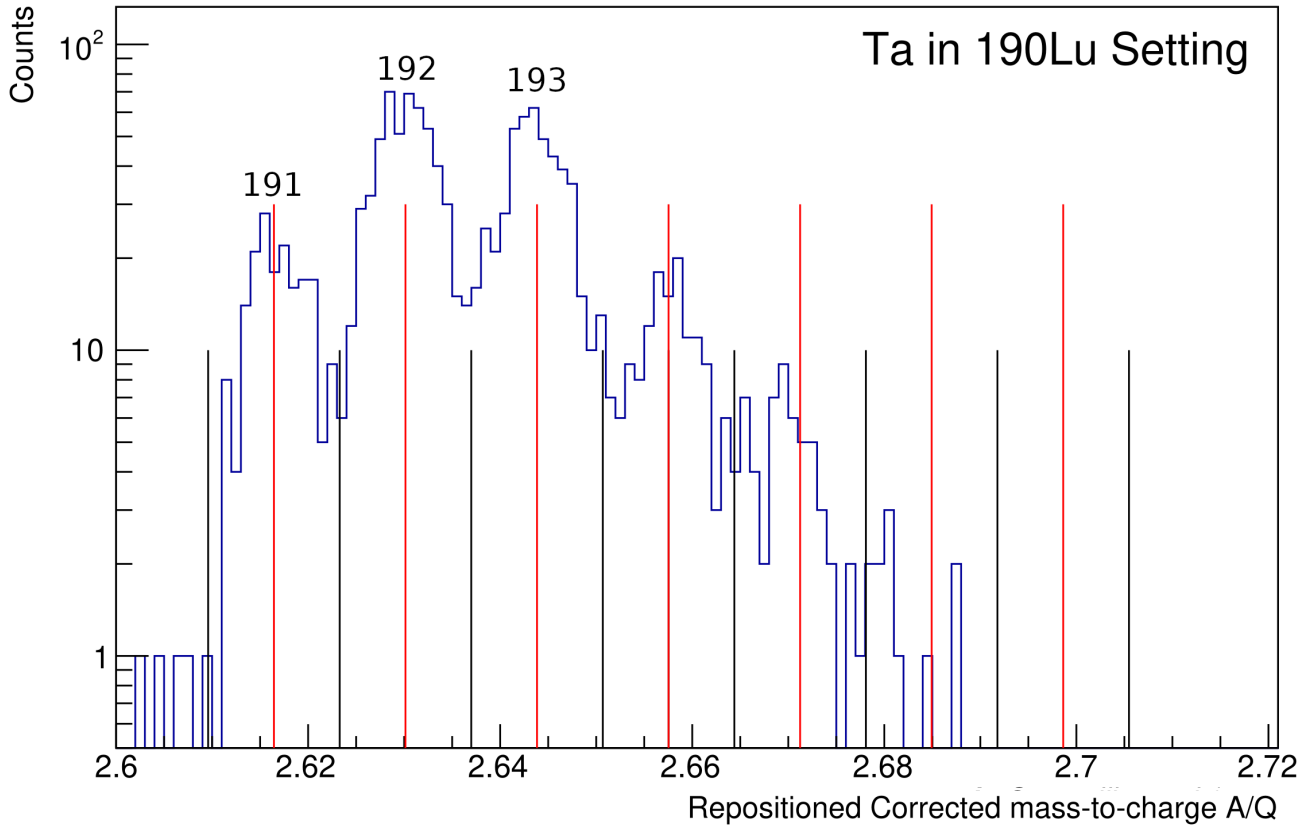


**Figure 13.49.:** AoQ spectrum for tantalum isotopes in the $^{190}$Lu setting together with theoretical isotopic AoQ values (red lines) and predefined selection intervals (black lines). The strongest peak in this distribution corresponds to $^{192}$Ta, which can be additionally confirmed by Fig. 13.51.

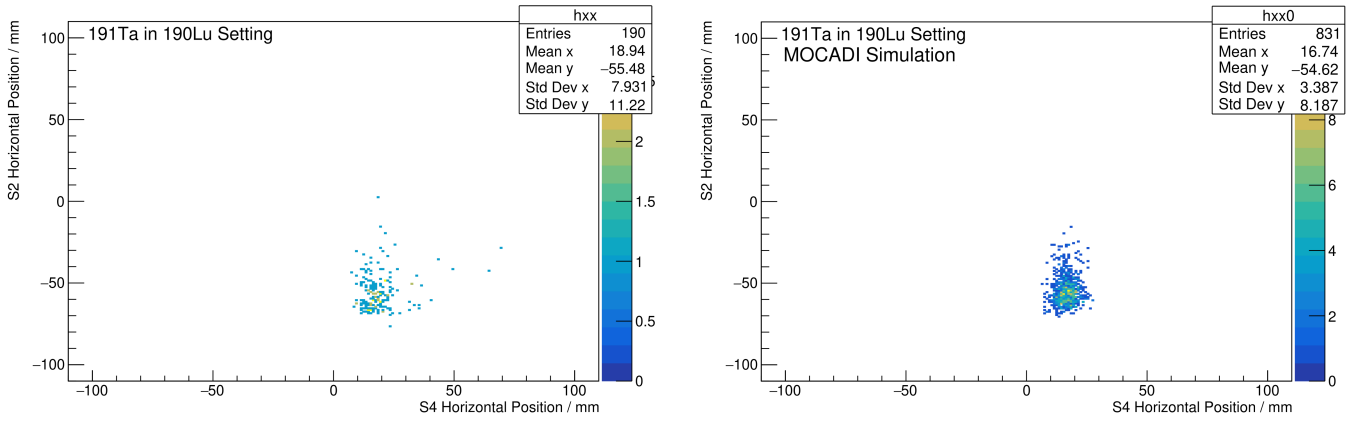


**Figure 13.50.:** S2 horizontal position plotted over S4 horizontal position for experimentally measured (left) and simulated (right) spectra. The experimental position of 16.89(35) mm at S4 agrees quite well with MOCADI.

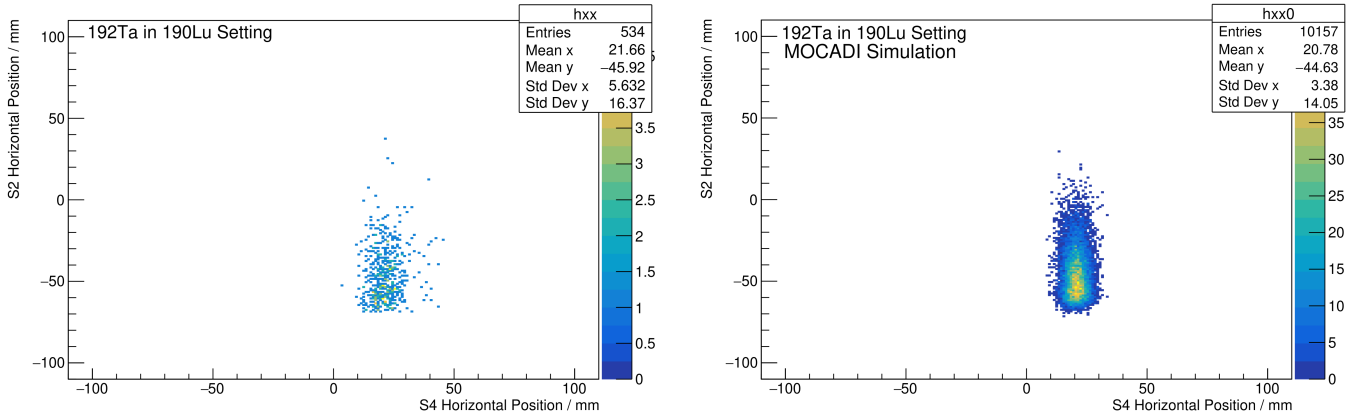


**Figure 13.51.:** S2 horizontal position plotted over S4 horizontal position for experimentally measured (left) and simulated (right) spectra. The experimental position of 21.46(22) mm at S4 agrees quite well with MOCADI.

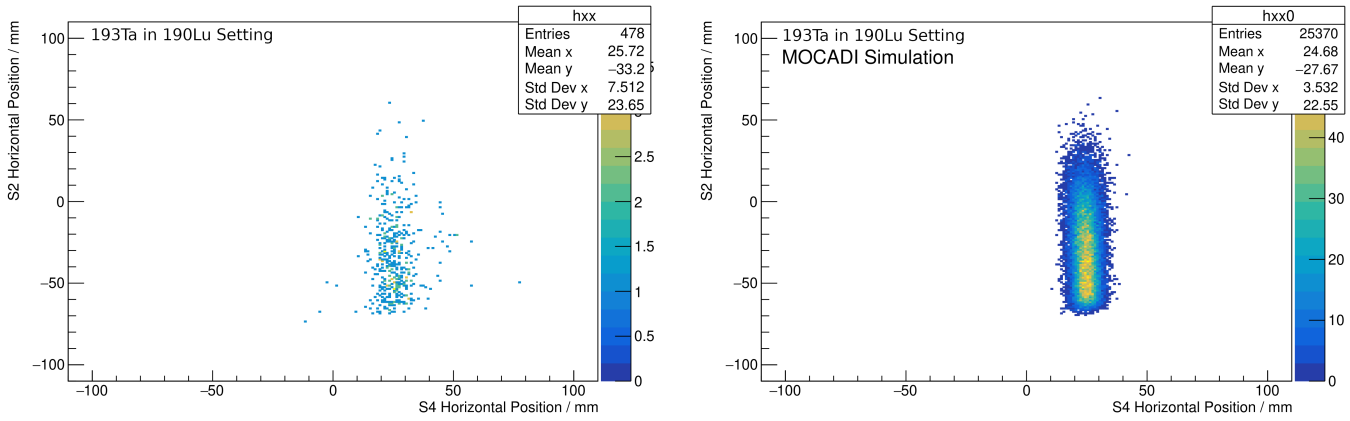


**Figure 13.52.:** S2 horizontal position plotted over S4 horizontal position for experimentally measured (left) and simulated (right) spectra. The experimental position of 25.21(29) mm at S4 agrees quite well with MOCADI.

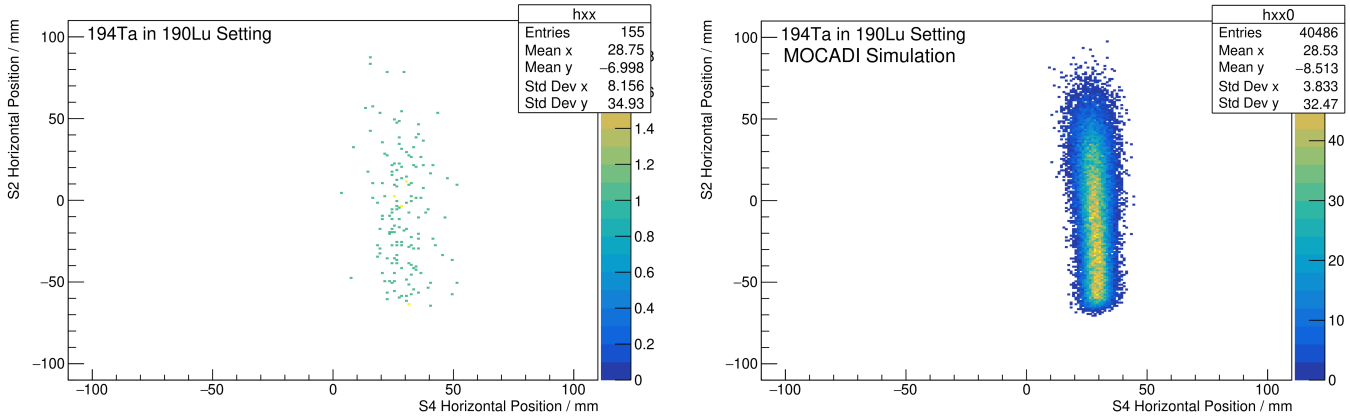


**Figure 13.53.:** S2 horizontal position plotted over S4 horizontal position for experimentally measured (left) and simulated (right) spectra. The experimental position of 27.81(83) mm at S4 agrees quite well with MOCADI.

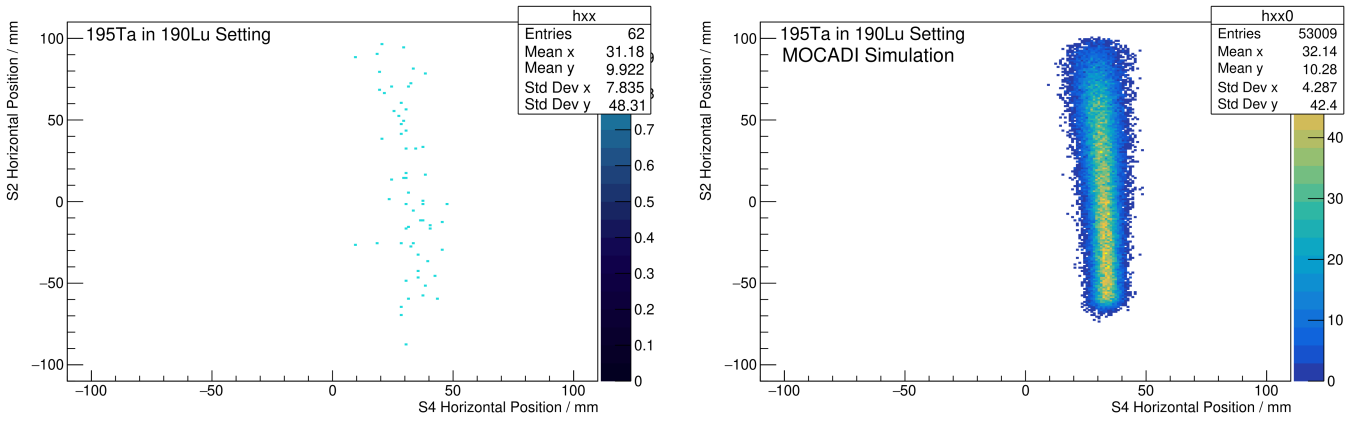


**Figure 13.54.:** S2 horizontal position plotted over S4 horizontal position for experimentally measured (left) and simulated (right) spectra. The experimental position of 31.58(353) $\mathrm{mm}$ at S4 agrees with MOCADI but the statistics are starting to break down.

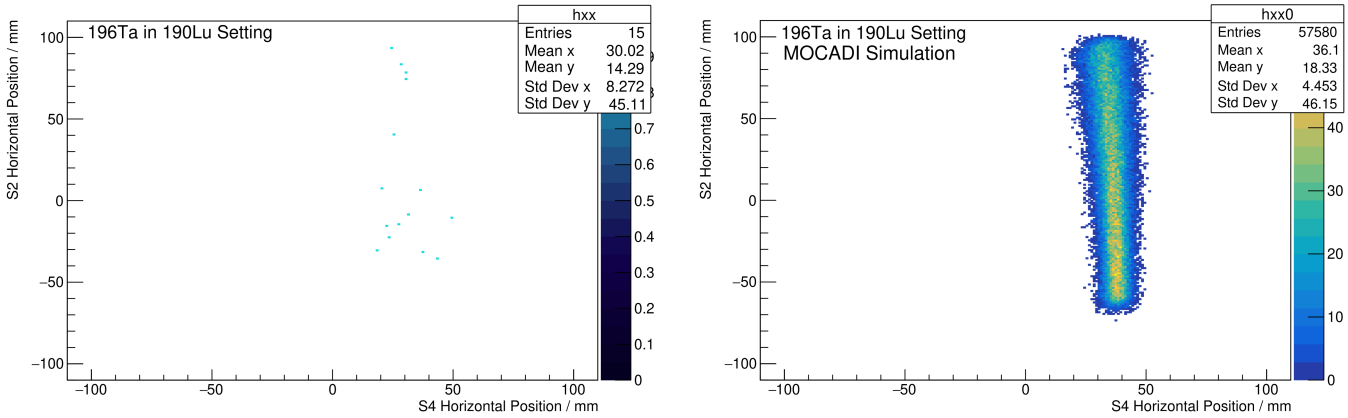


**Figure 13.55.:** S2 horizontal position plotted over S4 horizontal position for experimentally measured (left) and simulated (right) spectra. The experimental positioning at S4 (left) can not be determined via fitting due to the low statistics.

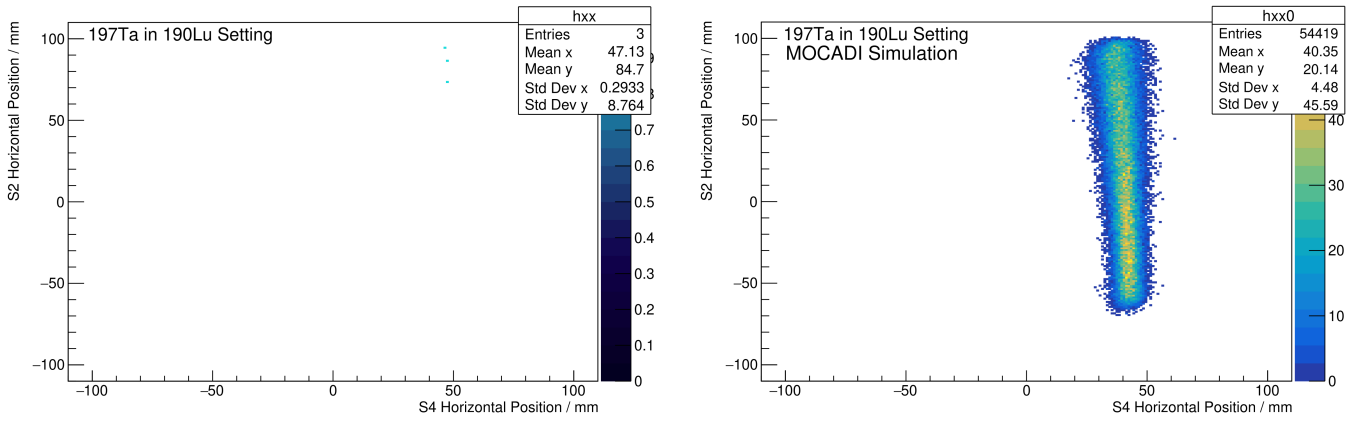


**Figure 13.56.:** S2 horizontal position plotted over S4 horizontal position for experimentally measured (left) and simulated (right) spectra. The experimental positioning at S4 (left) can not be determined via fitting due to the low statistics.

| Isotope | $^{195}$Ta | $^{196}$Ta | $^{197}$Ta |
|---|---|---|---|
| Counts | 58(8) | 13(4) | 3(2) |

**Table 13.3.:** Final counts for the new discovered $^{195}$Ta, $^{196}$Ta and $^{197}$Ta isotopes. It can be seen in Fig. 13.26 that for the elements tantalum and below, the background is significalnty reduced on the side of heavier isotopes and only dominant on the lighter side. Thus a background of 0 counts in this region has been determined for all subsequent elements.

### 13.2.5. Hf Isotopes

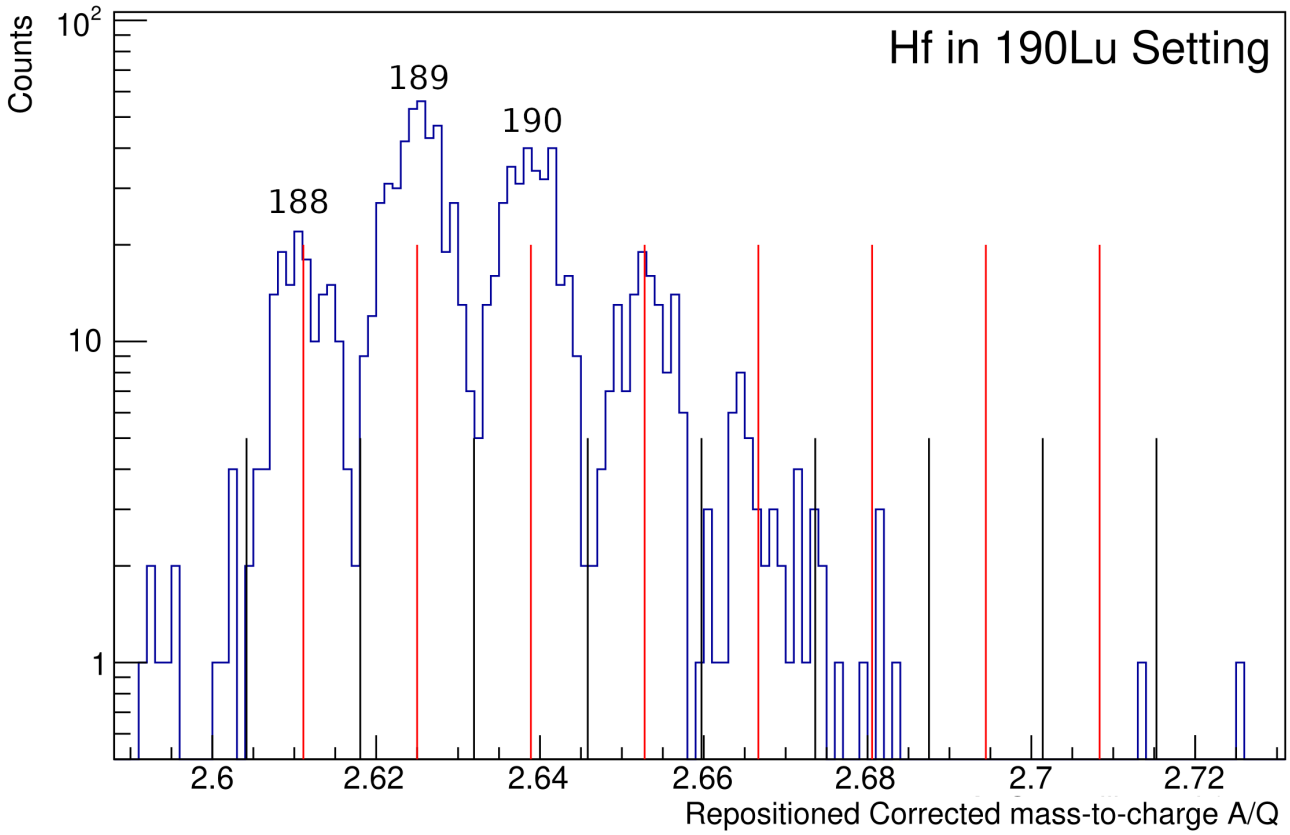


**Figure 13.57.:** AoQ spectrum for hafnium isotopes in the $^{190}$Lu setting together with theoretical isotopic AoQ values (red lines) and predefined selection intervals (black lines). The strongest peak in this distribution corresponds to $^{189}$Hf, which can be additionally confirmed by Fig. 13.59.

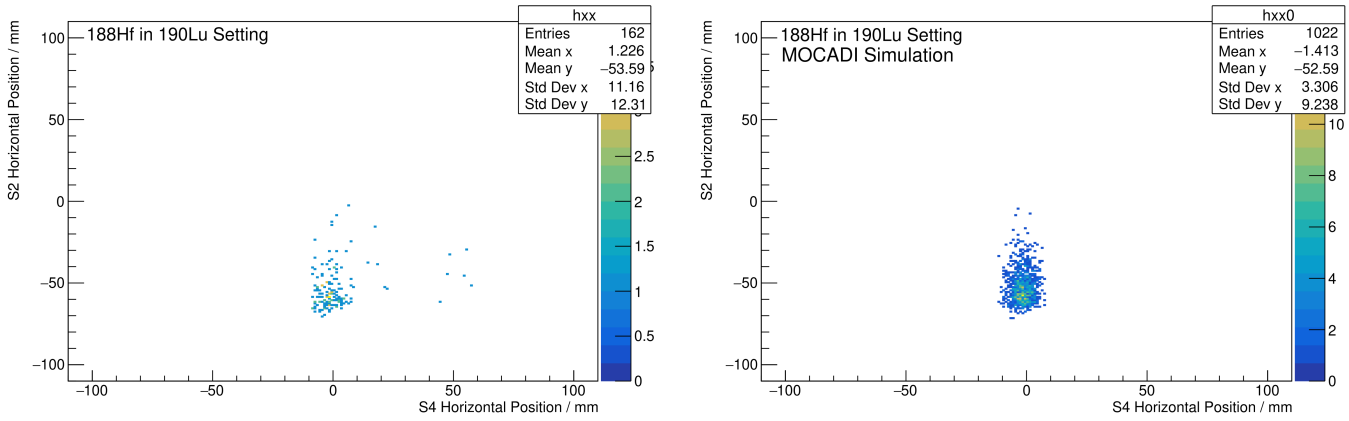


**Figure 13.58.:** S2 horizontal position plotted over S4 horizontal position for experimentally measured (left) and simulated (right) spectra. The experimental position of -1.55(75) mm at S4 agrees quite well with MOCADI.

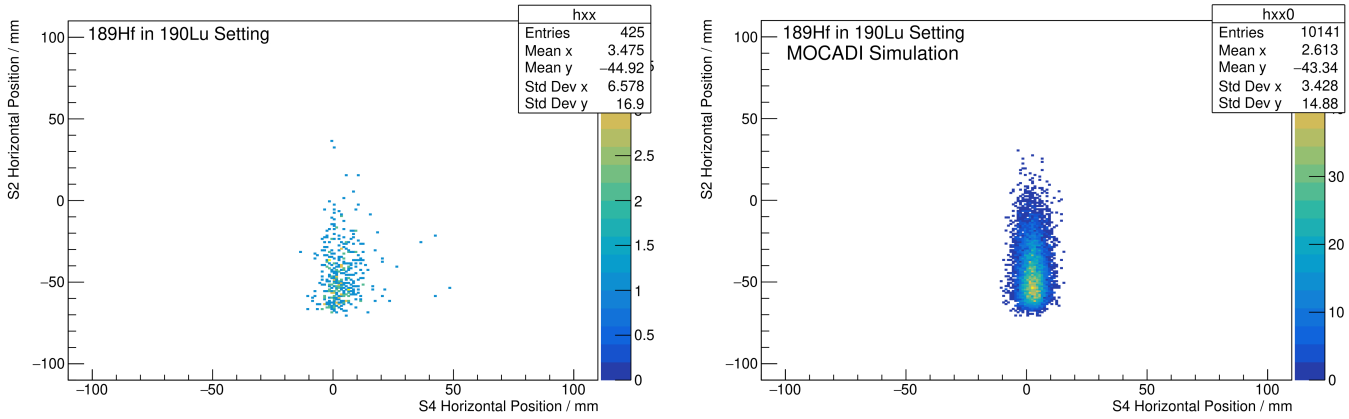


**Figure 13.59.:** S2 horizontal position plotted over S4 horizontal position for experimentally measured (left) and simulated (right) spectra. The experimental position of 2.36(31) mm at S4 agrees quite well with MOCADI.

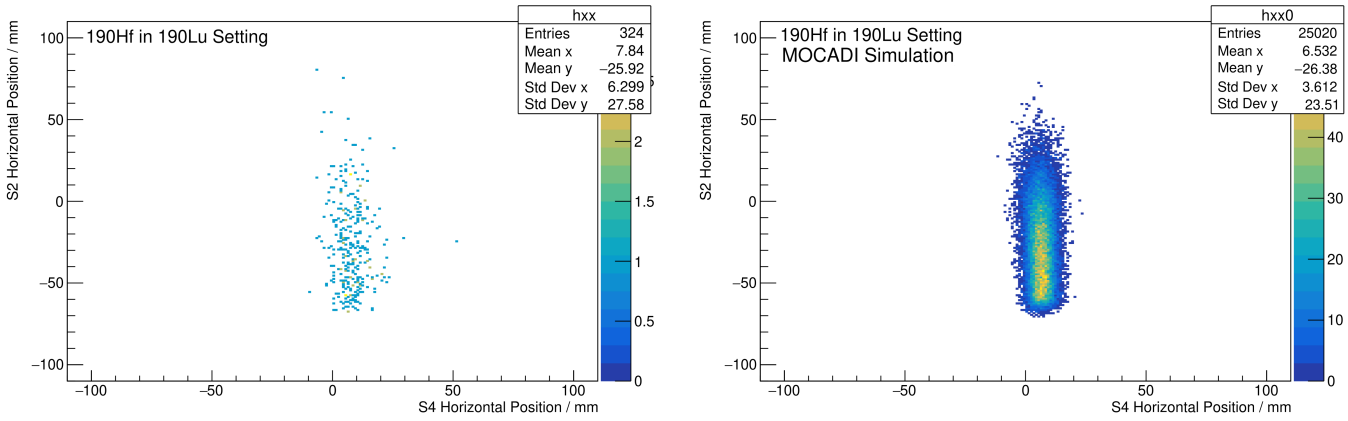


**Figure 13.60.:** S2 horizontal position plotted over S4 horizontal position for experimentally measured (left) and simulated (right) spectra. The experimental position of 7.51(31) $\mathrm{mm}$ at S4 agrees quite well with MOCADI.

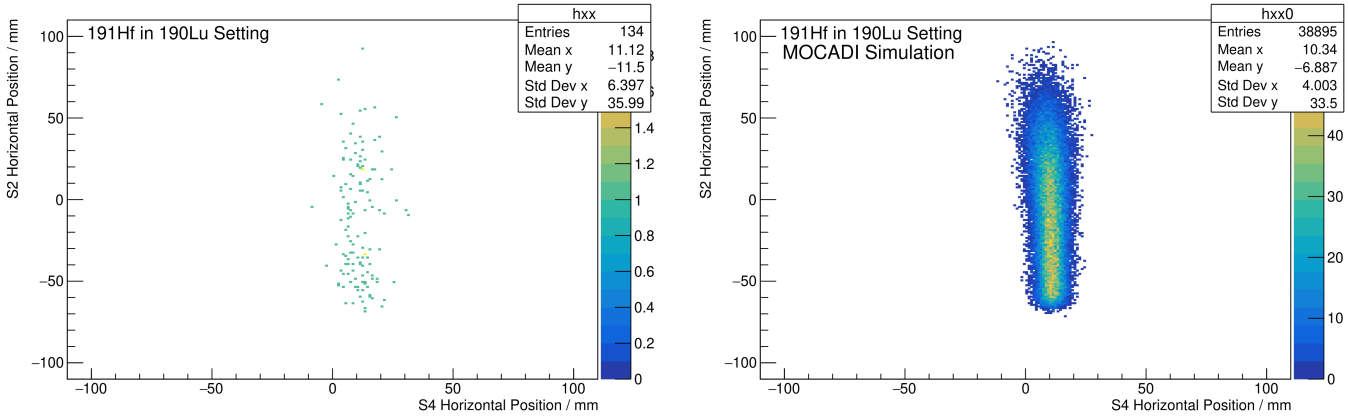


**Figure 13.61.:** S2 horizontal position plotted over S4 horizontal position for experimentally measured (left) and simulated (right) spectra. The experimental position of 10.69(58) $\mathrm{mm}$ at S4 agrees quite well with MOCADI.

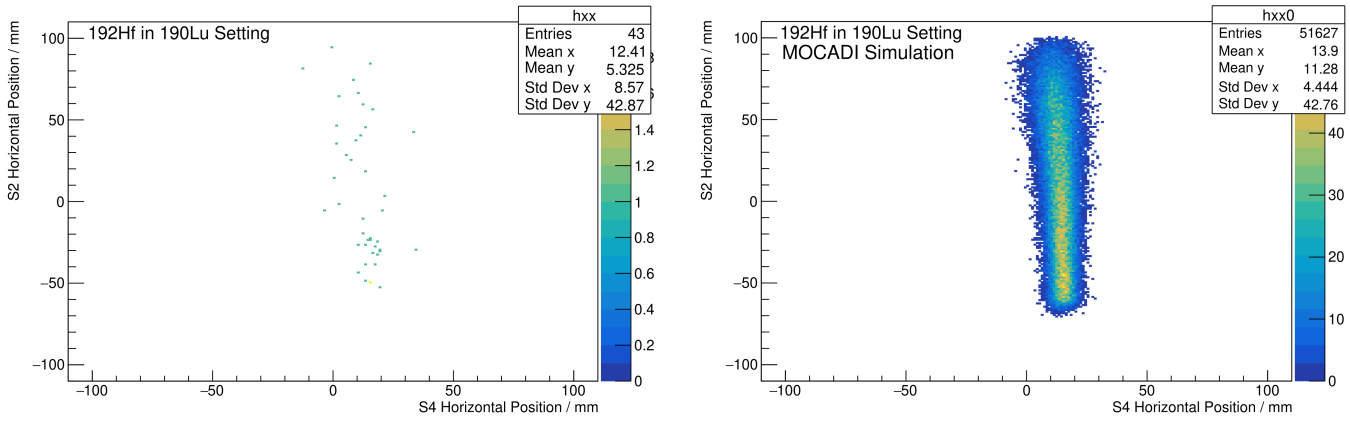


**Figure 13.62.:** S2 horizontal position plotted over S4 horizontal position for experimentally measured (left) and simulated (right) spectra. The experimental position of 15.44(830) $\mathrm{mm}$ at S4 agrees with MOCADI.

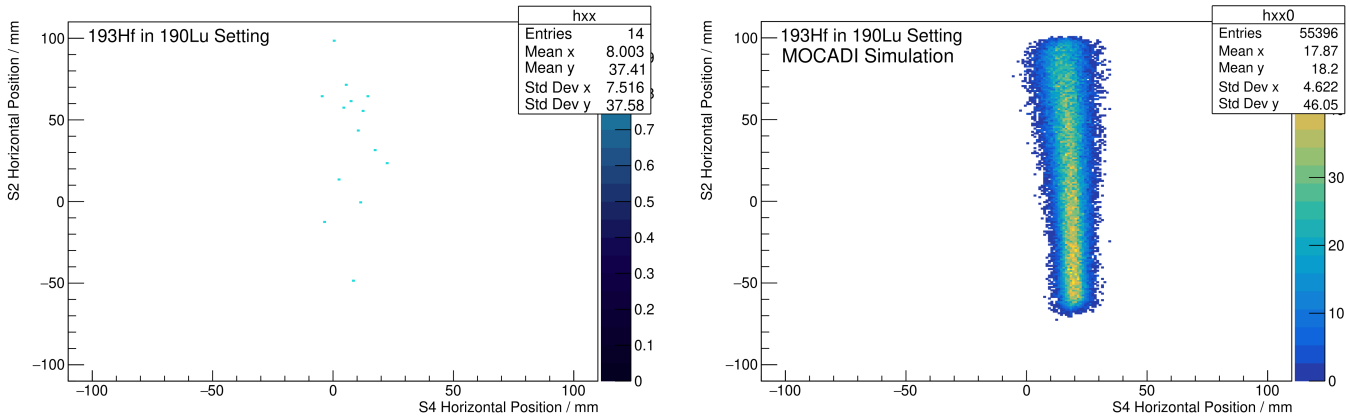


**Figure 13.63.:** S2 horizontal position plotted over S4 horizontal position for experimentally measured (left) and simulated (right) spectra. The experimental positioning can not be accurately determined via fitting due to the low statistics.

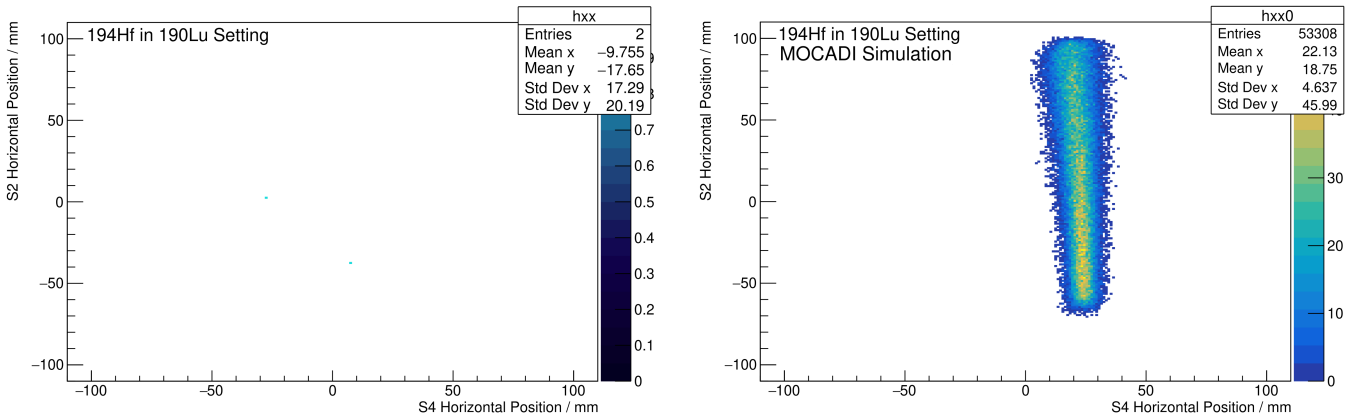


**Figure 13.64.:** S2 horizontal position plotted over S4 horizontal position for experimentally measured (left) and simulated (right) spectra. The experimental positioning can not be accurately determined via fitting due to the low statistics.

| Isotope | $^{191}$Hf | $^{192}$Hf | $^{193}$Hf | $^{194}$Hf |
|---|---|---|---|---|
| Counts | 125(11) | 38(6) | 12(3) | 1(1) |

**Table 13.4.:** Final counts for the new discovered $^{191}$Hf, $^{192}$Hf and $^{193}$Hf isotopes. $^{194}$Hf with only 1 count can not be confirmed according to [115], since 3 counts are required.

### 13.2.6. Lu Isotopes

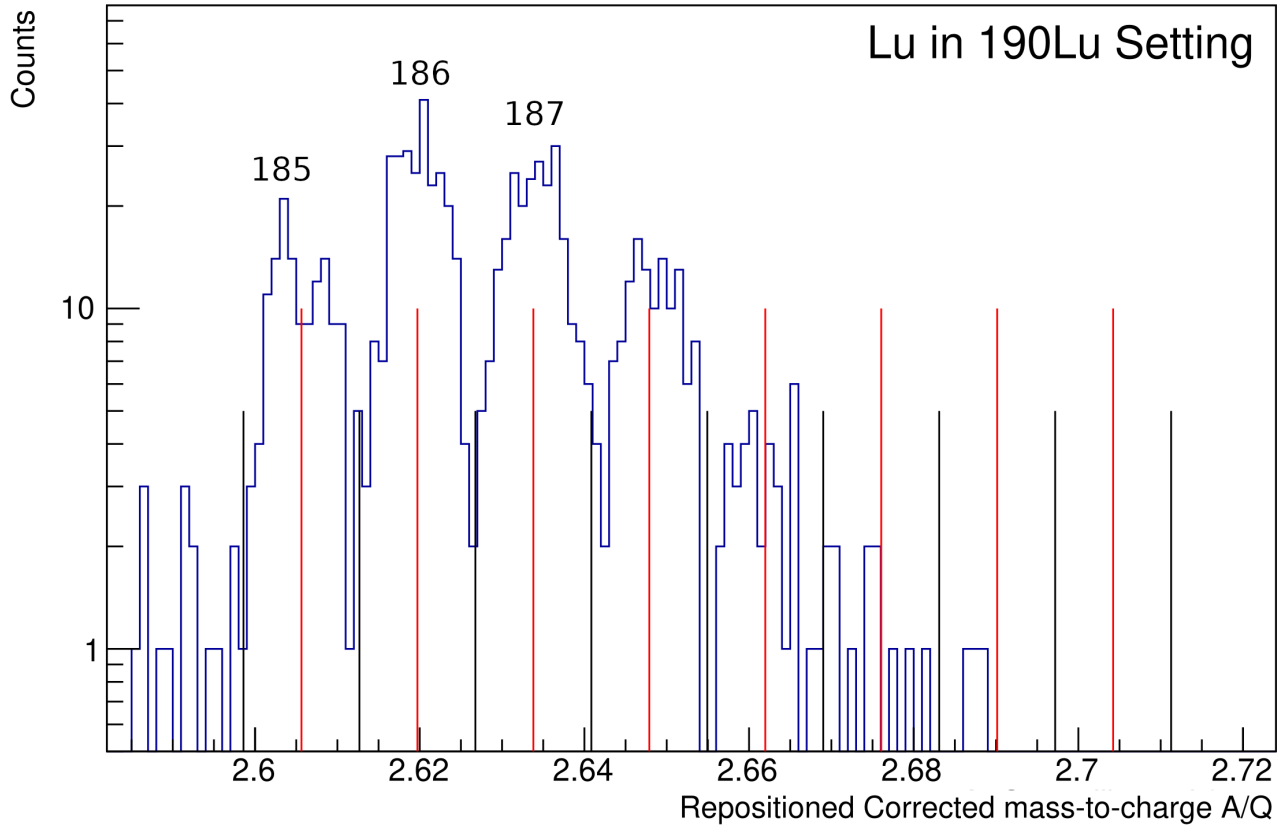


**Figure 13.65.:** AoQ spectrum for lutetium isotopes in the $^{190}$Lu setting together with theoretical isotopic AoQ values (red lines) and predefined selection intervals (black lines). The strongest peak in this distribution corresponds to $^{186}$Lu, which can be additionally confirmed by Fig. 13.67.

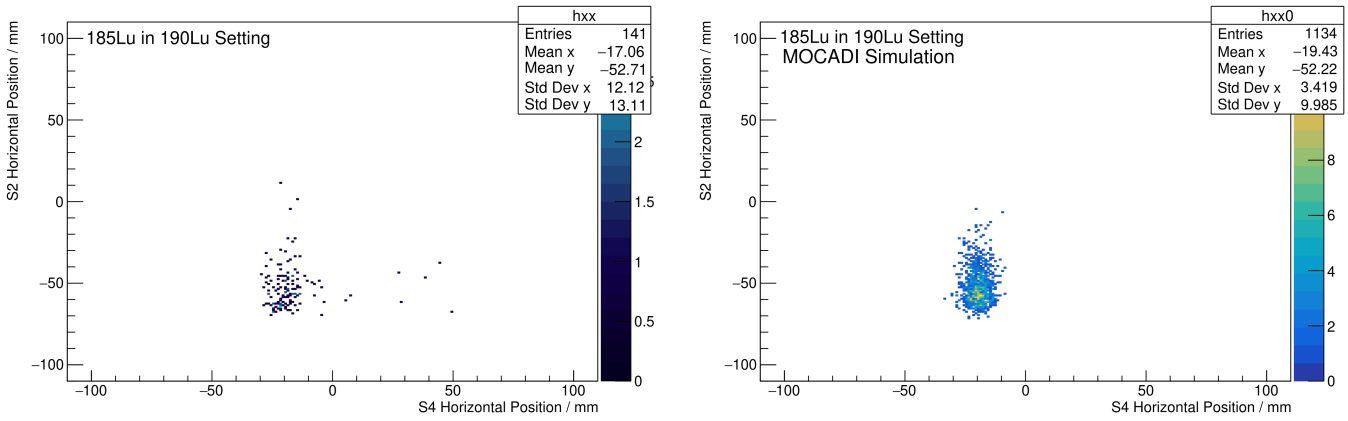


**Figure 13.66.:** S2 horizontal position plotted over S4 horizontal position for experimentally measured (left) and simulated (right) spectra. The experimental position of -19.12(79) mm at S4 agrees quite well with MOCADI.

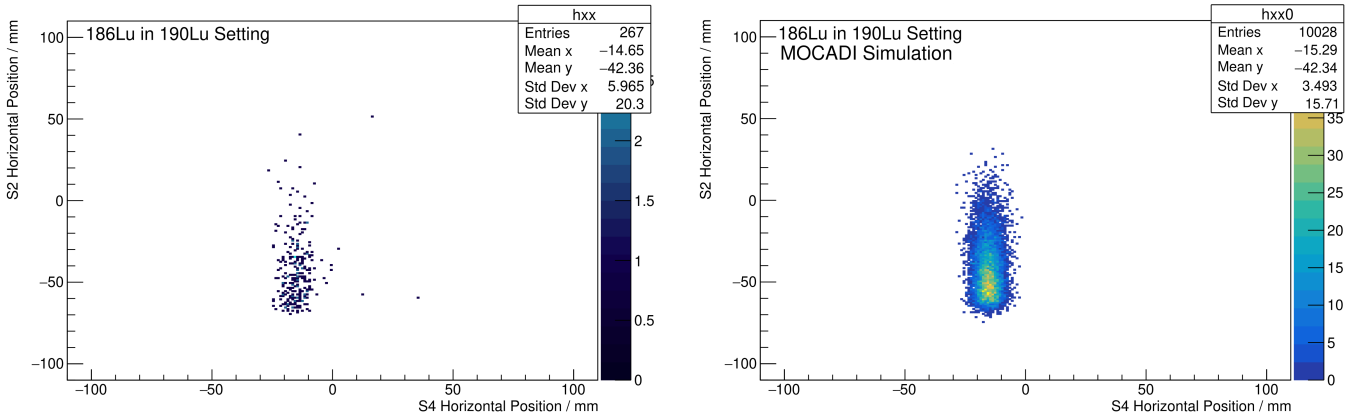


**Figure 13.67.:** S2 horizontal position plotted over S4 horizontal position for experimentally measured (left) and simulated (right) spectra. The experimental position of -15.22(29) mm at S4 agrees quite well with MOCADI.

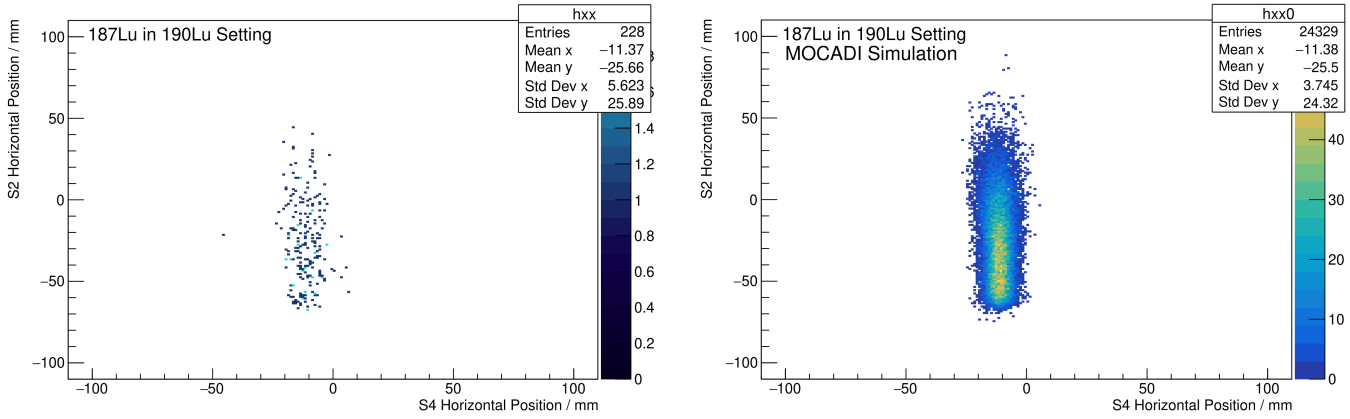


**Figure 13.68.:** S2 horizontal position plotted over S4 horizontal position for experimentally measured (left) and simulated (right) spectra. The experimental position of -11.61(35) $\mathrm{mm}$ at S4 agrees quite well with MOCADI.

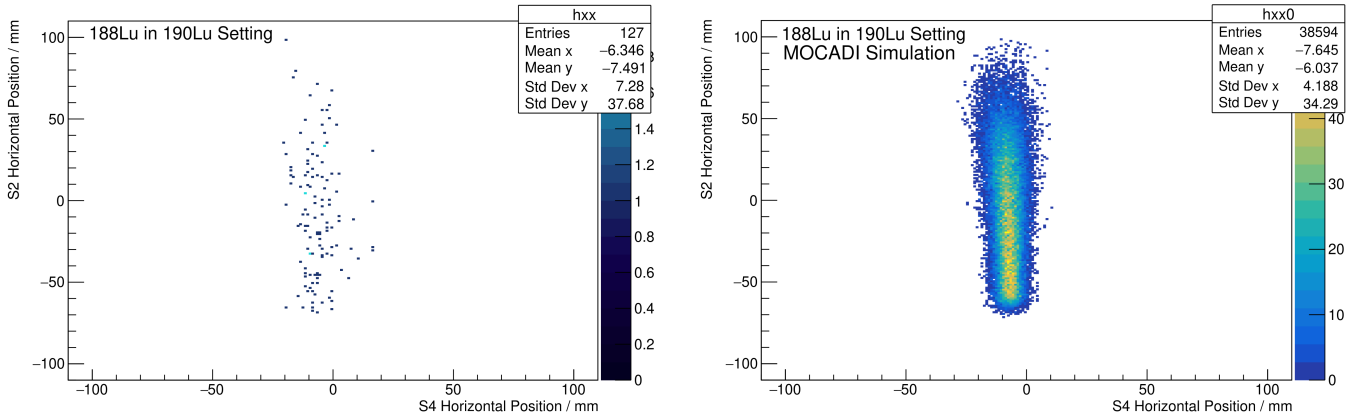


**Figure 13.69.:** S2 horizontal position plotted over S4 horizontal position for experimentally measured (left) and simulated (right) spectra. The experimental position of -6.12(70) $\mathrm{mm}$ at S4 agrees quite well with MOCADI.

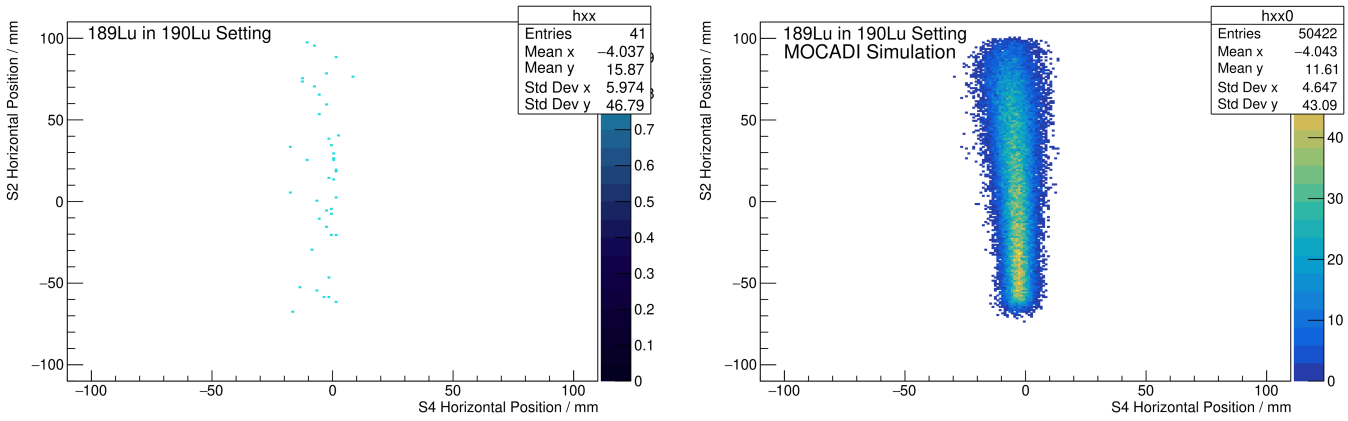


**Figure 13.70.:** S2 horizontal position plotted over S4 horizontal position for experimentally measured (left) and simulated (right) spectra. The experimental position of -3.99(530) $\mathrm{mm}$ at S4 agrees with MOCADI.

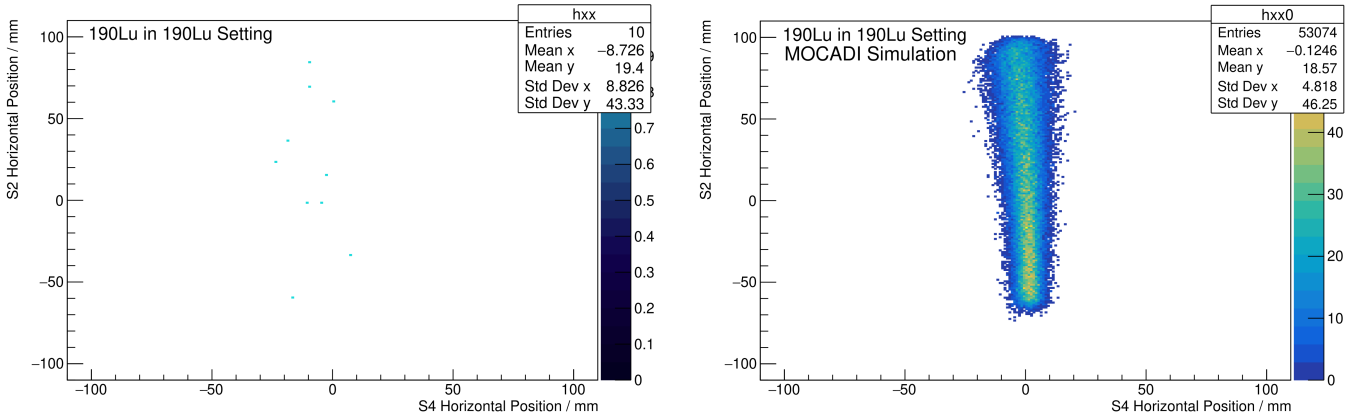


**Figure 13.71.:** S2 horizontal position plotted over S4 horizontal position for experimentally measured (left) and simulated (right) spectra. The experimental positioning can not be accurately determined via fitting due to the low statistics.

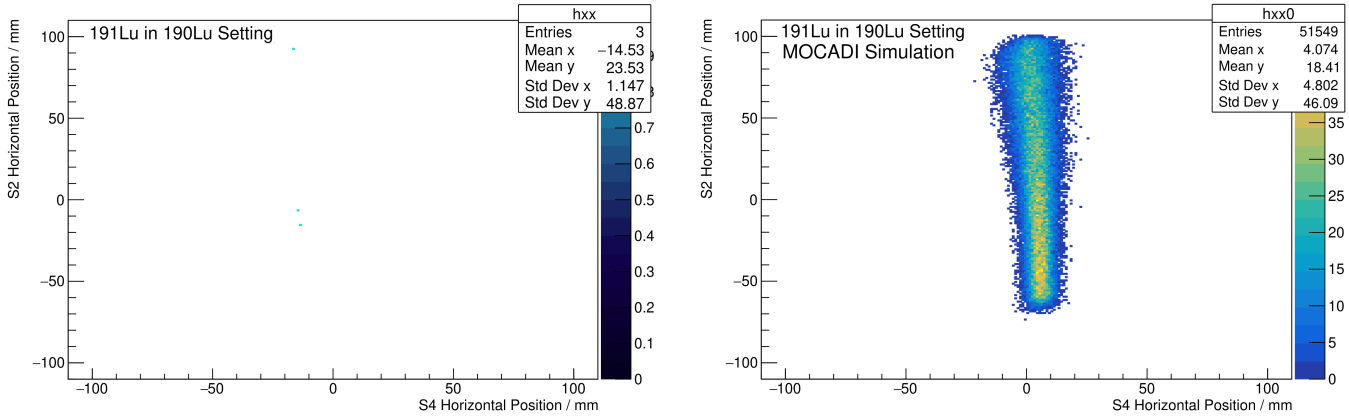


**Figure 13.72.:** S2 horizontal position plotted over S4 horizontal position for experimentally measured (left) and simulated (right) spectra. The experimental positioning can not be accurately determined via fitting due to the low statistics.

| Isotope | $^{189}$Lu | $^{190}$Lu | $^{191}$Lu |
|---|---|---|---|
| Counts | 40(6) | 9(3) | 3(2) |

**Table 13.5.:** Final counts for the new discovered $^{189}$Lu, $^{190}$Lu and $^{191}$Lu isotopes.

### 13.2.7. Yb Isotopes

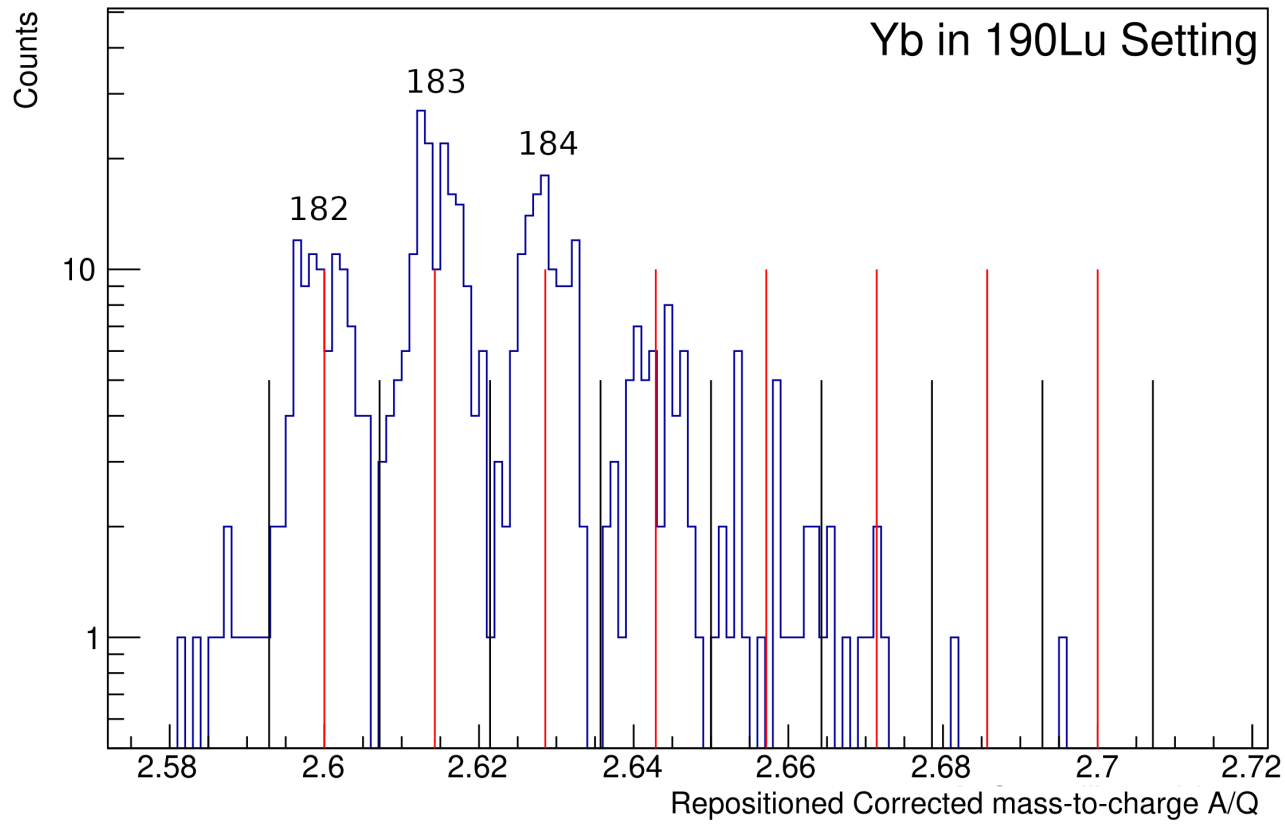


**Figure 13.73.:** AoQ spectrum for ytterbium isotopes in the $^{190}$Lu setting together with theoretical isotopic AoQ values (red lines) and predefined selection intervals (black lines). The strongest peak in this distribution corresponds to $^{183}$Yb, which can be additionally confirmed by Fig. 13.75.

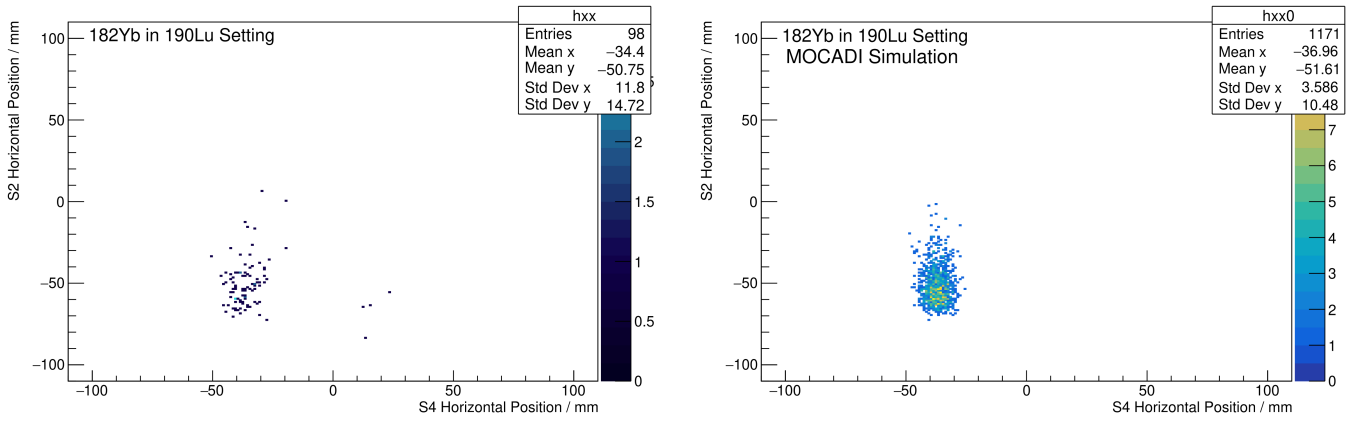


**Figure 13.74.:** S2 horizontal position plotted over S4 horizontal position for experimentally measured (left) and simulated (right) spectra. The experimental position of -36.72(66) $\mathrm{mm}$ at S4 agrees quite well with MOCADI.

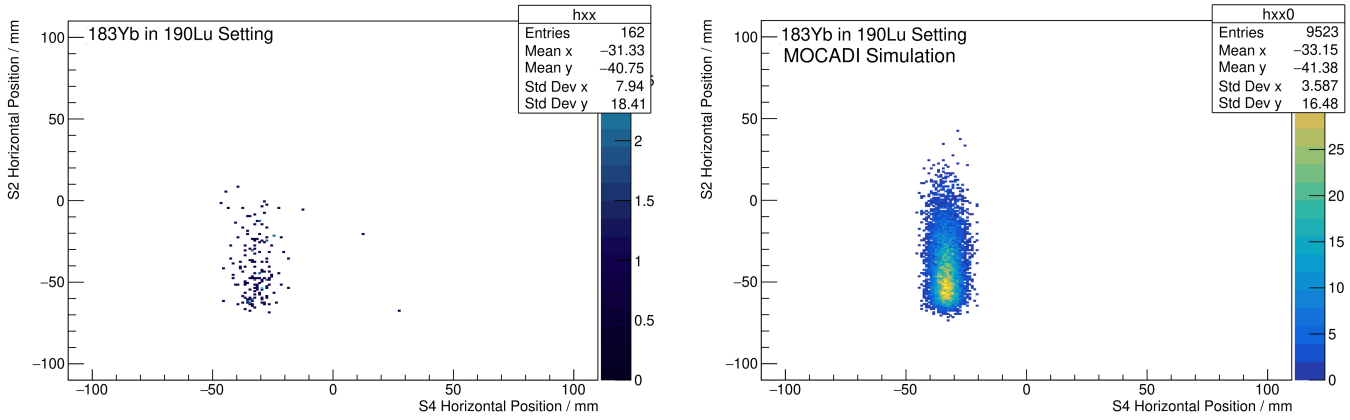


**Figure 13.75.:** S2 horizontal position plotted over S4 horizontal position for experimentally measured (left) and simulated (right) spectra. The experimental position of -32.22(43) $\mathrm{mm}$ at S4 agrees quite well with MOCADI.

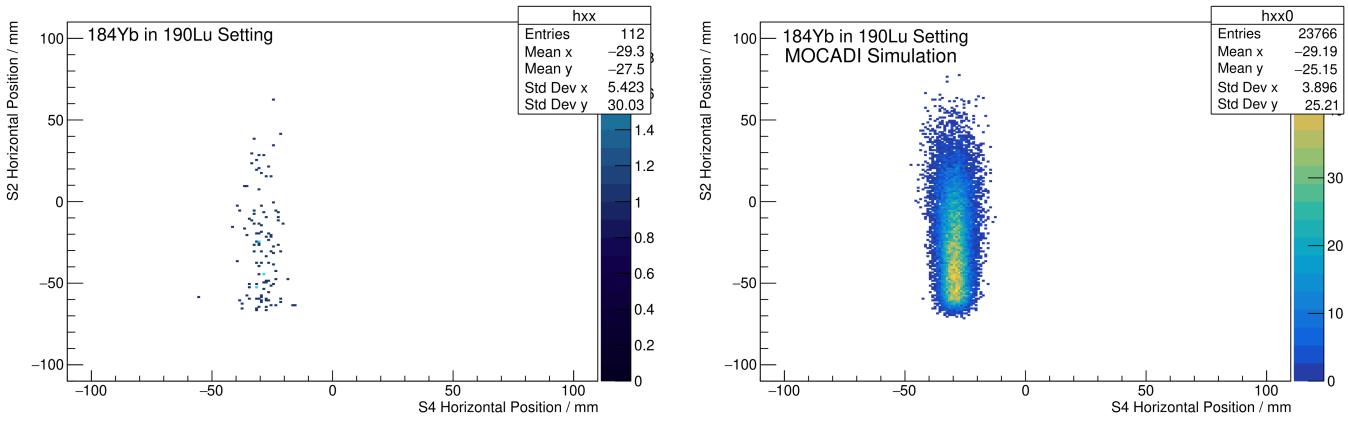


**Figure 13.76.:** S2 horizontal position plotted over S4 horizontal position for experimentally measured (left) and simulated (right) spectra. The experimental position of -28.85(84) mm at S4 agrees quite well with MOCADI.

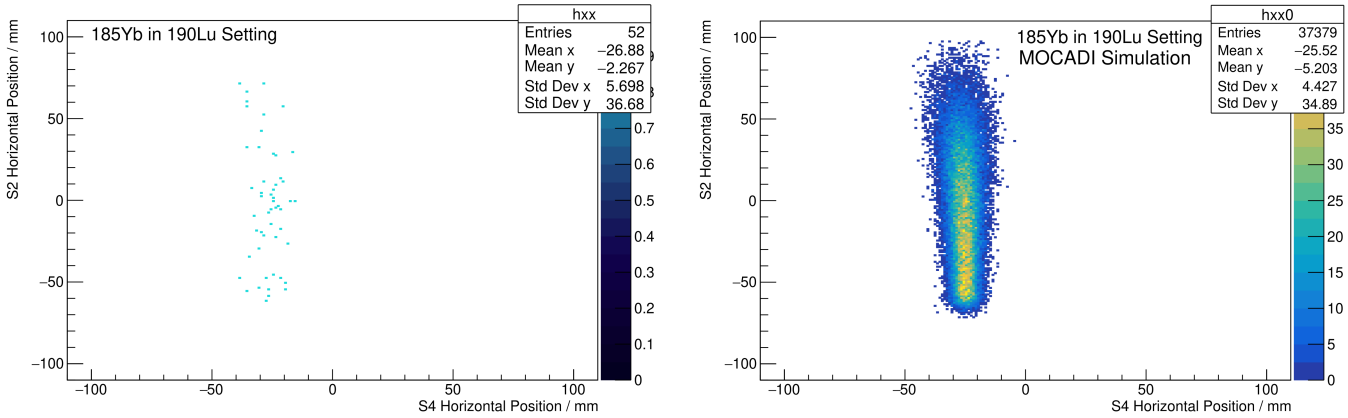


**Figure 13.77.:** S2 horizontal position plotted over S4 horizontal position for experimentally measured (left) and simulated (right) spectra. The experimental position of -26.00(130) mm at S4 agrees well with MOCADI.

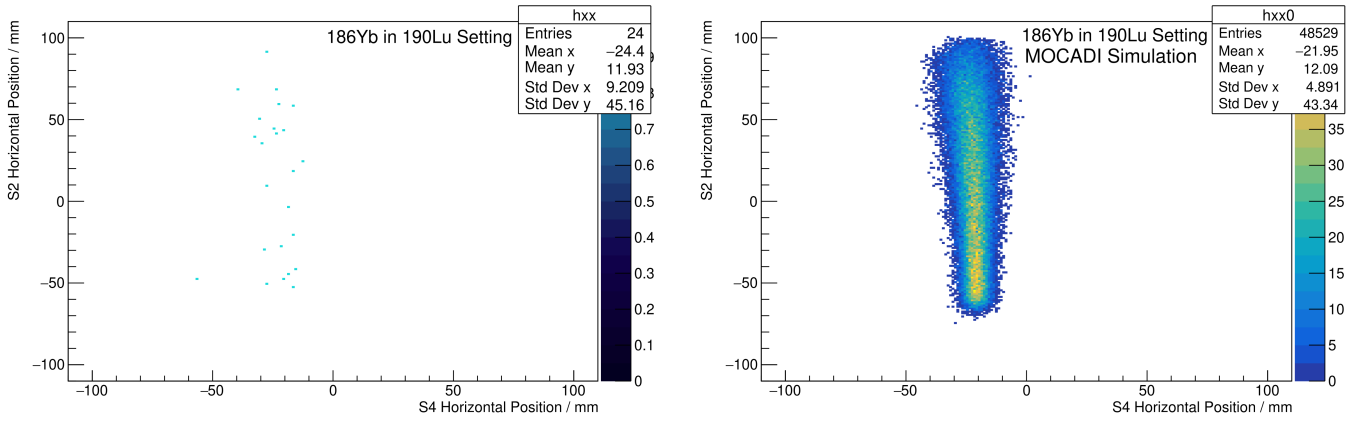


**Figure 13.78.:** S2 horizontal position plotted over S4 horizontal position for experimentally measured (left) and simulated (right) spectra. The experimental position of -19.23(770) $\mathrm{mm}$ at S4 agrees with MOCADI.

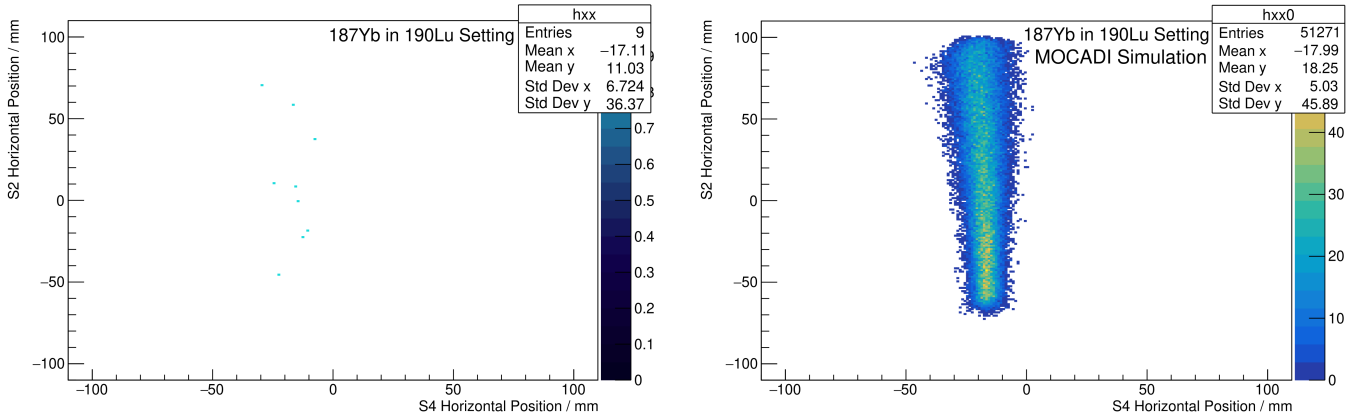


**Figure 13.79.:** S2 horizontal position plotted over S4 horizontal position for experimentally measured (left) and simulated (right) spectra. The experimental positioning can not be accurately determined via fitting due to the low statistics.

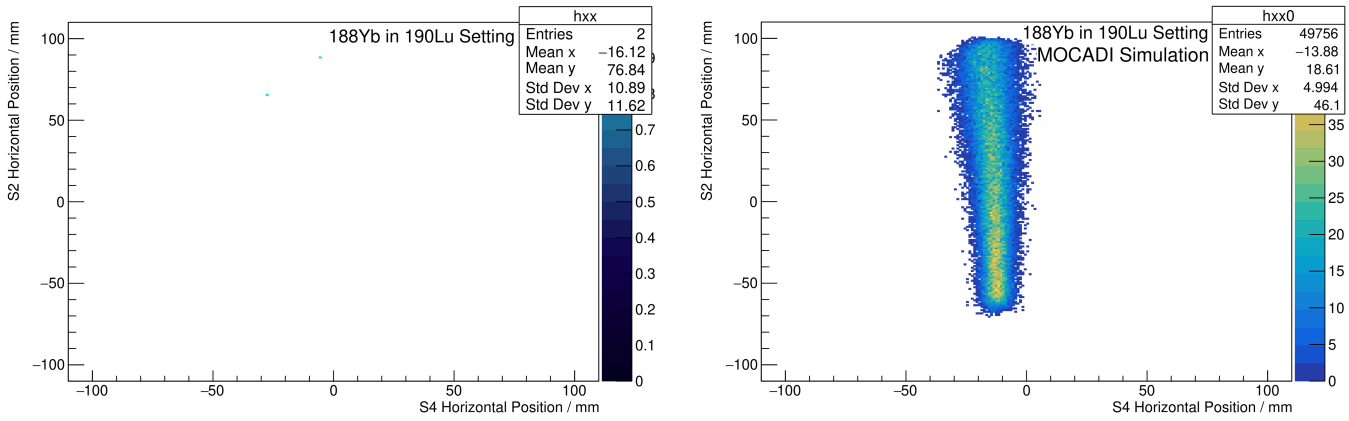


**Figure 13.80.:** S2 horizontal position plotted over S4 horizontal position for experimentally measured (left) and simulated (right) spectra. The experimental positioning can not be accurately determined via fitting due to the low statistics.

| Isotope | $^{186}$Yb | $^{187}$Yb | $^{188}$Yb |
|---|---|---|---|
| Counts | 23(5) | 9(3) | 2(1) |

**Table 13.6.:** Final counts for the new discovered $^{186}$Yb and $^{187}$Yb isotopes. $^{188}$Yb with only 2 counts can not be confirmed according to [115], since 3 counts are required.

### 13.2.8. Tm Isotopes

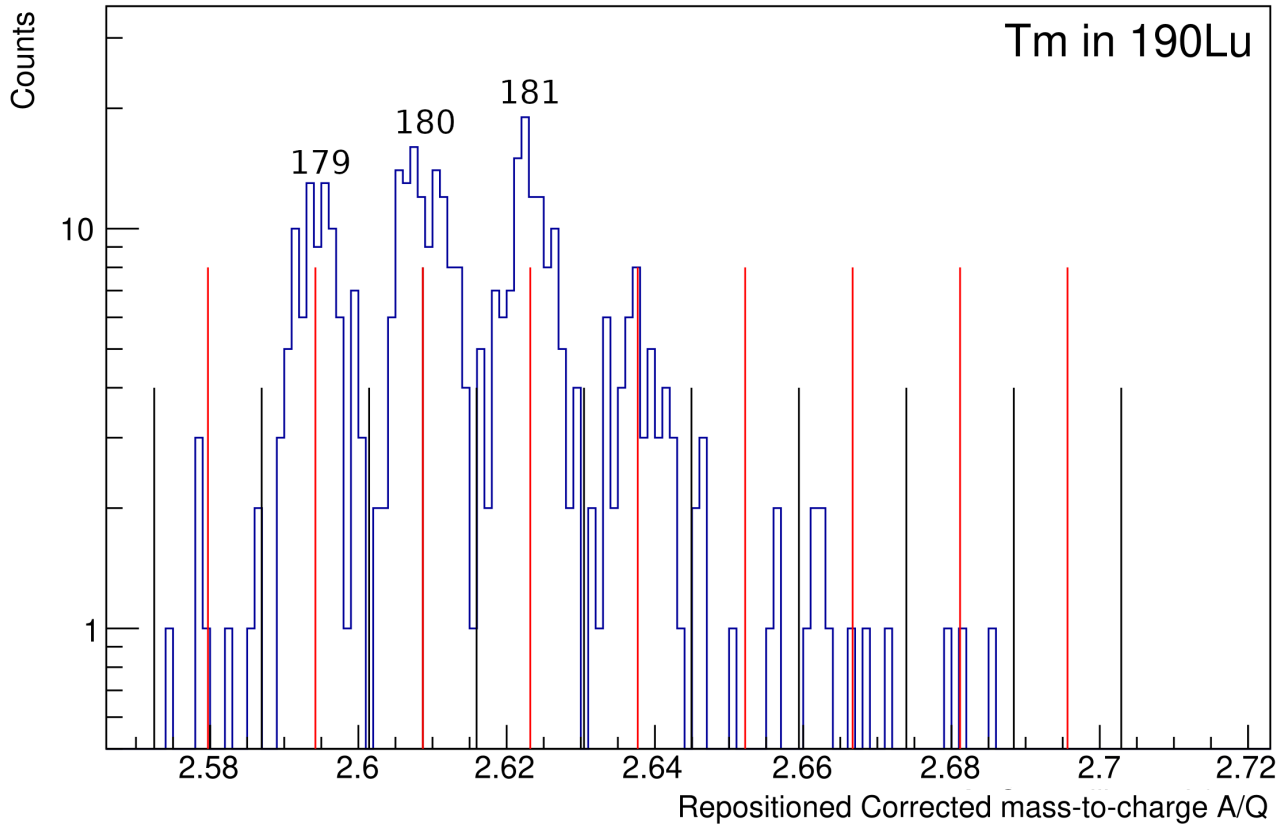


**Figure 13.81.:** AoQ spectrum for thulium isotopes in the $^{190}$Lu setting together with theoretical isotopic AoQ values (red lines) and predefined selection intervals (black lines). The strongest peak in this distribution corresponds to $^{180}$Tm, which can be additionally confirmed by Fig. 13.83.

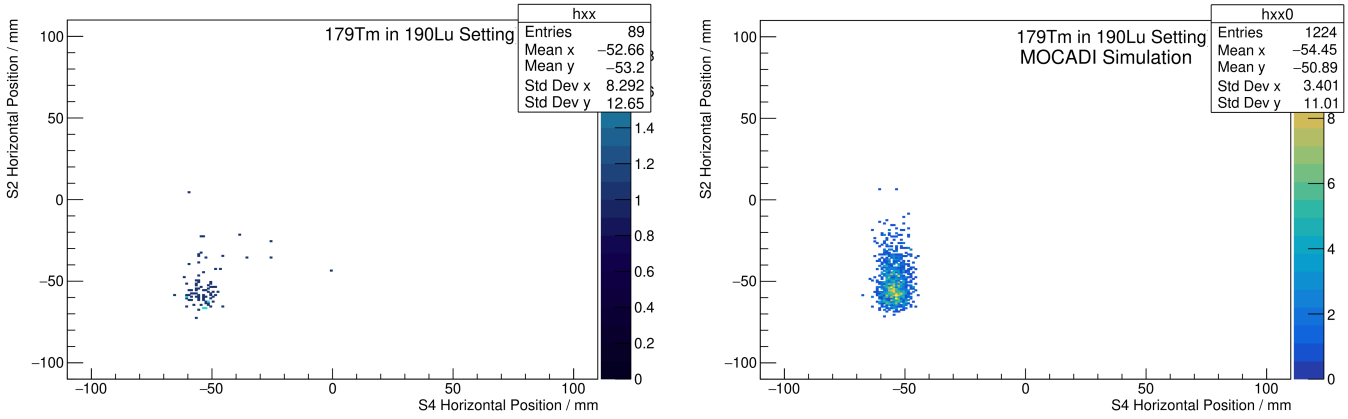


**Figure 13.82.:** S2 horizontal position plotted over S4 horizontal position for experimentally measured (left) and simulated (right) spectra. The experimental position of -53.90(59) mm at S4 agrees quite well with MOCADI.

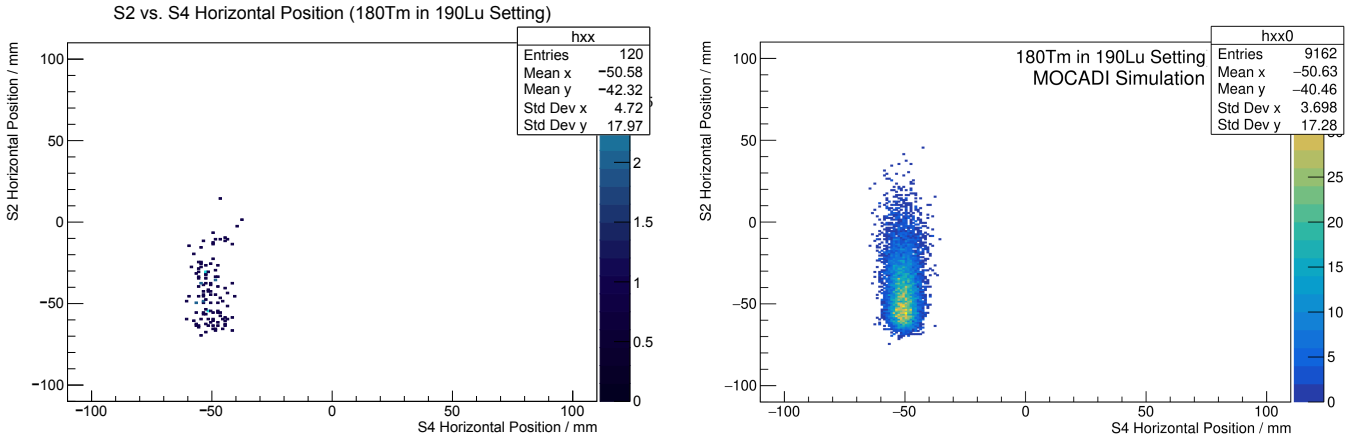


**Figure 13.83.:** S2 horizontal position plotted over S4 horizontal position for experimentally measured (left) and simulated (right) spectra. The experimental position of -50.61(55) mm at S4 agrees quite well with MOCADI.

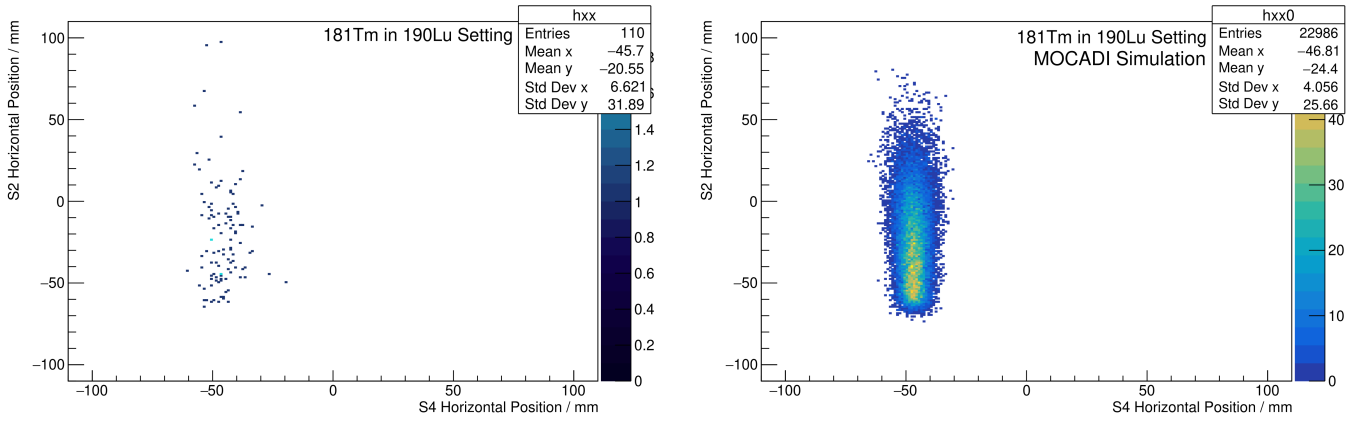


**Figure 13.84.:** S2 horizontal position plotted over S4 horizontal position for experimentally measured (left) and simulated (right) spectra. The experimental position of -46.01(86) $\mathrm{mm}$ at S4 agrees quite well with MOCADI.

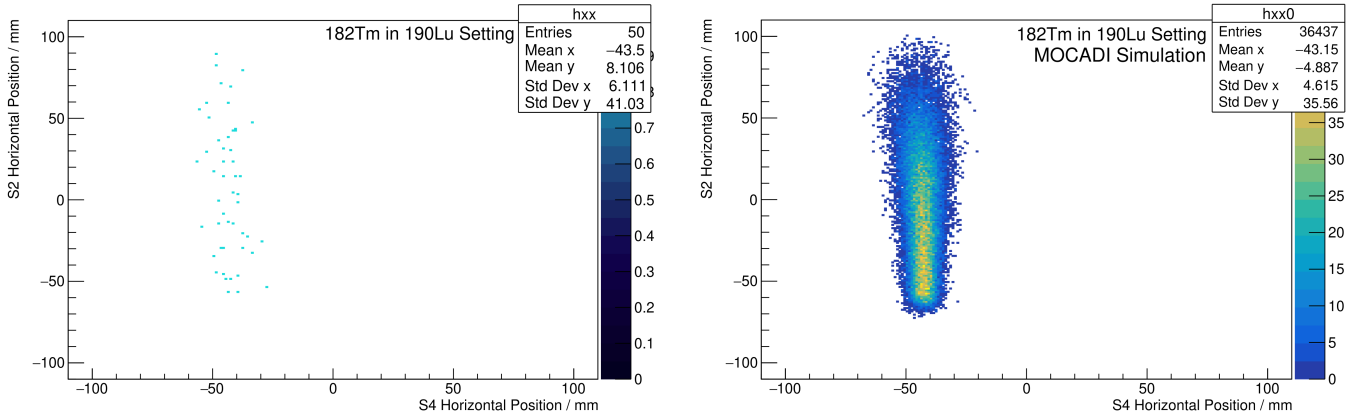


**Figure 13.85.:** S2 horizontal position plotted over S4 horizontal position for experimentally measured (left) and simulated (right) spectra. The experimental position of -43.09(230) at S4 $\mathrm{mm}$ agrees with MOCADI.

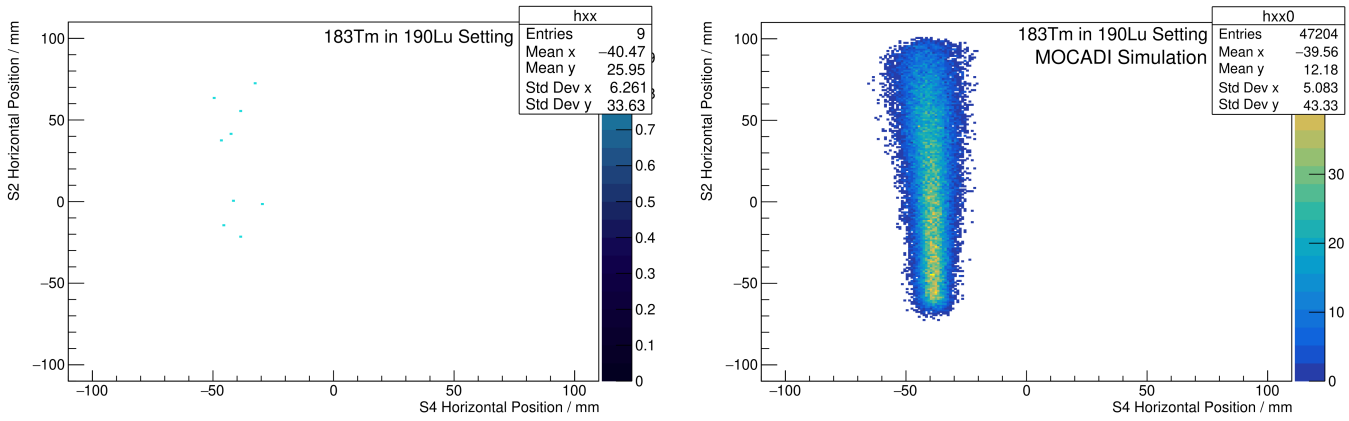


**Figure 13.86.:** S2 horizontal position plotted over S4 horizontal position for experimentally measured (left) and simulated (right) spectra. The experimental positioning can not be accurately determined via fitting due to the low statistics.

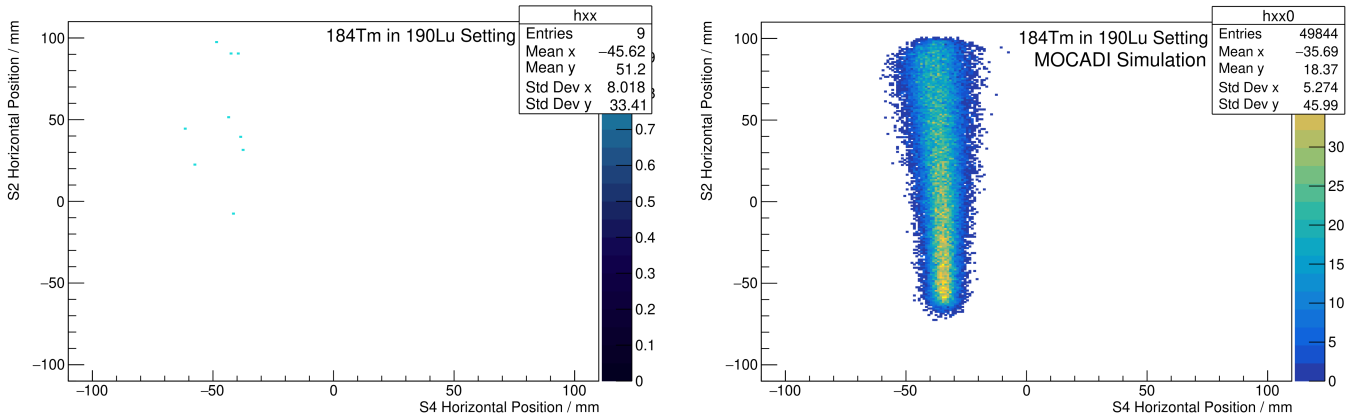


**Figure 13.87.:** S2 horizontal position plotted over S4 horizontal position for experimentally measured (left) and simulated (right) spectra. The experimental positioning in (a) can not be accurately determined via fitting due to the low statistics.

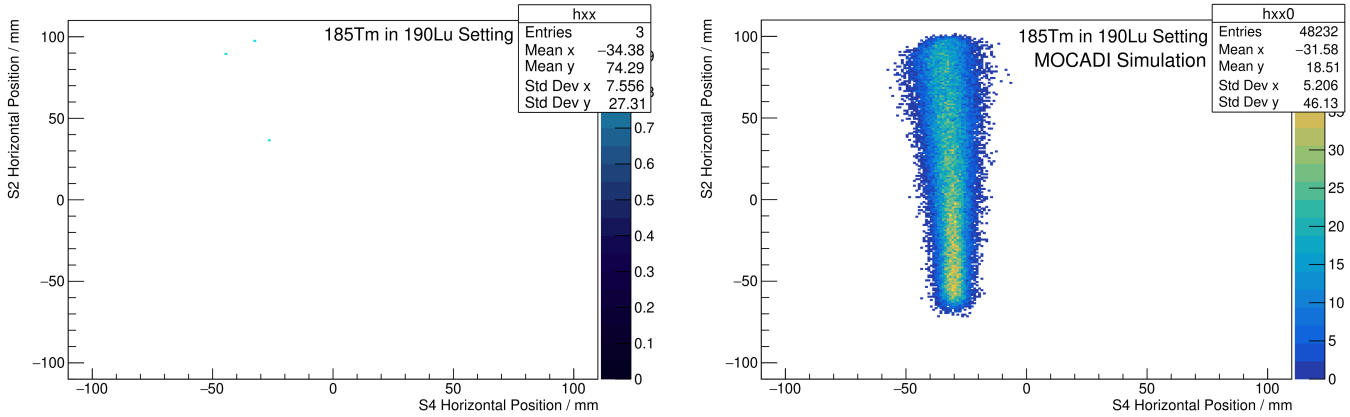


**Figure 13.88.:** S2 horizontal position plotted over S4 horizontal position for experimentally measured (left) and simulated (right) spectra. The experimental positioning can not be accurately determined via fitting due to the low statistics.

| Isotope | $^{182}$Tm | $^{183}$Tm | $^{184}$Tm | $^{185}$Tm |
|---|---|---|---|---|
| Counts | 47(7) | 9(3) | 7(3) | 3(2) |

**Table 13.7.:** Final counts for the new discovered $^{182}$Tm, $^{183}$Tm, $^{184}$Tm and $^{185}$Tm isotopes.

### 13.2.9. Er Isotopes

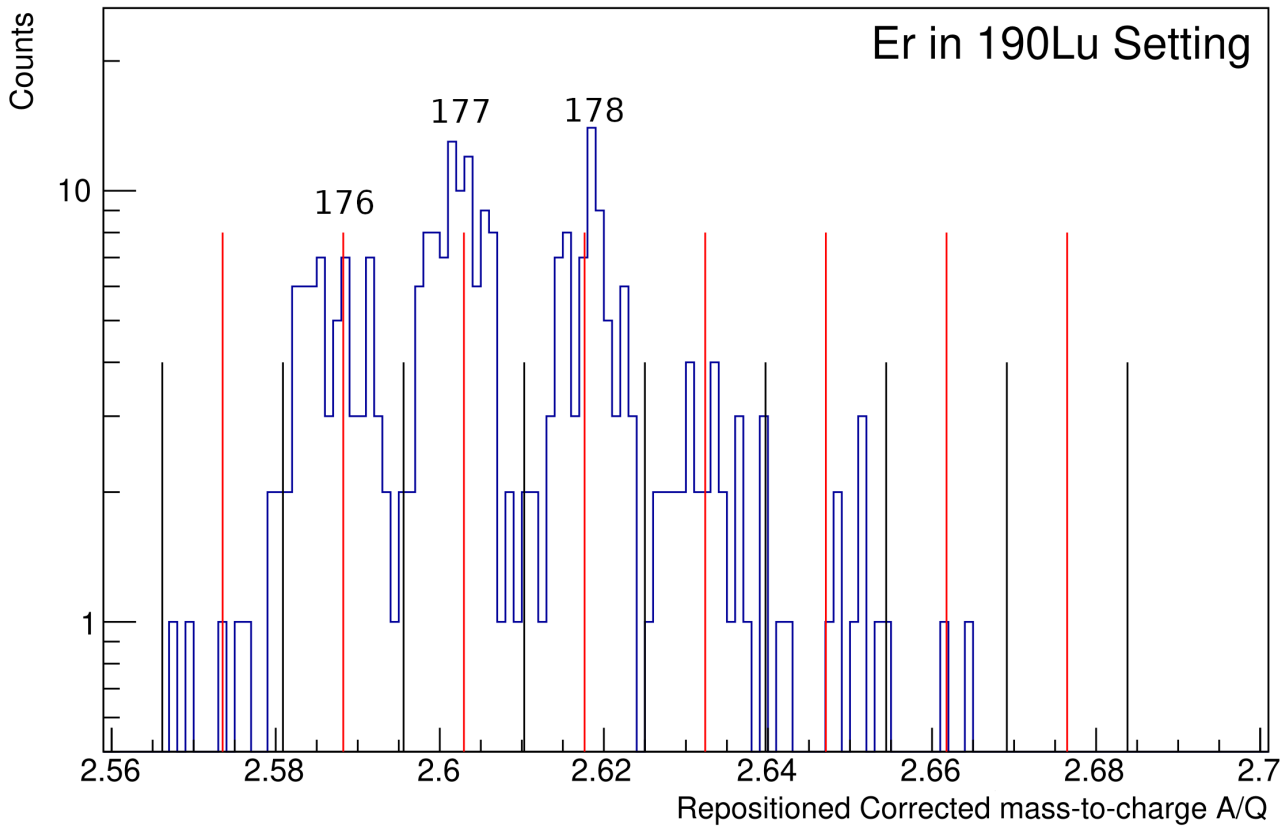


**Figure 13.89.:** AoQ spectrum for erbium isotopes in the $^{190}$Lu setting together with theoretical isotopic AoQ values (red lines) and predefined selection intervals (black lines). The strongest peak in this distribution corresponds to $^{177}$Er, which can be additionally confirmed by Fig. 13.91.

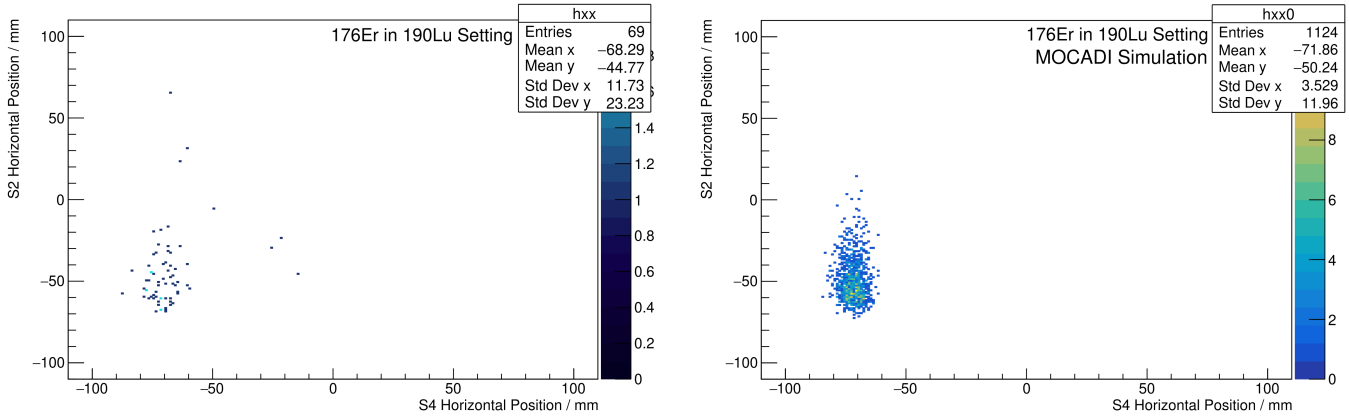


**Figure 13.90.:** S2 horizontal position plotted over S4 horizontal position for experimentally measured (left) and simulated (right) spectra. The experimental position of -71.10(160) mm at S4 agrees well with MOCADI.

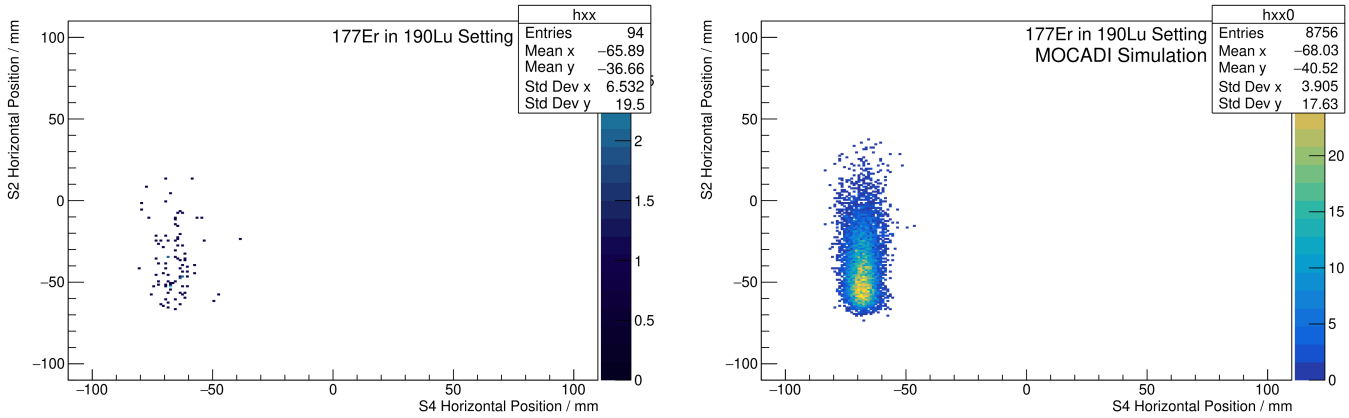


**Figure 13.91.:** S2 horizontal position plotted over S4 horizontal position for experimentally measured (left) and simulated (right) spectra. The experimental position of -65.88(100) mm at S4 agrees with MOCADI.

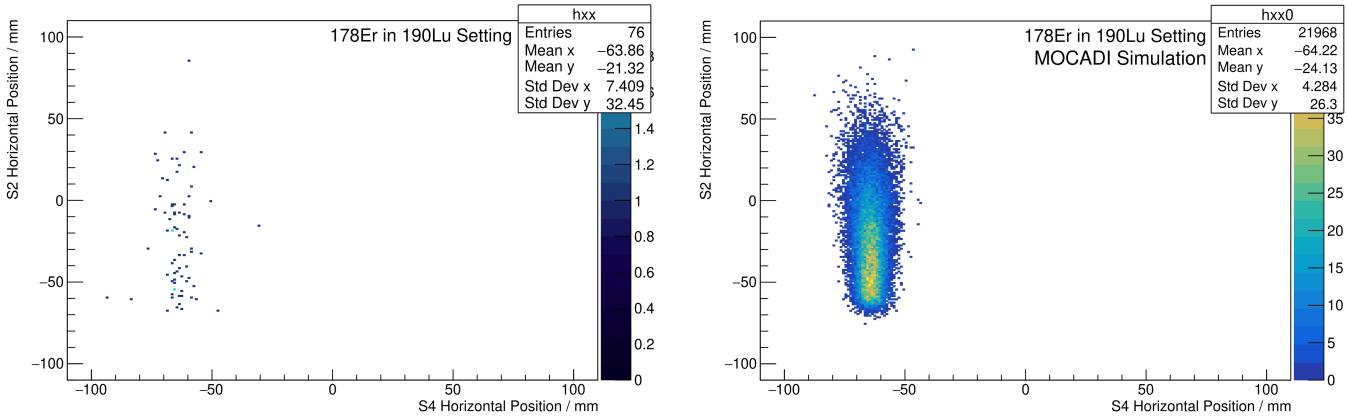


**Figure 13.92.:** S2 horizontal position plotted over S4 horizontal position for experimentally measured (left) and simulated (right) spectra. The experimental position of -63.04(70) mm at S4 agrees with MOCADI.

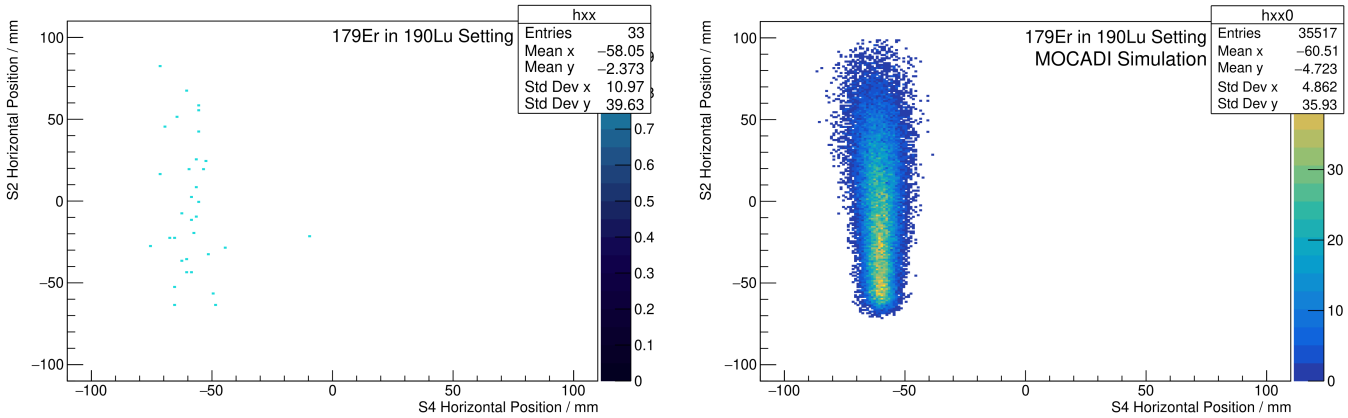


**Figure 13.93.:** S2 horizontal position plotted over S4 horizontal position for experimentally measured (left) and simulated (right) spectra. The experimental position of -61.39(530) mm at S4 agrees with MOCADI.

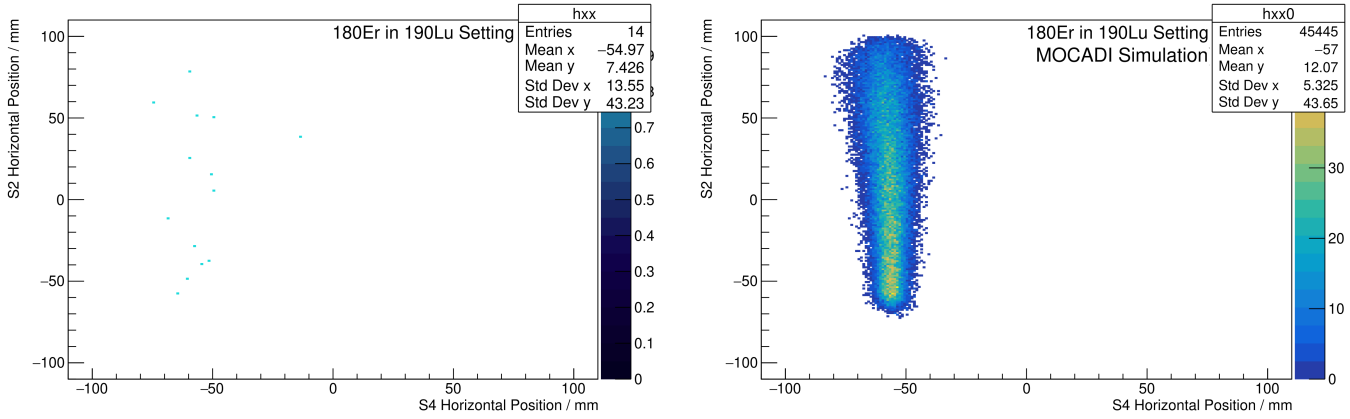


**Figure 13.94.:** S2 horizontal position plotted over S4 horizontal position for experimentally measured (left) and simulated (right) spectra. The experimental positioning can not be accurately determined via fitting due to the low statistics.

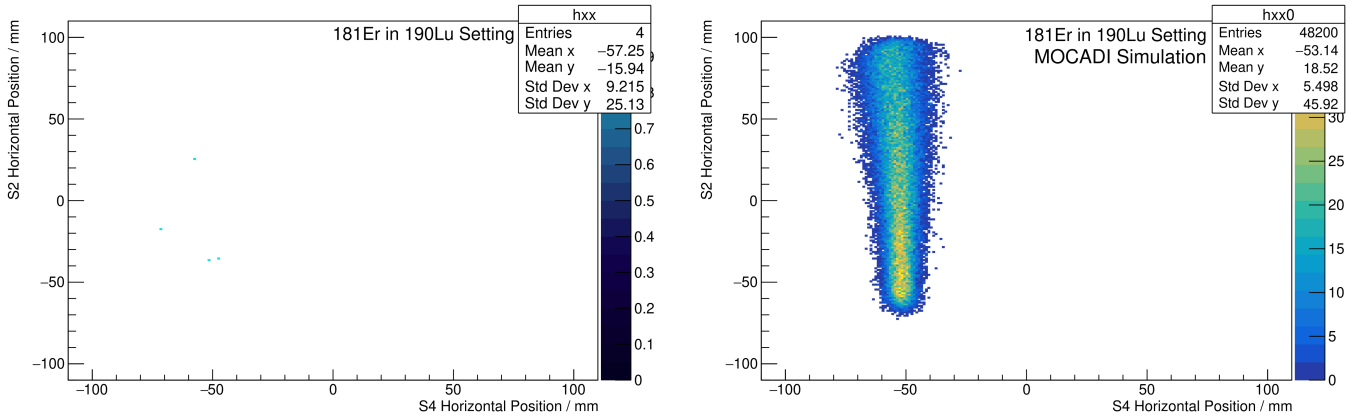


**Figure 13.95.:** S2 horizontal position plotted over S4 horizontal position for experimentally measured (left) and simulated (right) spectra. The experimental positioning not be accurately determined via fitting due to the low statistics.

| Isotope | $^{181}$Er |
|---|---|
| Counts | 3(2) |

**Table 13.8.:** Final counts for the new discovered $^{181}$Er isotope.

### 13.2.10. Ho Isotopes

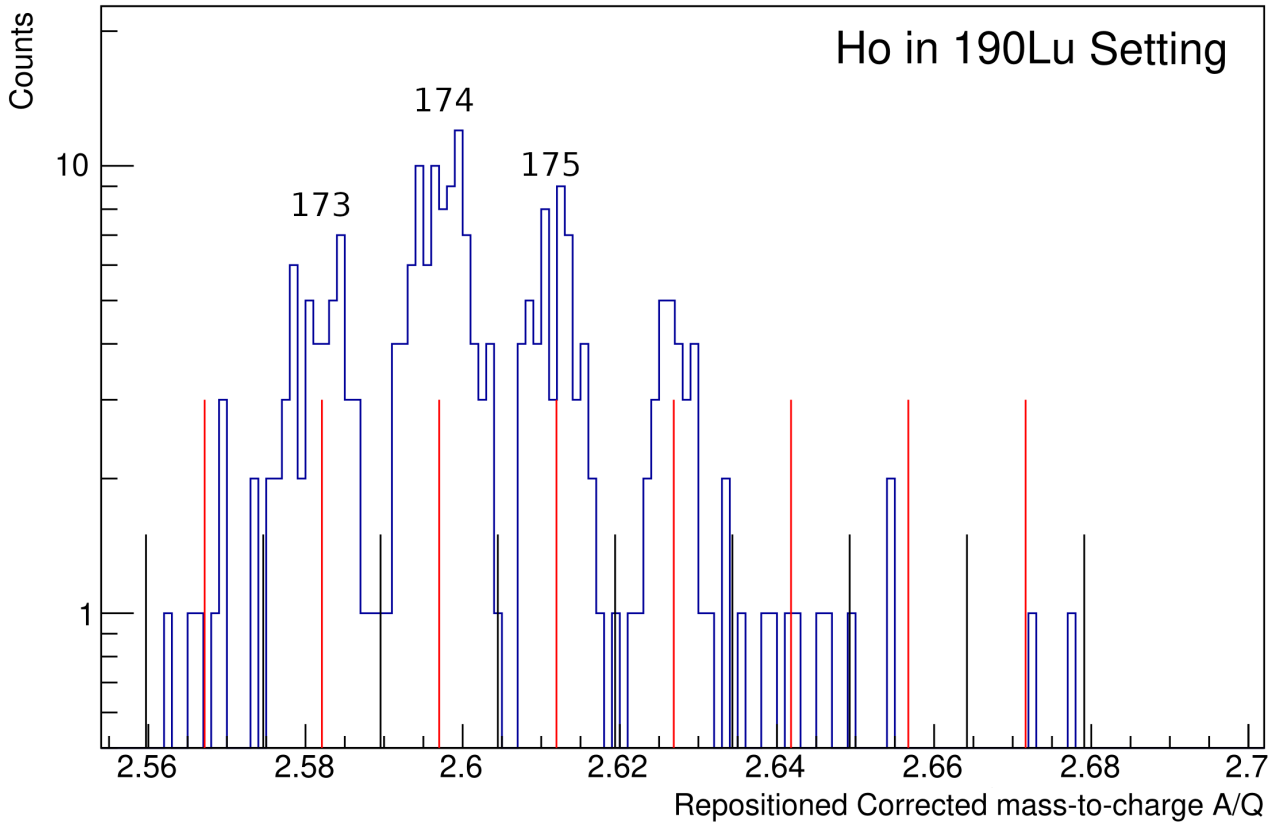


**Figure 13.96.:** AoQ spectrum for holmium isotopes in the $^{190}$Lu setting together with theoretical isotopic AoQ values (red lines) and predefined selection intervals (black lines). The strongest peak in this distribution corresponds to $^{174}$Ho, which can be additionally confirmed by Fig. 13.98.

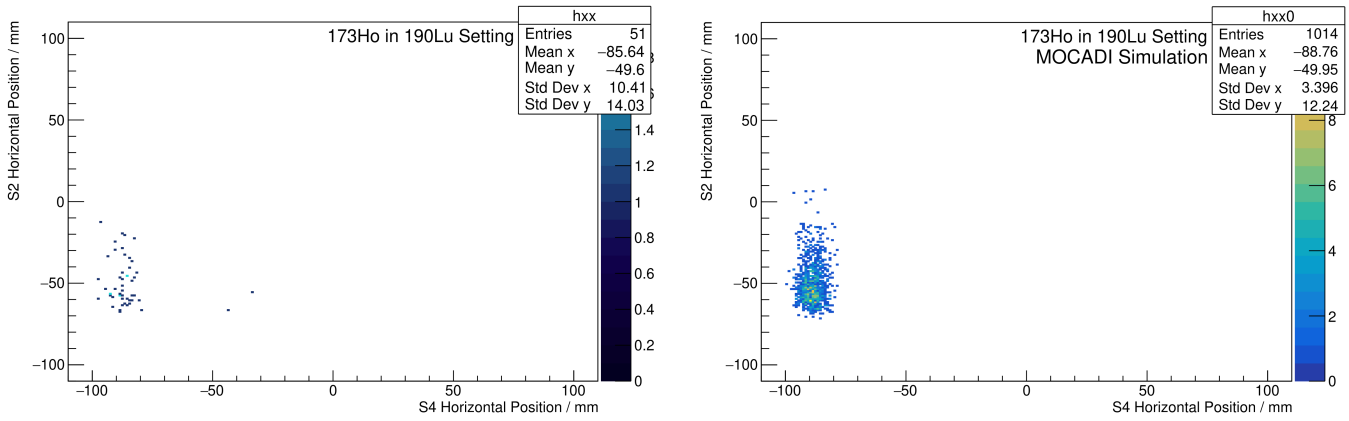


**Figure 13.97.:** S2 horizontal position plotted over S4 horizontal position for experimentally measured (left) and simulated (right) spectra. The experimental position of -87.35(67) $\mathrm{mm}$ at S4 agrees quite well with MOCADI.

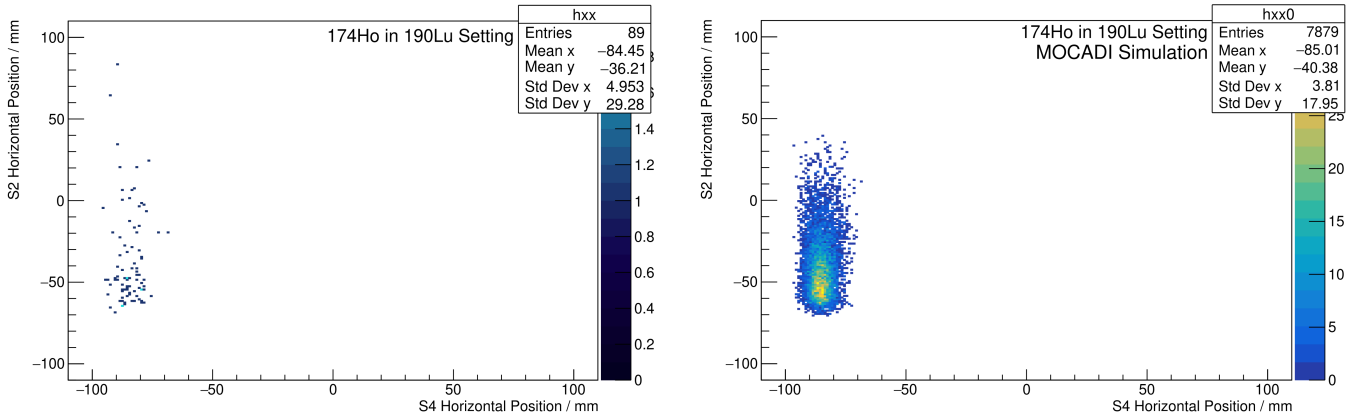


**Figure 13.98.:** S2 horizontal position plotted over S4 horizontal position for experimentally measured (left) and simulated (right) spectra. The experimental position of -84.70(60) $\mathrm{mm}$ at S4 agrees quite well with MOCADI.

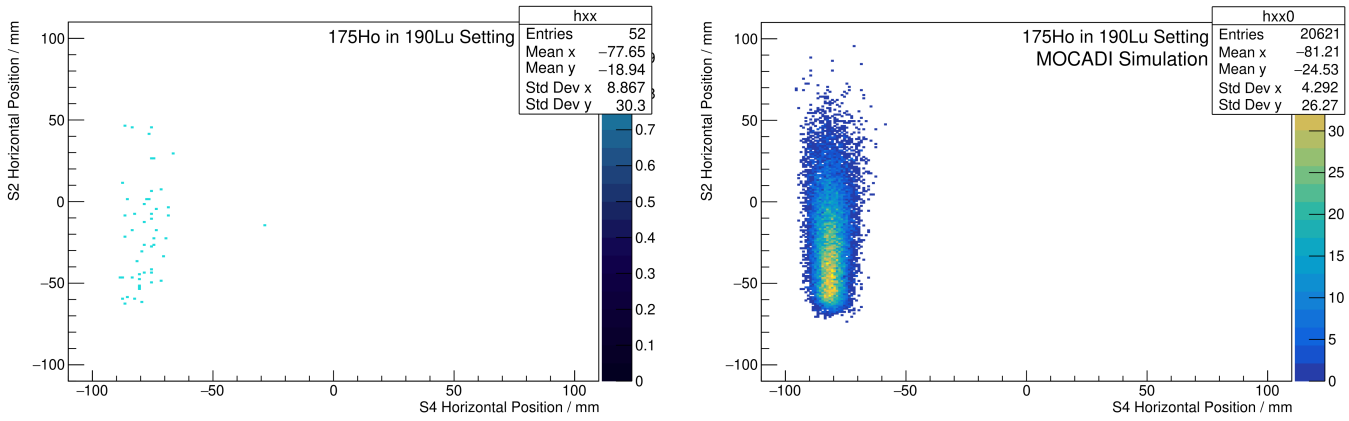


**Figure 13.99.:** S2 horizontal position plotted over S4 horizontal position for experimentally measured (left) and simulated (right) spectra. The experimental position of -80.18(410) $\mathrm{mm}$at S4 agrees with MOCADI.

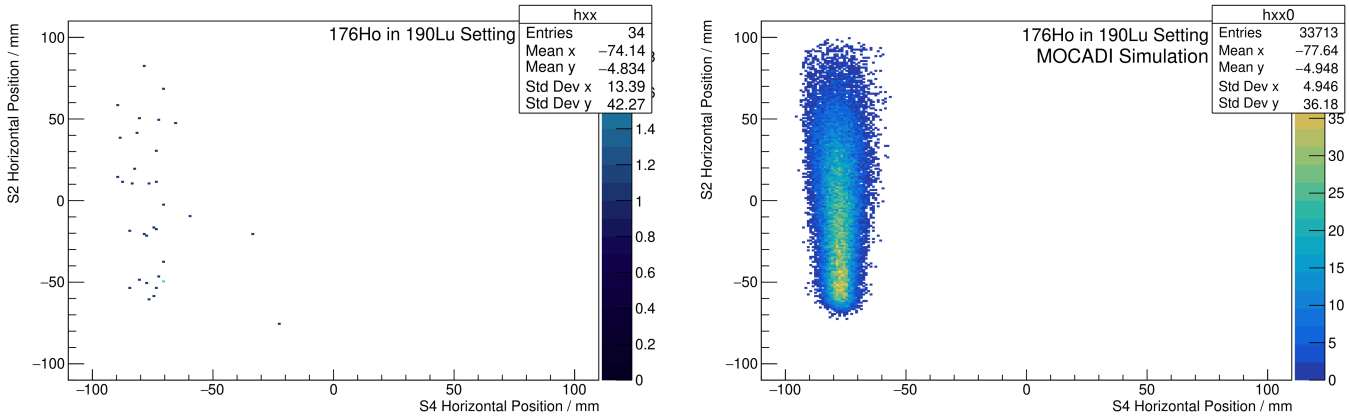


**Figure 13.100.:** S2 horizontal position plotted over S4 horizontal position for experimentally measured (left) and simulated (right) spectra. The experimental positioning can not be accurately determined via fitting due to the low statistics.

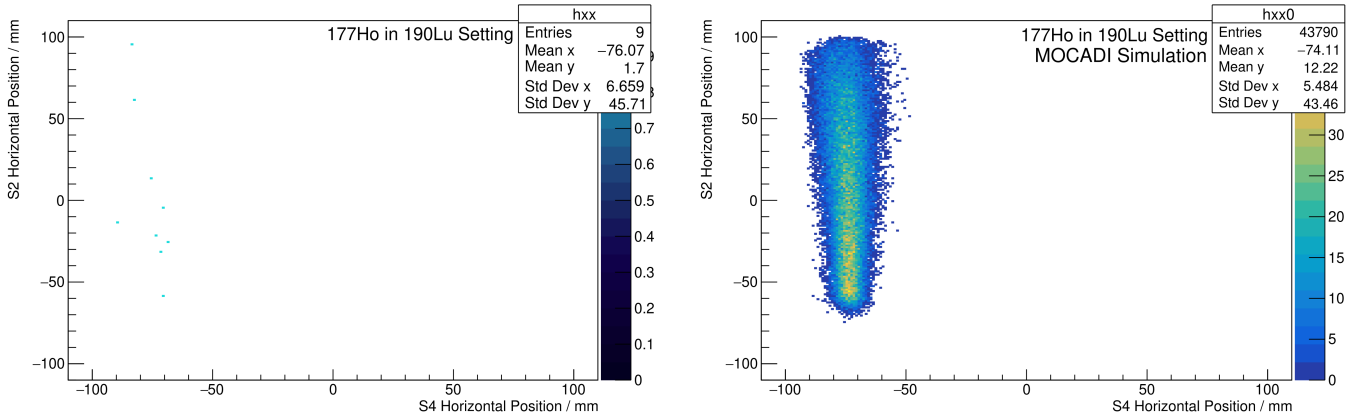


**Figure 13.101.:** S2 horizontal position plotted over S4 horizontal position for experimentally measured (left) and simulated (right) spectra. The experimental positioning can not be accurately determined via fitting due to the low statistics.

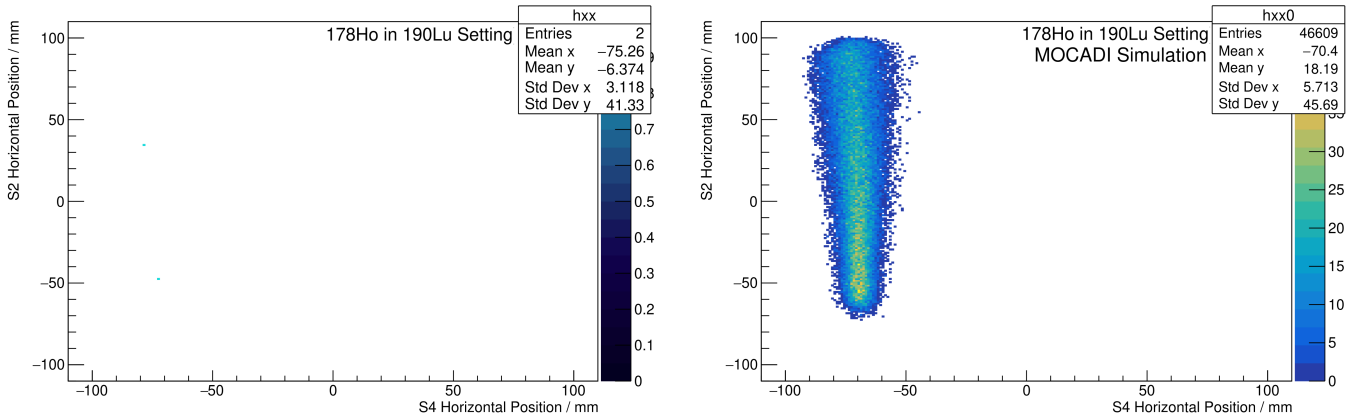


**Figure 13.102.:** S2 horizontal position plotted over S4 horizontal position for experimentally measured (left) and simulated (right) spectra. The experimental positioning can not be accurately determined via fitting due to the low statistics.

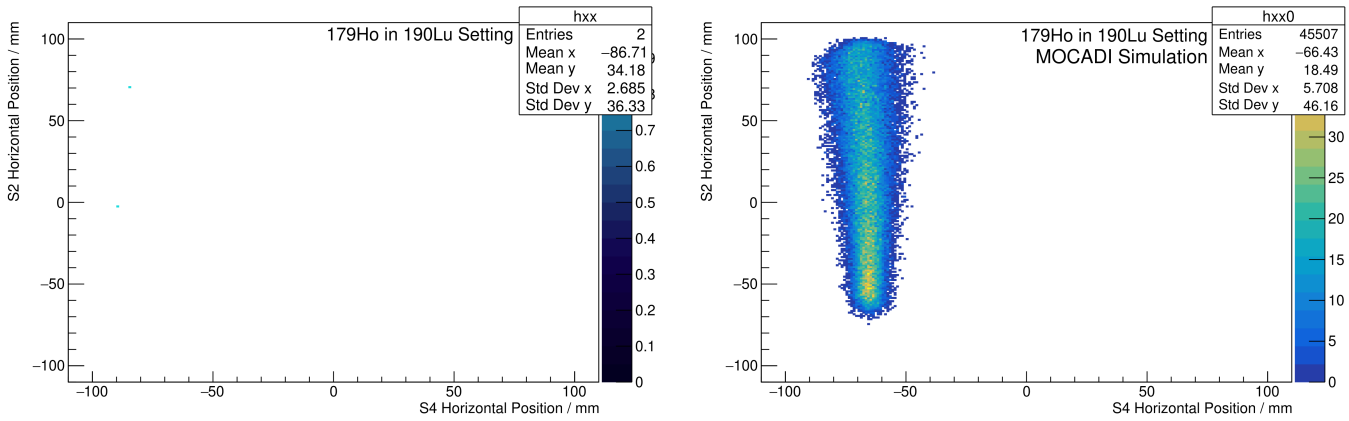


**Figure 13.103.:** S2 horizontal position plotted over S4 horizontal position for experimentally measured (left) and simulated (right) spectra. The experimental positioning can not be accurately determined via fitting due to the low statistics.

In the case of holmium no new isotopes could be discovered. Initially, for the proposal [25] it was expected to discover $^{177}$Ho and $^{178}$Ho. Due to delays in the FAIR-Phase 0 experimental beam time, the discovery of $^{177}$Ho and $^{178}$Ho was reported earlier by Fukuda et al. [116]. Nonetheless, it is possible to reconfirm the existence of $^{177}$Ho, see Fig. 13.101 (a), with eight counts. $^{178}$Ho, see Fig. 13.102 (a), falls short with two counts for reconfirmation. For $^{179}$Ho one count can be positively confirmed, which is not enough to confirm discovery.

### 13.2.11. Dy Isotopes

Dysprosium shows a similar situation to holmium, such that $^{175}$Dy and $^{176}$Dy were expected to be produced, but only dysprosium up to $^{174}$Dy could be produced, see Fig. 13.104. $^{175}$Dy and $^{176}$Dy were instead reported by [116].
It is important to note that the other charge-state selections (0e1e and 1e0e respectively) mentioned in 13.1.3 have been investigated as well for new isotopes counts, but for the sensitive cases in which only 2 or 1 counts could be determined, no additional isotopes could be confirmed.

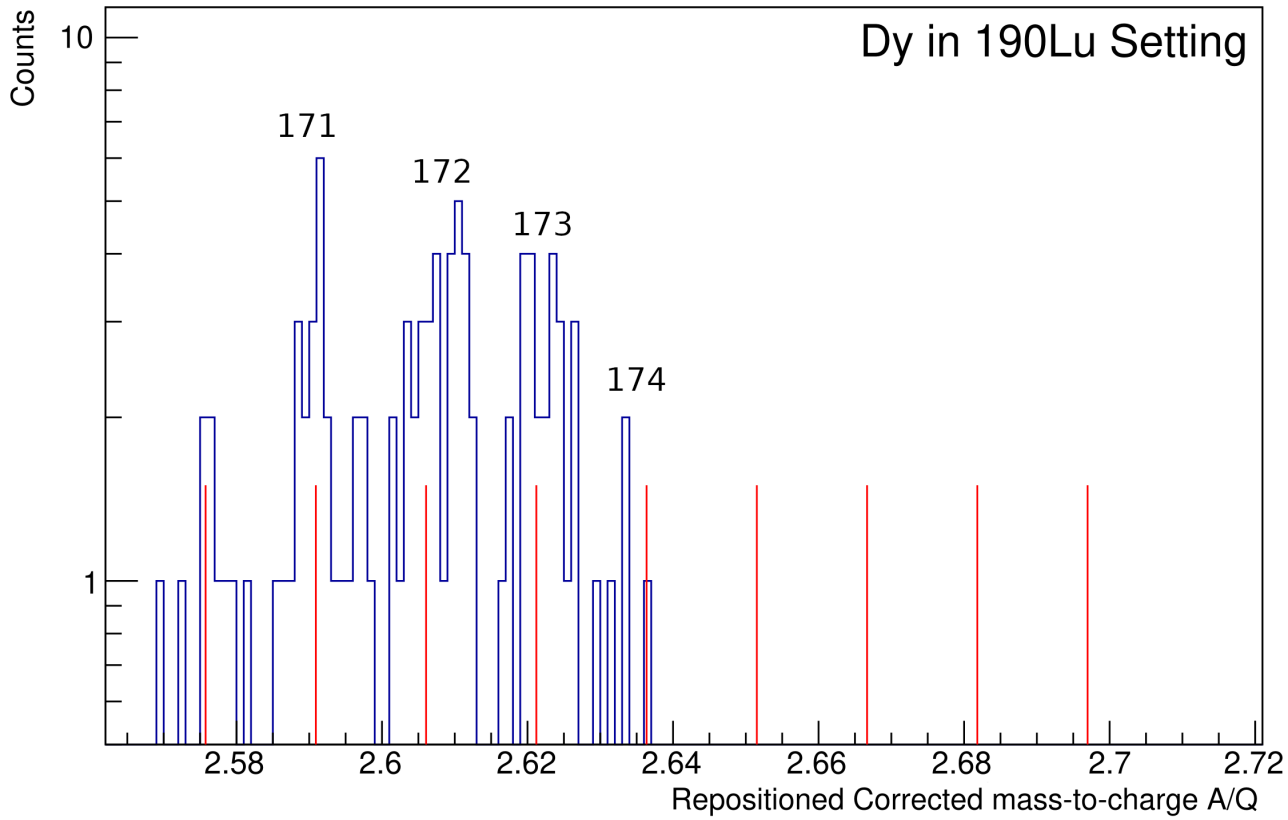


**Figure 13.104.:** AoQ spectrum for dysprosium isotopes in the $^{190}$Lu setting together with theoretical isotopic AoQ values (red lines). The last peak in this distribution corresponds to $^{174}$Dy.

# 14. Conclusion and Outlook

The scope of this work was two-fold, firstly to transfer the proof-of-concept setting generator for the FRS from [20] into a production environment as well as improve upon it such that the FRS can be realistically replicated as a machine-model within the LSA control system framework and secondly to use the implemented solution to conduct a nuclear physics experiment. Therefore this part of this dissertation is linked to the experiment S468 [25] by the Super-FRS Experimental Collaboration [26]in order to produce and identify newly discovered heavy neutron-rich isotopes in the region between osmium and erbium.
As the first step in the development of the machine-model, it was possible to integrate the full-scale of the FRS by integrating all devices from TA through S8 into LSA. As the next step in the development of the machine-model, the generic FRS General Target Hierarchy was introduced, which provides a Parameter hierarchy that encompasses targets, target ladders, degraders, degrader disks, degrader ladders, detectors and detector ladders paired with the implementation of the EOutMakeRule to allow for automated online energy-loss calculations in all cases of a heavy-ion beam passing through matter. The TargetProductionMakeRule has been introduced as well to account for reactions occurring in selected matter devices that change beam properties beyond a singular energy-loss calculation. On top of that, slit and drive hierarchies have been implemented in addition to their corresponding Makerules, which allow full motor control of all FRS stepper and pneumatic drives that are connected to each individual matter device respectively. These hierarchies and functionalities laid the foundation to introduce further functional hierarchies, which streamline and automate the operation process further. These are the $B\rho$ overwrite and target alignment features, that allow the individual adjustment of each dipole segment by the operator as well as the automated alignment and centering of the primary beam impinging on the FRS target station via ion-optical calculations derived from required position changes in current grid detectors.
Before the machine-model could be used in the FAIR Phase-0 experimental time, it was extensively tested and benchmarked. It was possible to show that CATIMA and LSA ATIMA yield identical deviations of output energies during engineering runs, and ATIMAPy showed a $10^{-8}$ relative deviation, well below the FRS accuracy for magnetic rigidity of $10^{-4}$. When LSA machine-model predictions are compared to modern experiments, set values for the magnetic rigidity and current can be reproduced that are identical with respect to the accuracy of the power supplies and Hall-probe measurements. Finally, during engineering runs with a $^{40}$Ar and $^{238}$U primary beam, it was possible to use the implemented Parameter hierarchies together with their Makerules to center at the FRS target station, transport the primary beam to S4 and produce a secondary beam of fragments, which could be successfully transported to S4. This was achieved by solely relying on the online on-the-fly calculation methods of the FRS machine-model within LSA and no prior settings calculation via LISE++. Consequently, the FRS machine-model development work in this dissertation provides the basis for controls of all future FRS, NUSTAR, R$^3$B, HISPEC/DESPEC, Super-FRS Experiment Collaboration and other NUSTAR@SIS18 experiments. Using the FRS as a benchmark for the machine-model and showing successful use in its prototyping phase, sets the next goal to implement the Super-FRS inside of the machine-model and adapt current functionalities, if necessary, in order to guarantee the smooth operation of all future NUSTAR@SIS100 experiments. Furthermore, has a status been achieved with LSA such that the whole GSI experimental facility can be controlled within the framework and be

easily and readily expanded unto the upcoming FAIR facility.
For the second part of this dissertation, the new isotope search, a relativistic $^{208}$Pb primary beam with an incident energy of 1050 $A\mathrm{MeV}$ was used to produce heavy-ion fragments in the range of gold to dysprosium in four different settings. The FRS $B\rho$-$\Delta E$-$B\rho$ method was utilized to successfully separate the secondary beam fragments and identify them. By using an AoQ path-length correction method, MUSIC $Q_{max}$ and degrader 0e0e charge-state selection it was possible to further improve separation and identification capabilities within the analysis. Proper identification of the heavy nuclear species, mainly produced by projectile fragmentation, required including cuts and procedures to improve maximum charge $Q_{max}$ and mass-to-charge ratio $A/Q_{max}$. The following Tab. 14.1 lists isotopes from the $^{190}$Lu setting for whose existence evidence was found at the present stage of analysis. Applying the most rigorous cuts, i.e. including the TPC Checksum requirement, the existence of seventeen heretofore unknown isotopes seems highly likely (✓✓✓in Tab. 14.1). Loosening analysis criteria indicates the possible existence of four further nuclei (✓✓), whereas statistics or background conditions are insufficient for confident observation of six further isotopes (✓).

| | | | | | | | | | | | |
|---|---|---|---|---|---|---|---|---|---|---|---|
| $^{204}$Os | ✓ | $^{200}$Re | ✓✓✓ | $^{198}$W | ✓✓✓ | $^{195}$Ta | ✓✓✓ | $^{191}$Hf | ✓✓✓ | $^{189}$Lu | ✓✓✓ |
| | | $^{201}$Re | ✓✓✓ | $^{199}$W | ✓✓✓ | $^{196}$Ta | ✓✓✓ | $^{192}$Hf | ✓✓✓ | $^{190}$Lu | ✓✓✓ |
| | | $^{202}$Re | ✓✓✓ | $^{200}$W | ✓ | $^{197}$Ta | ✓✓ | $^{193}$Hf | ✓✓✓ | $^{191}$Lu | ✓✓ |
| | | $^{203}$Re | ✓ | | | | | $^{194}$Hf | ✓ | | |
| $^{186}$Yb | ✓✓✓ | $^{182}$Tm | ✓✓✓ | $^{181}$Er | ✓✓ | $^{177}$Ho | [✓✓✓] | $^{175}$Dy | [✓] | | |
| $^{187}$Yb | ✓✓✓ | $^{183}$Tm | ✓✓✓ | | | $^{178}$Ho | [✓] | $^{176}$Dy | [✓] | | |
| $^{188}$Yb | ✓ | $^{184}$Tm | ✓✓✓ | | | $^{179}$Ho | ✓ | | | | |
| | | $^{185}$Tm | ✓✓ | | | | | | | | |

**Table 14.1.:** The current state of the analysis suggests the existence of twenty-one new isotopes (✓✓✓& ✓✓), of which seventeen are highly likely (✓✓✓), four likely (✓✓) and additional six isotopes could not be confirmed due to either low statistics or high background (✓). Checkmarks in brackets [] mean that isotopes were already seen by Fukuda et. al [116] and could either be reconfirmed or not.

The analysis of the new isotope search data has been challenging in a multitude of ways, and production cross-sections for projectile fragmentation exist only as preliminary data thus far. The challenges stem from the calibration of the detector systems, especially the AoQ mass-to-charge ratio highly depends on the time-of-flight and position calibration of the scintillator and TPC sub-systems at S2 and S4, respectively. It was discovered that both systems were showing subpar performances, which can be attributed to pile-up at S2 inside the TPC detector systems along with potential damage of the S2 and S4 plastic scintillators or PMTs. Both aspects are due to high incident particle rates at the respective positions. Whereas the pile-up effect on the TPCs was an imminent cause that could have been corrected by reducing the particle intensity, the effect seen in the scintillator systems could be observed retrospectively in previously run experiments. These aspects elucidate the high particle rate case at the Super-FRS, which has even higher rates expected during experiments than what was observed here, therefore imposing a high demand on equipment that can resolve isotopes with a low production yield in a high intensity environment. Furthermore, insight was gained into the response of TPC and scintillator systems for such high-intensity secondary particle beams, in order to avoid future mishaps.
Nonetheless, even with all the challenges in the analysis, it was possible to produce and identify new neutron-rich isotopes in the region between osmium and dysprosium via projectile fragmentation and move towards the $N = 126$ magic line, with $^{201}$Re being on it. This acts as a first access towards better understanding the r-process' waiting point around $N = 126$ and the mass peak around $A = 194$ [4].

Besides the verification of the existence of new isotopes, it was also possible to measure new masses and $\beta$-decay half-lives with the FRS Ion Catcher and Active Stopper detector setup in combination, respectively. These properties are currently analyzed [27, 28, 29] and will provide future insight into theoretical r-process model calculations, to better determine mass abundance yields by restricting the r-process path and waiting points. FAIR as the upgrade of the GSI accelerator facility, with one of its main points in the physics program being geared towards understanding the r-process path, will provide higher energetic and more intense beams that are able to probe deeper into the currently unknown regions past the new boundaries set by the new isotope search experiment S468 and investigate the r-process path along the magic $N = 126$ line in even greater detail.

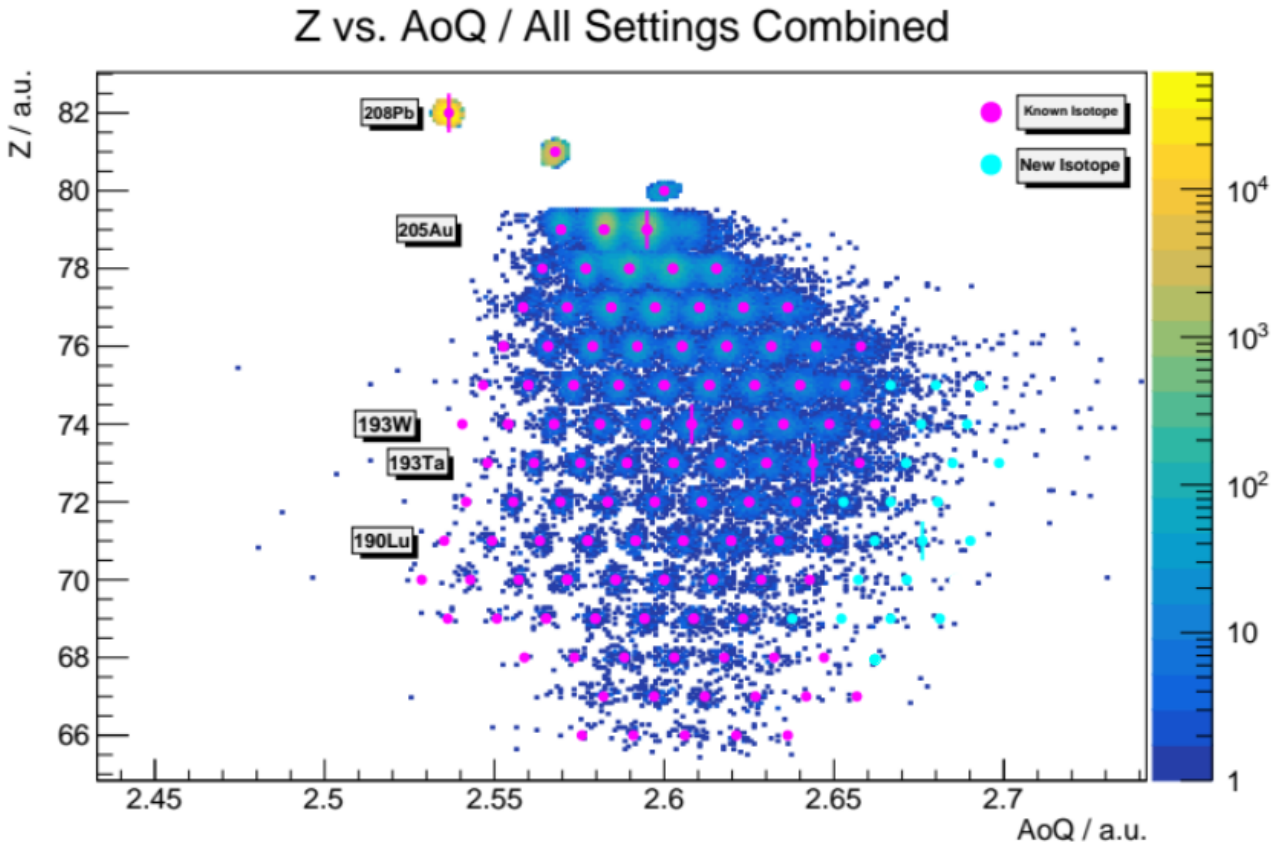


**Figure 14.1.:** Z versus AoQ identification plot for all setting combined. Magenta vertical lines indicate the used settings, magenta dots indicate already known isotopes and cyan coloured dots indicate newly discovered isotopes.

# Part V.

# Appendix

# A. FRS Setup

The following figures were taken from the FRS Setup online source [117] and used with permission. Device names with the suffix ”P” are pneumatic drives whereas names with the suffix ”S”,”_S”,”HS” or ”VS” are stepper motors attached to the respective devices. Slits follow their own convention where motors are denoted with the suffixes ”U”,”O”,”L” or ”R”, meaning ”unten”, ”oben”, ”links” and ”rechts”, respectively, and standing for ”lower”, ”upper”, ”left” and ”right”.

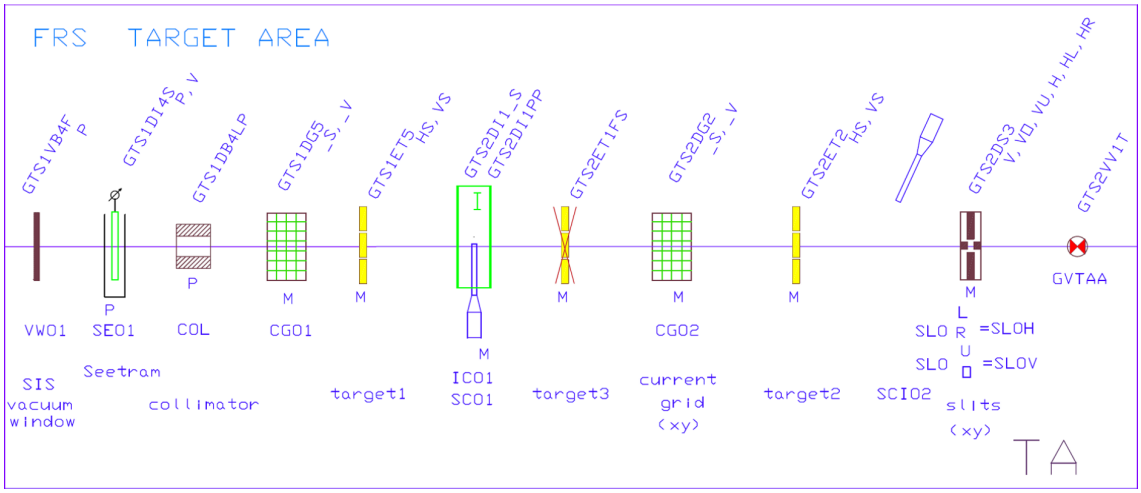


**Figure A.1.:** Schematic representation of matter and devices at target location (TA), taken from Ref. [117]. Crossed-out symbols indicate matter or devices that have been removed since the drawing of the sketch. Copyright at GSI/FAIR, used with permission.

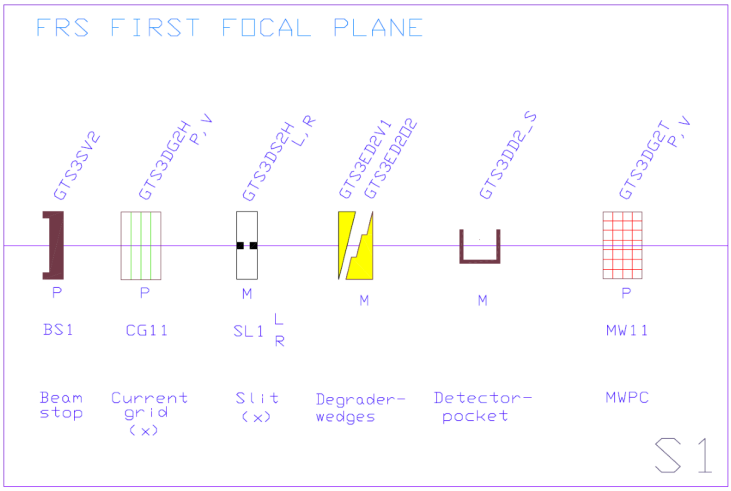


**Figure A.2.:** Schematic representation of matter and devices at focal plane S1, taken from Ref. [117]. Crossed-out symbols indicate matter or devices that have been removed since the drawing of the sketch. Copyright at GSI/FAIR, used with permission.

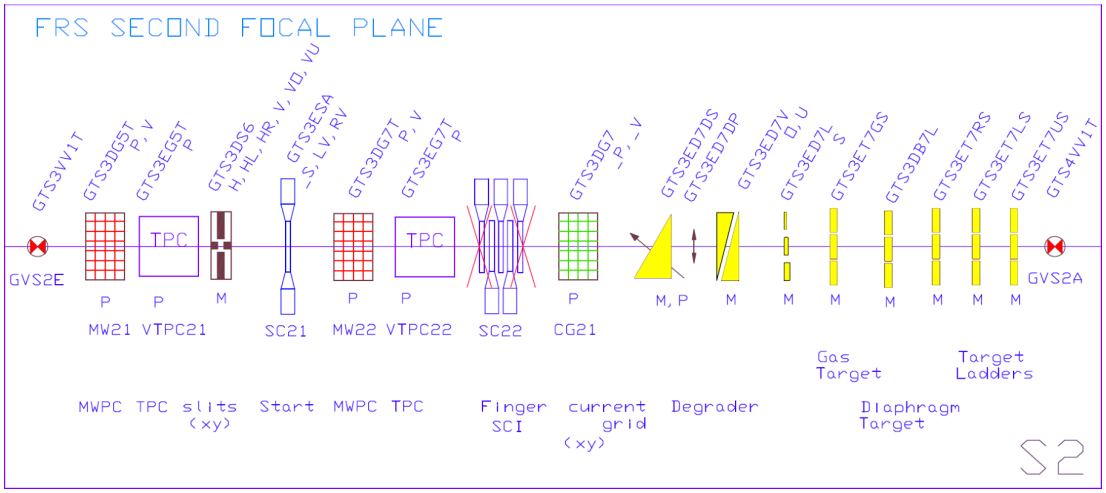


**Figure A.3.:** Schematic representation of matter and devices at focal plane S2, taken from Ref. [117]. Crossed-out symbols indicate matter or devices that have been removed since the drawing of the sketch. Copyright at GSI/FAIR, used with permission.

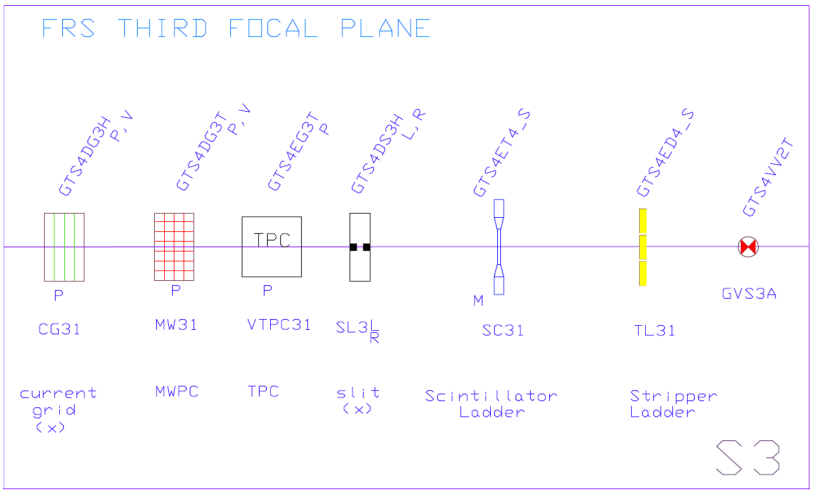


**Figure A.4.:** Schematic representation of matter and devices at focal plane S3, taken from Ref. [117]. Crossed-out symbols indicate matter or devices that have been removed since the drawing of the sketch. Copyright at GSI/FAIR, used with permission.

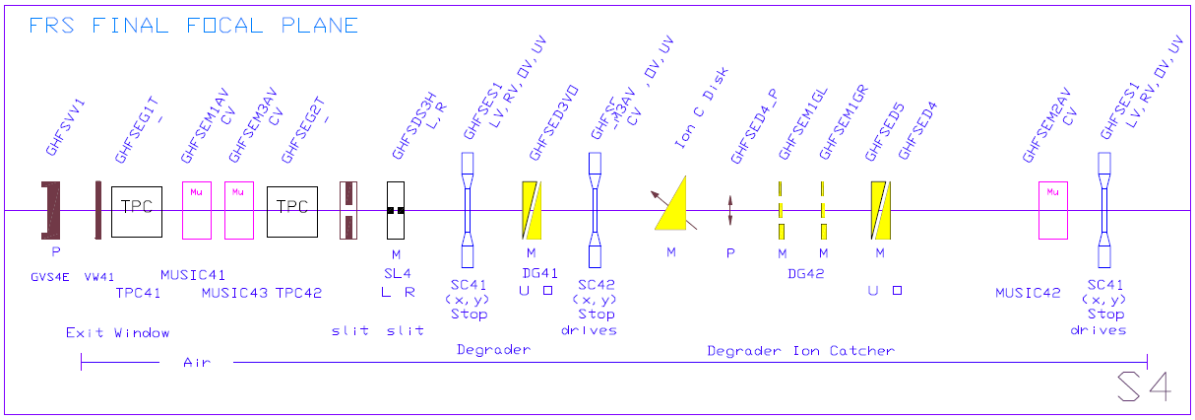


**Figure A.5.:** Schematic representation of matter and devices at focal plane S4, taken from Ref. [117]. Crossed-out symbols indicate matter or devices that have been removed since the drawing of the sketch. Copyright at GSI/FAIR, used with permission.

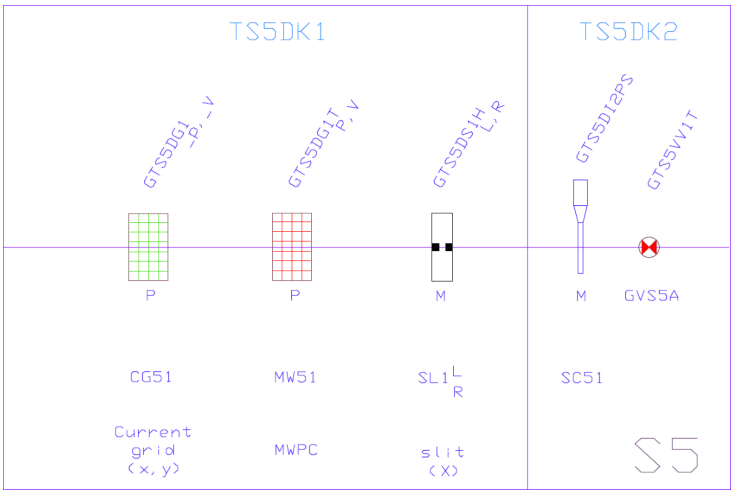


**Figure A.6.:** Schematic representation of matter and devices at focal plane S5, taken from Ref. [117]. Crossed-out symbols indicate matter or devices that have been removed since the drawing of the sketch. Copyright at GSI/FAIR, used with permission.

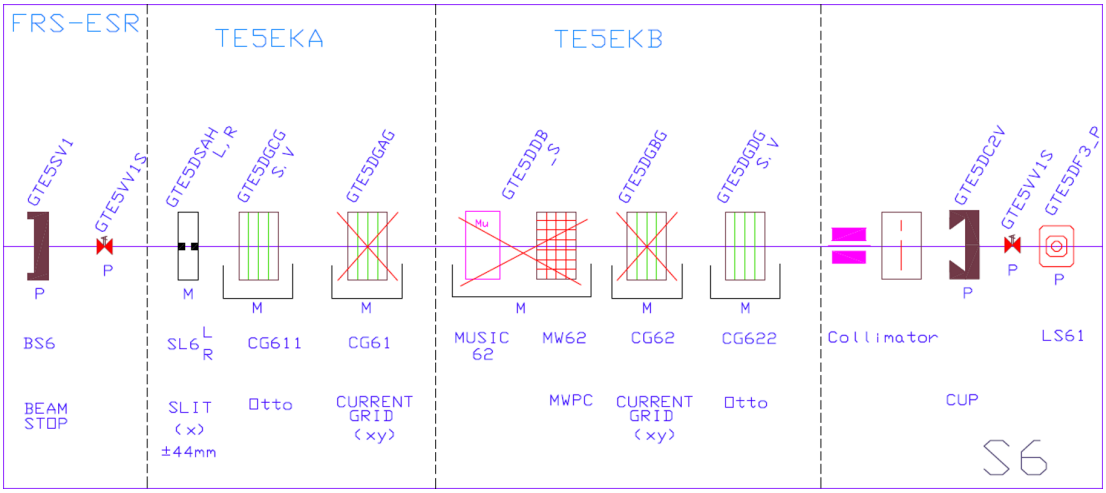


**Figure A.7.:** Schematic representation of matter and devices at focal plane S6, taken from Ref. [117]. Crossed-out symbols indicate matter or devices that have been removed since the drawing of the sketch. Copyright at GSI/FAIR, used with permission.

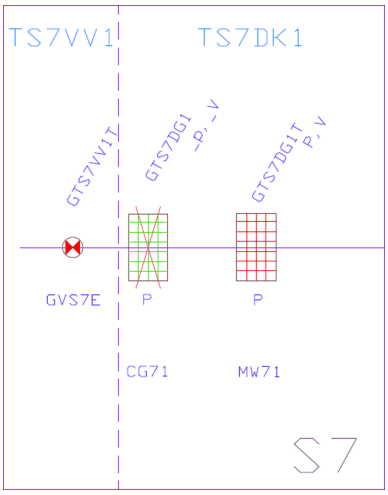


**Figure A.8.:** Schematic representation of matter and devices at focal plane S7, taken from Ref. [117]. Crossed-out symbols indicate matter or devices that have been removed since the drawing of the sketch. Copyright at GSI/FAIR, used with permission.

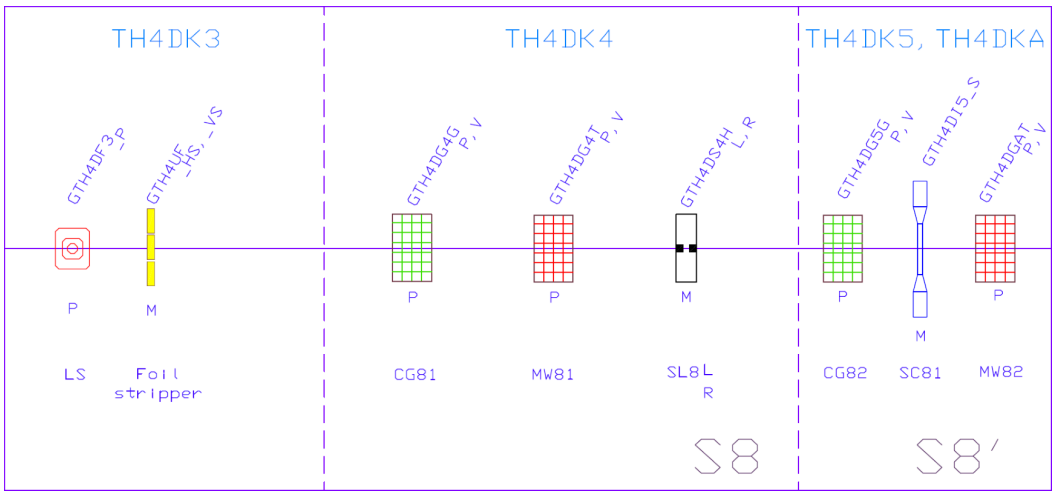


**Figure A.9.:** Schematic representation of matter and devices at focal plane S8, taken from Ref. [117]. Crossed-out symbols indicate matter or devices that have been removed since the drawing of the sketch. Copyright at GSI/FAIR, used with permission.

# B. LHC Software Architecture (LSA) Fundamentals

## B.1. Concepts

LSA is a framework written in Java, which is used to control accelerators at CERN and to ensure data supply. It has been developed and maintained there since 2001 [21]. LSA is already used to control the Large Hadron Collider (LHC), Super Proton Synchrotron (SPS), Low Energy Ion Ring (LEIR) and Antiproton Decelerator (AD). The idea for developing LSA was to create a generic framework for accelerator modeling with the following criteria:

- Separation of software engineering and accelerator modeling, meaning that someone creating a machine-model for an accelerator, storage ring or transfer path can work with the existing building blocks of the framework without having to have, for example, deeper knowledge of the inheritance hierarchy.
- Use of modern software techniques, which means, for example, the use of non-obsolete standards or APIs, which can also be replaced as soon as they turn out to be obsolete.
- Database-based, so that, among other things, device data is available centrally for control or that results of calculations already performed are archived to speed up control.
- Provide generic structures for accelerator modeling.

Since 2007, the data supply, i.e. the provision of all necessary data enabling the control of the accelerators (device data, calibration data, etc.), has been further developed and adapted at GSI and for the planned FAIR facility, so that all existing as well as planned accelerators, storage rings and beam transfer sections are to be controlled and monitored within LSA. In particular, emphasis is now being placed here on operating concepts that ensure parallel operation of the various accelerators, storage rings and transfers, enable integration of beam diagnostics, provide data for failure scenarios and define abort conditions or alternative cycles, enable data analysis of the equipment, create a control-room concept and, finally, create integration of experiments by incorporating the experiment hardware into the control software and developing the control software for the experiments by the groups themselves, as in this case for the FRS.

**Parameter** A Parameter is a predefinable or measurable quantity and is associated with the property of a device, such as the current provided by the power supply and the resulting magnetic field of a magnet. Devices of any kind are called devices and can be existing, controllable equipment, such as the power supply, non-controllable equipment, such as a magnet, or generally a virtual device, such as the beam itself. Parameters are named after the notation ”Device/Property” and have a type, for example Boolean, that describes the common properties of all Parameters of that type. Parameters are organized in a model, the Parameter hierarchy, which describes the linkage between Parameters. Top-level Parameters are called roots and must be specified, from which all dependent quantities are

calculated, including hardware Parameters such as power supply current. These are called leaves and are passed on to the hardware.

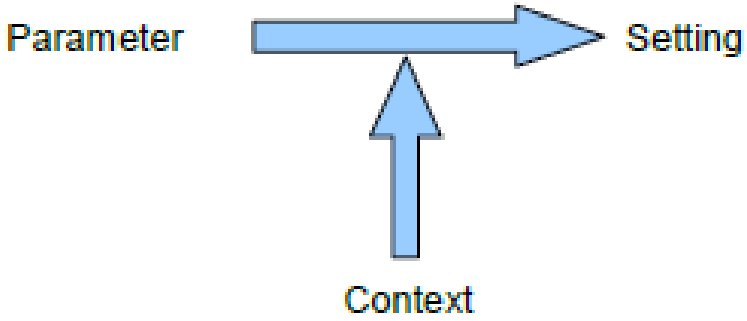


**Figure B.1.:** Figure, taken from [118], visualizing the relation between Parameter, Setting and Context. A setting is either a scalar or a function, which depends on the context. Copyright at GSI/FAIR, used with permission.

**Context** A Context is a time interval in which Parameters are assigned a value, see Fig. B.1. There are 5 types of Contexts.

**Cycle** defines a beam from injection to extraction including beam-out. Cycles can be organized into supercycles or exist as stand-alone Cycles. It should be noted that Cycles do not maintain the state of a machine, as remanence effects can occur in magnets, among other things.

**Supercycle** defines a set of Cycles to produce beams for appropriate applications. A Supercycle can be repeated in a cyclic machine and also ensures that the state of a machine is maintained. The interaction of Cycles and Supercycles is illustrated in Fig. B.2 using the SPS and the various magnets therein.

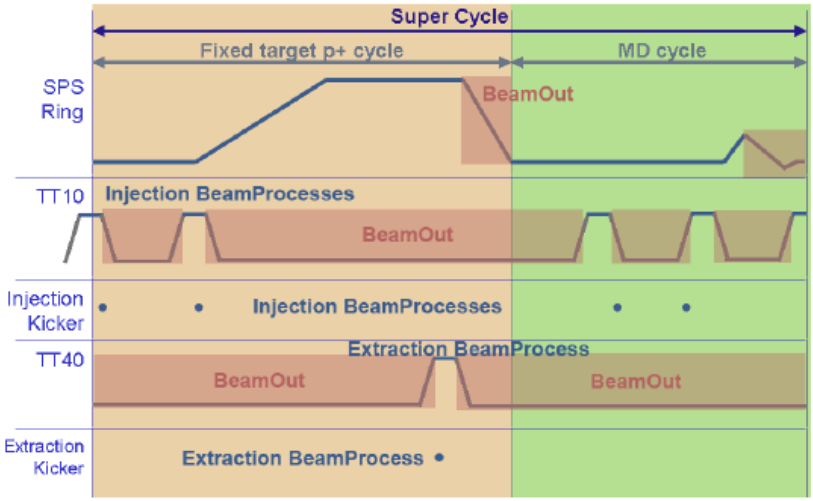


**Figure B.2.:** In this figure, taken from [119], the concepts of Cycle, Supercycle and Beamprocess are illustrated using the example of a production Cycle in SPS. Copyright at GSI/FAIR, used with permission.

**Beam Production Chain** describes the entire lifetime of a beam from its creation in the source to its destruction in the target or beam stop. Unlike the Cycle and Supercycle, the Beam Production

Chain can extend across multiple accelerators, storage rings, or transfer paths. This is to simplify the management of the machine complex for operators while maximizing the parallel operation of the machines. In Fig. B.3, example Beam Production Chains are shown.

**Pattern** can be compared to the Supercycle for Cycles. Here, the Pattern defines which Beam Production Chains are executed within the GSI Helmholtz Center or the future FAIR facility while the Pattern is active. Patterns can be repeated several times or infinitely until the stop signal is given manually or Patterns can also be executed on demand. Fig. B.3 illustrates the Patterns described.

**Beamprocess** defines a specific process within the Cycle of a machine, e.g. injection. A distinction is made between punctual Beamprocesses, which define a value at a point in time, and temporally extended Beamprocesses, which define a function for a time interval. In addition, there are beam-in and beam-out beam processes, which define the respective state of the machine with or without beam.

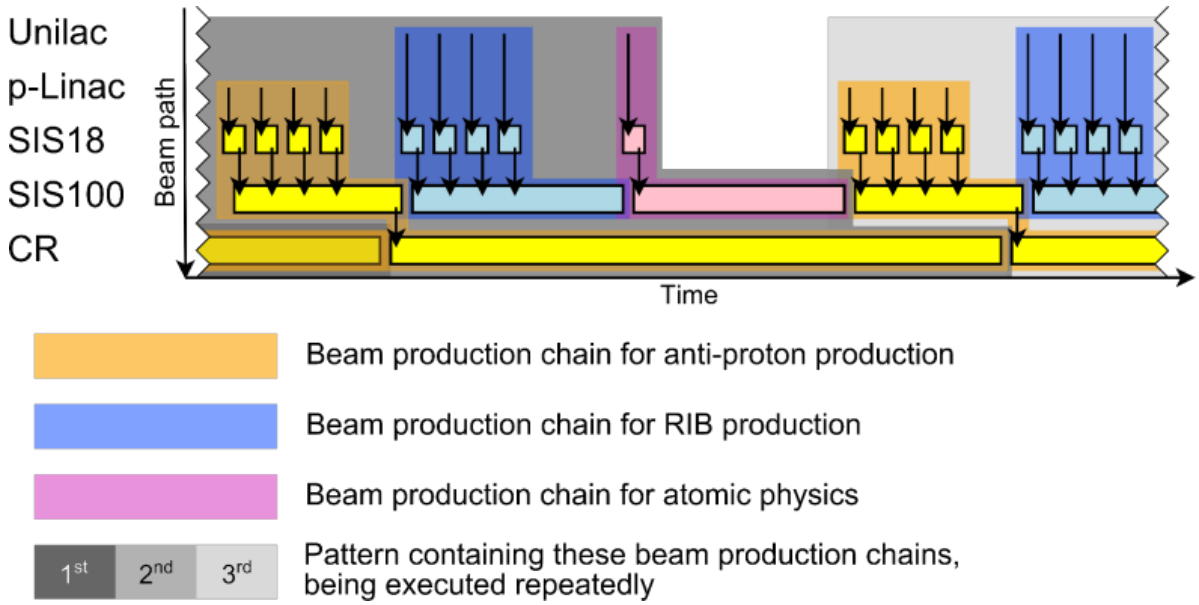


**Figure B.3.:** Example illustration of several Patterns (shades of gray), taken from [64]. On the left, the different accelerator sections are marked and the colored shades represent the different Beam Production Chains. The concept of Patterns and Beam Production Chains is a very good way to implement the desired goal of parallel operation, so that idle times are kept to a minimum. Copyright at GSI/FAIR, used with permission.

**Setting** A Setting is when a Parameter with a value is assigned to a beam process. This value now consists of two parts, the set value and the correction. The set value is either the specified value or the generated value resulting from the Parameter hierarchy, where the correction value can be specified manually or is the automatic empirical result of all modifications made to the setpoint during the operation of the machine to obtain the correct beam Setting. For example, from a given $B\rho$ value, the required current intensity is calculated. The correction can now be entered manually or is calculated automatically using algorithms in LSA.

**Rules** These define how a modification to one Setting affects other Settings. There are 3 types of Rules.

**Makerule** The Makerule describes how the Settings of one Parameter are used to generate the dependent Settings of another Parameter. The Makerule is defined as a relation between two

or more Parameter types, so that a Makerule is sufficient to establish a calculation rule for the dependency of two or more Parameters, which is used in the same way for all devices. As an example, the Makerule used for the calculation of the exit energy of a heavy-ion beam when passing through matter, which will be discussed in more detail in the next part of this thesis.

**Incorporationrule** This Rule now describes how the change of a Setting is incorporated into the next or previous Setting of a Supercycle. If the Trim, see ”Trim” below, of a Setting changes at least one endpoint, this change is propagated to the further Settings. Incorporation rules are used, for example, to incorporate a change at a particular time into the rest of the Settings.

**Linkrule** These Rules are finally used to describe the Setting of a Parameter during beam-out Beamprocess. Thus, Linkrules are written for each hardware type of a device to which the Parameter belongs. Although roots do not have Settings during beam-out Beamprocess, Settings must still be generated for all hardware Parameters.

**Trim** A Trim is not a Rule, but it is the preferred way to adapt generated Settings to machine-specific conditions, i.e. instead of specifying a correction value for the current strength of a magnet, for example, the value of the current strength is directly changed via a Trim instead. In addition, the hardware Parameters are generated based on the Settings of the physical Parameters. Each Trim is archived so that it is possible to undo changes. After a Trim has been performed, all remaining Settings are adjusted and the new hardware Settings are sent to the hardware.

# C. Makerule Code Snippets

### Type Hierarchy

```
package de.gsi.lsa.ext.fair.rules.makerule.target;

public class EoutMakeRule extends AbstractTargetMakeRule {

  private final double electronMass = 0.0005485799091; // given in units of u

  private GsiOpticsFinder gsiOpticsFinder;

  public void setGsiOpticsFinder(final GsiOpticsFinder gsiOpticsFinder) {
    this.gsiOpticsFinder = gsiOpticsFinder;
  }

  @Override
  protected ImmutableValue makeValueGsiImpl(final MakeRuleArguments mra) throws
    TrimException {
    ...
  }
}
```

**Listing C.1:** Full head and class definition of EoutMakeRule with the important method makeValueGsiImpl().

```
/**
* @author Holger Liebermann
*/
public abstract class AbstractTargetMakeRule extends AbstractGsiMakeRule {

  protected TargetReader readTargetFile(final String deviceName) {
    final TargetReader tr = new TargetReader();
    final String file = deviceName + ''.csv'';
    try {
      tr.readTarget(''lsa/frs_target_db/src/'' + file);
    } catch (final IOException e) {
      e.printStackTrace();
    }
    return tr;
  }

  protected static String extractDevicename(final Parameter indexParameter) {
    final String deviceproperty = Parameters.getDeviceProperty(indexParameter);
    final int pos = deviceproperty.indexOf(''/'');
    final String logicalDeviceName = pos >= 0 ? deviceproperty.substring(0, pos) :
    deviceproperty;
    final String deviceName = logicalDeviceName.replace(''LOGICAL.'', '''');
    return deviceName;
```

```
  }

}
```

**Listing C.2:** Complete definition of AbstractTargetMakeRule.

```
/**
* @author Jutta Fitzek
*/
public abstract class AbstractGsiMakeRule extends AbstractMakeRule {

  protected abstract ImmutableValue makeValueGsiImpl(MakeRuleArguments mra) throws
  TrimException;

  @Override
  protected final ImmutableValue makeValueImpl(final MakeRuleArguments mra) throws
  TrimException {
    ImmutableValue newValue = makeValueGsiImpl(mra);
    final Parameter dependentParameter = mra.getParameter();
    if ((newValue != null) && newValue.isDefined() &&
    dependentParameter.getValueType().equals(Type.FUNCTION)) {
      final ImmutableDiscreteFunction functionValue = (ImmutableDiscreteFunction) newValue;
      final BeamProcess beamProcess = mra.getBeamProcess();
      if (functionValue.getLength() != beamProcess.getLength()) {
        final String errMsg = String.format(
         ''Function length %d unequal to beam process length %d for parameter %s in beam
    process %s'', functionValue.getLength(), beamProcess.getLength(), dependentParameter.
    getName(), beamProcess.getName());
        throw new TrimException(errMsg);
      }
      newValue = createSparseFunctionIfConstant(functionValue);
    }
    return newValue;
  }

  ...

}
```

**Listing C.3:** Partial definition of AbstractGSIMakeRule and makeValueGsiImpl together with Implementation of makeValueImpl().

```
/**
* @author Lionel Mestre
* @author Raphael Mueller
* @author Grzegorz Kruk
*/
public abstract class AbstractMakeRule extends AbstractRule implements MakeRule {

  protected abstract ImmutableValue makeValueImpl(MakeRuleArguments mra) throws
    TrimException;

  @Override
  public final void makeValue(MakeRuleArguments mra) throws TrimException {
    BeamProcess bp = mra.getBeamProcess();
    ContextSettings ctxSettings = mra.getContextSettings();
    ParameterTreeNode depParameterNode = mra.getParameterTreeNode();
    Parameter depParameter = depParameterNode.getParameter();
    SettingPartEnum settingPart = mra.getSettingPart();
```

```
17      ImmutableValue newValue = makeValueImpl(mra);
18      if (logger.isDebugEnabled()) {
19        logger.debug(''      New value: {}'', newValue);
20      }
21      newValue = convertToCorrectValueType(bp, depParameter, newValue);
22      if (newValue != null && newValue.isDefined()
23       && !TrimCommandHelper.shouldInterruptProcessing(mra.getTrimCommand())) {
24        ctxSettings.updateSetting(bp, depParameter, newValue,
25        getUpdateSettingPart(settingPart));
26      } else if (newValue == null && mra.getTrimCommand().getTrimRequest().isForceProcessing()
27       && !TrimCommandHelper.shouldInterruptProcessing(mra.getTrimCommand())) {
28        updateSettingWithCurrentValue(bp, ctxSettings, depParameter, settingPart);
29      }
30    }
31
32    ...
33  }
```

**Listing C.4:** Partial definition of AbstractMakeRule and makeValueImpl together with Implementation of makeValue().

```
1  /**
2  * Abstract rule that is meant to be extended by all other rules (make rules, incorporation
       rules, etc). It contains
3  * dependencies on all typically used finders and a number of utility methods.
4  *
5  * @author Raphael Mueller
6  */
7  public abstract class AbstractRule {
8    ...
9  }
```

**Listing C.5:** Head of AbstractRule.

```
1  /**
2  * @author Lionel Mestre
3  * @author Markus Albert
4  * @author Wojciech Sliwinski
5  */
6  public interface MakeRule {
7
8    /**
9    * Calculates value of the dependent Parameter and adds it to the context setting object.
10   *
11   * @param args contains all information necessary for the calculation
12   * @throws TrimException if any trim-related problem occurs
13   */
14   void makeValue(MakeRuleArguments args) throws TrimException;
15 }
```

**Listing C.6:** Full implementation of the MakeRule interface.

### TargetAlignmentMakeRule Implementation

```
public class TargetAlignmentMakeRule extends AbstractGsiMakeRule {

  private final static String PARAMETER_TYPE_STRING_TARGET_MATERIAL =
   ''STRING_TARGET_MATERIAL'';

  private final static String DEVICE_GTE1KY1 = ''LOGICAL.GTE1KY1'';
  private final static String DEVICE_GTS1KY1 = ''LOGICAL.GTS1KY1'';
  private final static String DEVICE_GTS1MU1 = ''LOGICAL.GTS1MU1'';
  private final static String DEVICE_GTS1MU2 = ''LOGICAL.GTS1MU2'';
  private final static double GTS1MU1_ANGLE = 7.5 / 180 * Math.PI;
  private final static double GTS1MU2_ANGLE = 7.5 / 180 * Math.PI;

  final static String YD1 = ''yd1'';
  final static String BD1 = ''bd1'';
  final static String YY2 = ''yy2'';
  final static String BY2 = ''by2'';
  final static String YB2 = ''yb2'';
  final static String BB2 = ''bb2'';
  final static String YD2 = ''yd2'';
  final static String BD2 = ''bd2'';
  final static String XD1 = ''xd1'';
  final static String AD1 = ''ad1'';
  final static String XX2 = ''xx2'';
  final static String AX2 = ''ax2'';
  final static String XA2 = ''xa2'';
  final static String AA2 = ''aa2'';
  final static String XD2 = ''xd2'';
  final static String AD2 = ''ad2'';
  final static String DET1 = ''det1'';
  final static String DET2 = ''det2'';

  private enum Mode {
    X_MODE,
    Y_MODE;

  ...
}
```

**Listing C.7:** Head definition of TargetAlignmentMakeRule.

```
private static Mode getModeForDevice(final String deviceName) throws TrimException  {
  Mode mode;
  switch (deviceName) {
    case DEVICE_GTE1KY1:
      mode = Mode.Y_MODE;
      break;
    case DEVICE_GTS1KY1:
      mode = Mode.Y_MODE;
      break;
    case DEVICE_GTS1MU1:
      mode = Mode.X_MODE;
      break;
    case DEVICE_GTS1MU2:
      mode = Mode.X_MODE;
      break;
    default:
```

```
      throw new TrimException( ''No mode definition found for device ''' +
       deviceName.replaceFirst(''LOGICAL.'', '''') + '''.'');
  }
  return mode;
}
```

**Listing C.8:** Definition of method getModeForDevice.

```
private Pair<ImmutableScalar, ImmutableScalar> getChangeValuesForMode(final
    MakeRuleArguments mra, final Mode mode, final List<Parameter> parentParameters) {
  ImmutableScalar change1Scalar = null;
  ImmutableScalar change2Scalar = null;

  for (final Parameter parameter : parentParameters) {
    final String parameterName = parameter.getName();
    if (mode.equals(Mode.X_MODE)) {
      if (parameterName.contains(''XPOSITION_CHANGE_DET1'')) {
        final Setting xChange1Setting = getSettingOrNull(mra, parameter);
        if (xChange1Setting != null) {
          change1Scalar = xChange1Setting.getScalarValue();
        }
      }
      if (parameterName.contains(''XPOSITION_CHANGE_DET2'')) {
        final Setting xChange2Setting = getSettingOrNull(mra, parameter);
        if (xChange2Setting != null) {
          change2Scalar = xChange2Setting.getScalarValue();
        }
      }
    } else {
      if (parameterName.contains(''YPOSITION_CHANGE_DET1'')) {
        final Setting yChange1Setting = getSettingOrNull(mra, parameter);
        if (yChange1Setting != null) {
          change1Scalar = yChange1Setting.getScalarValue();
        }
      }
      if (parameterName.contains(''YPOSITION_CHANGE_DET2'')) {
        final Setting yChange2Setting = getSettingOrNull(mra, parameter);
        if (yChange2Setting != null) {
          change2Scalar = yChange2Setting.getScalarValue();
        }
      }
    }
  }
}
```

**Listing C.9:** Definition of method getChangeValuesForMode.

```
/**
* @author jhucka
*/
public class OpticsReader {

  HashMap<String, Double> opticsEntries = new HashMap<>();

  public void readOptics(final String location) throws IOException {
    final String webFile = PropertyConfig.getDefaultPropertyConfigLocation().replace(''
    cscoap/config/'', location);
    final BufferedInputStream webInputStream = new BufferedInputStream(new URL(webFile).
    openStream());
```

```
11
12      try (final BufferedReader bufferedReader = new BufferedReader(new InputStreamReader(
        webInputStream))) {
13        String line = bufferedReader.readLine();
14        while (line != null) {
15          if (line.contains(''#'')) {
16            line = bufferedReader.readLine();
17            continue;
18          }
19          String[] entries = line.split('','');
20          opticsEntries.put(''yd1'', Double.parseDouble(entries[0]));
21          opticsEntries.put(''bd1'', Double.parseDouble(entries[1]));
22          opticsEntries.put(''yy2'', Double.parseDouble(entries[2]));
23          opticsEntries.put(''by2'', Double.parseDouble(entries[3]));
24          opticsEntries.put(''yb2'', Double.parseDouble(entries[4]));
25          opticsEntries.put(''bb2'', Double.parseDouble(entries[5]));
26          opticsEntries.put(''yd2'', Double.parseDouble(entries[6]));
27          opticsEntries.put(''bd2'', Double.parseDouble(entries[7]));
28          line = bufferedReader.readLine();
29          entries = line.split('','');
30          opticsEntries.put(''xd1'', Double.parseDouble(entries[0]));
31          opticsEntries.put(''ad1'', Double.parseDouble(entries[1]));
32          opticsEntries.put(''xx2'', Double.parseDouble(entries[2]));
33          opticsEntries.put(''ax2'', Double.parseDouble(entries[3]));
34          opticsEntries.put(''xa2'', Double.parseDouble(entries[4]));
35          opticsEntries.put(''aa2'', Double.parseDouble(entries[5]));
36          opticsEntries.put(''xd2'', Double.parseDouble(entries[6]));
37          opticsEntries.put(''ad2'', Double.parseDouble(entries[7]));
38          line = bufferedReader.readLine();
39          entries = line.split('','');
40          opticsEntries.put(''det1'', Double.parseDouble(entries[0]));
41          opticsEntries.put(''det2'', Double.parseDouble(entries[1]));
42          line = bufferedReader.readLine();
43        }
44      }
45    }
46
47    public HashMap<String, Double> getOpticsEntries() {
48      return opticsEntries;
49    }
50  }
```

**Listing C.10:** Full definition of OpticsReader class.

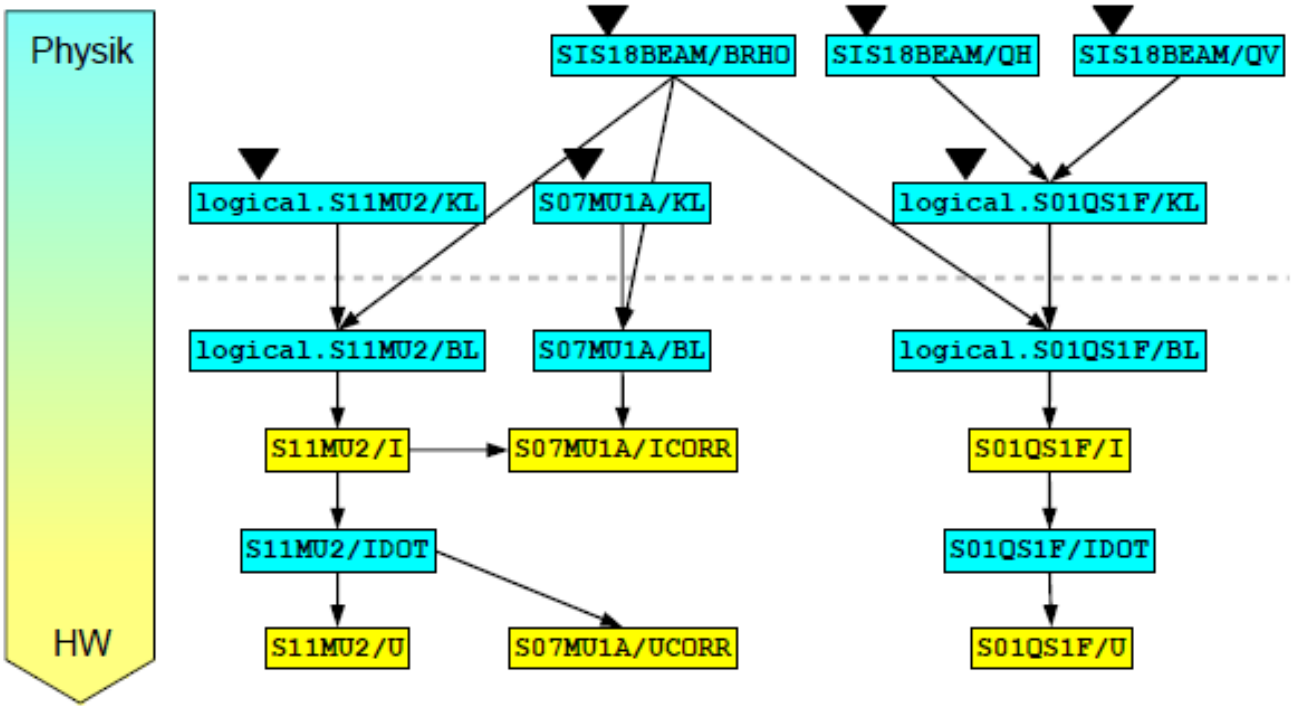


**Figure C.1.:** Visual representation of the parameter hierarchy for ion-optical devices in a section of the SIS18, taken from [64]. It is shown how the beam device top level physics parameters influence the underlying hardware parameters of different SIS18 dipoles and quadrupole. Copyright at GSI/FAIR, used with permission.

# D. Additional Benchmark Data

This Ch. of the appendix contains all additional necessary information and data used for benchmarking the FRS machine model during the engineering runs mentioned in Ch. 9.
Listing D.1 shows the necessary optical coefficients to calculate the beamshift on the respective target device at TA, when called by the TargetAlignmentMakeRule. The coefficients yd1 and xd1 are the first order ion-optical coefficients, describing the dependency of the vertical (y) or horizontal (x) position from the dimensionless horizontal momentum deviation (d), respectively. Its units are given in $\mathrm{m}$. Similarly, bd1 and ad1 describe the dependency of the vertical (b) or horizontal (a) angle from d, respectively. The unit is $\mathrm{mrad}$. The following coefficients express the second order ion-optical coefficients and the quadratic dependencies between each observable. The respective units in order are given in $\mathrm{m}^{-1}$, $\mathrm{mrad}\,\mathrm{m}^{-1}$, $\mathrm{m}\,\mathrm{mrad}^{-1}$, $\mathrm{mrad}^{-1}$, $\mathrm{m}$ and $\mathrm{mrad}$. Lastly the detector distances are given in units of $\mathrm{m}$.

```
# 1.yd1 2.bd1 3.yy2 4.by2 5.yb2 6.bb2 7.yd2 8.bd2
# 1.xd1 2.ad1 3.xx2 4.ax2 5.xa2 6.aa2 7.xd2 8.ad2
# 1.distance det1 from TA 2.distance det2 from TA
0.075838,0.010894,-0.637664,-0.268414,7.520080,1.597234,0.075200,0.015972
0.843274,-0.203990,1.000000,0.000000,2.683167,1.000000,0.252065,0.131087
-0.069,1.052
```

**Listing D.1:** Content of SISTA2019_TA1_LO.txt optics file used for the call of TargetAlignmentMakeRule in Ch. 9 to calculate the resulting values in Tab. 9.5.

# E. FRS Detector Calibrations

This Ch. with its Subsec. of the appendix contains all TPC, TAC, TOF and MUSIC calibration coefficients that were used for the respective functions mentioned in Sec. 12.3 in order to achieve unambiguous particle identification.

### E.0.1. TPC Calibration Functions

| TPC Number | Drift-Time 1 | Drift-Time 2 | Drift-Time 3 | Drift-Time 4 | Delay-Line 1 | Delay-Line 2 |
|---|---|---|---|---|---|---|
| 23 | -0.0355 | -0.0358 | -0.0356 | -0.0352 | 0.0739 | 0.0751 |
| 24 | -0.0335 | -0.0334 | -0.0366 | -0.0340 | 0.0749 | 0.0731 |
| 41 | -0.0425 | -0.0433 | -0.0425 | -0.0424 | 0.0854 | 0.0841 |
| 42 | -0.0413 | -0.0415 | -0.0425 | -0.0415 | 0.0823 | 0.0855 |

**Table E.1.:** Table containing the TPC calibration function factors. The unit for the factors is given in $\mathrm{mm/channel}$. With the coefficient of determination $R^2$ deviating from 1 by $1.25{\cdot}10^{-5}$, the inaccuracy of the given values is much smaller than the given values and thus irrelevant.

| TPC Number | Drift-Time 1 | Drift-Time 2 | Drift-Time 3 | Drift-Time 4 | Delay-Line 1 | Delay-Line 2 |
|---|---|---|---|---|---|---|
| 23 | 60.52 | 63.08 | 57.95 | 59.42 | 26.30 | 17.34 |
| 24 | 73.57 | 74.69 | 76.45 | 74.54 | 12.92 | 17.75 |
| 41 | 66.01 | 66.43 | 65.89 | 65.60 | 1.995 | 5.143 |
| 42 | 88.74 | 90.86 | 89.17 | 75.19 | -3.555 | -3.695 |

**Table E.2.:** Table containing the TPC calibration function offsets. The unit for the offsets is given in $\mathrm{mm}$. With the coefficient of determination $R^2$ deviating from 1 by $1.25{\cdot}10^{-5}$, the inaccuracy of the given values is much smaller than the given values and thus irrelevant.

### E.0.2. TAC and TOF Calibration Functions

| TAC | 41L-21L | 41R-21R | 42L-21L | 42R-21R | 41L-22L | 41R-22R |
|---|---|---|---|---|---|---|
| Offset / [ps/ch] | 0.0 | 0.0 | 0.0 | 0.0 | 0.0 | 0.0 |
| Factor / [ps/ch] | 11.15(11) | 10.97(11) | 10.81(11) | 10.61(11) | 10.09(10) | 10.80(11) |

**Table E.3.:** Table containing the TAC calibration coefficients. It is important to note that the TAC offset has been defined as 0.0 at all times. Instead the TAC offset should be represented and incorporated by the TOF calibration offset.

### E.0.3. MUSIC Calibration Functions

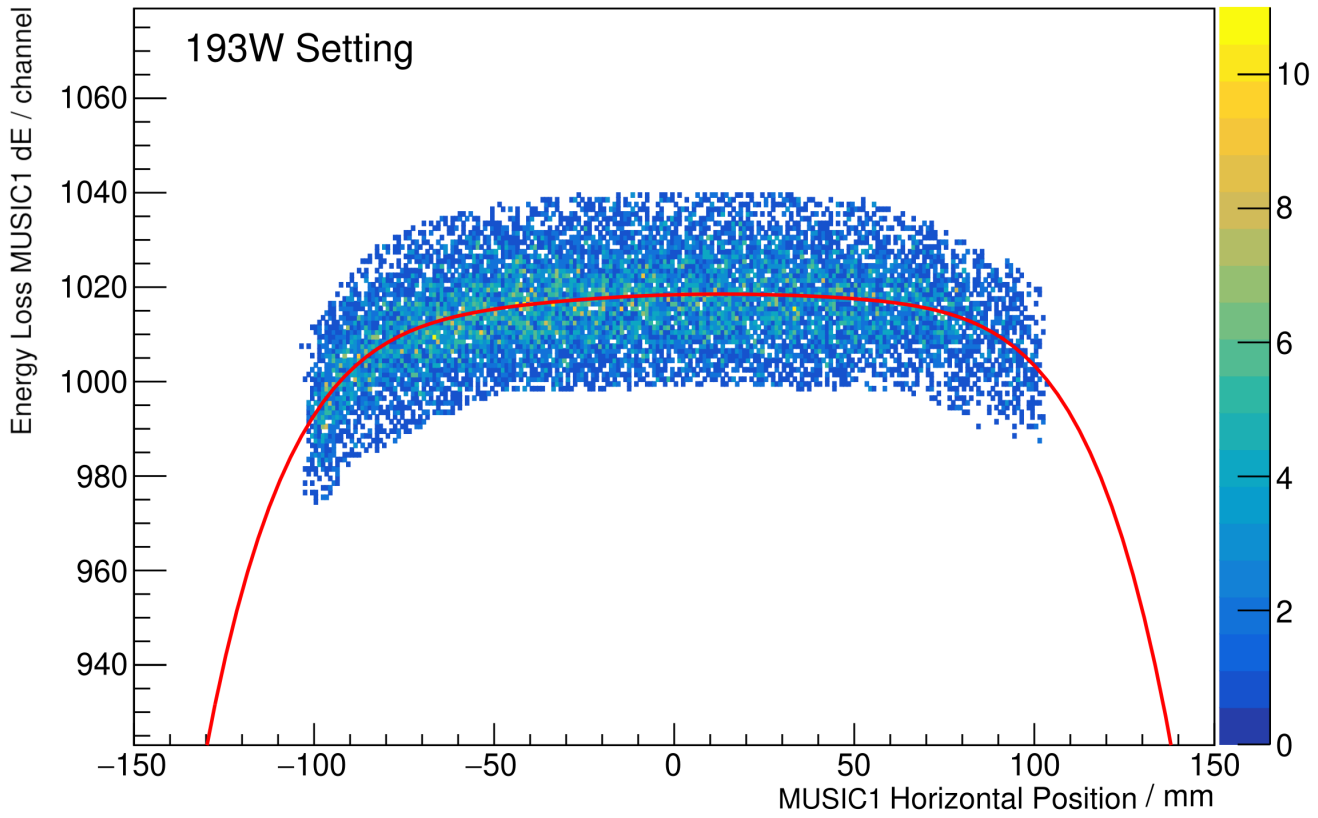


**Figure E.1.:** Examplary plot for position-dependent energy loss measurement with fragments covering the full horizontal width of MUSIC1 at S4 in the $^{193}W$ setting. The reduced energy-loss towards the edges of the detector is visible and fitted to a fifth-order polynomial represented by the red curve, whose parameters are documented in Tab. E.5 and was found to be sufficient to correct edge effects.

| $^{205}$Au | $a_0$ | $a_1$ | $a_2$ | $a_3$ | $a_4$ | $a_5$ |
|---|---|---|---|---|---|---|
| MUSIC1 | 1072.14(21) | 3.7(83)·$10^{-2}$ | -1.9(14)·$10^{-4}$ | -9.2(32)·$10^{-6}$ | -1.83(39)·$10^{-7}$ | 1.1(27)·$10^{-9}$ |
| MUSIC2 | 1048.13(22) | 4.5(88)·$10^{-2}$ | 1.6(13)·$10^{-4}$ | -1.52(59)·$10^{-5}$ | -2.15(38)·$10^{-7}$ | 1.6(30)·$10^{-9}$ |

**Table E.4.:** MUSIC position correction coefficients $a_n$ for the $^{205}$Au setting given in units of $\mathrm{channel}/\mathrm{mm}^n$.

| $^{193}$W | $a_0$ | $a_1$ | $a_2$ | $a_3$ | $a_4$ | $a_5$ |
|---|---|---|---|---|---|---|
| MUSIC1 | 1016.79(20) | 2.14(80)·$10^{-2}$ | 2.2(18)·$10^{-4}$ | -5.8(26)·$10^{-7}$ | -1.93(34)·$10^{-7}$ | 3.7(30)·$10^{-10}$ |
| MUSIC2 | 1037.36(20) | 3.4(10)·$10^{-2}$ | 3.3(28)·$10^{-4}$ | -8.7(62)·$10^{-6}$ | -2.36(45)·$10^{-7}$ | 1.2(12)·$10^{-9}$ |

**Table E.5.:** MUSIC position correction coefficients $a_n$ for the $^{193}$W setting given in units of $\mathrm{channel}/\mathrm{mm}^n$.

| $^{193}$Ta | $a_0$ | $a_1$ | $a_2$ | $a_3$ | $a_4$ | $a_5$ |
|---|---|---|---|---|---|---|
| MUSIC1 | 1041.61(51) | 1.87(78)·$10^{-2}$ | 3.7(31)·$10^{-4}$ | -4.6(36)·$10^{-6}$ | -2.25(45)·$10^{-7}$ | 7.6(27)·$10^{-9}$ |
| MUSIC2 | 1059.73(52) | 3.0(15)·$10^{-2}$ | 2.6(25)·$10^{-4}$ | -1.4(9)·$10^{-5}$ | -2.23(45)·$10^{-7}$ | 1.7(5)·$10^{-9}$ |

**Table E.6.:** MUSIC position correction coefficients $a_n$ for the $^{193}$Ta setting given in units of $\mathrm{channel}/\mathrm{mm}^n$.

| $^{190}$Lu | $a_0$ | $a_1$ | $a_2$ | $a_3$ | $a_4$ | $a_5$ |
|---|---|---|---|---|---|---|
| MUSIC1 | 1072(2) | 3.7(80)·$10^{-2}$ | -1.93(50)·$10^{-4}$ | -9.2(60)·$10^{-6}$ | -1.83(30)·$10^{-7}$ | 1.1(60)·$10^{-9}$ |
| MUSIC2 | 1048(2) | 4.5(95)·$10^{-2}$ | 1.60(45)·$10^{-4}$ | -1.5(12)·$10^{-5}$ | -2.15(38)··$10^{-7}$ | 1.6(65)·$10^{-9}$ |

**Table E.7.:** MUSIC position correction coefficients $a_n$ for the $^{190}$Lu setting given in units of $\mathrm{channel}/\mathrm{mm}^n$.

| All Settings | $b_0$ | $b_1$ | $b_2$ |
|---|---|---|---|
| MUSIC1 | 15712.3(786) | -24957(125) | 11630.2(582) |
| MUSIC2 | 15275.4(793) | -23944(120) | 10891.9(545) |

**Table E.8.:** MUSIC velocity correction coefficients $b_n$ for all settings in units of $\mathrm{channel}$. The fit to a second-order polynomial instead of a fourth order polynomial was proven to be sufficient and therefore these coefficients were used.

# F. Path-Length Correction Matrices

This Ch. contains all FRS ion-optical transfer matrices that were used for the mentioned LISE++ calculations, MOCADI simulations as well as all correction procedures introduced in Part IV. All matrices are given for their respective transfer line as indicated by ”A - B”, where A stands for TA2, S1, S2 or S3 and B for S1, S2, S3, S4, respectively. The unit of each coeffcient is derived by multiplying the column unit with its respective line unit for the coefficient in question.

```
FRS optics RUN81-TA2-2020, focus at S4 3.3m behind HFSQT13

TA2 - S1
NON SYMPL. SYSTEM TRANSFER MATRIX AT PATH-LENGTH L= 1.747267023E+01 M
*********************************************************************
                  X / [1/mm]   A / [1/mrad]   Y / [1/mm]   B / [1/mrad]   L / [1/mm]
---------------------------------------------------------------------------------
1 X / [mm]      -5.330829E-01 -1.637087E-01  0.000000E+00  0.000000E+00  2.631752E-01
2 A / [mrad]    -8.067119E-03 -1.878358E+00  0.000000E+00  0.000000E+00  4.037374E+00
3 Y / [mm]       0.000000E+00  0.000000E+00 -6.777438E+00 -3.853038E-01  0.000000E+00
4 B / [mrad]     0.000000E+00  0.000000E+00  3.819899E-02 -1.453767E-01  0.000000E+00
5 G / [mm]       2.603529E-09  2.017505E-10  0.000000E+00  0.000000E+00  5.056821E+00
6 P / [%]        2.150132E+00  1.666162E-01  0.000000E+00  0.000000E+00 -4.790988E+00

TA2 - S2
NON SYMPL. SYSTEM TRANSFER MATRIX AT PATH-LENGTH L= 3.554934045E+01 M
*********************************************************************
                  X / [1/mm]   A / [1/mrad]   Y / [1/mm]   B / [1/mrad]   L / [1/mm]
---------------------------------------------------------------------------------
1 X / [mm]       7.679624E-01  1.266808E-01  0.000000E+00  0.000000E+00  8.221816E-01
2 A / [mrad]    -2.075879E-03  1.301805E+00  0.000000E+00  0.000000E+00  8.448954E+00
3 Y / [mm]       0.000000E+00  0.000000E+00  1.596281E+00  6.491214E-01  0.000000E+00
4 B / [mrad]     0.000000E+00  0.000000E+00 -3.644217E-02  6.116371E-01  0.000000E+00
5 G / [mm]      -7.858769E-09  0.000000E+00  0.000000E+00  0.000000E+00  1.028845E+01
6 P / [%]       -6.490186E+00 -2.305909E-10  0.000000E+00  0.000000E+00 -1.085268E+01

TA2 - S3
NON SYMPL. SYSTEM TRANSFER MATRIX AT PATH-LENGTH L= 5.385601068E+01 M
*********************************************************************
                  X / [1/mm]   A / [1/mrad]   Y / [1/mm]   B / [1/mrad]   L / [1/mm]
---------------------------------------------------------------------------------
1 X / [mm]      -5.410140E-01 -2.037639E-01  0.000000E+00  0.000000E+00  5.215073E-01
2 A / [mrad]    -1.294978E-01 -1.897154E+00  0.000000E+00  0.000000E+00  4.048770E+00
3 Y / [mm]       0.000000E+00  0.000000E+00 -6.598789E+00  5.956754E-02  0.000000E+00
4 B / [mrad]     0.000000E+00  0.000000E+00 -1.272472E-02 -1.514281E-01  0.000000E+00
5 G / [mm]       2.570564E-09 -1.990502E-10  0.000000E+00  0.000000E+00  1.558664E+01
6 P / [%]        2.122907E+00 -1.643867E-01  0.000000E+00  0.000000E+00 -1.696241E+01
```

**Listing F.1:** FRS ion-optical Matrices for S468 [106]

For example the coefficient describing the horizontal position change at S1 in dependence of the horizontal position change at the target TA2 would be $(x_{S1}|x_{TA2}) = -0.5331$ and dimensionless, see Lst F.1, matrix TA2 - S1, column X, line X.

```
TA2 - S4
NON SYMPL. SYSTEM TRANSFER MATRIX AT PATH-LENGTH L= 7.306768090E+01 M
*****************************************************************
                  X / [1/mm]   A / [1/mrad]   Y / [1/mm]   B / [1/mrad]   L / [1/mm]
-----------------------------------------------------------------------------
1 X / [mm]       9.078734E-01  1.071849E-01  0.000000E+00  0.000000E+00  3.039788E-05
2 A / [mrad]     1.381298E-09  1.101475E+00  0.000000E+00  0.000000E+00  1.934776E-04
3 Y / [mm]       0.000000E+00  0.000000E+00  1.856163E+00  1.227309E+00  0.000000E+00
4 B / [mrad]     0.000000E+00  0.000000E+00 -4.492974E-10  5.387458E-01  0.000000E+00
5 G / [mm]      -2.149068E-13  1.523592E-14  0.000000E+00  0.000000E+00  2.114675E+01
6 P / [%]       -1.756419E-04  1.274464E-05  0.000000E+00  0.000000E+00 -2.225671E+01

S1 - S2
NON SYMPL. SYSTEM TRANSFER MATRIX AT PATH-LENGTH L= 1.807667023E+01 M
*****************************************************************
                  X / [1/mm]   A / [1/mrad]   Y / [1/mm]   B / [1/mrad]   L / [1/mm]
-----------------------------------------------------------------------------
1 X / [mm]      -1.442848E+00 -2.483505E-02  0.000000E+00  0.000000E+00 -3.278003E-01
2 A / [mrad]     7.301860E-03 -6.929478E-01  0.000000E+00  0.000000E+00 -2.347228E+00
3 Y / [mm]       0.000000E+00  0.000000E+00 -2.461034E-01  1.412990E-01  0.000000E+00
4 B / [mrad]     0.000000E+00  0.000000E+00  1.860083E-01 -4.170128E+00  0.000000E+00
5 G / [mm]      -4.103742E-09  2.044611E-10  0.000000E+00  0.000000E+00  5.231626E+00
6 P / [%]       -3.389088E+00  1.688549E-01  0.000000E+00  0.000000E+00 -4.965794E+00

S1 - S3
NON SYMPL. SYSTEM TRANSFER MATRIX AT PATH-LENGTH L= 3.638334045E+01 M
*****************************************************************
                  X / [1/mm]   A / [1/mrad]   Y / [1/mm]   B / [1/mrad]   L / [1/mm]
-----------------------------------------------------------------------------
1 X / [mm]       9.950183E-01  7.216090E-02  0.000000E+00  0.000000E+00 -4.833748E-01
2 A / [mrad]     6.466865E-02  1.009697E+00  0.000000E+00  0.000000E+00 -3.990785E-03
3 Y / [mm]       0.000000E+00  0.000000E+00  9.544075E-01 -6.700556E-02  0.000000E+00
4 B / [mrad]     0.000000E+00  0.000000E+00  3.383081E-01  1.024019E+00  0.000000E+00
5 G / [mm]      -3.304243E-11 -5.906301E-10  0.000000E+00  0.000000E+00  1.052982E+01
6 P / [%]       -2.728830E-02 -4.877739E-01  0.000000E+00  0.000000E+00 -1.113144E+01

S1 - S4
NON SYMPL. SYSTEM TRANSFER MATRIX AT PATH-LENGTH L= 5.559501068E+01 M
*****************************************************************
                  X / [1/mm]   A / [1/mrad]   Y / [1/mm]   B / [1/mrad]   L / [1/mm]
-----------------------------------------------------------------------------
1 X / [mm]      -1.705312E+00 -2.101045E-02  0.000000E+00  0.000000E+00 -1.666416E-01
2 A / [mrad]     7.323922E-03 -5.863129E-01  0.000000E+00  0.000000E+00  2.150029E+00
3 Y / [mm]       0.000000E+00  0.000000E+00 -2.698429E-01  2.915871E-02  0.000000E+00
4 B / [mrad]     0.000000E+00  0.000000E+00 -7.090354E-02 -3.698198E+00  0.000000E+00
5 G / [mm]       4.438137E-09  1.730056E-10  0.000000E+00  0.000000E+00  1.608993E+01
6 P / [%]        3.665249E+00  1.428772E-01  0.000000E+00  0.000000E+00 -1.746565E+01
```

**Listing F.2:** Continued FRS ion-optical Matrices for S468

```
S2 - S3
NON SYMPL. SYSTEM TRANSFER MATRIX AT PATH-LENGTH L= 1.830667023E+01 M
*********************************************************************
                  X / [1/mm]   A / [1/mrad]   Y / [1/mm]   B / [1/mrad]   L / [1/mm]
---------------------------------------------------------------------------
1 X / [mm]      -6.878897E-01 -2.492787E-02  0.000000E+00  0.000000E+00  1.659995E-01
2 A / [mrad]    -1.005726E-01 -1.457366E+00  0.000000E+00  0.000000E+00 -3.379800E+00
3 Y / [mm]       0.000000E+00  0.000000E+00 -4.027804E+00  1.347289E-01  0.000000E+00
4 B / [mrad]     0.000000E+00  0.000000E+00 -2.607864E-01 -2.395510E-01  0.000000E+00
5 G / [mm]      -2.835401E-09 -3.949530E-10  0.000000E+00  0.000000E+00  5.298191E+00
6 P / [%]       -2.341625E+00 -3.261732E-01  0.000000E+00  0.000000E+00 -5.032359E+00

S2 - S4
NON SYMPL. SYSTEM TRANSFER MATRIX AT PATH-LENGTH L= 3.751834045E+01 M
*********************************************************************
                  X / [1/mm]   A / [1/mrad]   Y / [1/mm]   B / [1/mrad]   L / [1/mm]
---------------------------------------------------------------------------
1 X / [mm]       1.181874E+00 -1.963709E-06  0.000000E+00  0.000000E+00  1.506244E-05
2 A / [mrad]     1.884637E-03  8.461140E-01  0.000000E+00  0.000000E+00 -6.490037E+00
3 Y / [mm]       0.000000E+00  0.000000E+00  1.135298E+00  4.009561E-01  0.000000E+00
4 B / [mrad]     0.000000E+00  0.000000E+00  6.764261E-02  9.047155E-01  0.000000E+00
5 G / [mm]       9.287856E-09 -3.013220E-16  0.000000E+00  0.000000E+00  1.085830E+01
6 P / [%]        7.670405E+00 -3.479085E-12  0.000000E+00  0.000000E+00 -1.140393E+01

S3 - S4
NON SYMPL. SYSTEM TRANSFER MATRIX AT PATH-LENGTH L= 1.921167023E+01 M
*********************************************************************
                  X / [1/mm]   A / [1/mrad]   Y / [1/mm]   B / [1/mrad]   L / [1/mm]
---------------------------------------------------------------------------
1 X / [mm]      -1.722376E+00  2.109468E-02  0.000000E+00  0.000000E+00  1.643684E-01
2 A / [mrad]     1.175676E-01 -5.820333E-01  0.000000E+00  0.000000E+00  2.122807E+00
3 Y / [mm]       0.000000E+00  0.000000E+00 -2.810752E-01 -2.179408E-01  0.000000E+00
4 B / [mrad]     0.000000E+00  0.000000E+00  2.361916E-02 -3.539453E+00  0.000000E+00
5 G / [mm]       4.450664E-09 -1.700640E-10  0.000000E+00  0.000000E+00  5.560110E+00
6 P / [%]        3.675595E+00 -1.404478E-01  0.000000E+00  0.000000E+00 -5.294278E+00
```

**Listing F.3:** Continued FRS ion-optical Matrices for S468

# G. Scintillator Timing Discussion

Subsection 13.1.5 of Ch. 13 from Part IV briefly introduces that a bend in each identification plot for all settings occurs due to a deviation in time-of-flight measurement, whose origin can be manifold. This Ch. of the appendix focuses on the discussion of the aforementioned measurement deviation and explains its origin. In order to understand it, all layers of the FRS analysis process have to be investigated, starting with the raw timing information from each scintillator. From Sec. 12.3, it is known that only the left-right time difference for each scintillator as well as the left-left and right-right time differences of different scintillators are measured and saved in TAC channels. From the left-right time difference, the position within a scintillator can be derived, whereas the left-left and right-right time differences are utilized for time-of-flight measurements between different focal planes.
In Figure G.1, the first indication can be seen in (a) where a discontinuous kink can be observed around the center position at S2, which is located between the TAC channels 1800 and 1820. In comparison (b) shows a continuous line with only slight deformations but no discontinuities, as would be expected. This can be traced back to the plastic scintillators, which can have non-linear light collection properties depending on the position at which the isotopes hit the material, due to age and sustained radiation damage. As a consequence, asymmetric light output and non-linear light dispersion throughout the material can occur to such a degree, that the time-of-flight measurement deviates from theoretically expected patterns. Furthermore, contribute the PMTs potentially in such a way, that when a defocused heavy-ion beam's or

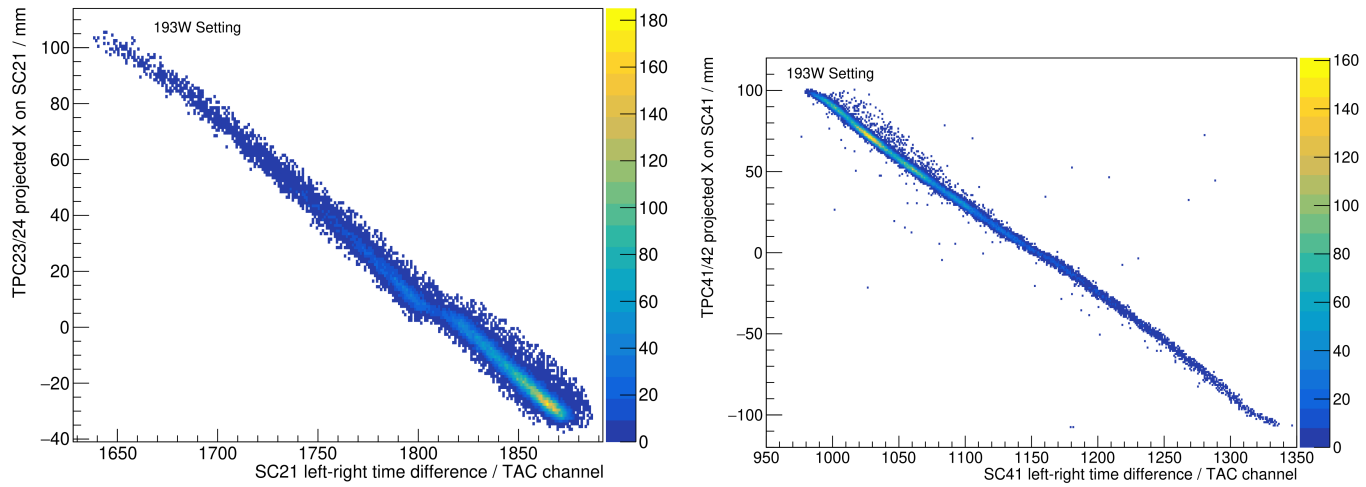


**(a)** **(b)**

**Figure G.1.:** Comparison of two different position measurements. Plot (a) shows the TPC23/24 position projected unto SC21 plotted over SC21 left-right time difference and plot (b) the TPC41/42 position projected unto SC41 plotted over SC41 left-right time difference, both from the $^{193}$W setting.

particle cocktail's intensity is asymmetrically distributed along the face of the scintillator, one side can appear blinded. Which in turn leads to wrong timing information. This wrong timing information would not only influence the left-right time difference of the same scintillator, but also the left-left or right-right time difference of two separate scintillators. Additional evidence can be seen in Fig. G.2, which shows the uncalibrated time-of-flight between SC21-SC41 plotted over the horizontal position in SC21 (a) and the horizontal position at S2 measured by TPC23/24 (b), in the $^{193}$W setting and a iridium selection applied. Even though isotopic separation via time-of-flight is achieved, a gap appears in (a) between 0 and 20 $\mathrm{mm}$. The number of events in (a) and (b) are identical. No loss in events is apparent but events appear shifted out of the gap of (a), due to the previously explained reasons.

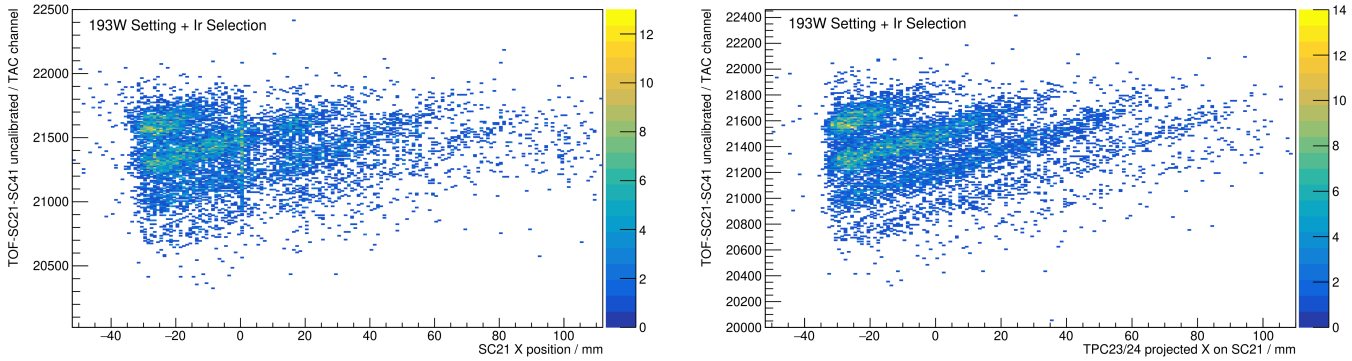


**(a)** **(b)**

**Figure G.2.:** Comparison of two different time-of-flight over position measurements. Plot (a) shows the TOF between SC21 and 41 plotted over the SC21 horizontal position and (b) the same TOF but over the TPC23/24 projection unto A2. Both plots are from the $^{193}$W setting with a selection of only iridium isotopes.

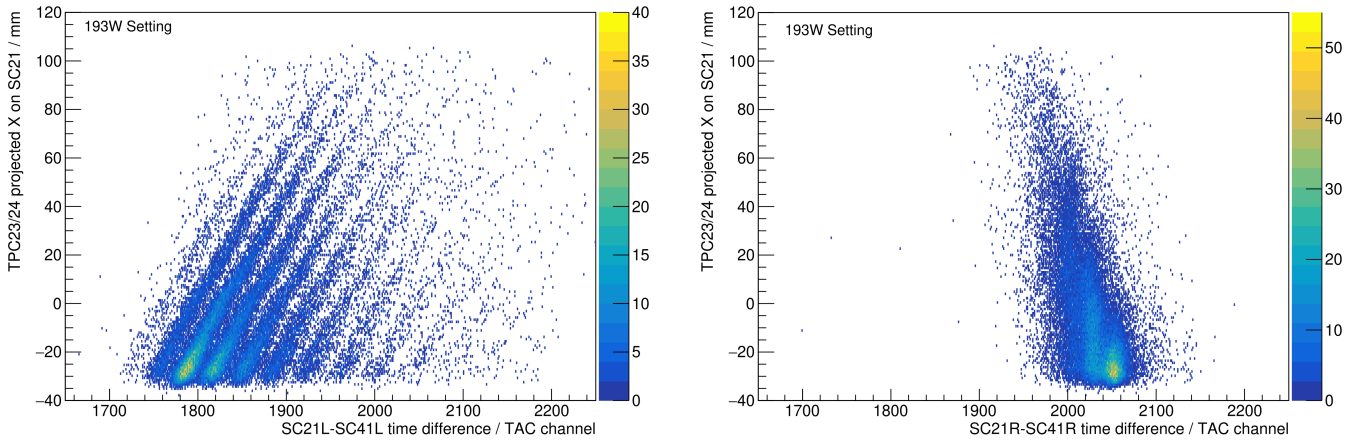


**(a)** **(b)**

**Figure G.3.:** Comparison of TPC horizontal position measurements over two different time-of-flight measurements. Here (a) shows the TPC23/24 projection unto S2 plotted over the SC21-41 left time difference and (b) the identical TPC projection but over the SC21-41 right time difference, for all elements in the $^{193}$W setting.

The investigation focused so far on the left-right time difference of SC21 and will now shift unto the left-left

and right-right time difference of SC21-SC41, which were used for the time-of-flight measurement between S2 and S4 for S468. Fig. G.3 shows the comparison of TPC23/24 projections unto S2 over different time-of-flight measurements restricted to only one side, left-left (a) and right-right (b), respectively. These plots show that the right time difference measurement can not differentiate between heavy-ions of different elements, even though a mass separation seems possible, as will be shown in Figs. G.5, G.7 and G.9 for platinum, tungsten and lutetium isotopes respectively. As a result, the final time-of-flight, derived as an average between the left-left and right-right difference, shows how fragments with low TAC channel numbers are shifted more towards higher TAC channels than fragments with high TAC channel numbers. It would be expected that the right-right time difference is a mirror image of the left-left time difference, which would then result in the bunching-up of fragments in the final TOF over a small window of TAC channels, contrary to what can be seen in Fig. G.4 with its wide distribution. As mentioned before, this is shown in great detail for isotopes of platinum, tungsten and lutetium in Figs. G.5 to G.10.

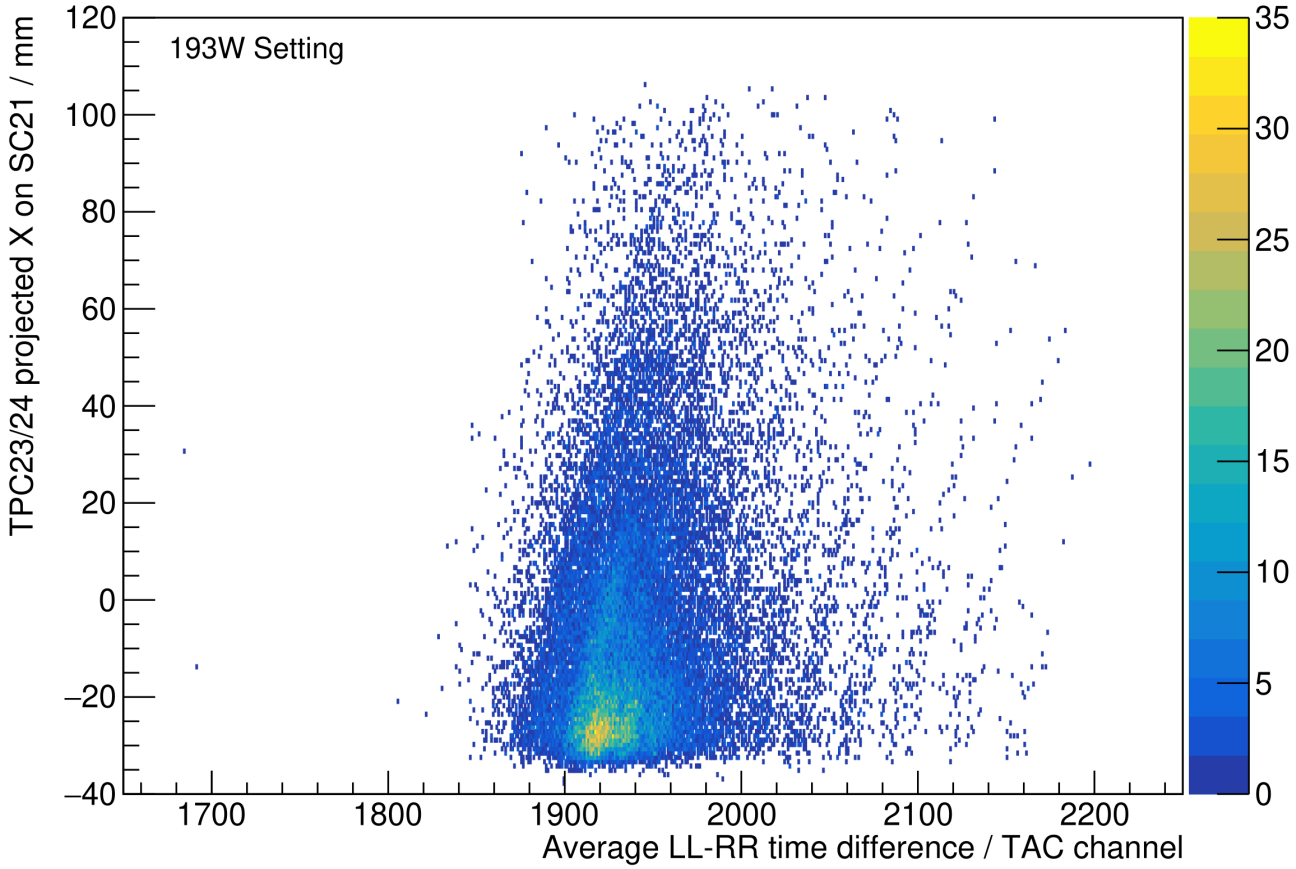


**Figure G.4.:** Plot of TPC23/24 horizontal position projection over the average ll+rr time difference. Fragments with low TAC channel numbers appear shifted much stronger than fragments for high TAC channels. Platinum, tungsten and lutetium fragments are investigated next with the same method.

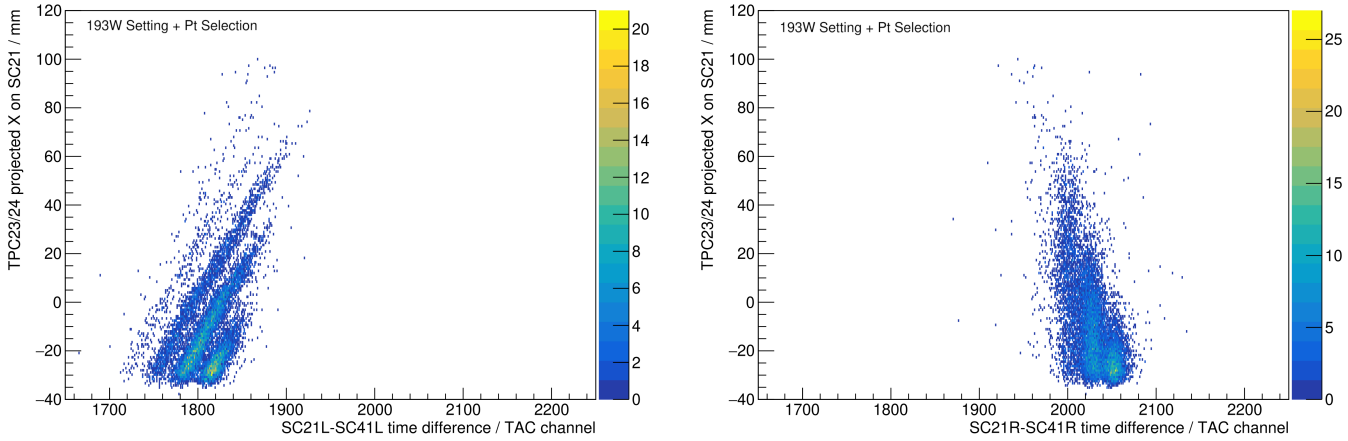


**(a)** **(b)**

**Figure G.5.:** Comparison of TPC horizontal position measurements over two different time-of-flight measurements. Here (a) shows the TPC23/24 projection unto S2 plotted over the SC21-41 left time difference and (b) the identical TPC projection but over the SC21-41 right time difference, for platinum isotopes in the $^{193}$W setting.

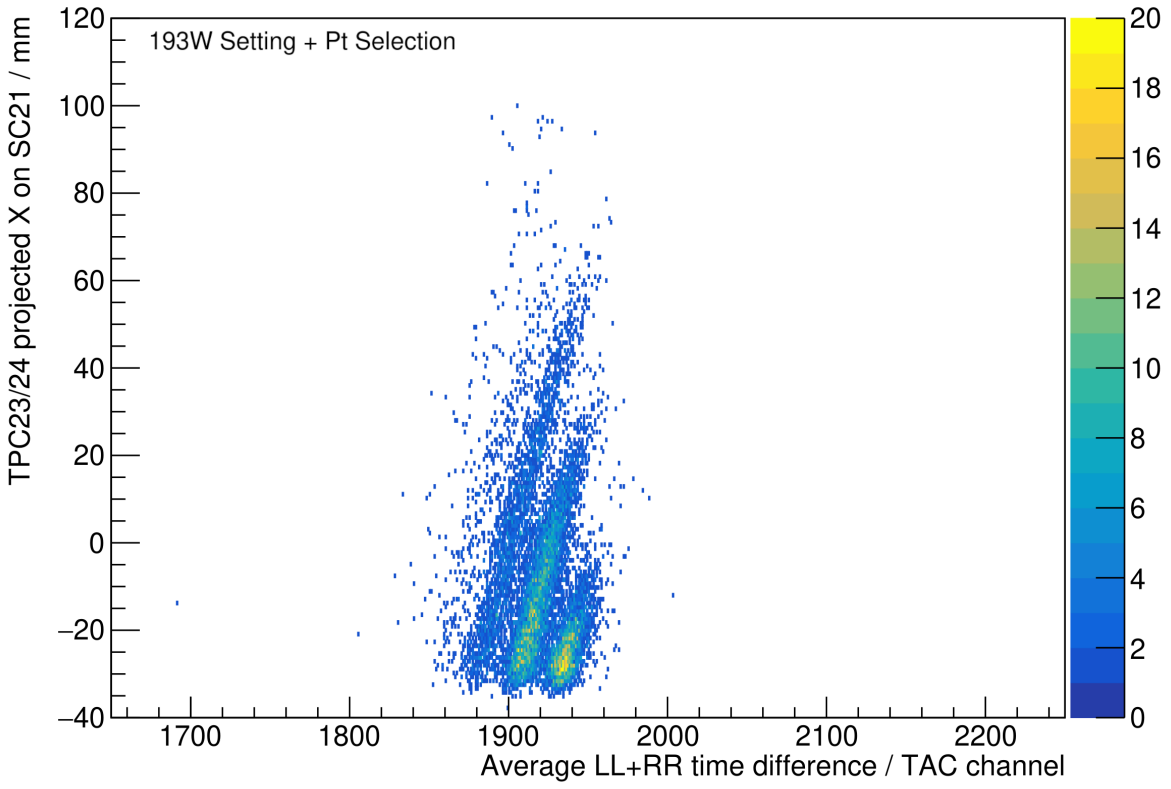


**Figure G.6.:** Plot of TPC23/24 horizontal position projection over the average ll+rr time difference for isotopes of platinum in the $^{193}$W setting. Fragments are shifted by ca. 120 channels towards high TAC channels, i.e. lower masses.

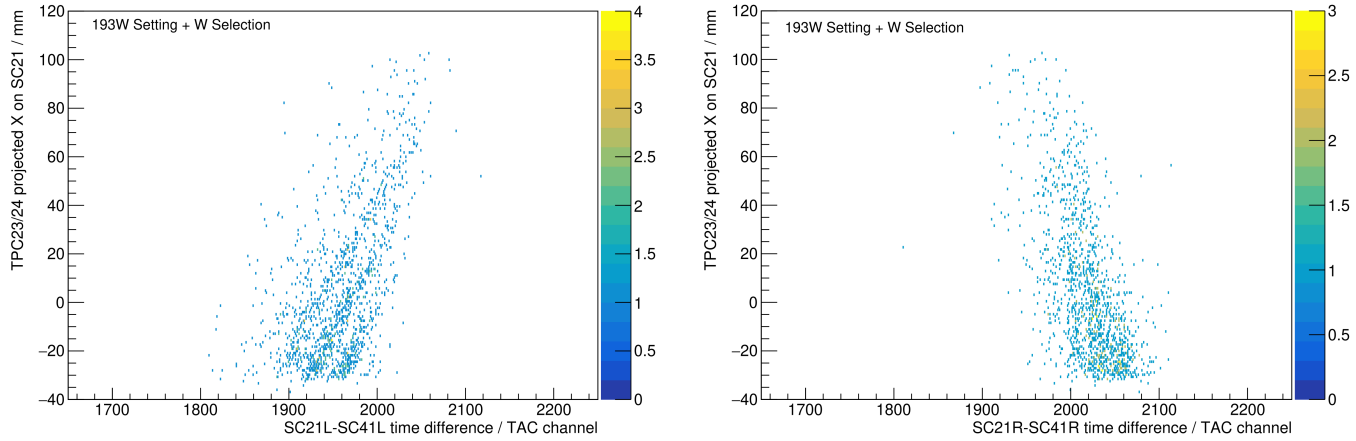


**(a)** **(b)**

**Figure G.7.:** Comparison of TPC horizontal position measurements over two different time-of-flight measurements. Here (a) shows the TPC23/24 projection unto S2 plotted over the SC21-41 left time difference and (b) the identical TPC projection but over the SC21-41 right time difference, for tungsten isotopes in the $^{193}$W setting.

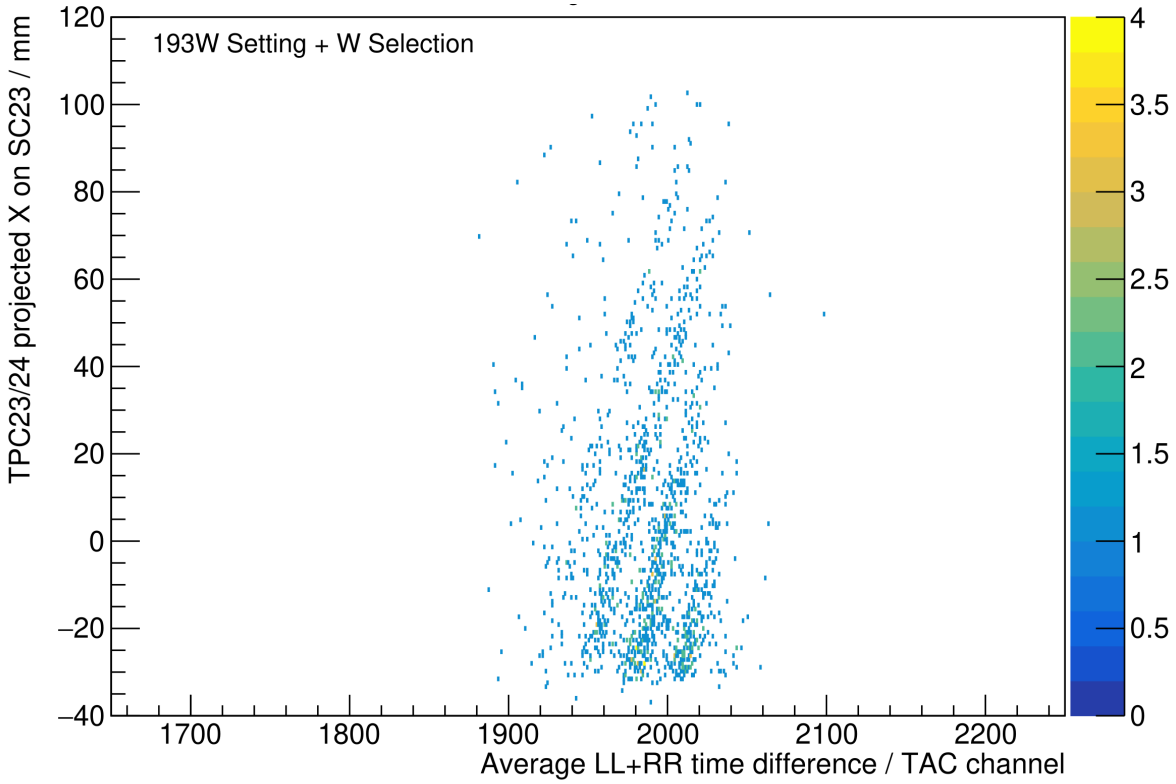


**Figure G.8.:** Plot of TPC23/24 horizontal position projection over the average ll+rr time difference for isotopes of tungsten in the $^{193}$W setting. Fragments are shifted by ca. 50 channels towards high TAC channels, but less than platinum isotopes.

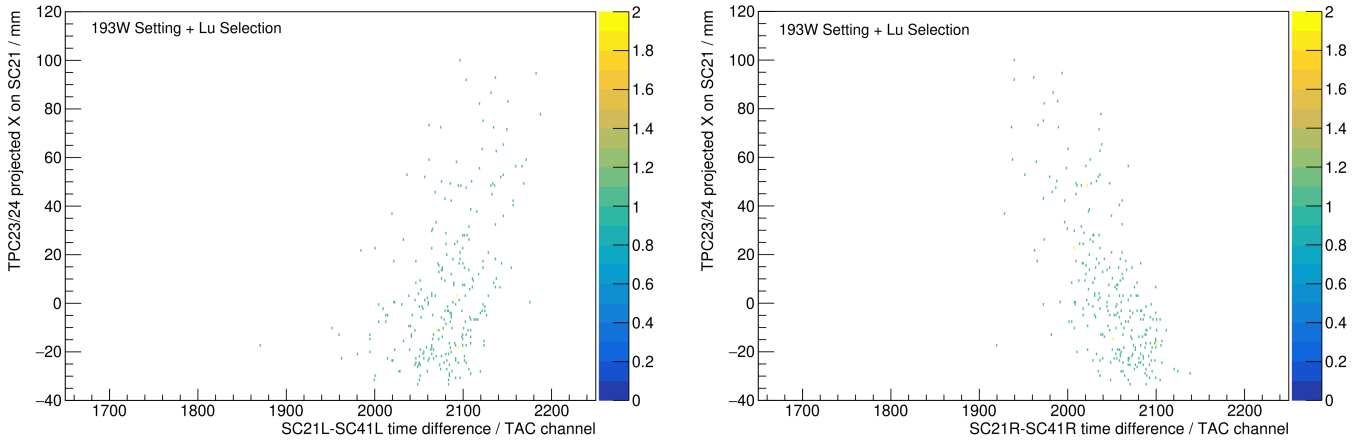


**(a)** **(b)**

**Figure G.9.:** Comparison of TPC horizontal position measurements over two different time-of-flight measurements. Here (a) shows the TPC23/24 projection unto S2 plotted over the SC21-41 left time difference and (b) the identical TPC projection but over the SC21-41 right time difference, for lutetium isotopes in the $^{193}$W setting.

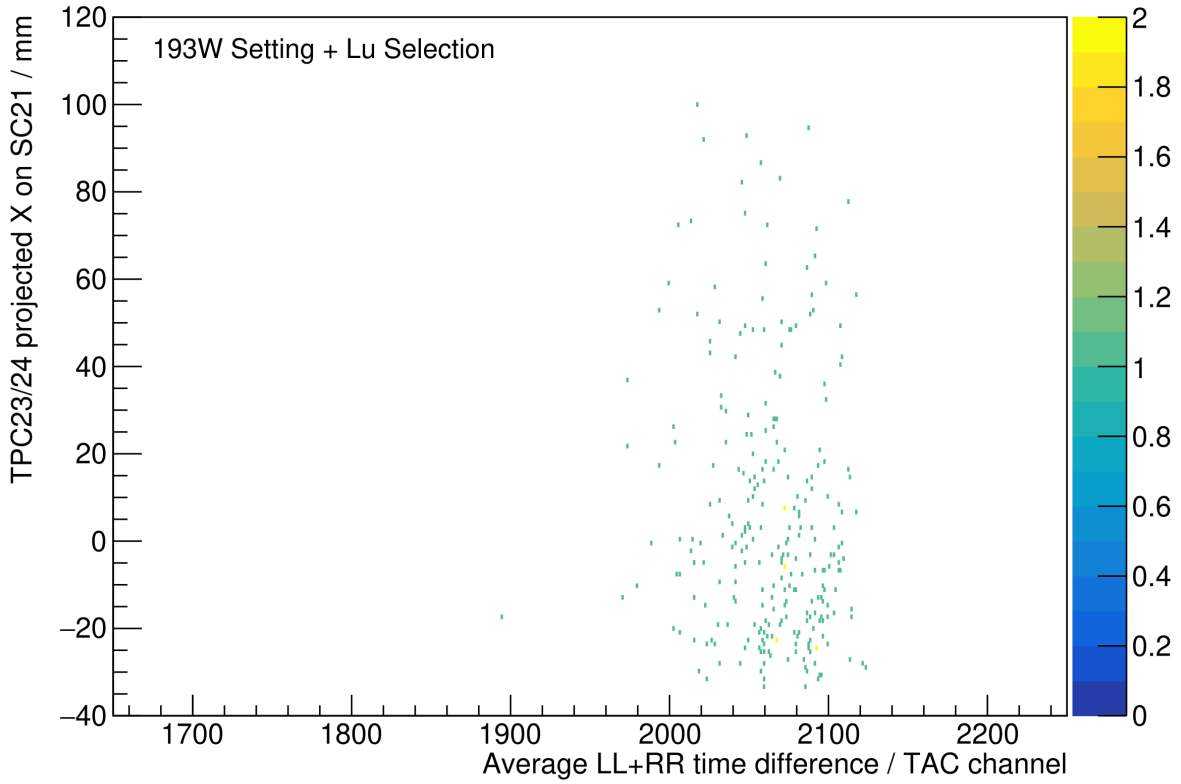


**Figure G.10.:** Plot of TPC23/24 horizontal position projection over the average ll+rr time difference for isotopes of lutetium in the $^{193}$W setting. Fragments do not appear shifted and stay in the light mass area.

Plot (a) from Fig. G.5 shows a similar separation quality of masses for platinum isotopes like Fig. G.3 (a). Through association with the ID plots from Subsec. 13.1.5, it is clear that higher mass isotopes possess

lower TAC channel numbers. Plot (b) shows a very similar bunched-up spectrum again. The result in Fig. G.6 shows a shift of the total spectrum by ca. 120 channels towards higher TAC channel numbers, thus lower masses. For the tungsten isotopes, Fig. G.7 (a) shows similar separation quality of masses as well as a shift by 120 channels compared to Pt. Plot (b) shows very similar spectrum again for the tungsten as well as the platinum isotopes. It would be expected, that a shift towards lower TAC channels occurs, instead the distribution stays nearly identical. The resulting average TOF in Fig. G.8 shows a shift of the total spectrum by ca. 50 channels towards higher TAC channel numbers, thus lower masses but less of a shift than for platinum. Therefore the tungsten isotopes appear in their correct region in the ID plot. In the final case of lutetium isotopes, Fig. G.9 (a) shows similar separation quality of masses as well as a shift towards higher TAC channel numbers, as is expected for lighter lutetium fragments. Although Plot (b) shows a very similar spectrum for the lutetium isotopes with no shift. It would be expected, that a shift towards lower TAC channels occurs, instead the distribution stays nearly identical again. The resulting average TOF in Fig. G.10 shows a negligible shift of the total spectrum, thus staying in the TAC channel region of lower masses and resulting in the ID plot as being identified with masses that are too low compared to their expectations. In conclusion, a comparison between SC21 and SC41, see Fig. G.1 and G.2, shows, that SC21 deviates in its position measurement from the expected spectrum similarly to SC41. Even though SC41 shows slight deviations in its own position measurement compared to what TPC41/42 would project unto SC41, those can be easily corrected by fitting a seventh-order polynomial and use it as a correction function for position measurements. In the case of SC21 a discontinuous shift appears around the center position, which usually entails another underlying issue other than irregular light transport through the plastic. Furthermore, the separate TOF measurement components, as defined in Ch. 12.3 in Eqs. 12.1 to 12.3 are investigated for the uncalibrated case in the $^{193}$W setting and platinum, tungsten and lutetium fragments in Fig. G.3 to G.10. When comparing the left TOF with the right TOF, it is expected that both distributions are mirrored to each other. This is clearly not the case in the right TOF channel, the distributions are bunched up in the same TAC region between channel number 2000 and 2100 with a very unclear separation of isotopes, compared to the left channel. Since the distribution in the right channel remains unchanged in position and shape, only the intensity changes, for each element. The average TOF value for each element changes differently. Platinum isotopes experience the strongest shift by ca. 120 channels towards higher TAC channels and are therefore shifted to lower masses, than are actually produced. For tungsten isotopes this shift becomes less, ca. 50-60 TAC channels, and shifts the fragments the closest towards their correct mass assignments in the ID plots. In the final selection for lutetium, the average TOF plot shows no clear shift in TAC channels, thus the lutetium fragments remain in the region of lighter isotopes. This can be observed for every utilized setting, such that elements with higher $Q_{max}$ than the isotope of interest are shifted towards lighter masses, the isotope of interest shows the closest agreement with its mass and isotopes with a lower $Q_{max}$ are as well shifted towards lower masses.

| Rates per spill | $^{205}$Au | $^{193}$W | $^{193}$Ta | $^{190}$Lu |
|---|---|---|---|---|
| Spill Length / s | 10 | 2 | 1 | 0.7 |
| SC21L | $6.8{\cdot}10^4$ | $2.9{\cdot}10^5$ | $4.9{\cdot}10^4$ | $2.8{\cdot}10^4$ |
| SC21R | $1.6{\cdot}10^5$ | $5.2{\cdot}10^5$ | $1.5{\cdot}10^5$ | $7.3{\cdot}10^4$ |
| SC22L | $1.7{\cdot}10^5$ | $7.3{\cdot}10^5$ | $1.4{\cdot}10^5$ | $9.5{\cdot}10^4$ |
| SC22R | $1.9{\cdot}10^5$ | $9.9{\cdot}10^5$ | $2.2{\cdot}10^5$ | $1.3{\cdot}10^5$ |
| SC41L | $2.3{\cdot}10^3$ | $4.7{\cdot}10^3$ | $1.0{\cdot}10^3$ | $5.5{\cdot}10^2$ |
| SC41R | $2.5{\cdot}10^3$ | $5.9{\cdot}10^3$ | $1.5{\cdot}10^3$ | $7.2{\cdot}10^2$ |

**Table G.1.:** Averaged scaler counts per spill for different settings and channels.

The shape of the distribution for the right TOF component also suggests that especially the right PMT of SC21 was either blinded by a high rate of fragments, be it fission fragments or high $Q_{max}$ projectile fragments or not properly installed. A lowered threshold for the right side could also be the case, but it could not be confirmed. It can be seen by the FRS scalers, which throughout the whole experiment, for every setting had a higher rate at the right side of SC21. Lastly, it cannot be ruled out, that a damage of scintillators at S4 contributed to this observation as well.

# H. S2 TPC Checksum Discussion

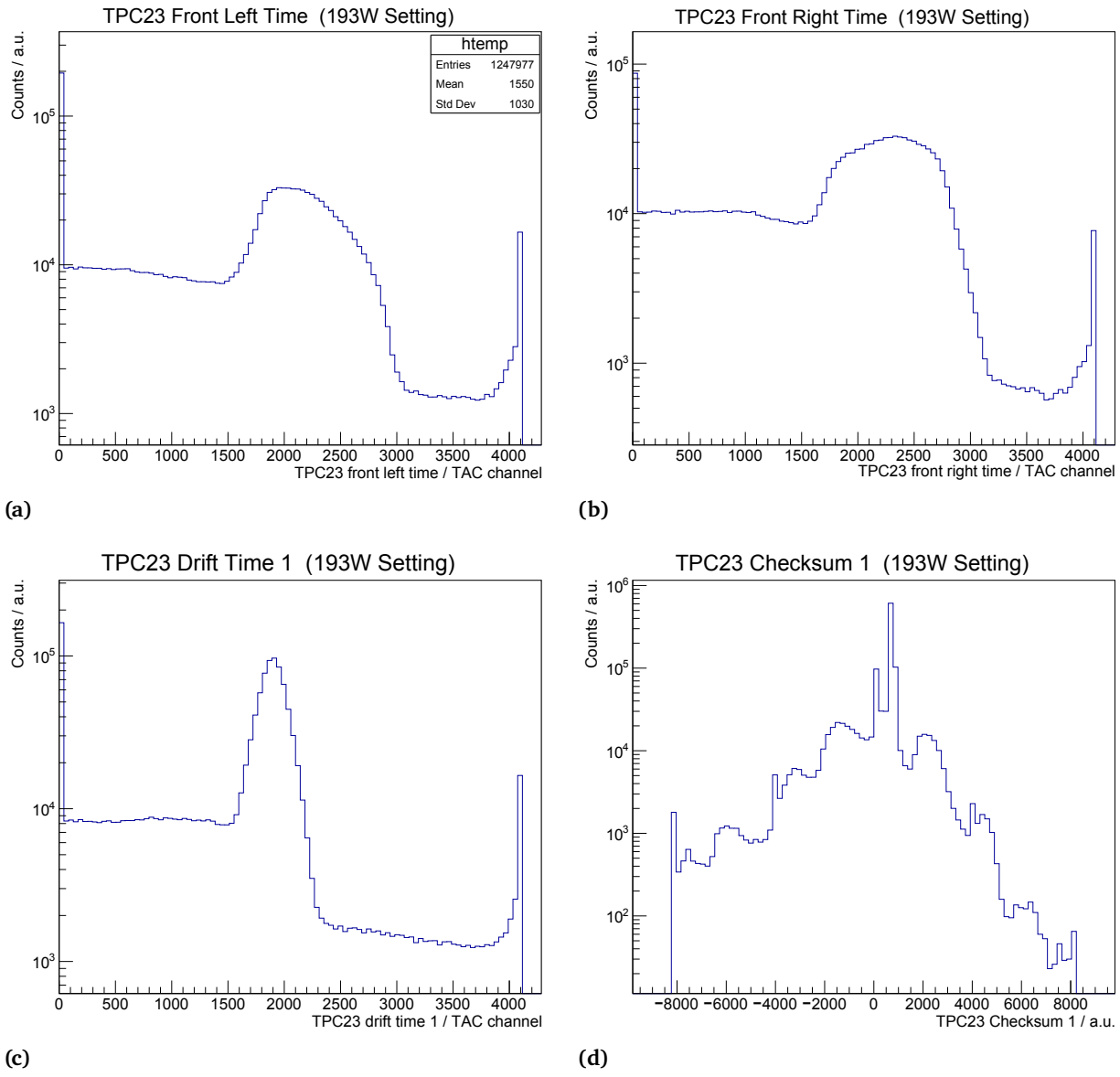


**Figure H.1.:** TPC23 Time and Checksum Spectra for the $^{193}$W Settings

From the initial definition of AoQ, which derives from Eqs. 2.4, 2.5 and 2.9, we see that it depends on the time-of-flight and position measurements at S2 as well as S4. With the additional path-length

correction of Subsec. 13.1.1, and even stronger dependency on position measurements is introduced into the determination and correction of AoQ, especially from S2. TPC calibration and TPC even clean-up are introduced in Sec. 12.3 and Subsec. 13.1.4 respectively. It is thereby important to understand how the checksum for each focal plane behaves. This will be shown representatively for the $^{193}$W settings, as it has the highest particle intensity per spill when normalized to the spill length, see Tab. G.1. Figures H.1 (a) to (d) together with H.2 (a) to (d) show the different time channels in TPCs 23 and 41 respectively together with the resulting checksum from said channels. The first important thing is to see how many events can not be assigned a timing information. This information is extracted from the events having exactly 0 as their TAC channel assignment. For H.1 (a) to (d) this would be 193270, 84950, 162957 and 75304 respectively. For H.2 (a) to (d) the values are 1053990, 968874, 813319 and 812621.

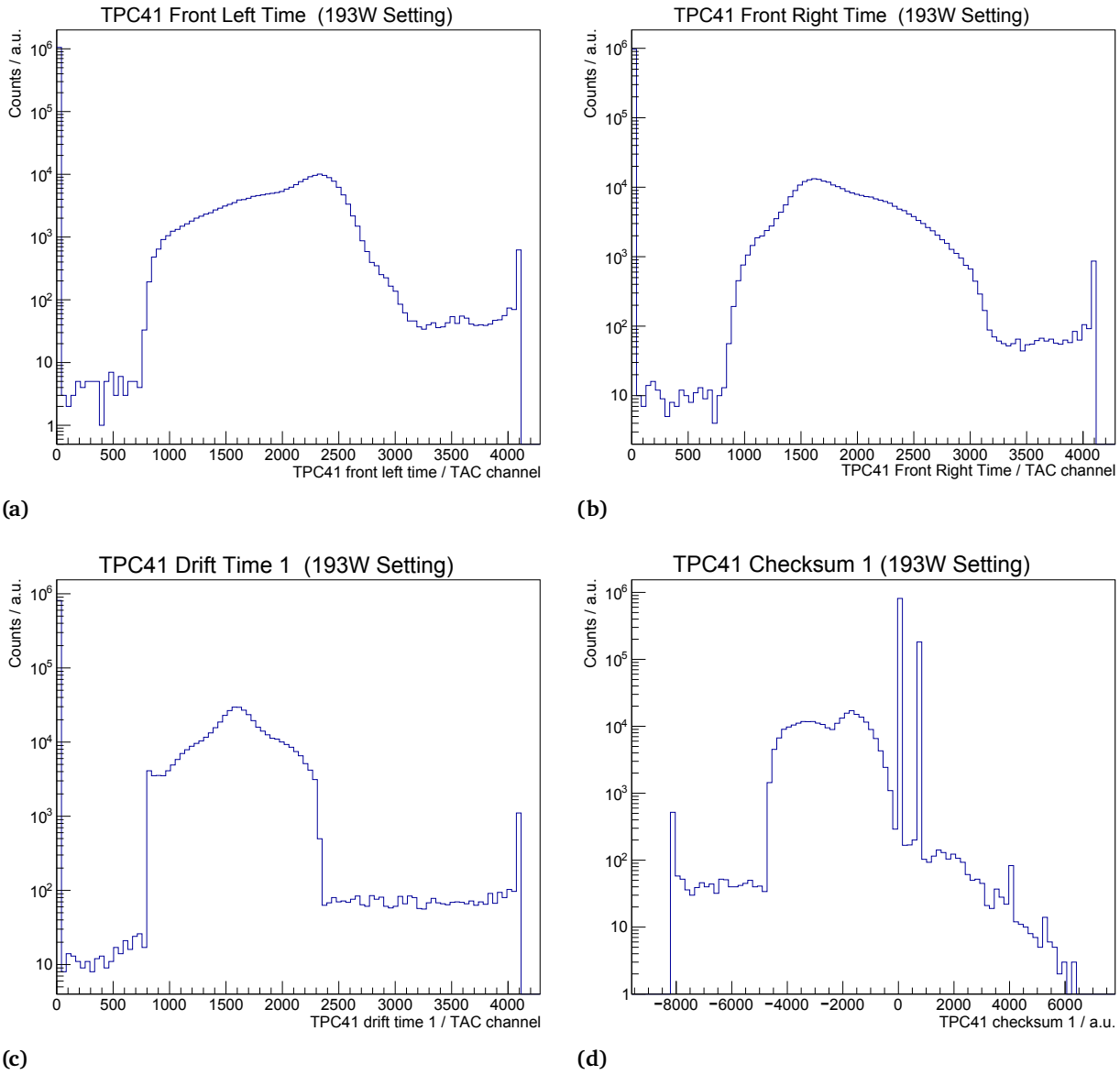


**Figure H.2.:** TPC41 Time and Checksum Spectra for the $^{193}$W Settings

This can be easily understood with Tab. G.1, since less particles reach S4 and thus more events with no timing information exist for TPC41 than TPC23. More importantly, when comparing S2 and S4 TPC time spectra it appears that S2 TPC time spectra possess a plateau before the timing distribution ($t$ <1500 channel number), whereas S4 TPC time spectra show a much smaller plateau ($t$ <800 channel number). Keeping in mind that during the $^{193}$W setting an S1 slit configuration of (10/-100) $\mathrm{mm}$ was used, thus the S2 horizontal position and TPC timing spectra show a sharp cut off, whereas S4 TPC timing spectra show a wider distribution. Nonetheless, a plateau in TPC timing spectra and unclear checksum distributions are an indication, that the rate at S2 was too high for the TPCs to handle and a similar effect to pile-up occurred, in which, instead of a measured charge which is higher than the actual particle charge, due to overlapping charge signals, the timing information within the S2 TPCs was distorted, because of other particles passing through the TPC too close to another. This leads to wrong position measurements and thus a wrong AoQ value. Assuming the ID plot from Fig. 13.10 (a) with no selections applied, it can be shown that, events from outside the defined checksum selection for each TPC still contribute to the individual isotopes, see Fig H.3. As a conclusion for the lutetium setting, all checksum selections have to be lifted and instead of relying on S2 information, all available S4 information has to be utilized to maximize the confirmed counts for each isotope, especially new ones.

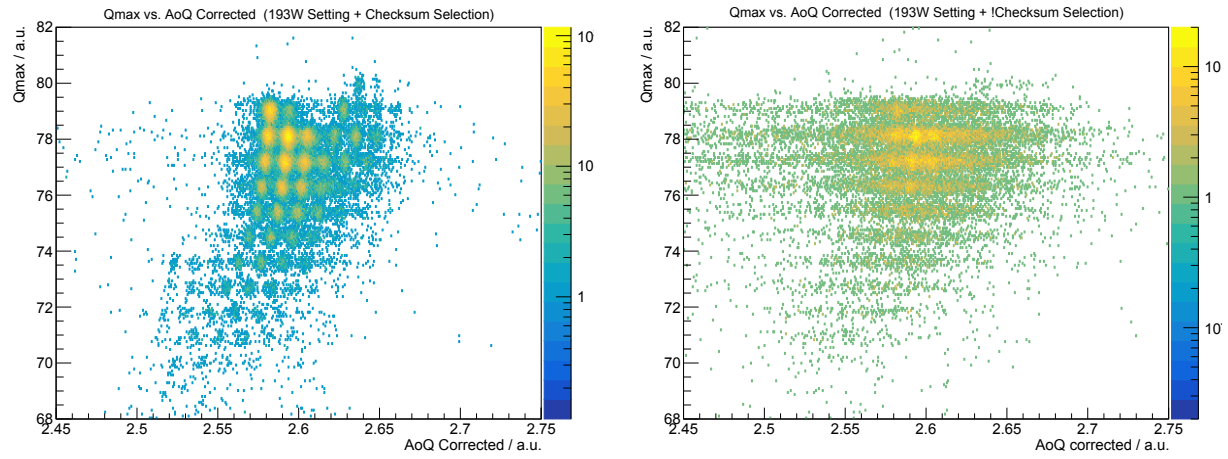


**(a)** **(b)**

**Figure H.3.:** (a) ID plot for $^{193}$W setting with only the checksum selections applied and (b) ID plot with the inverse checksum selection applied. It can be seen in (b) that not only background is removed but also potentially valid counts for isotopes.

# I. ID Reposition Coefficients

## I.1. $^{208}$Pb Setting

| $Q_{max}$ Repositioning | $^{208}Pb^{+82}$ | $^{208}Pb^{+82}$ | $^{208}Pb^{+82}$ |
|---|---|---|---|
| Offset | -0.31 | -0.52 | -0.63 |

**Table I.1.:** $Q_{max}$ repositioning coefficients for $^{208}$Pb setting. An individual offset in $Q_{max}$ was applied to each charge-state.

| $A/Q$ Repositioning | $^{208}Pb^{+82}$ | $^{208}Pb^{+82}$ | $^{208}Pb^{+82}$ |
|---|---|---|---|
| Offset | 0.00258 | 0.0179 | 0.034 |

**Table I.2.:** $A/Q$ repositioning coefficients for $^{208}$Pb setting. An individual offset in $A/Q$ was applied to each charge-state.

## I.2. $^{205}$Au Setting

| $Q_{max}$ Repositioning | $a_0$ | $a_1$ | $a_2$ |
|---|---|---|---|
| $^{205}$Au | $1.681{\cdot}10^{-3}$ | $8.636{\cdot}10^{-1}$ | $1.132{\cdot}10^{-4}$ |

**Table I.3.:** $Q_{max}$ repositioning coefficients for $^{205}$Au setting. The fit to a second-order polynomial resulted in the above coefficients.

| $A/Q$ Repositioning | Au | Pt | Ir | Os | Re |
|---|---|---|---|---|---|
| Offset | $-1.8964{\cdot}10^{-2}$ | $-5.6864{\cdot}10^{-2}$ | $4.3343{\cdot}10^{-2}$ | $9.2523{\cdot}10^{-2}$ | $1.3588{\cdot}10^{-1}$ |
| Slope $(1+\Delta)$ | $8.090{\cdot}10^{-3}$ | $2.301{\cdot}10^{-2}$ | $-1.545{\cdot}10^{-2}$ | $-3.370{\cdot}10^{-2}$ | $-4.955{\cdot}10^{-2}$ |

**Table I.4.:** $A/Q$ repositioning coefficients for $^{205}$Au setting. The fit to a linear function resulted in the above coefficients for each element.

## I.3. $^{193}$W Setting

| $Q_{max}$ Repositioning | $a_0$ | $a_1$ | $a_2$ |
|---|---|---|---|
| $^{193}$W | 1.543·10$^{-3}$ | 8.780·10$^{-1}$ | -2.163·10$^{-4}$ |

**Table I.5.:** $Q_{max}$ repositioning coefficients for $^{193}$W setting. The fit to a second-order polynomial resulted in the above coefficients.

| $A/Q$ Repositioning | Au | Pt | Ir | Os | Re |
|---|---|---|---|---|---|
| Offset | -1.6858·10$^{-1}$ | -1.4852·10$^{-1}$ | -2.4963·10$^{-1}$ | -1.9341·10$^{-1}$ | -2.1532·10$^{-1}$ |
| Slope (1+$\Delta$) | 7.0011·10$^{-2}$ | 6.0716·10$^{-2}$ | 9.8477·10$^{-2}$ | 7.5560·10$^{-2}$ | 8.3040·10$^{-2}$ |

**Table I.6.:** $A/Q$ repositioning coefficients for $^{193}$W setting. The fit to a linear function resulted in the above coefficients for each element.

| $A/Q$ Repositioning | W | Ta | Hf | Lu | Yb |
|---|---|---|---|---|---|
| Offset | -8.9479·10$^{-2}$ | 4.1901·10$^{-3}$ | -2.4827·10$^{-2}$ | -4.5446·10$^{-2}$ | -2.5143·10$^{-2}$ |
| Slope (1+$\Delta$) | 3.4004·10$^{-2}$ | -2.1714·10$^{-3}$ | 9.7594·10$^{-3}$ | 1.8971·10$^{-2}$ | -7.4292·10$^{-3}$ |

**Table I.7.:** $A/Q$ repositioning coefficients for $^{193}$W setting. The fit to a linear function resulted in the above coefficients for each element. Tm Offset = 2.0515·10$^{-1}$ and $\Delta$ = -7.6776·10$^{-2}$.

## I.4. $^{193}$Ta Setting

| $Q_{max}$ Repositioning | $a_0$ | $a_1$ | $a_2$ |
|---|---|---|---|
| $^{193}$Ta | 1.560·10$^{-3}$ | 8.813·10$^{-1}$ | -2.205·10$^{-4}$ |

**Table I.8.:** $Q_{max}$ repositioning coefficients for $^{193}$Ta setting. The fit to a second-order polynomial resulted in the above coefficients.

| $A/Q$ Repositioning | Ir | Os | Re | W | Ta |
|---|---|---|---|---|---|
| Offset | -1.5572·10$^{-1}$ | -1.9263·10$^{-1}$ | -2.0606·10$^{-1}$ | -8.9808·10$^{-2}$ | -3.6838·10$^{-2}$ |
| Slope (1+$\Delta$) | 6.1898·10$^{-2}$ | 7.4874·10$^{-2}$ | 7.8916·10$^{-2}$ | 3.3588·10$^{-2}$ | 1.3017·10$^{-2}$ |

**Table I.9.:** $A/Q$ repositioning coefficients for $^{193}$W setting. The fit to a linear function resulted in the above coefficients for each element.

| $A/Q$ Repositioning | Hf | Lu | Yb | Tm | Er |
|---|---|---|---|---|---|
| Offset | -3.8125·10$^{-2}$ | 9.9442·10$^{-2}$ | 3.8342·10$^{-2}$ | 9.9871·10$^{-2}$ | 1.2692·10$^{-1}$ |
| Slope (1+$\Delta$) | 1.3755·10$^{-2}$ | -3.8716·10$^{-2}$ | -1.4361·10$^{-2}$ | -3.7077·10$^{-2}$ | -4.6520·10$^{-2}$ |

**Table I.10.:** $A/Q$ repositioning coefficients for $^{193}$W setting. The fit to a linear function resulted in the above coefficients for each element.

## I.5. $^{190}$Lu Setting

| $Q_{max}$ Repositioning | $a_0$ | $a_1$ | $a_2$ |
|---|---|---|---|
| $^{190}$Lu | 1.568·$10^{-3}$ | 8.826·$10^{-1}$ | -2.230·$10^{-4}$ |

**Table I.11.:** $Q_{max}$ repositioning coefficients for $^{190}$Lu setting. The fit to a second-order polynomial resulted in the above coefficients.

| $A/Q$ Repositioning | Os | Re | W | Ta | Hf |
|---|---|---|---|---|---|
| Offset | -4.9826·$10^{-1}$ | -1.7311·$10^{-1}$ | -8.9731·$10^{-2}$ | -6.9376·$10^{-2}$ | -9.7302·$10^{-2}$ |
| Slope (1+$\Delta$) | 1.9063·$10^{-1}$ | 6.6051·$10^{-2}$ | 3.3668·$10^{-2}$ | 2.4582·$10^{-2}$ | 3.4395·$10^{-2}$ |

**Table I.12.:** $A/Q$ repositioning coefficients for $^{190}$Lu setting. The fit to a linear function resulted in the above coefficients for each element.

| $A/Q$ Repositioning | Lu | Yb | Tm | Er | Ho |
|---|---|---|---|---|---|
| Offset | -6.1757·$10^{-2}$ | 1.6490·$10^{-3}$ | 7.9550·$10^{-2}$ | -6.4017·$10^{-2}$ | 1.1732·$10^{-1}$ |
| Slope (1+$\Delta$) | 2.0722·$10^{-2}$ | -3.2649·$10^{-3}$ | -3.2461·$10^{-2}$ | 2.3168·$10^{-2}$ | -4.5383·$10^{-2}$ |

**Table I.13.:** $A/Q$ repositioning coefficients for $^{190}$Lu setting. The fit to a linear function resulted in the above coefficients for each element. Dy Offset = 1.4587·$10^{-1}$ and $\Delta$ = -5.4389·$10^{-2}$.

# List of Figures

# Listings

# List of Tables

# Bibliography


[1] H. Geissel, G. Münzenberg, and K. Riisager. “Secondary Exotic Nuclear Beams”. In: *Annual Review of Nuclear and Particle Science* 45 (1995), pp. 163–203. DOI: https://doi.org/10.1146/annurev.ns.45.120195.001115.

[2] A.C. Mueller. “Recent advances in exotic nuclear beams”. In: *Hyperfine Interactions* 127 (2000), pp. 21–29. DOI: https://doi.org/10.1023/A:1012685921375.

[3] J.S. Al-Khalili and E. Roeckl. In: *The Euroschool Lectures on Physics With Exotic Beams, Vol. II*. Ed. by J.S. Al-Khalili and E. Roeckl. Vol. Lecture Notes in Physics 700. Springer Berlin, Heidelberg, 2006. DOI: https://doi.org/10.1007/b11743651.

[4] E.M. Burbidge et al. “Synthesis of the Elements in Stars”. In: *Reviews of Modern Physics* 29 (1957), pp. 547–650. DOI: 10.1103/RevModPhys.29.547.

[5] C.J. et al. Horowitz. “r-process nucleosynthesis: connecting rare-isotope beam facilities with the cosmos”. In: *Journal of Physics G: Nuclear and Particle Physics* 46 (2019), p. 083001. DOI: https://dx.doi.org/10.1088/1361-6471/ab0849.

[6] G. Muenzenberg. “Radioactive beams at GSI”. In: *Progress in Particle and Nuclear Physics* 46.1 (2001), pp. 335–342. DOI: https://doi.org/10.1016/S0146-6410(01)00140-5.

[7] N. Kalantar-Nayestanaki and A. Bruce. “NUSTAR: NUclear STructure Astrophysics and Reactions at FAIR”. In: *Nuclear Physics News* 28.3 (2018), pp. 5–11. DOI: https://doi.org/10.1080/10619127.2018.1495476.

[8] D.E. Greiner et al. “Momentum Distributions of Isotopes Produced by Fragmentation of Relativistic $^{12}$C and $^{16}$O Projectiles”. In: *Physical Review Letters* 35 (1975), p. 152. DOI: https://doi.org/10.1007%2FBF02769517.

[9] R. Serber. “Nuclear Reactions at High Energies”. In: *Phys. Rev.* 72 (1947), pp. 1114–1115. DOI: https://link.aps.org/doi/10.1103/PhysRev.72.1114.

[10] URL: https://www.gsi.de/en/about_us/history (visited on 11/01/2021).

[11] H. Geissel et al. “The GSI projectile fragment separator (FRS): a versatile magnetic system for relativistic heavy ions”. In: *Nuclear Instruments and Methods in Physics Research B* 70 (1992), pp. 286–297.

[12] H. Geissel et al. “The Super-FRS project at GSI”. In: *Nuclear Instruments and Methods in Physics Research B* 204 (2003), pp. 71–85.

[13] G. Münzenberg et al. “Identification of element 107 by $\alpha$ correlation chains”. In: *Zeitschrift für Physik A Atoms and Nuclei* 300 (1981), pp. 107–108. DOI: https://doi.org/10.1007%2FBF01412623.

[14] G. Münzenberg et al. “Observation of one correlated $\alpha$-decay in the reaction $^{58}$Fe on $^{209}$Bi$\rightarrow^{267}$109”. In: *Zeitschrift für Physik A Atoms and Nuclei* 309 (1982), pp. 89–90. DOI: https://doi.org/10.1007%2FBF01420157.

[15] G. Münzenberg et al. “The identification of element 108”. In: *Zeitschrift für Physik A Atoms and Nuclei* 317 (1984), pp. 235–236. DOI: https://doi.org/10.1007/BF01421260.

[16] S. Hofmann et al. “Production and decay of 269110”. In: *Zeitschrift für Physik A Hadrons and Nuclei* 350 (1995), pp. 277–280. DOI: https://doi.org/10.1007%2FBF01291181.

[17] S. Hofmann et al. “The new element 111”. In: *Zeitschrift für Physik A Hadrons and Nuclei* 350 (1995), pp. 281–282. DOI: https://doi.org/10.1007%2FBF01291182.

[18] S. Hofmann et al. “The new element 112”. In: *Zeitschrift für Physik A Hadrons and Nuclei* 354 (1996), pp. 229–230. DOI: https://doi.org/10.1007%2FBF02769517.

[19] K. Blasche and H. Prange. “Die GSI in Darmstadt I”. In: *Physikalische Blätter* 33 (1977), pp. 249–261. DOI: https://doi.org/10.1002/phbl.19770330602.

[20] J.P. Hucka. “Implementation and Benchmark of a setting generator for the fragmenseparator FRS in the LHC Software Architecture LSA”. M.Sc. Thesis. Institut für Kernphysik, Technische Universität Darmstadt, unpublished, 2016.

[21] M. Lamont et al. “LHC Software Architecture: TI8 Commissioning”. In: *LHC Project Note* 368 (2005).

[22] H Weick. *ATIMA*. URL: https://web-docs.gsi.de/~weick/atima/ (visited on 11/09/2021).

[23] GSI Webmaster. *FAIR The Accelerator Facility*. URL: https://www.gsi.de/en/researchaccelerators/fair/the_machine (visited on 10/28/2021).

[24] The University of Tennessee Knoxville. *Experimental Nuclear Structure*. URL: http://www.phys.utk.edu/expnuclear/astro3.jpg (visited on 11/08/2021).

[25] S. Pietri et al. *Proposal: ”Search for new neutron-rich isotopes and exploratory studies in the element range from terbium to rhenium”*.

[26] I. Tanihata et al. *Conceptual Design Report for the Scientific Program of the Super-FRS Experiment Collaboration*. Tech. rep. Gesellschaft Für Schwerionenforschung mbH Darmstadt, 2016. URL: https://repository.gsi.de/record/200601.

[27] H. Rösch-Kabadayi. Dissertation in preparation. Technische Universität Darmstadt.

[28] M. Luoma. Dissertation in preparation. University of Jyväskylä.

[29] D. Amanbayev. Dissertation in preparation. Justig-Liebig-Universität Gießen.

[30] A. Prochazka. “Nuclear Structure Studies Via Precise Momentum Measurements”. Doctoral Dissertation. Justus-Liebig-Universität Gießen, 2011.

[31] F. Farinon. “Unambiguous Identification and Investigation of Uranium Projectile Fragments and Discovery of 63 New Neutron-rich Isotopes in the Element Range $61 \leq Z \leq 78$”. Doctoral Dissertation. Justus-Liebig-Universität Gießen, 2011.

[32] H Weick. *GICOSY Website*. URL: https://web-docs.gsi.de/~weick/gicosy/ (visited on 02/08/2022).

[33] H. Weick. *MOCADI Data Download Area*. URL: https://web-docs.gsi.de/~weick/mocadi/download/run81-ta2-2020.pdf (visited on 10/25/2022).

[34] C. Ziegler. “Aufbau und Einsatz eines Sekundärelektronen Transmissions-Monitors zur Messung des absoluten Teilchenstroms am Fragmentseparator”. Diploma Thesis. Technische Universität Darmstadt, 1992.

[35] M. Weber et al. *Beam-Profile Monitors with Gas Amplification and Current Readout for the Projectile-Fragment Separator*. Tech. rep. Gesellschaft Für Schwerionenforschung mbH Darmstadt, 1990.

[36] R. Janik et al. “Time Projection Chambers with C-pads for heavy ion tracking”. In: *Nuclear Instruments and Methods in Physics Research A* 640 (2011), pp. 54–57. DOI: 10.1016/j.nima.2011.02.052.

[37] *TPC Online Manual*. URL: https://www-win.gsi.de/frs/technical/FRSsetup/detectors/tpc/tpcmanual.pdf (visited on 11/15/2021).

[38] *Technical Manual Ionization Chamber MUSIC80*. URL: https://www-win.gsi.de/frs/technical/FRSsetup/detectors/music80/music80_manual.pdf (visited on 02/08/2022).

[39] S. Schlemme. “Nucleon-knockout Reactions from Neutron-deficient Carbon Isotopes and Characterization of a Particle Detector Combination for the Super-FRS at FAIR”. Doctoral Dissertation. Technische Universität Darmstadt, 2019.

[40] S. Schlemme et al. “Long-term exposure of a polycrystalline diamond detector irradiated by 62MeV/nucleon carbon beams”. In: *Diamond and Related Materials* 99 (2019), p. 107536. DOI: https://doi.org/10.1016/j.diamond.2019.107536.

[41] H. Geissel et al. *Technical Design Report on the Super-FRS*. Tech. rep. Gesellschaft Für Schwerionenforschung mbH Darmstadt, 2008. URL: https://repository.gsi.de/record/54552.

[42] J.S. Winfield et al. “Ion-optical developments tailored for experiments with the Super-FRS at FAIR”. In: *Nuclear Instruments and Methods in Physics Research Section B* 491 (2021), pp. 38–51. DOI: https://doi.org/10.1016/j.nimb.2021.01.004.

[43] N. Kalantar-Nayestanaki. Private communication. 2022.

[44] R. Bennett et al. *NuPECC Report - The NuPECC Working Group on Radioactive Nuclear Beam Facilities*. Tech. rep. Nuclear Physics European Collaboration Committee, 2000. URL: https://www.nupecc.org/pub/radioactive_nuclear_beam_facilities_2000.pdf.

[45] C. Scheidenberger et al. “Charge states of relativistic heavy ions in matter”. In: *Nuclear Instruments and Methods in Physics Research B* 142 (1998), p. 441. DOI: https://doi.org/10.1016/S0168-583X(98)00244-4.

[46] J. Beringer et al. “Review of Particle Physics”. In: *Physical Review D* 86 (2012), pp. 324–326. URL: https://journals.aps.org/prd/pdf/10.1103/PhysRevD.86.010001.

[47] H. Weick. URL: https://www-windows.gsi.de/frs-setup/AREAS/AREAS%20TA/TS1ET5-26062014.png (visited on 11/22/2021).

[48] H. Weick. URL: https://www-windows.gsi.de/frs-setup/AREAS/AREAS%20S2/S2_Degrader-Overview.htm (visited on 11/22/2021).

[49] ACC-nomen Team. *System for Nomenclatures of Accelerator Devices at FAIR and GSI v15.9*. URL: https://www-acc.gsi.de/wiki/pub/Accnomen/WebHome/acc-nomen.pdf (visited on 11/22/2021).

[50] H. Weick et al. “Slowing down of relativistic few-electron heavy ions”. In: *Nuclear Instruments and Methods in Physics Research B* 164/165 (2000), pp. 168–179.

[51] J. Lindhard and A.H. Sörensen. “Relativistic theory of stopping for heavy ions”. In: *Physical Review A* 53 (1996), p. 2443. DOI: https://doi.org/10.1103/PhysRevA.53.2443.

[52] W.H. Barkas and M.J. Berger. *Tables of Energy Losses and Ranges of Heavy Charged Particles*. Tech. rep. California. Univ., of Berkeley. Lawrence Radiation Lab.; National Bureau of Standards, Washington, D.C., 1964. URL: https://www.osti.gov/biblio/4682091-tables-energy-losses-ranges-heavy-charged-particles.

[53] J.D. Jackson and R.L. McCarthy. “$z^3$ Corrections to Energy Loss and Range”. In: *Physical Review B* 6 (1972), p. 4131. DOI: https://doi.org/10.1103/PhysRevB.6.4131.

[54] J. Lindhard. “The Barkas effect - or $Z_1^3$, $Z_1^4$-corrections to stopping of swift charged particles”. In: *Nuclear Instruments and Methods* 132 (1976), pp. 1–5. DOI: https://doi.org/10.1016/0029-554X(76)90702-3.

[55] R.M. Sternheimer and R.F. Peierls. “General Expression for the Density Effect for the Ionization Loss of Charged Particles”. In: *Physical Review B* 3 (1971), p. 3681. DOI: https://doi.org/10.1103/PhysRevB.3.3681.

[56] J.F. Ziegler. *SRIM - The Stopping and Range of Ions in Matter*. URL: http://www.srim.org/ (visited on 11/24/2021).

[57] J.F. Ziegler and J.P. Biersack. “The Stopping and Range of Ions in Matter”. In: *Treatise on Heavy-Ion Science*. Boston, MA: Springer, 1985, pp. 93–129. DOI: https://doi.org/10.1007/978-1-4615-8103-1_3.

[58] C. de Boor. “A Practical Guide to Splines”. In: *Mathematics of Computation* 34 (1980), pp. 325–326. DOI: https://doi.org/10.2307/2006241.

[59] H. Weick. Private communication. 2016.

[60] W.H. Press et al. “Parabolic Interpolation and Brent’s Method in One Dimension”. In: *Numerical Recipes in C: The Art of Scientific Computing, Third Edition*. New York, NY: Cambridge University Press, 2007, pp. 496–498.

[61] *EPICS Website*. URL: https://epics-controls.org/ (visited on 11/26/2021).

[62] *TANGO Website*. URL: https://www.tango-controls.org/ (visited on 11/26/2021).

[63] D. Ondreka, J. Fitzek, and R. Müller. Presentation "LSA for GSI/FAIR". 2010. URL: https://www-acc.gsi.de/wiki/pub/Applications/LsaPresentationsAndPublications/20100621_Overview_LSA_at_GSI_final.pdf.

[64] D. Ondreka. Presentation "Die Zukunft der Datenversorgung für GSI und FAIR". 2009. URL: https://www-acc.gsi.de/wiki/pub/Applications/LsaPresentationsAndPublications/Zukunft_Datenversorgung_GSI_FAIR_20090924.pdf.

[65] D. Ondreka. Presentation "Die Zukunft der Datenversorgung für GSI und FAIR". 2009. URL: https://www-acc.gsi.de/wiki/pub/Applications/LsaPresentationsAndPublications/Zukunft_Datenversorgung_GSI_FAIR_20090924.pdf.

[66] E.M. Friedlander and H.H. Heckman. In: *Treatise on Heavy-Ion Science*. Ed. by D.A. Bromley. Vol. 4. New York, NY: Plenum, 1985, p. 403.

[67] S. Pietri. Presentation "First Results from the stopped beam isomer RISING campaigns at GSI". 2006.

[68] S. Pietri et al. “First Results from the stopped beam isomer RISING campaigns at GSI”. In: *Acta Physica Polonica B*. Vol. 38. Regular Series 4. 2007, p. 1255.

[69] T. Kurtukian Nieto. “Production and decay half-lives of heavy neutron-rich nuclei approaching the stellar nucleosynthesis r-process path around A=195”. Doctoral Dissertation. Universidade de Santiago De Compostela, 2007.

[70] E. Casarejos. “Isotopic production cross sections of spallation-evaporation residues from reactions of $^{238}$U(1A GeV) with deuterium”. In: *Physical Review C* 74 (2006), p. 044612. DOI: https://doi.org/10.1103/PhysRevC.74.044612.

[71] A.S. Goldhaber. “Statistical models of fragmentation processes”. In: *Physics Letters B* 53 (1974), pp. 306–308. DOI: https://doi.org/10.1016/0370-2693(74)90388-8.

[72] K. Sümmerer et al. “Target fragmentation of Au and Th by 2.6 GeV protons”. In: *Physical Review C* 42 (1990), pp. 2546–2561. DOI: https://doi.org/10.1103/PhysRevC.42.2546.

[73] K. Sümmerer and B. Blank. “Modified empirical parametrization of fragmentation cross sections”. In: *Physical Review C* 61 (2000), p. 034607. DOI: https://doi.org/10.1103/PhysRevC.61.034607.

[74] K. Sümmerer. “Improved empirical parametrization of fragmentation cross sections”. In: *Physical Review C* 86 (2012), p. 014601. DOI: https://doi.org/10.1103/PhysRevC.86.014601.

[75] O.B. Tarasow and D. Bazin. *LISE++ Website*. URL: http://lise.nscl.msu.edu/lise.html (visited on 12/01/2021).

[76] O.B. Tarasow and D. Bazin. “LISE++: Exotic beam production with fragment separators and their design”. In: *Nuclear Instruments and Methods in Physics Research B* 376 (2016), pp. 185–187. DOI: http://dx.doi.org/10.1016/j.nimb.2016.03.021.

[77] H. Weick. *MOCADI Website*. URL: https://web-docs.gsi.de/~weick/mocadi/ (visited on 12/01/2021).

[78] N. Iwasa, H. Weick, and H. Geissel. “New features of the Monte-Carlo code MOCADI”. In: *Nuclear Instruments and Methods in Physics Research Section B: Beam Interactions with Materials and Atoms* 269 (2011), pp. 752–758. DOI: https://doi.org/10.1016/j.nimb.2011.02.007.

[79] T. Kurtukian-Nieto et al. “Production cross sections of heavy neutron-rich nuclei approaching the nucleosynthesis r-process path around A=195”. In: *Physical Review C* 89 (2014), p. 024616. DOI: https://doi.org/10.1103/PhysRevC.89.024616.

[80] *COFRA Website*. URL: http://www.usc.es/genp/cofra/ (visited on 12/02/2021).

[81] *ABRABLA Website*. URL: https://www.gsi.de/work/forschung/nustarenna/nustarenna_divisions/kernreaktionen/r3b_project_group/software-nuclear_reaction_models (visited on 12/02/2021).

[82] J.P. Hucka. “Implementation of a control system for the fragmenseparator FRS in the LHC Software Architecture LSA”. M.Sc. Proposal. Institut für Kernphysik, Technische Universität Darmstadt, unpublished, 2016.

[83] *Spring Website*. URL: https://spring.io/ (visited on 01/31/2022).

[84] B.J. Franczak. *Mirko Website*. URL: https://www.gsi.de/work/gesamtprojektleitung_fair/sis100sis18_sis/system_design_sis100sis18_sys/projekte_system_design_sis100sis18/mirko (visited on 02/01/2022).

[85] A. Prochazka. *CAtima extended Interface*. URL: https://www.isotopea.com/webatima/ (visited on 03/01/2022).

[86] F. Schirru. *MagStat Git repository, only accessible from within acc.gsi.de*. URL: https://git.acc.gsi.de/fcc-applications/frs-magstat-app (visited on 03/24/2022).

[87] R. Steinhagen. Presentation "Dry-Run Procedures and Sequencer Tutorial". 2017. URL: https://fair-wiki.gsi.de/foswiki/pub/FC2WG/HardwareCommissioning/Sequencer/20171207_Sequencer_tutorial.pdf.

[88] F. Schirru. *DriveStat Git repository, only accessible from within acc.gsi.de*. URL: https://git.acc.gsi.de/fcc-applications/frs-drivestat-app (visited on 03/15/2022).

[89] F. Schirru. *FMGSKAL Git repository, only accessible from within acc.gsi.de*. URL: https://git.acc.gsi.de/fcc-applications/frs-fmgskal-app (visited on 03/15/2022).

[90] A. Walter. *Parammodi Git repository, only accessible from within acc.gsi.de*. URL: https://git.acc.gsi.de/fcc-applications/parammodi-app (visited on 03/15/2022).

[91] A. Walter. *DeviceControl Git repository, only accessible from within acc.gsi.de*. URL: https://git.acc.gsi.de/fcc-applications/device-control-app (visited on 03/15/2022).

[92] Apache Software Foundation (ASF). *Apache Maven Project*. URL: https://maven.apache.org/ (visited on 03/15/2022).

[93] A. Herlert et al. "The NUSTAR program at FAIR". In: *EPJ Web of Conferences* 71 (2014), p. 00064. DOI: https://doi.org/10.1051/epjconf/20147100064.

[94] J. Erler et al. "The limits of the nuclear landscape". In: *Nature* 486 (2012), pp. 509–512. DOI: https://doi.org/10.1038/nature11188.

[95] T. Davinson et al. *Advanced Implantation Detector Array (AIDA)*. URL: https://www2.ph.ed.ac.uk/~td/AIDA/ (visited on 04/05/2022).

[96] L. M. Fraile et al. *FATIMA - FAst TIMing Array*. URL: http://nuclear.fis.ucm.es/fasttiming/ (visited on 04/05/2022).

[97] W. R. Plaß et al. "The FRS Ion Catcher - A facility for high-precision experiments with stopped projectile and fission fragments". In: *Nuclear Instruments and Methods in Physics Research Section B: Beam Interactions with Materials and Atoms* 317 (2013), pp. 457–462. DOI: https://doi.org/10.1016/j.nimb.2013.07.063.

[98] J. J. Cowan et al. "Heavy element synthesis in the oldest stars and the early Universe". In: *Nature* 440 (2006), pp. 1151–1156. DOI: https://doi.org/10.1038/nature04807.

[99] T. Dickel. Private communication. 2020.

[100] R. Kumar et al. "Testing of a DSSSD detector for the stopped RISING project". In: *Nuclear Instruments and Methods in Physics Research Section A: Accelerators, Spectrometers, Detectors and Associated Equipment* 598 (2009), pp. 754–758. DOI: https://doi.org/10.1016/j.nima.2008.08.155.

[101] N. Kuzminchuk-Feuerstein. *Hamamatsu R9800 Specifications*. URL: http://web-docs.gsi.de/~nkuzminc/Images/R9800_H10580.pdf (visited on 04/07/2022).

[102] N. Kuzminchuk-Feuerstein. *Hamamatsu R2083, R3377 Specifications*. URL: http://web-docs.gsi.de/~nkuzminc/Images/R2083.pdf (visited on 04/07/2022).

[103] E. Haettner et al. "New high-resolution and high-transmission modes of the FRS for FAIR phase-0 experiments". In: *Nuclear Instruments and Methods in Physics Research Section B: Beam Interactions with Materials and Atoms* 463 (2019), pp. 455–459. DOI: https://doi.org/10.1016/j.nimb.2019.04.025.

[104] D. J. Morrissey. "Systematics of momentum distributions from reactions with relativistic ions". In: *Physical Review C* 39 (1989), p. 460. DOI: https://doi.org/10.1103/PhysRevC.39.460.

[105] H. Weick. Private communication. 2020.

[106] H. Weick. *FRS Optics*. URL: http://web-docs.gsi.de/%7Eweick/mocadi/download/run81-ta2-2020.mtx (visited on 05/06/2022).

[107] J. L. Rodriguez-Sánchez. Private communication. 2022.

[108] J. L. Rodriguez-Sánchez et al. "Study of $\Delta$ excitations in medium-mass nuclei with peripheral heavy ion charge-exchange reactions". In: *Physics Letters B* 807 (2020), p. 135565. DOI: https://doi.org/10.1016/j.physletb.2020.135565.

[109] A. Boudard et al. "Intranuclear cascade model for a comprehensive description of spallation reaction data". In: *Physical Review C* 66 (2002), p. 044615. DOI: https://doi.org/10.1103/PhysRevC.66.044615.

[110] J. Benlliure et al. “Calculated nuclide production yields in relativistic collisions of fissile nuclei”. In: *Nuclear Physics A* 628 (1998), pp. 458–478. DOI: https://doi.org/10.1016/S0375-9474(97)00607-6.

[111] GEANT 4 collaboration. “GEANT4 - a simulation toolkit”. In: *Nuclear Instruments and Methods in Physics Research Section A: Accelerators, Spectrometers, Detectors and Associated Equipment* 506 (2003), p. 250. DOI: https://doi.org/10.1016/S0168-9002(03)01368-8.

[112] A. Heikkinen et al. “Implementation of INCL cascade and ABLA evaporation codes in GEANT4”. In: *Journal of Physics: Conference Series* 119 (2008), p. 032024. DOI: https://doi.org/10.1088/1742-6596/119/3/032024.

[113] D. Amanbayev. Private communication. 2022.

[114] J. Kurcewicz et al. “Discovery and cross-section measurement of neutron-rich isotopes in the element range from neodymium to platinum with the FRS”. In: *Physics Letters B* 717 (2012), pp. 371–375. DOI: https://doi.org/10.1016/j.physletb.2012.09.021.

[115] M. Thoennessen. *Discovery of Nuclides Project*. URL: https://people.nscl.msu.edu/~thoennes/isotopes/ (visited on 05/29/2022).

[116] N. Fukuda et al. “Identification of New Neutron-Rich Isotopes in the Rare-Earth Region Produced by 345 MeV/nucleon $^{238}$U”. In: *Journal of the Physical Society of Japan* 87 (2018), p. 014202. DOI: https://doi.org/10.7566/JPSJ.87.014202.

[117] H. Weick. *FRS Setup Page*. URL: https://www-windows.gsi.de/frs-setup/ (visited on 11/19/2021).

[118] J. Netzel and R. Müller. Presentation "LSA Course part 1: parameter hierarchy and makerules". 2009. URL: https://edms.cern.ch/ui/file/1057494/1/20090113_LSA_Course_1_Parameter_Makerules.pdf.

[119] J. Netzel and R. Müller. Presentation "LSA Course part 3: Context and rules". 2009. URL: https://edms.cern.ch/ui/file/1057494/1/20090128_LSA_Course_3_Context_and_Rules.pdf.